

Model-Based Lower-Limb Powered Prosthesis Control:
Developing and Realizing Nonlinear Subsystem Control
Methods for Generalizable Prosthesis Control

Thesis by
Rachel Gehlhar

In Partial Fulfillment of the Requirements for the
Degree of
Doctor of Philosophy in Mechanical Engineering

The logo for the California Institute of Technology (Caltech), featuring the word "Caltech" in a bold, orange, sans-serif font.

CALIFORNIA INSTITUTE OF TECHNOLOGY
Pasadena, California

2023
Defended December 2nd, 2022

© 2023

Rachel Gehlhar

ORCID: 0000-0002-4838-8839

All rights reserved except where otherwise noted

ACKNOWLEDGEMENTS

To Dr. Ames, to whom I will always be grateful for our conversation in my 2nd year of grad school where you essentially told me to find a way to “use the force” in prosthesis control. This provided the initial condition for my PhD trajectory which converged on the work in this thesis. I also appreciated the vision you shared with me as I made steps forward in my research. Without your vision, I would only be able to say “I did a thing, here’s the thing,” but you helped me understand and see the relevance and significance of my contributions in the broader field. I also thank you for the opportunity to join your lab in the first place and your guidance and support in my faculty position search.

To my thesis committee, Dr. Joel Burdick, Dr. Richard Murray, and Dr. Michael Dickinson for taking the time to become familiar with my research and to give me helpful feedback and suggestions to guide my research path. Dr. Burdick, thank you for your advice and support through the years and helping me navigate grad school at Caltech. Dr. Murray, thank you for giving me the opportunity to be a TA for your class and mentoring me in that role. It was a great learning experience that led me to pursue a faculty position and will serve me well in this upcoming role. Dr. Dickinson, thank you for bringing your perspective from a biomechanics standpoint, sharing ideas from this field that could be useful in my work and explaining what results would be important to this community.

To the people I had the opportunity to collaborate with: Jenna Reher, Chang Gao, Tobi Delbruck, Shih-Chii Liu, Yuxiao Chen, You Yu, Amy (Kejun) Li, Maegan Tucker, Je-han Yang, and Aaron Young. Thank you for your help in my research and for giving me the opportunity to be involved in your own.

To my labmates. Eric Ambrose, you helped me become integrated in the lab and always were there to assist me with mechanical issues and design projects. Christian Hubicki, you and Jenna Reher helped me in my NSF proposal, especially when I rewrote the entire research statement the day before the due date. You were welcoming and supportive to me when I joined the lab. Jenna Reher, I have always aspired to acquire just half of your knowledge. You answered countless questions of mine and helped me in so many aspects of my research project and PhD journey. In addition to your vast knowledge of robotics, you were also so kind. Thomas Gurriet, thank you for your help with getting started with code and hardware things

and for sharing your expertise with me. Meagan Tucker, I so appreciate all of our conversations during grad school, it was great to have someone I could relate to and talk so freely with. I also really enjoyed working with you on papers. Andrew Taylor, Amy (Kejun) Li, Noel Csomay-Shanklin, Min Dai, and Ryan Cosner, thank you for the assistance you gave me at various times and for the camaraderie in lab.

To my undergraduate professors. To Dr. AnnMarie Thomas, my undergraduate advisor, who instilled courage and confidence in me to pursue my interests. You were the most valuable part of my St. Thomas education and what you gave me through your mentorship is something no one could have taught me through a classroom lecture. To Dr. Jeff Jalkio, my first undergraduate research advisor, who saw potential in me for research that I did not yet see in myself and gave me the opportunity to discover those skills and interests for myself at a time when I did not even know what “research” was. Thank you also for connecting me with Dr. Ames so I could have this research experience. To Dr. Brittany Nelson-Cheeseman, who led and supported me to pursue a Research Experience for Undergraduates opportunity and continued to support me in my pursuit of graduate school.

To my family. To my parents who have been my biggest cheerleaders. Dad, it is because of you that I went to St. Thomas for undergrad and received such an impactful mentorship experience. Mom, it is because of your support that I was able to keep my head up in those initial years of grad school. Thank you for helping me move twice in a few months, for flying to California and showing up on my doorstep less than 24 hours after you found out I was sick, and for unpromptedly asking me to talk when you thought I may need to my first week of finals at Caltech. To my sisters, Marie and Laura, who gave me a space where I was known while I was far away from what I knew. To my nephew Levi, who has brought me so much joy in grad school from the moment I found out he existed. The ways you continued to find joy in the world and rapidly grew and changed added so much excitement and joy to my life while research moved seemingly slowly. To my Aunt Jo and Uncle Bob who have been there for me throughout my life and continue to celebrate the successes with me and encourage me in the in between. And to my other relatives that have encouraged me through cards prayers, and our visits.

To the Graduate Christian Fellowship group at Caltech and all of my friends from there who gave me a community during my time here. I previously felt isolated between two worlds, those that understood grad school and those that understood my

faith. Finding a group that understood both and could help me navigate questions at the intersection was such a fulfilling and supportive experience to me.

To my friends from earlier walks of life: Briteigh Garcia, Audra Erickson, Lauren Miller, Becca Shultz, Maria Hammon, and Laura Spittlemeister. Thank you for your continued support to me in this journey based on your history of knowledge of me and the time you took to understand how I and my life was changing.

To the friends I met during my time at Caltech: Shilpa Joy, Kimberley MacDonald, Ellen Novoseller, Beth Behmer, Amanda Bouman, Hannah Manestch, Maria Camarca, Sami Chang, Connor McMahan, Filippos Filippitzis, and Apurva Badithela. Thank you for taking the time to get to know me, meeting for lunch, and talking with me about grad school and life and whatever was happening at the time. You helped me make it through and provided a sense of connection to me during a time of so much uncertainty. Thank you for making my time here so much more enjoyable as well.

To James Humann who has been my rock of consistency throughout all the ups and downs of grad school. I am grateful for having met you 3 days after passing quals and not 3 days before. While I previously thought I did not need someone that had been through grad school and I did not want to date another engineer, I am so grateful to have met you who had been through engineering graduate school. You understood what it was like and had already finished so I could be the stressed out one. I appreciated the perspective you shared with me about what really mattered having made it to the other side, the help you gave me in navigating different situations that arose, and the encouragement you offered when I did not know if I had what it took. I also appreciated your help in talking through research and presentation ideas with me and helping me with application essays. Your ability to capture the essence of what I am trying to convey and be able to express it in a clearer and more concise way astounds me and was a huge asset to my essay writing. Getting to bike, hike, cook, eat, watch TV, and just talk and hang out with you provided a huge source of stress relief and support to me to keep facing the daily grind of research. Finding someone who can support me in my career path, emotionally, and in my faith is a rare combination to find, and for that, I am so grateful to have met you and have had you in my life for so much of grad school.

Finally, I am grateful to my God whose hand was so evident in leading me to Caltech and has continued to care for me while here. I am grateful for the line up of friends you provided for me as friends kept moving away. You created my inmost being

and have helped me to understand, embrace, and figure out how to live out who you made me to be.

ABSTRACT

While there are over 600,000 lower-limb amputees in the US, commercially available prostheses remain limited to mostly passive devices. People that walk with a passive prosthesis experience an increase in energy expenditure, a decrease in comfortable walking speed, and gait asymmetry which leads to degenerative conditions. To address these limitations, researchers have developed powered prostheses with the aim of replicating the net positive energy biological limbs supply to humans in walking. These active devices have been shown to decrease users' metabolic cost and increase their comfortable walking speed. However, the control methods to achieve these results typically require hours of heuristic tuning for every user and every behavior. This motivates developing more formal prosthesis control methods that generalize between users.

Formal nonlinear control methods have been developed to realize energy efficient, human-like walking on bipedal robots. These model-based approaches provide a systematic approach to generate and realize provably stable walking gaits. However, these methods cannot be directly applied to prostheses since they depend on a dynamic model of the entire system, and in the case of the prosthesis, the human dynamics are unknown.

To address this challenge, we develop a theoretical framework to translate model-based bipedal control methods to prostheses with the aim of realizing a generalizable prosthesis control method. We separate the prosthesis subsystem from the remaining human portion of the system and model the human's impact on the prosthesis dynamics with a measure of the interaction forces between the human and the prosthesis. We theoretically prove that a model-based controller developed in this separable subsystem framework is equivalent to one developed with knowledge of the full-order human-prosthesis system. With control Lyapunov functions, we develop a wider class of subsystem controllers that solely depend on local information but provide full-order system guarantees, even in the presence of force estimate errors. This work bridges the gap between bipedal control methods and prostheses, allowing us to leverage the benefits of model-based approaches on prostheses.

We demonstrated a controller of this class through an online optimization-based approach on a powered knee-ankle prosthesis, realizing the first model-dependent lower-limb prosthesis controller that accounts for the interaction force between the

human and the prosthesis. For a first pass, a force-estimation method was used that yields improved tracking of the desired trajectories over model-independent prosthesis control methods. Then, we incorporated a load cell into the prosthesis platform at the human-prosthesis attachment point to measure the interaction forces, and an inertial measurement to measure the rotation and velocity of the human's thigh. These two sensors completed the prosthesis dynamics model. A pressure sensor incorporated into the prosthesis' shoe measured the ground reaction forces, enabling the prosthesis to respond to its real-world environment, proving robust to 4 different terrains. We extended this controller to a multi-domain hybrid system approach to model the changing contact points occurring in human heel-toe roll. By allowing the prosthesis to sense the human's large varying dynamic load and respond accordingly, this model-based prosthesis controller emulated subject-specific human kinematic trends on a knee-ankle prosthesis for two subjects with no tuning in between, suggesting this approach could yield a method that generalizes between users. Leveraging the structure of nonlinear control methods to incorporate human sensory feedback could close the loop between human behavior and prosthesis control to bring these devices into everyday use.

PUBLISHED CONTENT AND CONTRIBUTIONS

- [1] R. Gehlhar and A. D. Ames, “Emulating human kinematic behavior on lower-limb prostheses via multi-contact models and force-based nonlinear control,” in *Submitted to 2023 IEEE International Conference on Robotics and Automation (ICRA)*, IEEE, 2022. [Online]. Available: <https://arxiv.org/abs/2209.13739>,
R.G. contributed to the conception of the project, developed the software, conducted the experiments, and led the writing of the manuscript.
- [2] R. Gehlhar, M. Tucker, A. J. Young, and A. D. Ames, “A review of current state-of-the-art control methods for lower-limb powered prostheses,” *Submitted to Annual Reviews in Control*, 2022,
R.G. wrote this review article in collaboration with M. Tucker, Dr. Aaron J. Young, and Dr. Aaron D. Ames.
- [3] R. Gehlhar, J.-h. Yang, and A. D. Ames, “Powered prosthesis locomotion on varying terrains: Model-dependent control with real-time force sensing,” *IEEE Robotics and Automation Letters*, vol. 7, no. 2, pp. 5151–5158, 2022. doi: 10.1109/LRA.2022.3154810,
R.G. contributed to the conception of the project, designed mechanical parts for the prosthesis platform, selected appropriate sensors, developed the prosthesis specific software, led the experiments, and led the writing of the manuscript.
- [4] K. Li, M. Tucker, R. Gehlhar, Y. Yue, and A. D. Ames, “Natural multicontact walking for robotic assistive devices via musculoskeletal models and hybrid zero dynamics,” *IEEE Robotics and Automation Letters*, vol. 7, no. 2, pp. 4283–4290, 2022. doi: 10.1109/LRA.2022.3149568,
R.G. developed the prosthesis-specific software, participated in discussions about the project, and contributed to the experiments.
- [5] R. Gehlhar and A. D. Ames, “Estimate-to-state stability for hybrid human-prosthesis systems,” in *2021 60th IEEE Conference on Decision and Control (CDC)*, IEEE, 2021, pp. 705–712. doi: 10.1109/CDC45484.2021.9683029,
R.G. contributed to the conception of the project, developed the theoretical proofs, conducted the simulations, and led the writing of the manuscript.
- [6] —, “Model-dependent prosthesis control with interaction force estimation,” in *2021 IEEE International Conference on Robotics and Automation (ICRA)*, IEEE, 2021, pp. 3226–3232. doi: 10.1109/ICRA48506.2021.9561250,
R.G. contributed to the conception of the project, developed the force estimation algorithm, developed the software, conducted the experiments, and led the writing of the manuscript.

- [7] ———, “Separable control lyapunov functions with application to prostheses,” *IEEE Control Systems Letters*, vol. 5, no. 2, pp. 559–564, 2021. DOI: 10.1109/LCSYS.2020.3004181,
R.G. contributed to the conception of the project, developed the theoretical proofs, conducted the simulations, and led the writing of the manuscript.
- [8] C. Gao, R. Gehlhar, A. D. Ames, S.-C. Liu, and T. Delbruck, “Recurrent neural network control of a hybrid dynamical transfemoral prosthesis with edgedrnn accelerator,” in *2020 IEEE International Conference on Robotics and Automation (ICRA)*, IEEE, 2020, pp. 5460–5466. DOI: 10.1109/ICRA40945.2020.9196984,
R.G. contributed to the conception of the ideas, developed the prosthesis-specific software, conducted the experiments on the prosthesis, contributed to writing the manuscript.
- [9] R. Gehlhar, Y. Chen, and A. D. Ames, “Data-driven characterization of human interaction for model-based control of powered prostheses,” in *2020 IEEE/RSJ International Conference on Intelligent Robots and Systems (IROS)*, 2020, pp. 4126–4133. DOI: 10.1109/IROS45743.2020.9341388,
R.G. contributed to the conception of the ideas, the data collection experiments, development of the simulation, and writing of the manuscript.
- [10] Y. Yu, J. Nassar, C. Xu, *et al.*, “Biofuel-powered soft electronic skin with multiplexed and wireless sensing for human-machine interfaces,” *Science robotics*, vol. 5, no. 41, eaaz7946, 2020. DOI: 10.1126/scirobotics.aaz7946,
R.G. contributed to the conception of the application to the prosthesis, developed the prosthesis software, and participated in the prosthesis experiments.
- [11] V. Azimi, T. Shu, H. Zhao, R. Gehlhar, D. Simon, and A. D. Ames, “Model-based adaptive control of transfemoral prostheses: Theory, simulation, and experiments,” *IEEE Transactions on Systems, Man, and Cybernetics: Systems*, vol. 51, no. 2, pp. 1174–1191, 2019. DOI: 10.1109/TSMC.2019.2896193,
R.G. conducted the experiments on two of the subjects and wrote the respective test procedure section and about the questionnaire results for this paper.
- [12] R. Gehlhar, J. Reher, and A. D. Ames, “Control of separable subsystems with application to prostheses,” *arXiv preprint arXiv:1909.03102*, 2019. DOI: 10.48550/arXiv.1909.03102,
R.G. developed the theoretical framework and proofs, conducted the simulations, and led the writing of the manuscript.

TABLE OF CONTENTS

| | |
|--|------|
| Acknowledgements | iii |
| Abstract | vii |
| Published Content and Contributions | ix |
| Table of Contents | x |
| List of Illustrations | xiii |
| List of Tables | xix |
| Chapter I: Introduction | 1 |
| 1.1 Contributions | 3 |
| 1.2 Brief Description of Chapters | 3 |
| Chapter II: A Review of Current State-of-the-Art Control Methods for Lower- Limb Powered Prostheses | 5 |
| 2.1 Introduction | 5 |
| 2.2 Control Objectives for Prostheses | 10 |
| 2.3 Sensing for Prosthesis Control | 14 |
| 2.4 High-Level Task Estimators | 16 |
| 2.5 High-Level Gait Phase Estimators | 20 |
| 2.6 Mid-Level Control via Torque Computation Without Reference Tra- jectories | 25 |
| 2.7 Mid-Level Control via Kinematic Reference Trajectories Tracking . . | 33 |
| 2.8 User-Specific Customization | 42 |
| 2.9 Discussion | 47 |
| 2.10 Conclusion | 55 |
| Chapter III: Preliminaries | 57 |
| 3.1 Background Nonlinear Control Theory | 57 |
| 3.2 Nonlinear Control of Robotic Systems | 65 |
| 3.3 Human-Prosthesis Model and Powered Prosthesis Platform | 70 |
| Chapter IV: Separable Subsystems | 72 |
| 4.1 Introduction | 72 |
| 4.2 Separable Subsystem Control | 73 |
| 4.3 Separable Robotic Control Systems | 78 |
| 4.4 Amputee-Prosthesis Application | 83 |
| 4.5 Conclusion | 87 |
| Chapter V: Separable Control Lyapunov Functions | 88 |
| 5.1 Introduction | 88 |
| 5.2 Composite RES-CLF for Separable Systems | 89 |
| 5.3 Separable CLF Construction | 93 |
| 5.4 Amputee-Prosthesis Application | 96 |
| 5.5 Conclusion | 97 |
| Chapter VI: Estimate-to-State Stability | 99 |

| | | |
|--|---|-----|
| 6.1 | Introduction | 99 |
| 6.2 | ISS and Estimate to State Stability | 101 |
| 6.3 | ISS and ESS Hybrid Control Systems | 103 |
| 6.4 | ESS-ID-CLF-QP for Human-Prosthesis System | 111 |
| 6.5 | Conclusion | 115 |
| Chapter VII: Model-Based Prosthesis Control Realization with Force Estimation | | 117 |
| 7.1 | Introduction | 117 |
| 7.2 | Controller Realization for Hardware | 119 |
| 7.3 | Human-Prosthesis Simulation | 121 |
| 7.4 | Human-Prosthesis Experimentation | 122 |
| 7.5 | Conclusion | 124 |
| Chapter VIII: Model-Based Prosthesis Control Realization with Real-Time Force Sensing | | 126 |
| 8.1 | Introduction | 126 |
| 8.2 | Controller Realization for Hardware | 128 |
| 8.3 | Prosthesis Platform for Controller Realization | 129 |
| 8.4 | Human-Prosthesis Experimentation | 132 |
| 8.5 | Conclusion | 136 |
| Chapter IX: Model-Based Multi-Contact Prosthesis Walking | | 138 |
| 9.1 | Introduction | 138 |
| 9.2 | Generating Subject-Specific Human-Inspired Walking Trajectories | 140 |
| 9.3 | Controller Realization | 142 |
| 9.4 | Multi-Contact Model-Based Controller Realization | 144 |
| 9.5 | Conclusion | 145 |
| Chapter X: Conclusion | | 147 |
| 10.1 | Future Work | 148 |
| Bibliography | | 150 |

LIST OF ILLUSTRATIONS

| <i>Number</i> | <i>Page</i> |
|--|-------------|
| 2.1 Existing Powered Prostheses. While several dual-actuated (knee-ankle) prostheses have been developed and demonstrated in research settings, there are currently only two commercially-available powered prostheses and they are both single-actuated. These commercially-available devices are shown on the left, with some of the dual-actuated devices used in research settings shown on the right. Note that the images are taken from the publications listed below, with the references for the first versions of the devices indicated by “V1”. . . . | 8 |
| 2.2 Prosthesis Control Architecture. While there exist various prosthesis control strategies, most control architectures utilize the illustrated hierarchy. Overall, the controller receives sensor data from the human-prosthesis system and returns (typically joint-level) torques. Furthermore, all controllers generally contain the following shared components: high-level task and gait phase estimation; mid-level desired torque computation either with or without a reference trajectory, and a low-level controller that commands the desired torque from the actuators. The various control methods that will be discussed in the survey are illustrated in green. | 9 |
| 2.3 Finite State Machine. An example of an FSM used to determine gait phase, based on [17]. Here the gait cycle is divided into four phases, or states, and conditions based on the joint angle, velocity, and ground reaction forces dictate state transitions. In state 1, when the ankle angle q_{ankle} reaches the threshold q^{thr} , state 2 begins. Once the foot lifts off the ground, determined when the ground reaction force F_g is less than a threshold F_g^{thr} , the controller switches to state 3. This state ends when the knee velocity, \dot{q}_{knee} becomes negative. Finally, the controller starts back at state 1 when the foot strikes the ground in state 4, causing F_g to exceed its threshold. | 21 |

- 2.4 Progression of Monotonic Phase Variable. The horizontal forward progression of the stance hip relative to the ankle is an example of a physical quantity that is monotonic in a gait cycle, as explained in [150], allowing it to be used as a phase variable in a prosthesis stance controller. The initial and final positions of the hip provide the parameters p_0 and p_f , respectively, to parameterize the phase variable such that it goes from 0 to 1 during stance phase. 22
- 2.5 Common Process for Mid-Level Control via Kinematic Reference Trajectories. (i) Motion capture data is collected from able-bodied subject walking. (ii) The average and standard deviation is computed of each joint trajectory, such as the trajectory of the knee angle, q_{knee} , with respect to the percent gait cycle. (iii) A function, $y_d(\tau_{q,t})$, is fit to the average data, parameterized by some state- or time-based phase variable $\tau_{q,t}$. (iv) A torque, τ , is computed based on this desired trajectory and the actual trajectory, $y_a(q_p)$, of the prosthesis. (v) This torque is commanded of the prosthesis actuators. (vi) The resultant joint trajectory of the prosthesis, $y_a(q_p)$ is close to the desired trajectory, $y_d(\tau_{q,t})$. Steps (i) - (iii) are part of data-driven approaches to generate reference trajectories, described in Subsection 2.7, and steps (iv) - (vi) are part of tracking controller methods, described in Subsection 2.7. 32
- 2.6 Methods of User-Specific Customization. We present four methods of customization, each illustrated using a different color: (red) biologically-inspired tuning which leverages relationships derived from biological systems and data; (grey) simulation-based tuning which leverages computer-based environments to predict which parameters would result in optimal behavior; (green) heuristic tuning which selects new parameters in each experimental iteration based on a clinician or user's observations; and (blue) human-in-the-loop tuning which assigns numerical metrics to the experimentally-obtained prosthesis walking and uses algorithmic tools to predict new parameters to try in the subsequent iteration. 43
- 3.1 Human-Prosthesis Model and Platform. (Left) Human-prosthesis model with generalized coordinates. (Right) AMPRO3 powered prosthesis platform with components and coordinates labeled. 70

| | | |
|-----|---|----|
| 4.1 | Amputee-Prosthesis Separable System and Equivalent Subsystem. (Left) Amputee-prosthesis separable system (blue), with separable prosthesis subsystem AMPRO3 (red). (Right) Equivalent prosthesis subsystem. (Middle) Control input from inverse dynamics of human-prosthesis motion capture walking data, determined with full-order system dynamics (blue) and with equivalent subsystem dynamics (red). | 74 |
| 4.2 | Robotic Models with Generalized Coordinates. (Left) Model of the full amputee-prosthesis system labeled with its generalized coordinates, where q_r is notated in blue and q_s in red. (Right) Model of prosthesis subsystem with its generalized coordinates, where F_f is notated in violet. | 80 |
| 4.3 | Control inputs of prosthesis knee (left) and prosthesis ankle (right) for subsystem control law u_s and \bar{u}_s over stance and non-stance domains. | 86 |
| 4.4 | Phase portraits of prosthesis knee (left) and prosthesis ankle (right) for stance and non-stance domains. | 86 |
| 4.5 | Output functions of prosthesis knee and ankle for \mathcal{D}_{ps} (right) and \mathcal{D}_{pns} (left) for 65.8 kg Model 1 and 90.7 kg Model 2. | 87 |
| 5.1 | Human-prosthesis separable system (left) with separable prosthesis subsystem (red) and remaining human system (blue). Equivalent prosthesis subsystem (right) with base coordinates and interaction force inputs \mathcal{F} . The composite CLF of the remaining system RES-CLF (blue) and equivalent subsystem RES-CLF (red) yields a RES-CLF for the whole system (purple). | 90 |
| 5.2 | Phase Portraits and Output Tracking Simulation Results. (a) Phase portraits of subsystem states (left) and zero dynamics coordinates (right) showing stability for 20 steps with perturbed initial condition (triangle). (b) Actual output prosthesis trajectory $y_v^{a,s}$ tracking desired trajectory $y_v^{d,s}$, designed to match human data. | 97 |
| 5.3 | RES-CLF Convergence and Control Input Simulation Results. (a) RES-CLF derivatives for remaining system (blue) and subsystem (red) show convergence for prosthesis stance domain (left) and prosthesis swing (right) and yield a RES-CLF for the full-order system (purple) satisfying its RES-CLF bound (gray). (b) Prosthesis control input from CLF-QP. | 97 |
| 5.4 | Gait tiles of human-prosthesis system, prosthesis in red, demonstrating human-like walking in simulation. | 98 |

| | | |
|-----|--|-----|
| 6.1 | Human-prosthesis system. Prosthesis exponentially converges according to CLF $V_{\varepsilon, \bar{\varepsilon}}$ to a set bounded by force estimation error ΔF . Human exponentially converges according to zero dynamics Lyapunov function $V_{\bar{z}}$ to a set bounded by a disturbance created by the deviation of the prosthesis control input u_s^* from expected control law $u_p^{\text{nom}}(\bar{\eta}, \bar{z})$ | 100 |
| 6.2 | Four step cycles of prosthesis knee output tracking for ESS-ID-CLF-QP with different values of $\bar{\varepsilon}$ compared to the human data the desired trajectory was generated to match, the desired trajectory, and the output when no $\frac{1}{\bar{\varepsilon}} L_{G_s} V_{\varepsilon^s}(\bar{\eta}) J_{y^s} \bar{\kappa} ^2$ term is used in the CLF constraint. | 115 |
| 6.3 | Phase portraits of unactuated human torso (left purple) and prosthesis knee (right purple) from simulation using ESS-ID-CLF-QP with $\bar{\varepsilon} = 10$. (green) Prosthesis knee stability with 5x the disturbance. (yellow) Prosthesis knee instability with 10x the disturbance. | 116 |
| 7.1 | Gait tiles of powered prosthesis AMPRO3 worn by able-bodied human user walking with model-dependent prosthesis controller. Top shows prosthesis stance, bottom shows prosthesis non-stance. Numbers align with phases of gait trajectory shown in Figure 7.4. | 118 |
| 7.2 | Joint outputs from optimization (blue) align closely with human motion capture data (black) showing the trajectories we use to test the human-prosthesis model in simulation and implement on the prosthesis device are human-like. | 121 |
| 7.3 | Control Input and Force Estimation Simulation Results. (a) Prosthesis stance control input for the knee from 3 simulations of the human-prosthesis model walking with variations of the ID-CLF-QP applied to the prosthesis. (b) The summation of the constraint forces and interaction forces projected into joint space. | 123 |
| 7.4 | Simulation and Experimental Output Tracking Results. (Top left) Output tracking from 3 simulations with variations of the ID-CLF-QP on the prosthesis in stance plotted with the desired trajectory and the human data with respect to the phase variable. Experiment output tracking with the PD controller (top right), ID-CLF-QP (bottom left), and ID-CLF-QP+ \hat{F}^{est} (bottom right) applied in stance plotted with the desired trajectory in time. \mathcal{D}_{ps} white, \mathcal{D}_{pns} shaded. Numbers in bottom right plot indicate phase of gait corresponding to gait tiles in Figure 7.1 | 124 |

| | | |
|-----|---|-----|
| 7.5 | Results of four phases of stance from experiment. (Top) The RES-CLF derivative (blue) plotted against its bound (red). (Bottom) The prosthesis knee control input. | 125 |
| 8.1 | Gait Tiles of Experimental Results with Force Sensor Measurements. (top) Gait tiles of human subject walking with model-dependent prosthesis knee controller using real-time force sensing on four terrains: rubber floor, outdoor track, grass, and sidewalk. (middle) Insole pressure sensor maps in the stance phases of a walking cycle. (bottom) Measured socket and ground force profiles during stance for respective terrain. | 127 |
| 8.2 | Transfemoral powered prosthesis AMPRO3 with labeled hardware components, including newly integrated force sensors (load cell and pressure sensor). | 130 |
| 8.3 | Block diagram depicting how the Beaglebone microprocessor, motion controllers, IMU, load cell, and pressure sensor are involved in the control scheme. | 131 |
| 8.4 | Gait tiles of 2 subjects walking on a rubber floor with the force sensing ID-CLF-QP prosthesis controller. | 133 |
| 8.5 | Phase Portrait and CLF Convergence Experimental Results. (a) Phase portrait of first 18 steps using the force sensing ID-CLF-QP controller (8.1) on a sidewalk, showing the system yields a stable periodic orbit. (b) (top) CLF bound and derivative for first 4 steps of the same experiment, showing the prosthesis usually satisfies the stability condition, (bottom) magnified plot of the CLF bound, w.r.t. phase variable $\tau(x_s)$ | 133 |
| 8.6 | Control Input and Output Tracking Experimental Results for Four Terrains. (a) Control input (mean and 3 standard deviations) and (b) output tracking with force sensing ID-CLF-QP and the ID-CLF-QP without force sensors for four different terrains for 11 step cycles, w.r.t. to phase variable $\tau(x_s)$ | 134 |
| 8.7 | Control Input and Output Tracking Experimental Results for Four Controllers. (a) Control input (mean and 3 standard deviations) and (b) output tracking (mean) with force sensing ID-CLF-QP, no sensor ID-CLF-QP, force estimating ID-CLF-QP, and PD controller for 11 step cycles, w.r.t. phase variable $\tau(x_s)$ | 135 |

| | | |
|-----|--|-----|
| 9.1 | (top) Subject 1 and (bottom) Subject 2 walking with powered prosthesis controlled by multi-domain model-based prosthesis controller with real-time force sensing following provably stable human-like walking trajectories. Labels indicate the respective domain the human-prosthesis is in in the multi-domain hybrid-system graph shown in Figure 9.2 | 139 |
| 9.2 | Six-domain directed graph of human-prosthesis hybrid system, modeling respective foot contact points for different phases of walking. . . | 141 |
| 9.3 | Phase portraits of the knee and ankle for 2 subjects for 8 continuous steps cycles using the ID-CLF-QP. | 145 |
| 9.4 | Ground Reaction Forces and Output Tracking Experimental Results. (a) The vertical GRF F_g^z and moment M_g^y measured by the pressure sensor and horizontal GRF $\bar{\lambda}_{g,x}$ during one step of walking with the ID-CLF-QP (9.1). (b) The mean of the actual outputs of the knee and ankle for 2 subjects and 3 controllers for 8 continuous step cycles plotted against the desired trajectory and the averaged human joint data. | 146 |

LIST OF TABLES

| <i>Number</i> | | <i>Page</i> |
|---------------|---|-------------|
| 8.1 | Tracking RMSE of 4 Terrains for 2 Controllers | 136 |
| 8.2 | Tracking RMSE of 4 Controllers for 2 Subjects | 136 |
| 9.1 | Tracking RMSE of 3 Controllers for 2 Subjects | 144 |

Chapter 1

INTRODUCTION

There are over 600,000 lower-limb amputees in the US, and this number is expected to double by 2050 due to the increasing rate of diabetes [1]. Currently, this population is limited to mostly passive commercially available devices. Because these devices do not contribute net positive work to the user the way biological limbs do [2], [3], amputees walking with these passive devices experience increased metabolic cost [4]–[6] and slower comfortable walking speed [6], [7]. These users also tend to shorter step length and favor their intact leg, leading to changes in biomechanical motion, pain in their joints and back, and degenerative conditions such as osteoarthritis [8]. In addition to having an asymmetric and less efficient gait, amputees also have less robust gaits and are more prone to falling [9], [10].

Powered prostheses could help this instability, improve gait energy efficiency [11]–[14], and increase a user’s self-selected walking speed [11], [13]. Despite these potential benefits, there are few commercially available powered lower-limb prostheses. Those that exist only have a single powered joint [15], [16], meaning there are no dual actuated knee-ankle prostheses currently commercially available. While these devices exist in research settings, [17]–[24], challenges exist to bring these devices to the real-world. One of these challenges, which will be the focus of this thesis, is the requirement for control.

Currently the state-of-the-art control method for knee-ankle prostheses is impedance control [25]. This approach divides the gait cycle into a discrete number of phases and defines an impedance torque law for each joint in each phase [17], [26]–[29]. The parameters that define these torque laws are tuned to yield comfortable amputee-prosthesis walking with kinematic trends that resemble healthy human walking. While this approach has led to the first instances of powered knee-ankle prosthesis upslope walking [30], running [31], and variable cadence bilateral amputee walking [32], these methods take several hours to tune and must be retuned for every subject and locomotion type [33]. The heuristic nature of this approach yields no formal guarantees of stability or optimality and the time-exhaustive pose limitations to bringing the advantages of powered prostheses to the large population of lower-limb amputees.

An effort was made by bipedal control researchers to develop a more systematic method to find impedance parameters [34]. This strategy determined impedance parameters through a bipedal robot simulation. Researchers then improved controller performance by including a feedback term implemented with a model independent quadratic program [35]. This approach, along with others [36], used bipedal trajectory generation methods to systematically generate human-like walking trajectories for prostheses. These model-based trajectories are designed to satisfy formal stability guarantees, however to adhere to these stable periodic orbits and maintain these guarantees online, a tracking controller with a sufficient convergence rate is required.

Control Lyapunov functions provide a stability condition based on the modeled dynamics, such that a control input chosen to satisfy this condition yields a sufficient convergence certificate. Including the model in the tracking control problem allows inputs to be chosen to satisfy constraints on the physical system [37] and lowers dependence on high-gain PD control by using a feedforward term. Also, through consideration of the nonlinear dynamics, controllers can establish formal guarantees on the stability of the system [38], [39]. Model-based control methods hold potential to yield a more transferable method between devices, users, and behaviors since they rely on measurable model parameters and inputs instead of a large set of heuristic tuning parameters. This motivates developing model-based prosthesis control methods that lend a more transferable method between applications, and guarantee stability for the user.

However two problems arise when trying to translate these model-based formal methods to prostheses. One, the control laws depend on the full system dynamics, but here the *human dynamics are unknown*. Two, the prosthesis dynamics depend on the full system states, but here the *human states are unknown*. This thesis addresses these challenges by developing a theoretical framework that allows construction of model-based controllers for a subsystem of a nonlinear system. These controllers solely depend on local information available to the subsystem, such that, in the case of the prosthesis, the inclusion of a force sensor enables model-based prosthesis control. After developing a class of stabilizing subsystem controllers and establishing stability guarantees for these controllers in the presence of force estimation error through theoretical work, this thesis experimentally *realizes the first model-based lower-limb prosthesis control with consideration of the human-prosthesis interaction forces*. This controller yields improved tracking performance across subjects and

terrains, without requiring tuning in between these varied conditions, suggesting this control approach could lead to a method that generalizes across users to bring these devices into the real-world.

1.1 Contributions

The main contributions of this thesis are:

- Development of a class of model-based subsystem controllers that solely rely on local information with application to a general class of nonlinear control systems and any open-chain manipulator capable of sensing its global orientation and velocity and its interaction forces with another subsystem.
- Formal proofs of stability for these subsystem controllers, guaranteeing full-order system stability under certain conditions, even in the presence of impacts, zero dynamics, and measurable input estimate errors.
- Realization of the first and only model-based lower-limb prosthesis controller, integrating and utilizing real-time in-the-loop force sensing at the human-prosthesis interface and at the ground, resulting in improved tracking performance across subjects and terrains.

1.2 Brief Description of Chapters

Chapter 2 presents a review on current state-of-the-art powered prosthesis control methods. This begins with motivation for why powered prosthesis control research is important. Then it discusses control objectives for prostheses and available sensing techniques, followed by an overview of different control approaches for high- and mid-level control. Finally, it outlines methods to customize prosthesis controllers in a user-specific way and concludes with a discussion regarding outstanding needs in this field.

Chapter 3 sets up the preliminary theory used as a basis for the work presented in this thesis. This theory is not a novel contribution of this thesis, but provides the necessary background to understand the contributions of this thesis.

Chapter 4 introduces the separable subsystem framework used in the rest of the paper to develop the theoretical contributions of this thesis. The equivalency of the subsystem feedback linearizing control laws for a separable subsystem and equivalent subsystem is proven.

Chapter 5 establishes full-order system stability guarantees through a subsystem controller through control Lyapunov functions. This defines a whole class of subsystem controllers that solely rely on local sensing but yield provably stable hybrid periodic orbits for separable systems with zero dynamics.

Chapter 6 proves these aforementioned stability guarantees are maintained even when the measurable input to the subsystem has an estimation error. A form of a control law, that reduces the effect of this estimation error, is constructed both for a general nonlinear system and in a hardware implementable form for a robotic system.

Chapter 7 formulates a force estimation method to synthesize model-based robotic subsystem controllers and realizes the first instance of fully model-dependent prosthesis control on a lower-limb prosthesis, via a controller of the subsystem CLF class.

Chapter 8 integrates a load cell and an inertial measurement unit (IMU) into the prosthesis platform to “complete the model” of the prosthesis dynamics to realize model-based prosthesis control with in-the-loop real-time force sensing. Additionally, a pressure sensor is incorporated into the prosthesis shoe to provide real-time force feedback at the ground, leading to stable human-prosthesis walking across 4 terrains and for 2 subjects.

Chapter 9 extends the methods of the previous chapter to more human-like multi-contact behavior involving both the knee and the ankle. Human-prosthesis walking is realized for 2 subjects, demonstrating improved tracking performance compared to traditional model-independent approaches, without tuning between subjects.

Chapter 10 concludes this thesis with a summary of the work, description of the implications of these contributions, and a discussion of future directions for this work.

Chapter 2

A REVIEW OF CURRENT STATE-OF-THE-ART CONTROL METHODS FOR LOWER-LIMB POWERED PROSTHESES

Lower-limb prostheses aim to restore ambulatory function for individuals with lower-limb amputations. While the design of lower-limb prostheses is important, this chapter focuses on the complementary challenge—the control of lower-limb prostheses. Specifically, a subset of lower-limb prostheses, powered prostheses, which utilize actuators to inject mechanical power into the walking gait of a human user.

In this chapter, we present a review of existing control strategies for lower-limb powered prostheses, including the control objectives, sensing capabilities, and control methodologies. We separate the various control methods into three main tiers of prosthesis control: high-level control for task and gait phase estimation, mid-level control for desired torque computation (both with and without the use of reference trajectories), and low-level control for enforcing the computed torque commands on the prosthesis. We focus on the high- and mid-level control approaches in this review. Additionally, we outline existing methods for customizing the prosthetic behavior for individual human users, including techniques from machine learning. Finally, we conclude with a discussion on future research directions for powered lower-limb prostheses based on the potential of current control methods and open problems in the field.

This chapter was adapted from:

R. Gehlhar, M. Tucker, A. J. Young, and A. D. Ames. “A Review of Current State-of-the-Art Control Methods for Lower-Limb Powered Prostheses”. In: *Submitted to Annual Reviews in Control*, 2022.

2.1 Introduction

Advantages of Powered Prostheses

Foremost, powered lower-limb prostheses better replicate the functionality of biological limbs. Specifically, while passive prostheses are able to provide some energy absorption, they are unable to provide energy generation as human muscles do [2], [3]. Hence, powered prostheses pose an advantage through their contribution of net positive work. This is especially important considering that intact ankles are

responsible for providing up to 60% of the energy generated by a limb in a gait cycle [3], [40]. As a result, when individuals experience reduced energy generation due to amputation, they often develop compensatory behaviors from the intact muscles. In stair climbing, for example, transtibial (amputation above the ankle) and transfemoral (amputation above the knee) amputees often develop compensatory strategies [41]–[44] due to the inability to produce the net positive work required (in either the stance knee or stance ankle) to raise the user's center of mass [45]. Through the addition of net positive work, powered prostheses have demonstrated reduction in these compensatory behaviors [46]. Additionally, it has been shown that increasing ankle push-off with an active prosthesis reduces the loading impulse of the sound limb and the risk of knee osteoarthritis [47].

Lastly, powered prostheses are hypothesized to enable more energy efficient behavior relative to passive prosthesis, which require increased metabolic energy compared to healthy walking [4]–[6]. A few studies have supported this hypothesis through the reduction of metabolic rate [11]–[14]. This potential advantage heightens for above-the-knee amputees, considering that higher levels of amputation have been shown to result in less efficient gaits and higher O₂ costs [48], [49]. Additionally, powered prostheses have demonstrated an increase in self-selected walking speed [11], [13]. In comparison, passive prosthesis users experience shorter step length [8], slower walking cadence [7], and a decrease in comfortable walking speed [6] compared to able-bodied walking.

Current Limitations of Powered Prostheses

While there are clear benefits associated with powered lower-limb prostheses, there are also drawbacks that limit their ability to be commercially viable. First, powered lower-limb prostheses tend to have increased weight compared to microprocessor or passive prostheses due to the addition of sensing, actuation, and batteries. This increased weight increases the load on an amputee's intact limb, inducing further stresses at the socket interface. Additionally, the increase in weight has been shown to cause increases in human joint torque and metabolic expenditure. For example, a study conducted on healthy walking found that net metabolic rate increased with both increased loading and more distal placements of the mass [50].

Second, this increase in mechanical and electrical complexity drives up the cost of powered prostheses, decreasing the likelihood of insurance covering these devices and inhibiting their potential viability. Furthermore, the addition of sensors and

actuators introduces more opportunities for failures, including both electronic and mechanical failures. Third, powered prostheses rely on a control system to drive the actuation, which introduces unique challenges. Predominately, these controllers are specifically designed for certain conditions including the environmental terrain, the locomotion mode, and characteristics of the prosthesis user. Thus, it can be challenging to develop prosthesis controllers that perform well across a variety of conditions. To date, the benefits of powered prostheses only emerge once the prosthesis control is customized to each subject and each locomotion mode (i.e. level-ground walking or stair climbing). Similarly, since most prosthesis controllers only consider level-ground walking, it is challenging for powered prostheses to handle varying terrain like water/snow/sand/mud.

Lastly, the limitations associated with developing prosthesis controllers are amplified for dual-actuated knee-ankle prostheses since the controller needs to coordinate the motion of two joints simultaneously. In this case, the number of control parameters that require tuning at least doubles. In addition to needing satisfactory control algorithms for each joint individually, coordination between joints also becomes an important consideration in the control paradigm for these devices. This motivates developing systematic control methods that extend to high-dimensional parameter spaces and faster methods of user-customization. While powered knee-ankle prostheses present additional challenges to become clinically feasible to customize to users, they also hold greater potential advantages because of the increased hindrances that confront transfemoral amputees [48], [49]. For these reasons, this survey places an emphasis on the advantages and limitations control methods pose for powered knee-ankle prostheses.

Commercial Availability of Powered Prostheses

Ultimately, the benefits of powered prostheses observed in research settings are not yet high enough to outweigh the disadvantages, which likely contributes to why there are only two powered lower-limb prostheses currently available on the commercial market. Each of these devices are illustrated in Figure 2.1. The first device is a powered ankle prosthesis, named “Empower”, from Ottobock, formerly known as the “Biom” [15], released in 2010. The second device shown is a powered knee prosthesis called “Power Knee” from [16], first released in 2006. While the addition of these devices to the commercial market emphasizes the potential impact of powered prostheses, it is important to note that there are currently no powered dual-actuated lower-limb prostheses commercially available. This poses

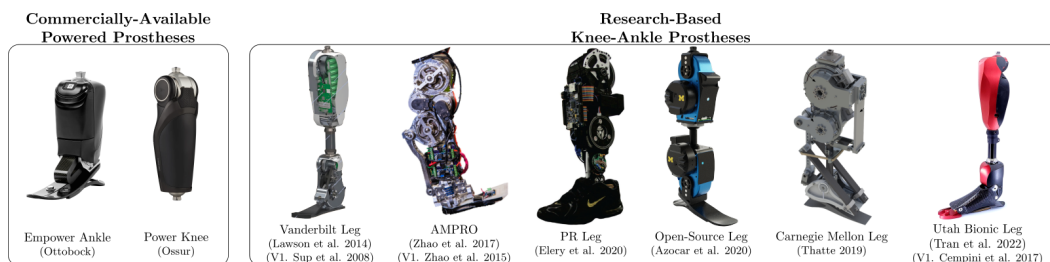


Figure 2.1: Existing Powered Prostheses. While several dual-actuated (knee-ankle) prostheses have been developed and demonstrated in research settings, there are currently only two commercially-available powered prostheses and they are both single-actuated. These commercially-available devices are shown on the left, with some of the dual-actuated devices used in research settings shown on the right. Note that the images are taken from the publications listed below, with the references for the first versions of the devices indicated by “V1”.

a disadvantage to transfemoral amputees considering that dual-actuated knee-ankle prostheses offer a unique solution towards controlling the coordination of multiple joints which plays an important role in ankle push-off [3].

However, there exist many dual-actuated powered prostheses utilized in research settings, including those illustrated in Figure 2.1. The purpose of these devices is predominantly to develop and evaluate novel control strategies [17]–[19], [21], [23], [24]. Notably, since the difference between various devices hinders comparisons between control strategies, there has been a push towards developing open-source prostheses which can serve as common test beds for control [24]. Another notable knee-ankle prosthesis design is the Utah Knee [22] used with the a powered polycentric ankle prosthesis [20]. This design is an example of recent research efforts to decrease the weight of powered prosthesis devices to be closer to that of commercially available microprocessor controlled knee prostheses.

It is speculated that one of the reasons why passive prostheses are still more common than powered prostheses, despite the apparent benefits, is largely due to the time-consuming nature of tuning control parameters for individual prosthesis users [51]. This tuning process becomes increasingly complex when considering multiple locomotion modes (e.g., level-ground walking and stair climbing) as well as multiple joints. Towards this, we survey the control strategies for powered lower-limb prostheses, followed by a discussion on existing techniques for user-specific customization.

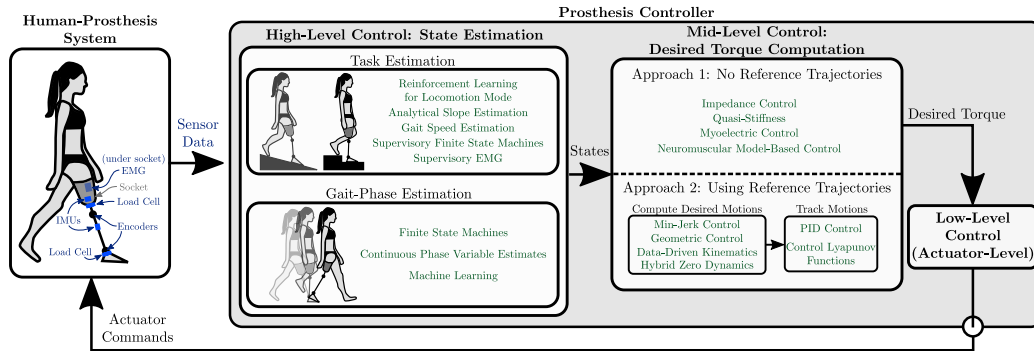


Figure 2.2: Prosthesis Control Architecture. While there exist various prosthesis control strategies, most control architectures utilize the illustrated hierarchy. Overall, the controller receives sensor data from the human-prosthesis system and returns (typically joint-level) torques. Furthermore, all controllers generally contain the following shared components: high-level task and gait phase estimation; mid-level desired torque computation either with or without a reference trajectory, and a low-level controller that commands the desired torque from the actuators. The various control methods that will be discussed in the survey are illustrated in green.

Overview of the Chapter

It is important to note that while there exist several reviews on the design and control of lower-limb powered prostheses [52]–[55], many of these reviews focus on the mechanical design and provide a high-level treatment of the available control methodologies. In contrast, this survey focuses solely on the existing control strategies. This more in-depth survey allows us to explore the heuristic and formal nature of current methods to examine their customizability and their potential to generalize across users. Ultimately, a method that can both generalize across users and have clinically friendly methods for user-customization could bring these devices into every day use.

To provide context for the control methods presented in this chapter, this chapter will begin by discussing specific challenges amputees face with passive prostheses that then motivate various control objectives. Section 2.2 will explain these aims researchers have in prosthesis control design and the metrics used to evaluate the performance of these control methods. Following, Section 2.3 will introduce the various sensing methods available as inputs to prosthesis control methods. We categorized the control method components into four components, as shown in Figure 2.2. The first component in Section 2.4 is a high-level controller that estimates the desired task for the prosthesis, such as walking speed, walking incline, and locomotive modes. A high-level controller that generally follows task estimation,

is gait phase estimation, discussed in Section 2.5. The phase of the gait cycle is generally determined in a discrete way through a finite state machine or in a continuous way through a phase variable. We consider the mid-level controllers to fit under one of two approaches. We discuss the first approach in Section 2.6, that are focused on computing torque using task and phase estimates, kinematics, EMG signals, or a combination of these. The second approach, in Section 2.7, consists of two steps. The first step, in Subsection 2.7, determines a desired reference trajectory for the prosthesis, which is a desired motion of a joint defined with respect to time or gait phase. The second step, in Subsection 2.7, determines a torque to track the reference trajectories. In the prosthesis control-architecture, a low-level controller commands the desired torques from the actuators. These low-level controllers will not be discussed in this survey. All of the control methods we present require some level of tuning. Various tuning approaches used for user-customization will be outlined in 2.8. Section 2.9 will then discuss open questions regarding prosthesis control methods and important considerations in working towards better prosthesis performance, followed by a brief conclusion in Section 2.10.

2.2 Control Objectives for Prostheses

A major consideration when developing controllers for powered prostheses is how to *assess* the performance for any given controller. We consider three categories that encompass the main control metrics used: *naturalness* of the gait, *efficiency* of the gait for the human and prosthetic device, and the prosthesis' *responsiveness* to the human's behavior and the environment.

Naturalness

One of the most common control objectives addresses how well a prosthesis is able to *mimic* healthy human walking patterns. This goal is motivated by the gait asymmetry prosthesis users exhibit kinematically [56], [57], kinetically [58], [59], and temporally [60], [61]. Part of this asymmetry arises from the limitations of passive devices as well as from amputees favoring their intact leg. Favoring one side leads to loading asymmetry [62], [63], which increases with walking speed [59]. This tendency also leads to changes in biomechanical motion, degenerative changes to their limbs, and pain in their joints and back [8].

To assess this loading asymmetry, controls researchers examine the ground reaction force profiles and center of pressure (CoP) trajectories between a prosthesis foot and a biological foot in able-bodied walking [64], [65]. By looking at the ground reaction

forces, researchers can assess the amount of body weight lifted by the prosthesis and the loading symmetry between legs [66]–[68]. Researchers work to improve the kinetic “naturalness” at the joint level, perhaps with the intent of improving the loading asymmetry. Researchers compare prosthesis torques, power, and work to that of able-bodied walking [14], [36], [65], [69], [70], to name a few. While this comparison considers the torques with respect to percent gait cycle, researchers will also compare the relationship between torques and the joint angles, in other words, the quasi-stiffness [71]–[73].

There are certain kinematic features that biomechanics have found play an important role in human gait, such as knee flexion in early stance to cushion the transition to weight-bearing mode [74] and ankle plantar flexion in late stance to propel the body forward [3], [75]. Motivated by the way these kinematic behaviors lead to desirable full body dynamic effects, researchers commonly assess the performance of their prosthesis by comparing the joint kinematic profiles to able-bodied kinematic data [14], [17], [65], [69], [76], [77], to name a few. Researchers will also compare the kinematic trajectories of the prosthesis to the sound side to assess gait symmetry [78].

Another method of comparing prosthesis walking to healthy walking is via spatio-temporal parameters, such as symmetry and step length. Types of symmetry include time spent on each leg, duration of gait phases between each limb, and maximum joint angles in specific phases of walking [73]). To examine the work done and work symmetry at the muscle level, researchers will measure human muscle activation through electromyography (EMG). Researchers use the EMG activity to assess the muscle effort used in walking with a prosthesis and compare the muscle activation symmetry between limbs [67], [68], [79]. Lastly, one can assess kinematic properties of the prosthesis walking using postural observations including the evolution of the center of mass during walking [80].

In addition to measuring specific elements of an amputee-prosthesis gait, researchers will also investigate whether certain relationships exist between these elements, like the biomechanical relationships observed in human walking. Researchers examine whether ankle work increases with faster walking speeds [73] and with increasing walking slopes [69]. [73] also assessed how the maximum flexion angles changed with speed compared to able-bodied walking. This provides insight into how well the control method captures a human’s underlying objectives to exhibit similar responses to given conditions.

Efficiency

To measure a human's locomotive efficiency, metabolic cost of transport is most commonly used. This metric is determined by both the metabolic rate and the speed at which the subject traveled at. Researchers aim to decrease metabolic rate and increase a user's comfortable walking speed to improve this unified metric of metabolic cost of transport. This section will discuss how performance assessed with this metric degrades with an amputation, which then motivates researchers to use powered prostheses to restore higher levels of energy efficiency.

Humans tend to walk at a speed that is close to optimal with respect to energy expenditure [81], [82], suggesting that energy efficiency is a control objective for humans. Walking with passive prostheses, however, increases hip power and metabolic cost [83]. Transfemoral amputees, specifically, exert three times more hip power and torque on their amputated side in walking than able-bodied individuals [83]. With regards to metabolic energy, transtibial amputees expend around 20% more energy in walking [5] and transfemoral amputees, 33% [6]. To try to mitigate this decline in efficiency, prosthesis control researchers aim to reduce metabolic cost of transport [54], [67].

However, it is unclear whether powered prostheses are yet capable of restoring metabolic expenditure to a level comparable to walking with intact limbs. While there exists previous work that has demonstrated metabolic reduction using a powered ankle prosthesis [11]–[14], it should be noted that these results have not been repeatable across powered prosthetic devices [84]. Specifically, other results indicate that powered ankle prostheses fail to reduce metabolic cost across a wide variety of ankle push-off strategies [85]. Also, note that these existing results are largely limited to powered ankle prostheses. Thus, the potential for dual-actuated prostheses to reduce metabolic expenditure for transfemoral amputees is still an open question.

While lowering energy expenditure for the human seems important, how to directly improve upon this metric through prosthesis control is unclear. Some control methods will determine mid-level control parameters to minimize cost of transport through optimizing a gait cycle of a modeled amputee-prosthesis system [70], [86], [87]. In addition to reducing the energy cost to the human, these offline optimization approaches and other online optimizations [35] can also reduce the mechanical work of the device. This objective is advantageous to reduce the required actuator size and power.

With regards to walking speed, typically humans' *self-selected walking speed* is between 1.3 and 1.5 m/s, slower than their maximum speed of around 2 m/s [81], but close to their optimal speed, of 1.2 m/s, with respect to energy expenditure [82]. Amputees walking with passive prostheses experience a significant decrease in self-selected walking speed [61]—an 11% speed decrease for transibial amputees, and 35% for transfemoral [6]. Motivated by this decline in performance, researchers investigate how a given prosthesis control method affects a user's self-selected walking speed and aim to increase it [11], [13], [67], [88].

Responsiveness

The final control objective for powered prostheses is the ability to respond appropriately to both the prosthesis user and the environment. This requires a prosthetic device to adapt its behavior to satisfy user intent. Responsiveness also refers to a prosthesis' ability to respond to disturbances in way that keeps the user stable and safe.

First, the ability of a prosthesis to respond to a human user is often characterized as *volitional ability*. This objective is especially used in the context of controllers that allow for precise movements (such as direct EMG control) and is quantified by the precision of motion under the user's volition. Specifically, the following metrics have been examined to assess volitional control: excess distance traveled when moving to a target angle, time the subject held the prosthesis in target window, and total wasted motion of the prosthesis in accomplishing various tasks [89]. Similarly, [67] assessed the range of cadences a user could achieve while walking with a powered knee-ankle prosthesis.

Second, powered prostheses must also be responsive to changes in the environment. This includes both transitioning between locomotion modes as well as maintaining stability. In terms of transitions, it is expected that for daily locomotion, prostheses must be able to traverse a variety of terrain types: upward and downward slopes, ascending and descending stairs, and uneven terrain. Researchers generally take two approaches towards realizing these various types of locomotion: develop task estimators that discretely classify the terrain type or locomotive mode [90], or focus on developing a unified control method that adapts to the user's behavior [68], [78], [91], [92]. The metrics corresponding to a prosthesis' responsiveness to the environment can be evaluated using classification accuracy and response time.

To put the importance of such responsiveness into context, even for small mode transition errors (1%), a user who ambulates 5000 steps a day would experience 50 transition errors daily [90]. To decrease the number of potential falls from misclassifications, powered prostheses must have both highly accurate methods of task estimation as well as controllers that can seamless recovery from misclassification errors. More generally, this notion of recovery refers to a prosthesis' ability respond to unexpected disturbances (i.e., maintaining balance in the event of a trip).

Lastly, locomotive stability is important, reflected by the fact that amputees have a greater risk of falling than healthy individuals [9]. Passive prosthesis users tend to have less robust gaits [93], falling more often than non-amputees [10]. [94] polled amputees and found 45% had fallen while wearing their prosthesis in the previous year. However, there is currently no universal metric for stability/balance apart from recording falls in a long term study [95], [96]. Thus, it is difficult to compare the effect of various controllers on locomotive stability. Though, it should be noted that researchers are developing test environments to introduce walking disturbances in a controlled setting to assess a human and prosthesis' stability in the presence of perturbations. These efforts along with other research focused around fault detection and fall prevention will be discussed in Section 2.9.

2.3 Sensing for Prosthesis Control

One factor that influences a controller's capabilities to achieve these objectives is the sensing available as input. We present four categories of sensing used in powered prosthesis control: kinematic sensors, such as inertial measurement units (IMUs) and encoders, to measure joint and limb motion; force sensors to provide force feedback at the ground and the user's socket; electromyographic (EMG) sensors to detect human muscle activity; and computer vision and range sensors to infer information about the user's environments.

Kinematics—IMU, Encoders

Almost all microprocessor controlled devices have an encoder for joint angle measurements and many devices also include an IMU for additional state feedback [18], [19], [21]–[24]. Encoders measure prosthesis joint angles and velocities, and an IMU is typically used to measure the global orientation and velocity of the prosthesis-side shank or the human's residual limb. These measurements are used in many forms of prosthesis control, including impedance control laws, reference trajectory tracking controllers, and gait phase estimators.

Forces Sensors

Many devices include a force sensor, typically a load cell distal to the ankle joint [23], [65], in the shank [18], [24], or proximal to the knee joint [17], [22], to detect ground contact, ground reaction forces, or Center of Pressure (CoP). Most commonly, these force sensor measurements are used to determine transitions between discrete gait phases in a finite state machine (FSM), especially between stance and swing phase. The work of [65] used the CoP to encode and modulate virtual constraints. Recently, a load cell was incorporated at the socket interface of a transfemoral prosthesis and a pressure sensor into the shoe of the prosthesis to provide real-time force feedback to complete the modeled prosthesis dynamics for model-based control [97].

EMG Sensors

EMG sensors measure electrical signals generated by muscles during contraction. Broadly speaking, there are two kinds of EMG sensors: surface-mount and implantable EMG sensor interfaces [98]. To our knowledge, there is only one study that utilized surgically implanted wireless intramuscular EMG sensors in lower-limb amputees for prosthesis control [99]; these surgically implanted EMG sensors are more commonly used in upper-limb prostheses [100]–[103]. Instead, the majority of existing studies on myoelectric control of lower-limb prostheses use bipolar surface EMG electrodes [68], [89], [98], [104].

A major limitation of surface electromyographic (EMG) signals is the recorded signals vary over time due to changes in skin impedance, day-to-day variations in electrode placement, and relative motion between the electrodes and underlying muscles during movements [100]. Moreover, electrode placement within the prosthesis socket can cause physical disturbances that induce noise in the EMG recordings, can compromise the socket suspension, and ultimately degrade user comfort [105]–[107]. Solutions for improving EMG signal reliability include further investigating implantable sensors [100]–[102], novel flexible electrode design [108], [109], custom prosthesis sockets with integrated electrodes [104], and developing EMG decoding algorithms and control paradigms [98]. Notably, novel flexible electrodes are particularly promising for improving the reliability and comfort of EMG sensors since they 1) are more compatible with a subject's prescribed prosthetic socket and liner compared to other within-socket surface EMG sensor, 2) will likely be less expensive than fabricating a custom socket and liner for each individual subject, and 3) have been shown to be more comfortable than commercial surface-mount electrodes [109].

Lastly, another challenge with using EMG signals in prosthesis control is that individuals with limb loss often exhibit variations in residual muscle activation and coordination [110], [111]. Thus, before EMG control can be effective for subjects who exhibit abnormal muscle patterns, further research is needed towards understanding how limb amputation influences EMG sensing.

Computer Vision and Range Sensors

To translate prosthetic walking to environments other than level-ground walking, additional sensors are required to estimate elements of the environment. Most commonly these sensors include cameras and range sensors.

Notably, cameras used for computer vision have demonstrated highly accurate predictions of complex terrain environments. For example, large datasets of wearable camera images of walking environments have been used to train convolutional neural networks for real-world stair environments [112]. Additionally, researchers have extracted visual features from similar large datasets and classified the images using a Bag of Words method for terrain identification [113]. Furthermore, some researchers use specialized cameras, such as depth cameras, to directly estimate various properties of the environment such as stair height and stair depth [114].

Similarly, range sensors provide depth information about the terrain. One example of range sensors is laser distance meters, which have been used with decision trees to classify terrain type as either ascending/descending ramps, ascending/descending stairs, or level ground [115]. Another example is LIDAR, which has been used (in combination with an IMU and joint encoders) to estimate the position of the prosthesis leg with respect to the ground for real-time reactive control for trip avoidance [116]. Notably, this was the first work to incorporate visual feedback into real-time planning of prosthesis control.

2.4 High-Level Task Estimators

As shown in Figure 2.2, after receiving input signals from the aforementioned sensors, the first component of the prosthesis controller is determining the desired tasks (i.e., locomotion mode and walking speed). This component can also be otherwise interpreted as deciphering user intent. In this section we will discuss the approaches to high-level control for estimating both locomotion mode and gait speed.

Estimating Locomotion Mode

The goal of locomotion mode estimation is to quickly and accurately predict the intended locomotion modes of a prosthesis user, based on real-time input signals (including kinematic, dynamic, and neuromuscular signals collected from both the device and human user). Example locomotion modes include level ground walking, ramp ascent and descent, and stair ascent and descent [90], [117]. In general, there are two approaches for this: analytical algorithms and machine learning classifiers. Additionally, some machine learning classifiers include the use of EMG sensing, which has been shown to improve classification accuracy but at the cost of relying on user-dependent classifiers.

First we will discuss analytical algorithms, which use predefined event triggers with sensor information to switch between locomotion modes. For example, [118] used a finite state machine (FSM) as a supervisory controller to switch between stair ascent, stair descent, standing, and level-ground walking modes. The transitions between these behaviors are based on foot contacts, direction of ankle motion, shank position, and time. Additionally, [92] estimated slope incline based on the angle of the foot during midstance—when the foot was flat on the ground. The researchers determined foot angle through forward kinematics with prosthesis joint encoders and an IMU on the residual thigh, and they detected midstance phase by a load cell below the ankle joint. Lastly, [30] also estimated ground slope when the foot was flat on the ground, as detected through foot load sensors, through a method similar to [119], [120].

The second method of estimating locomotion mode is to train machine learning classifiers using precollected training data. Such classifiers enable smooth and automatic transitions between locomotion modes, reducing the cognitive burden placed on prosthesis users, but require the collection of training data. Some common methods of classification for lower-limb prosthesis mode include support vector machines [121], artificial neural networks, linear discriminant analysis, maximum likelihood [122], [123], and Bayesian networks [124], [125]).

As mentioned, some machine learning classifiers involve EMG sensors [126]–[130]. The use of EMG for estimating locomotion mode is often termed *supervisory EMG*. One important component to supervisory EMG control is extracting features from the EMG signals and classifying patterns of these features for various locomotion modes. However, since EMG signals are non-stationary over walking gait cycles, it can be difficult to extract key features for walking; In comparison, extracting

key features is easier for upper-limb prosthesis control. One common approach of supervisory EMG control for lower-limb prostheses is to divide the gait cycle into discrete phases, and extract key features for each phase separately [127].

Generally, researchers have found that adding EMG signals to classifiers tends to improve classification accuracy [123], [131], [132] compared to only using mechanical sensors. However, the performance of such classifiers relies on the accuracy of EMG signals from the prosthesis user. While many studies have demonstrated supervisory EMG using EMG signals from residual limb muscles [127], studies have found that including additional sensors to intact muscles improves accuracy but also consequently increases complexity for daily use and sensor setup [98]. For example, [123], [127] used a combination of 10-16 EMG signals across both the residual and intact limbs. It is interesting to note that the reliability of EMG signals on the residual limb depends on the amputation level of the subject. One solution to improve the accuracy of EMG signals is to leverage TMR surgery to record signals directly from reinnervated residual muscles [128], [131]. Lastly, since EMG data is inherently noisy, researchers have discovered that the accuracy of classifiers that use EMG sensors can be improved by combining these signals with additional mechanical measures [117], [123], [131].

One open question when training machine learning classifiers is how much data should be provided during the model training (or specifically, how much “time history”). Recent work comparing strategies with and without time history found that including time history improved locomotion mode intent recognition accuracy [117]. Another open question regarding classifiers for locomotion modes is if the classifiers should be user-independent or user-dependent. The benefit of developing user-independent classifiers is that they generalize to new users without requiring new training data to be collected per subject. However, research has found such classifiers to be less accurate than user-dependent classifiers. For example, [90] found misclassification rates for user-independent classifiers to be significantly higher than those for the user-dependent system. It was hypothesized that this is in part due to the variance in subjects’ walking patterns. Similarly, [133] compared subject-independent and subject-dependent intent recognition across three machine learning algorithms (linear discriminant analysis (LDA), neural networks (NN), and a gradient tree boosting method called XGBoost) and also found that subject-independent classifiers result in significantly higher misclassification errors.

A major limitation of classifiers for locomotion modes is the reliance on rich sensor information. As argued in [134], although additional sensors and features tend to increase the performance of machine learning models, their inclusion also greatly increases the model complexity. Future research includes studying the minimum complexity of sensor information required for accurate classifiers. For example, [134] performed an analysis of sensor importance for a knee-ankle prosthesis and concluded that mechanical sensors (IMUs and Goniometers) were generally more important than EMG sensors. Another major limitation is that even for a user-independent classifier, a prosthesis with different sensors would require a new set of training data. Thus, future research directions include strategies for reducing the initial user-independent misclassification rate.

Estimating Gait Speed

The second component of high-level task estimation for lower-limb prosthesis control is to estimate the gait speed. As explained in [135], there are three existing techniques for determining walking speed 1) analytical algorithms 2) kinematic gait modeling, and 3) regression modeling or machine learning. Analytical algorithms are the most commonly used method because of its simplicity, but it suffers from long-term drift. One specific example is that of [92] which estimates gait speed based the displacement of the foot (approximated by the prosthesis-side leg geometry) and the time between steps.

Alternatively, kinematic models have also proven successful but are less accurate without subject-dependent calibration [136]–[139]. One example of this method is [73] which uses prosthesis shank, knee, and angle angles in a three-link planar leg model to compute the forward hip velocity in the sagittal plane. In stance, these researchers use gyroscope data, and in swing, they integrate accelerometer outputs.

One disadvantage associated with both analytical estimation and kinematic gait modeling is that they typically only update their prediction of gait speed once per gait cycle. This motivates the final method, machine learning classifiers, which provides a continuous estimation for gait speed. This method leverages similar classifiers as discussed for estimating locomotion mode [135], [140]–[142]. Specifically, the work of [135] evaluates three algorithms for determining gait speed: linear regression (LR), extreme gradient boosting (XGBoost), and neural networks (NN) for both subject-independent and subject-dependent datasets. The results found that

the machine learning algorithms performed competitively or better than analytical algorithms for both subject-independent and subject-dependent models.

Another advantage of leveraging machine learning classifiers is that they can also be trained to detect multiple important control variables simultaneously. For example, [134] introduces a combined locomotion mode classifier and environmental parameter estimator to provide accurate information on a user's current ambulation state. Specifically, the classifier in [134] identified mode classification, walking speed estimation, ground slope estimation, and stair height estimation.

Overall, the presented methods have demonstrated promising success towards accurately estimating gait speed. However, it is important to note that none of the existing methods easily generalize across users without either manual tuning or collecting additional training data. This limitation is common across many methods of prosthesis control and will be discussed further in Section 2.9.

2.5 High-Level Gait Phase Estimators

In addition to estimating locomotive tasks, the other component of a high-level control is estimating gait phase. It is widely agreed-upon that quickly and accurately estimating gait phase during prosthetic locomotion is an important component of prosthesis control [143]. Typically, a full gait cycle is defined as the periodic cycle starting from the impact of one foot on the ground to the following occurrence of the same impact event for the same foot. Note that researchers can estimate gait phase in either a discrete or continuous manner.

Finite State Machines for Gait Phase

In biomechanics, the human gait cycle is divided into different phases [144]. Controls researchers have commonly modeled lower-limb prosthesis controllers in a similar fashion using finite state machines (FSMs) [17], [26], [69], [145]. Each state represents a phase of the gait cycle and a fixed set of rules dictate when the FSM should switch to a different state. These transition conditions are based on thresholds of ground reaction forces and joint configuration. Within each state, different control laws are defined, often impedance control laws, which will be discussed in 2.6. Due to their simplicity and flexibility, FSMs are widely used in powered prosthesis control methods and are also used in commercial microprocessor-controlled knee prostheses (passive) [98], [146] Figure 2.3 depicts an example FSM.

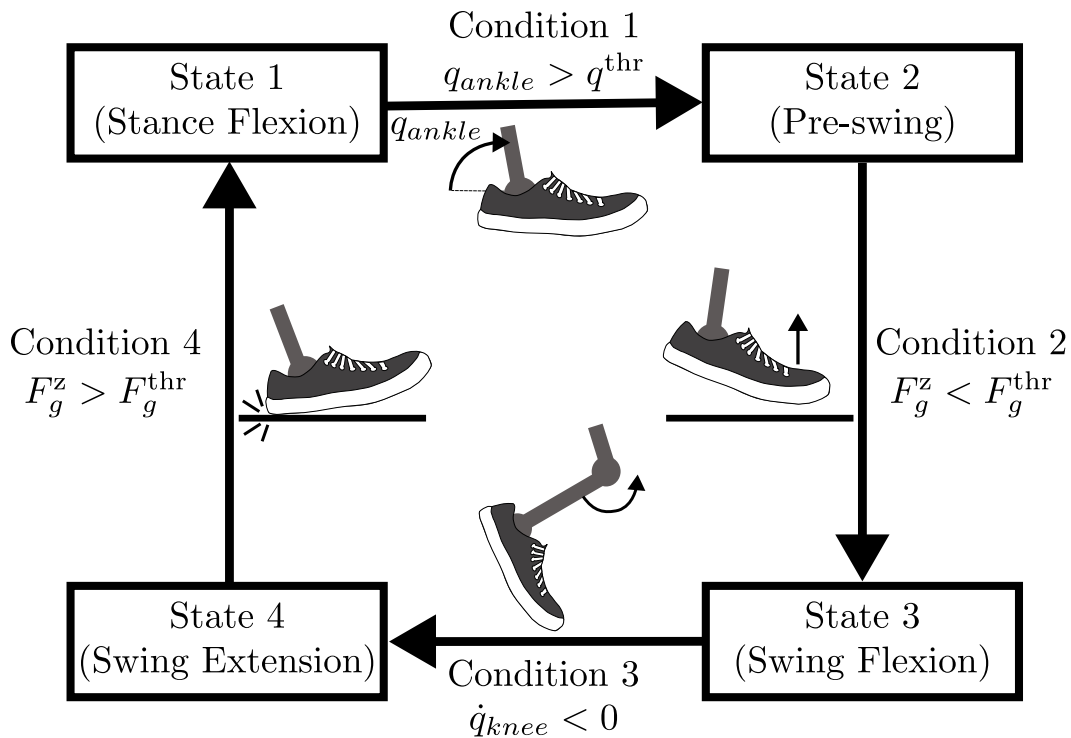


Figure 2.3: Finite State Machine. An example of an FSM used to determine gait phase, based on [17]. Here the gait cycle is divided into four phases, or states, and conditions based on the joint angle, velocity, and ground reaction forces dictate state transitions. In state 1, when the ankle angle q_{ankle} reaches the threshold q^{thr} , state 2 begins. Once the foot lifts off the ground, determined when the ground reaction force F_g is less than a threshold F_g^{thr} , the controller switches to state 3. This state ends when the knee velocity, \dot{q}_{knee} becomes negative. Finally, the controller starts back at state 1 when the foot strikes the ground in state 4, causing F_g to exceed its threshold.

Separate gait phase FSMs can be constructed for different locomotive modes [147], and a supervisory FSM, as described in 2.4, can switch between these modes. For example, [118] constructed gait phase FSMs for stair ascent, stair descent, standing, and level-ground walking modes and a supervisory FSM dictated which gait phase FSM to use. An alternative approach to realize multiple locomotive modes with an FSM involves using multiple transition conditions for a single gait phase FSM state, such that the controller can execute different sequences of states to realize modes. [148], for example, used a 6-state FSM, with multiple transition conditions between states, to realize 8 different activities of daily living (ADLs), both rhythmic and non-rhythmic behavior, without explicitly identifying the ADL. The FSM transitions were determined by the knee and shank angle, shank axial force and acceleration, and time.

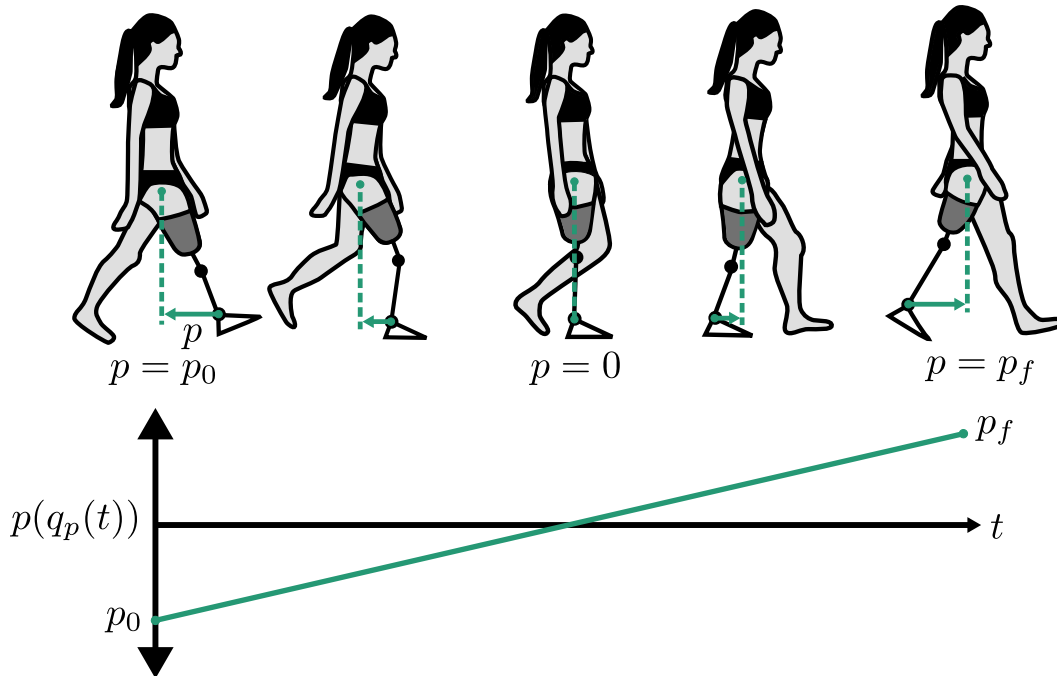


Figure 2.4: Progression of Monotonic Phase Variable. The horizontal forward progression of the stance hip relative to the ankle is an example of a physical quantity that is monotonic in a gait cycle, as explained in [150], allowing it to be used as a phase variable in a prosthesis stance controller. The initial and final positions of the hip provide the parameters p_0 and p_f , respectively, to parameterize the phase variable such that it goes from 0 to 1 during stance phase.

FSMs are simple to develop, flexible in their application, and the transition rules are intuitive to tune given the threshold parameters are typically based on ground reaction forces and joint angles. However, realizing multiple locomotive modes often requires more FSMs or more complex FSMs. This increases the number of parameters to tune and some of these parameter need to retuned for each user. Even after tuning, FSMs have robustness issues in performance. Researchers have found that when the user encountered unexpected ground height disturbances, the user's resultant abnormal kinematics led the FSM to skip a state. This led to large, sudden torque changes, which sometimes resulted in a fall [76], [149].

Continuous Phase Variables

To avoid the tuning and torque discontinuities that can accompany discretizing a gait cycle, researchers have investigated developing unified and continuous control methods using phase variables [65], [151], [152]. A phase variable approach provides a continuous mechanical representation of the gait cycle. Bipedal robotics

researchers use state-based phase variables to parameterize desired kinematic trajectories for a robot in a time-invariant way, such that motion being enforced on the robot is dictated by the state of the robot [153], [154].

Any measurable quantity of a walker's motion that is monotonic during a gait cycle can be used for the phase variable. One example of this is the linearized horizontal forward progression of the stance hip, which continuously increases during the stance phase of a gait cycle [150], as shown in Figure 2.4. This choice is an example of how a phase variable can be a function of multiple joint coordinates. By defining $q_p \in \mathbb{R}^{n_p}$ to be the vector of the n_p prosthesis configuration coordinates measured by kinematic sensors, a phase variable $\tau_q(q_p) : \mathbb{R}^{n_p} \rightarrow \mathbb{R}$ is generally defined by,

$$\tau_q(q_p) = \frac{p(q_p) - p_0}{p_f - p_0}.$$

Here, the state-based monotonic function $p(q_p) : \mathbb{R}^n \rightarrow R$ is parameterized by its initial and final values, $p_0, p_f \in \mathbb{R}$, respectively, in the gait cycle, such that $\tau_q(q_p)$ goes from 0 to 1 over the gait cycle.

One consideration in selecting a phase variable for a prosthesis is finding a quantity that the human has some volitional control over, such that speed of gait progression will be continuously modulated by the human body's progression. These options can vary with the level of amputation to ensure the selected variable is both affected by the human's motion and measurable by the prosthetic device. In the first instance of phase-based prosthesis control, [151] used the global tibia angle as the phase variable for a powered ankle prosthesis. This quantity is piece-wise monotonic in a gait cycle and can be measured by a sensor on an ankle prosthesis. However, when the foot of a knee-ankle prosthesis is flat on the ground, the prosthesis fully controls the tibia angle, removing the human's volitional control. To address this, other researchers used the linearized forward hip progression [35], [152], the center of pressure trajectory [65], and multiple joint angle and velocity measurements fused in an extended Kalman filter (EKF) [76] to estimate gait phase when the prosthesis was in stance.

While these methods achieved human-prosthesis walking on a knee-ankle prosthesis with phase-based control in stance, these phase variables cannot be used to realize phase-based control in swing since they require sensing on the human stance leg. [36] placed IMUs on the human's sound leg to use the human's linearized forward hip position for a phase variable, but wearing these IMUs in daily life would be inconvenient to the user. To avoid cumbersome sensors on the human, [155],

[156] examined potential phase variable candidates and determined that the polar coordinate of the hip's phase portrait provides a robust parameterization of the human gait cycle for both stance and swing phase. This phase variable proved beneficial in rhythmic tasks (i.e. walking) [157], [158], but its requirement of a well-defined thigh orbit inhibits its applicability to non-rhythmic tasks (i.e. kicking a ball). With the global residual thigh angle, shown to be piece-wise monotonic in gait [159], researchers were able to realize both rhythmic and non-rhythmic tasks [92], [158]. [92] showed how the phase variable could realize walking at different inclines by online automatic updating of phase parameters based on the user's behavior.

Phase-based control approaches pose an advantage by providing some volitional control to the user through the use of a mechanical sensors while avoiding the challenges posed by EMG control methods, which will be discussed in 2.6. Phase-based strategies also naturally adapt to changes in walking speed. [65], [92], [158], [160] demonstrated benefits of phase-based control for multi-joint prostheses including coordinating ankle and knee motion, realizing walking patterns that resembled healthy human patterns, and enabling amputees to walk at different speeds and inclines with a single controller. Ideally, the phase variable will be invariant across subjects [155], such that the control strategy will generalize across subjects. Compared to impedance and neuromuscular methods that require tuning of a large number of parameters, these approaches can reduce the number of tuning parameters and depend on clinically intuitive parameters [157]. The strategy of [65], for example, only required five parameters to be tuned.

One outstanding challenge with phase-based methods for multi-joint prostheses is the uncertainty regarding whether the prosthesis should be fully dictated by a state-based phase variable or when a time-dependent term is beneficial. When using the global thigh-angle as a phase variable, researchers have observed a slow ankle push-off [160] and a pause in the kinematic reference trajectories [92]. This issue was mitigated by introducing a time-based component in the controller [161]. The approaches in [35], [36] required a velocity modulating output in one phase which also introduced a time-based component into the phase-based controller. However, introducing a time-based component removes some volitional control from the human. It remains unclear what the best choice of phase variable is that the prosthesis can detect in both stance and swing, provides human volitional control,

and will progress forward at a natural rate in the closed-loop human-prosthesis system.

Machine Learning for Gait Phase

Another method of estimating gait phase is to leverage machine learning models. As with machine learning methods for estimating gait speed, these algorithms can provide either discrete estimates gait cycle events or continuous estimates throughout the gait cycle. Some examples of machine learning algorithms for estimating gait phase include: neural network classifiers to estimate gait phase discretized to 1% intervals using offline IMU data [162]; using offline data with hidden Markov models to detect 4-6 gait cycle events [163]–[167]; neural network models to filter raw measurements and provide an HMM with classifications [168]; neural networks to classify stance and swing phases based on EMG data [169]; and estimation of foot strike and toe off events using deep learning with neural networks [170], [171].

It is known that the choice of sensor used with the ML algorithm heavily influences the classification accuracy. A review of machine learning methods for gait phase detection found that after comparing several available wearable sensors for gait phase detection algorithms, foot switches and foot pressure insoles yielded the highest accuracy [172]. However, due to the sensitivity of these sensors to wear and placement, they are not considered suitable for daily activity applications. In comparison, IMUs are a more favorable sensor since they provide rich information about the walking cycle and are low-cost, low-energy, and durable. However, since they can be sensitive to movement artifacts, these sensors still require pre-processing. This pre-processing step can be accomplished within the learning framework [162].

2.6 Mid-Level Control via Torque Computation Without Reference Trajectories

After identifying the behavior and gait phase, some control methods will directly compute torque based on the task and gait phase estimates without a reference trajectory. This section will cover the various methods used to accomplish this.

Impedance Control

Impedance control was one of the first mid-level control techniques implemented on powered prostheses [17], and continues to be one of the most popular methods because of its simplicity and ability to replicate natural walking; the motivation behind why impedance control produces natural walking is that human joints have

been shown to behave like variable impedance controllers [173]. However, this technique requires careful tuning of various parameters per subject. Specifically, an impedance control law for the torque $u_{p,j}$ of a single joint, joint j , is as follows:

$$u_{p,j} = -k_j(q_{p,j} - q_{p,j}^e) - b_j\dot{q}_{p,j} \quad (2.1)$$

where $q_{p,j}, \dot{q}_{p,j} \in \mathbb{R}$ denote the position and velocity of the corresponding j^{th} joint measured through kinematic sensing, $k \in \mathbb{R}$ is the stiffness coefficient, $q_{p,j}^e \in \mathbb{R}$ is the equilibrium point (reference set-point), $b_j \in \mathbb{R}$ is the damping coefficient. Simply put, this control law relates position and velocity to torque, thus regulating joint torque by the state of the system and imposing a spring-damper behavior on a joint [25].

Impedance control strategies are typically paired with an FSM, as described in 2.5, where impedance control laws with constant parameters are defined for each discrete phase within the FSM and thus enforce passive dynamics within a state. These parameters differ between states of an FSM, which in part replicates the variable impedance observed in human joints and allows for the injection or removal of net energy. This creates a piecewise control law for the gait cycle. Some recent work [161], [174], [175] has defined impedance control laws with parameters that vary within a state, which do not enforce passive dynamics and may be able to better capture the variable impedance behavior of human limbs [176]–[178].

Impedance control is also capable of accomplishing behaviors other than walking through the adjustment of coefficients. For example, [26] realized the first instance of powered transfemoral prosthesis stair ascent and descent. Notably, this control strategy achieved knee and ankle kinematic profiles that matched healthy human profiles more closely than that of a passive knee-ankle prosthesis in stair ascent, and matched ankle profiles more closely in stair descent. Other achievements of impedance control within an FSM include the first powered knee-ankle prosthesis running [31], upslope walking [30], and variable cadence bilateral amputee walking [32].

As mentioned, the primary disadvantage of impedance control is the need to tune the coefficients within each FSM state for each prosthesis user and locomotion mode. Thus, there exist several methods in the literature for how to select these parameters. These user-customization methods are discussed further in Section 2.8.

Quasi-Stiffness Control

A subset of impedance control strategies is quasi-stiffness control. This approach determines the impedance parameters, used to define the state-torque relationship, through matching the relationship between a human's joint torque u_p^h and angle q_p^h . The slope, $\frac{du_p^h}{dq_p^h}$, of this relationship is called "quasi-stiffness" [71], [72]. The desired prosthesis torque $u_{p,j}$ for joint j is then determined by,

$$u_{p,j} = \frac{du_{p,j}^h}{dq_{p,j}^h}(q_{p,j})(q_{p,j} - q_{p,j}^e)$$

where the quasi-stiffness, $\frac{du_{p,j}^h}{dq_{p,j}^h} : \mathbb{R} \rightarrow \mathbb{R}$, is a function of the joint angle $q_{p,j}$. While quasi-stiffness and stiffness are equivalent in passive prostheses that only contain a spring, these concepts are distinct in powered prosthesis control [72]. [179] showed these torque-angle relationships in human ankles change as walking speed changes. For normal walking speeds, the torque-angle relationship is approximately linear for most of the stance phase with a notable shift at the beginning of push-off.

The work of [73] created a look up table of quasi-stiffness profiles from able-bodied walking experiments for both an ankle and a knee joint for each phase of walking. By inputting current joint angle and walking speed, the table gave a desired joint torque, normalized by the body mass of the user. The quasi-stiffness profiles were interpolated between based on walking speed. To realize stair climbing, [78] changed the torque-angle relationship with respect to the knee landing angle, an indicator of stair height. The algorithm increased the torque with taller stair heights, imitating the biomechanical relationship observed in humans [45]. The peak knee torque, timing of the peak knee torque, and the power and energy injected into the prosthesis changed with stair heights and climbing patterns.

The approach of [73] realized biological gait energetics over a wide range of walking speeds without any subject or speed specific tuning. Enforcing quasistiffness profiles allowed the prosthesis to modulate its mechanical work independent of the actual joint velocity. The net energy of the ankle increased proportionally with gait speed, a relationship that exists in healthy human walking [179]. The knee extension torque increased with speed. The maximum prosthesis ankle dorsiflexion in midstance and maximum plantarflexion in late stance increased with walking speed, another biomechanical trend [144], [179]. As explained in 2.7, this control method resulted in good temporal symmetry between the prosthesis and intact leg.

Torque-Based Controllers

Instead of aiming to emulate the human kinetics through an impedance model, some researchers directly command torque based on a predetermined desired torque profile. There are two main methods for obtaining reference torque profiles: using human joint torque data and handcrafting a profile. These profiles are generally parameterized by a progression variable $\tau_{q,t}$, which can be a state-based phase variable, i.e. $\tau_q = \tau_q(q_p)$, or be time, i.e. $\tau_t = t$. Very simply, this means the commanded joint torque u_p is equal to the reference torque profile u_{ref} at $\tau_{q,t}$:

$$u_p = u_{\text{ref}}(\tau_{q,t}).$$

Sometimes additional terms are added to this expression, such as a PD controller on a kinematic reference trajectory, as done in [76].

The first approach can be used to generate desired torque profiles in a task-dependent way, such as the control surfaces developed with respect to phase velocity and gait phase in [76]. The level of assistance can also be altered by scaling the desired peak torque magnitude, as done in [180]. This approach allows desired torque to be determined directly from human data, instead of depending on a large set of tuned parameters, and could be conducted in a subject- and task-specific way with appropriate datasets. However, replaying human torque profiles on a prosthesis may yield different performance results on various devices given their differing physical parameters, such as mass and inertia, which would influence the device dynamics as well.

The second approach typically handcrafts desired torque profiles based on a pre-specified function form and tunable shape parameters. While this method of control is not as common in the field of lower-limb prostheses, it is widely prevalent in the field of lower-limb exoskeletons [181]. One example on lower-limb prostheses is that of [84]. In this work, a time-based torque profile was constructed for an ankle prosthesis emulator using four parameters: peak time, rise time, fall time, and peak magnitude. The benefit of such a parameterized profile is that the behavior of the device can be adjusted via the control parameters for individual prosthesis users using a human-in-the-loop optimization problem. However, the results of [84] found that despite the user-specific customization (which has been shown to reduce metabolic cost for lower-limb exoskeleton users [182]), the controller failed to significantly reduce metabolic expenditure.

Neuromuscular Model-Based Control

Thus far in this section, the control approaches focused on replicating recorded torque profiles through an impedance or gait phase parameterized model. These methods depend on human data for the specific scenario at hand, meaning they require different sets of data to achieve various locomotive tasks. Neuromuscular model-based control methods instead aim to model the human's underlying neuromuscular system that produced these torques in various scenarios. If a human's high-level objectives are encoded in their neuromuscular system, controlling a prosthesis in a similar manner may provide a single, unified control method that leads to more natural and robust walking in a variety of environments.

As described in [70], joint torque, for joint j , produced by muscle (modeled using a Hill-type muscle tendon units (MTU) [183]) forces can be calculated using the formula:

$$u_{p,j} = r^m(q_{p,j})\mathbf{F}^m(\mathbf{S}^m(t), l_{\text{mtu}}^m, l_{\text{ce}}^m)$$

where $r^m : \mathbb{R} \rightarrow \mathbb{R}$ is the moment arm of muscle m around joint j depending on the joint angle $q_{p,j} \in \mathbb{R}$. Additionally, $\mathbf{F}^m : \mathbb{R} \times \mathbb{R} \times \mathbb{R} \rightarrow \mathbb{R}$ is the force produced by the MTU that depends on the time-varying muscle stimulation $\mathbf{S}^m : \mathbb{R} \rightarrow \mathbb{R}$, MTU overall length $l_{\text{mtu}}^m \in \mathbb{R}$, and MTU contractile element length $l_{\text{ce}}^m \in \mathbb{R}$. Here, the stimulation value is computed using various muscle-specific parameters:

$$\mathbf{S}^m(t) = \mathbf{S}_0^m + \sum_n \mathbf{G}_n^m \mathbf{P}_n^m(t - \Delta t_n^m)$$

where $\mathbf{S}_0^m \in \mathbb{R}$ is a constant pre-stimulation parameter and $\mathbf{G}_n^m \in \mathbb{R}$ is the gain on the time-delayed length or force signal $\mathbf{P}_n^m(t - \Delta t_n^m) : \mathbb{R} \rightarrow \mathbb{R}$ from muscle n acting on muscle m . Here Δt_n^m is the time step from the last time point. Lastly, the MTU lengths l_{mtu}^m and l_{ce}^m are computed using several muscle-specific reference parameters such as the ones explicitly listed in [184].

Some researchers determine these neuromuscular model parameters through optimization. For example, [69] optimizes the parameters of one MTU to fit the ankle torque-angle profile to that measured from a weight- and height-matched able-bodied subject. For multi-joint control, [70], optimizes the parameters of 7 MTUs to minimize the cost of transport and maximize the distance traveled for a human-prosthesis model.

With the resultant parameter sets, these control strategies led to adaptive behavior on prostheses when confronted with unexpected slope changes and trips. These results

suggest this neuromuscular model-based approach captures some balance recovery techniques that humans exhibit, making it more robust to variations in terrain and disturbances without explicit detection or change in control policy. However, one potential drawback of using neuromuscular models is the large number of parameters that are not clinically intuitive, making it difficult to tune.

Myoelectric Control

Another neuromuscular-inspired approach is *myoelectric* control which, instead of trying to emulate the neuromuscular function of biological limbs through a model, leverages neuromuscular control signals recorded directly from muscles. These signals are typically recorded by EMG sensors located inside the socket on the residual limb as mentioned in Section 2.3. The advantage of utilizing these signals in prosthesis control is that they provide real-time insight into the motions of the human user. Thus, unlike autonomous prosthesis controllers which are limited to cyclic movements during locomotion, prosthesis controllers that utilize EMG signals are advantageous in that they enable non-cyclic tasks and adaptation to different environments. For example, [104] introduced a volitional electromyographic (EMG) controller to modulate powered ankle plantar flexion by proportionally increasing the plantar flexion ankle torque based on EMG activity of the calf. The specific control law used in this work was of the form:

$$u_{ankle} = K_{emg}s_{emg} + K_0(q_{ankle} - q_{ankle,0}), \quad (2.2)$$

where $u_{ankle} \in \mathbb{R}$ is the torque applied to the ankle joint, $K_{emg} \in \mathbb{R}$ is the gain term that is adjusted based on the walking velocity and $s_{emg} \in \mathbb{R}$ is the muscle activation recorded captured by the EMG signal. Note that $K_0 \in \mathbb{R}$ is an initial stiffness term based on an equilibrium joint angle $q_{ankle,0} \in \mathbb{R}$ and actual joint ankle angle $q_{ankle} \in \mathbb{R}$ that is added to ensure a biomimetic plantar-flexion toe-off angle.

Additionally, [68] used proportional EMG control for a prosthesis knee in stance phase, normalizing the EMG signal by the average EMG peak recorded while a given subject walked with their passive prosthesis. This peak value is the only parameter that was tuned between users. This control method allowed the user to volitionally control the timing and amount of energy of the prosthesis actuation. With this approach, users were able to adapt the prosthesis movements to perform sit-to-stand motion, squat, lunge, walk, and smoothly transition between these activities without explicit classification of desired movement. Compared to using their own passive prosthesis, using an active prosthesis with this control method improved the users'

weight bearing symmetry and decreased the users' muscle effort in their sound limb and residual limb.

Other work with myoelectric control directly studies whether it is possible to utilize residual muscle activation signals for proportional myoelectric control during walking. Specifically, [79] implemented proportional myoelectric control to vary ankle mechanics during walking on a powered ankle prosthesis. Specifically the control signal sent to the device was proportional to the smoothed residual gastrocnemius electromyography (EMG) signal. The results showed that the a transtibial amputee subject was able to walk with a more normal gait than with his prescribed passive prosthesis, suggesting that using residual muscle signals for prosthesis control is possible, although it still requires further research.

In summary, the advantage of myoelectric control is that by interfacing directly with the prosthesis human user, EMG sensing enables versatile prosthesis control that is able to adapt to various situations [98]. Despite this clear advantage, there are several limitations inherent to EMG sensing, as discussed in Section 2.3. Also, in the case of transfemoral amputation, the muscles used for controlling the ankle joint are no longer available for EMG sensing.

Neural Engineering of Human Physiology

A possible solution to handle the lack of ankle musculature in transfemoral amputation is to engineer human physiology to recover amputated neural pathways using techniques such as targeted motor reinnervation (TMR) surgery. This surgery transfers residual nerves to alternative muscle sites during scheduled amputation procedures. To date, this technique has been predominantly applied towards upper-limb control of prosthetic arms [185]–[187] but there are few studies that demonstrates the potential of TMR towards lower-limb prosthetic control. In particular, [128] demonstrated improved dual-actuated prosthesis control through the use of reinnervated residual thigh muscles. The results found the classification accuracy of prosthesis user's attempted movements was higher for TMR amputees compared to non-TMR amputees, and that TMR amputees also completed virtual movements much faster.

The second example of reengineering neural pathways is an agonist-antagonist myoneural interface (AMI) [89]. This technique surgically connects two muscle-tendons in series such that the contraction of one muscle stretches the other. The purpose of this surgical connection is to provide proprioceptive information to the

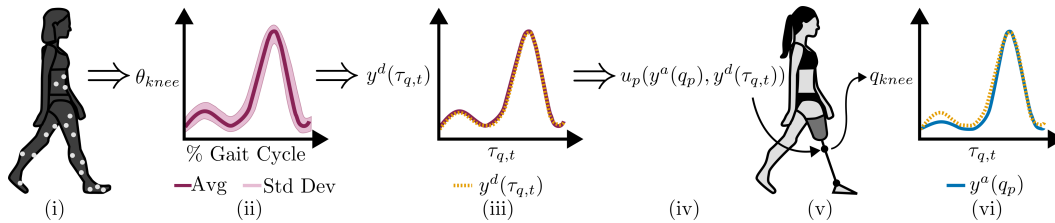


Figure 2.5: Common Process for Mid-Level Control via Kinematic Reference Trajectories. (i) Motion capture data is collected from able-bodied subject walking. (ii) The average and standard deviation is computed of each joint trajectory, such as the trajectory of the knee angle, q_{knee} , with respect to the percent gait cycle. (iii) A function, $y_d(\tau_{q,t})$, is fit to the average data, parameterized by some state- or time-based phase variable $\tau_{q,t}$. (iv) A torque, τ , is computed based on this desired trajectory and the actual trajectory, $y_a(q_p)$, of the prosthesis. (v) This torque is commanded of the prosthesis actuators. (vi) The resultant joint trajectory of the prosthesis, $y_a(q_p)$ is close to the desired trajectory, $y_d(\tau_{q,t})$. Steps (i) - (iii) are part of data-driven approaches to generate reference trajectories, described in Subsection 2.7, and steps (iv) - (vi) are part of tracking controller methods, described in Subsection 2.7.

human subject. Additionally, [89] developed a bidirectional efferent-afferent neural control architecture by affixing bipolar surface electrodes adjacent to the two muscles comprising each AMI. The researchers demonstrated that this approach improved volitional control of a 2DOF ankle-foot prosthesis. Additionally, the subject reported that the prosthesis aligned more closely with the perceived motion of their phantom limb. However, it should be noted that as with most forms of myoelectric control, the control method required extensive tuning that required retuning for each new subject and each time electrodes were placed. The parameters that required tuning included activation threshold for each muscle, relative torque-producing capacity of each virtual muscle, and the minimum co-activation for increasing joint impedance.

The last example of neural engineering is the replacement of sensory information about motion or interaction for lower-limb amputees. For example, researchers have demonstrated how residual neural pathways can be stimulated using implanted intraneural stimulation electrodes for the purpose of reducing phantom limb pain [188]. A case study on two transfemoral amputees found that the neural stimulation not only reduced phantom limb pain, but also increased walking speed and self-reported confidence while decreasing mental and physical fatigue [189]. These results suggest that sensory restoration is a promising novel technology for improving prosthesis walking.

2.7 Mid-Level Control via Kinematic Reference Trajectories Tracking

Instead of indirectly aiming to realize human kinematic trajectories through shaping of a torque model based on the system states, phase, and task, other mid-level control strategies design a torque law to track a specific reference trajectory. These approaches first generate a desired kinematic reference trajectory for the prosthesis joints. The control objective becomes having the actual trajectory of the system match the desired trajectory. These desired responses of the system are often referred to as *outputs*, or virtual constraints [154], which we denote with y and can be represented by the following,

$$y = y^a(q_p) - y^d(\tau_{q,t}, \alpha) \quad (2.3)$$

where y^a is the actual measured output of the system, y^d is the desired trajectory that is a function of the progression variable $\tau_{q,t}$. While some researchers construct outputs as functions of multiple joints [35], [190], most researchers prescribe outputs for individual joints. For simplicity, we write the outputs in this manner, as a function of an individual joint, i.e. $y_j^a(q_{p,j})$, and represent the vector of all of the outputs as $y^a(q_p)$. Based on these outputs, a torque is computed to track these trajectories, directly prescribing a desired kinematic motion for the given behavior and phase. The steps of a common process for this approach are illustrated in Figure 2.5.

Reference Trajectory Generators

This subsection will discuss the various methods used to generate prosthesis reference trajectories.

Minimum Jerk

[191] developed a minimum jerk control method that generates trajectories optimized to minimize the rate of change of acceleration, or jerk, and found these patterns to resemble human motion. The total jerk, $\mathcal{J} \in \mathbb{R}$, in a desired trajectory $y^d(t, \alpha)$ from time t_0 to t_f can be represented by,

$$\mathcal{J} = \int_{t_0}^{t_f} \ddot{y}_d(t, \alpha)^2 dt.$$

Modifying the desired trajectory y^d to minimize this cost function \mathcal{J} provides a way to maximize smoothness of trajectories over the given time span.

[73] used a minimum jerk trajectory generator to determine a prosthesis swing trajectory based on a starting swing angle and velocity; a desired swing duration,

and desired final joint angles, velocities, and accelerations. This control method provides a way to generate a smooth swing trajectory that spans a time duration proportional to the duration of the previous stance phase, encoding an adaptive response to the human's behavior. This method also allows direct dictation of the foot clearance by prescribing a maximum knee flexion angle determined through the human-prosthesis kinematics and desired clearance. Additionally the accelerations at maximum knee flexion are optimized based on able-bodied data.

This approach worked to address the limitation of impedance control methods with regards to speed adaptation. Impedance control parameters do not linearly relate to walking speed, forcing amputees to rely on compensatory strategies to walk at different speeds. This research resulted in a speed-adaptive prosthesis demonstrated on three transfemoral amputees. This control methods required no tuning between subjects, but solely relied on the input of the subject's body mass and height. Across various speeds, this controller emulated human kinematic trends better than the subject's passive prosthesis. The duration of stance, swing, and stride of the prosthesis had good temporal symmetry with that of the subject's intact leg. Additionally, the ratio of stance and swing duration of the prosthesis leg was very similar to that of the intact leg. The controller also increased ankle work proportionally with increased speed, a trend observed in healthy human walking.

Minimum jerk trajectory generators can also be used to continuously optimize a trajectory for a changing desired final position, as [91] did for a swing trajectory. While this approach and that of [73] applied jerk-minimization in its most basic form to generate a trajectory between desired points in a given time, jerk-minimization can be included as just a component of other more complex trajectory generation methods. For example, [192] minimized jerk when developing continuous functions that model human kinematics, to improve the smoothness of the functions to resemble natural human motion. This method will be discussed further in 2.7. Overall, minimum jerk strategies pose a benefit in their ability to yield smooth trajectories. However, the optimality of other aspects of the determined trajectory relies on the inputted target angles and duration, which minimum jerk control alone does not direct a user in how to select these.

Heuristic Algorithms

To determine desired angles for a reference position or trajectory of the prosthesis joints, [68], [78], [91] developed heuristic algorithms to modify these references

based on current angles, velocities, and accelerations of the prosthesis joints and residual thigh. These heuristic algorithms were comprised of handcrafted function forms and hand-selected parameters that define the functions. The researchers designed these algorithms to emulate the biomechanical relationships between joints observed in human locomotion. [91] created more human volition in their minimum jerk swing controller by continuously optimizing the swing trajectory for updated desired maximum knee flexion angles. These desired angles were modified based on the user's residual thigh movement. This approach did not require user-specific tuning and allowed users to volitionally modulate foot clearance to smoothly traverse over obstacles without explicit classification of the environment obstacle. [78] continuously modified the desired knee and ankle angles in swing based on the residual thigh's motion. This allowed the swing trajectory to vary between stair heights and gait patterns (step-by-step, step-over-step, two-step), providing sufficient foot clearance and proper foot placement for tested stair heights and climbing patterns without explicit classification of the environment and gait pattern. This controller also allowed the user to change their cadence when climbing different stair heights or using different climbing patterns. [68] and [78] modified the desired stance ankle position based on the prosthetic knee's current position.

Although these methods do not use a phase variable, similar to phase-based control approaches, they continuously modulate the prosthesis behavior based on the current behavior of the prosthesis-side limb. These heuristic algorithms provide some volitional control to the human in a way that generalizes between subjects and does not pose the challenges EMG control does, as described in 2.6. One limitation of these methods is their heuristic nature. It is unclear what the optimality of these methods are or what is a systematic approach to realize these behaviors on different devices or for different locomotion modes.

Geometric Control

One aspect of human walking motion that is invariant for different subject weights [193] and gait speeds [194] is the center of pressure (CoP) trajectory, or effective shape. [190] encoded the effective shape into prosthesis output functions and used control to virtually constrain the distances from the CoP to the center of rotation of the knee and thigh to a constant radius of curvature. An advantage of this continuous control approach for stance is that the effective radii and rotation centers to determine the effective shape are defined with respect to the user's height, and

therefore do not require tuning. These five gains are the only hand-tuned parameters, which is significantly less than impedance and neuromuscular model approaches, and these are normalized by a subject's body mass as a starting point. Also, control switches were eliminated in the stance phase. Assumptions made for this approach introduce some limitations. The researchers modeled the effective shape with constant curvature, however the curvature is typically non-constant in human walking. Also, they modeled the foot contact as holonomic, but in reality it is not truly holonomic. Additionally, the prosthesis can only measure and enforce effective shape while in stance and hence requires a different swing controller.

Data-Driven Kinematics

An alternative way to encode human-like motion into prostheses is to design joint output functions to match human joint kinematic trajectories. Researchers typically parameterize these trajectories with a state-based phase variable. Different human data is used for different behaviors, such as slopes and speeds. For example, [158] defined desired output functions with discrete Fourier transforms, that provided linear transformations of able-bodied human data. Here, different virtual constraint sets were generated for various level-ground walking speeds and walking inclines. These virtual constraints were all parameterized with the same phase variable, the phase of the prosthesis-side hip.

Instead of having separate sets of outputs for different speeds and inclines, [192] developed a continuous model that encoded human gait kinematics for various tasks. The kinematic predictive model y_{kin}^d was comprised of continuous functions of gait phase τ , a subject's walking speed v , and ground incline angle β . These functions were defined by a summation of N basis function $B_i(\tau)$ weighted by task functions $C_i(v, \beta)$,

$$y_d^{\text{kin}}(\tau_{q,t}, v, \beta) = \sum_{i=1}^N B_i(\tau_{q,t}) C_i(v, \beta) \approx q_p^h(\tau_{q,t}, v, \beta).$$

The researchers generated these basis model functions through a convex optimization desired to make the basis model fit human kinematic data q_p^h while minimizing jerk and constraining range of motion. [92] used this model as a reference trajectory generator of a knee-ankle prosthesis by inputting ground incline, speed, and phase estimates.

[76] constructed another form of a continuous model of human kinematic data through sparse Gaussian process (GP) regression models. These GP functions

formed control surfaces of joint angles, velocities, and torques with respect to gait phase based on able-bodied data. Given the phase variable and phase velocity as inputs, desired angles, velocities, and feedforward torques were determined through these control surfaces.

These approaches provide smooth kinematic models with respect to gait phase and task variables allowing prostheses to replicate human kinematic trajectories for varying conditions. However, while these kinematic trajectories may be what humans have deemed optimal for walking with their biological limbs, it is unclear whether matching kinematic trajectories of able-bodied individuals improves physiological outcomes for individuals with amputation. Additionally, it remains unknown how optimal trajectories for an artificial limb may vary for devices with differing physical properties.

Hybrid Zero Dynamics

To account for the physical parameters of the prosthesis device and determine trajectories in an optimal way, researchers have leveraged model-based control methods from bipedal robots. Bipedal robotics control researchers developed the framework of hybrid zero dynamics (HZD) to generate human-like periodic walking motion with formal guarantees of stability [153], [195]. They employed a hybrid system to model both domains \mathcal{D} of continuous dynamics, during stance and swing phases, and impact dynamics, Δ , at foot strike, present in bipedal walking [154]. These impact dynamics are triggered in the hybrid model when the system reaches a certain condition, called the guard S . In the case of a bipedal walker, this condition is when the foot reaches the ground. When the system is underactuated, the dynamics also contain uncontrollable dynamics, or *zero dynamics*, which evolve on the zero dynamics surface \mathcal{Z} . During the ankle push-off phase, the center of mass exits a biped's support base and the biped becomes underactuated, meaning it cannot fully control its motion [196], [197]. To guarantee these zero dynamics will adhere to a periodic orbit even through impact, i.e. impact invariance, researchers generate trajectories for bipedal robots with the following stability constraint in an HZD framework [198]:

$$\Delta(S \cap Z) \subseteq Z.$$

This constraint restricts the system such that when the evolution of the system on the zero dynamics surface Z reaches the guard surface S , the impact map Δ maps the states back to the zero dynamics surface Z . In other words, the underactuated

dynamics remain stable even after a bipedal walker's foot strikes the ground. These methods realized stable bipedal robotic walking in various works [195], [199]–[202].

The work of [35] applied HZD in the context of prosthesis control, generating desired trajectories for the prosthesis system that satisfied these formal guarantees of stability for the human-prosthesis model. [36] extended this hybrid model to a multi-domain hybrid system to model the changing contact points that occur in walking, and realize human heel-toe roll behavior on a knee-ankle prosthesis.

This approach provides a systematic method to generate prosthesis trajectories that resemble able-bodied joint trajectories while also satisfying formal guarantees of stability for the specific subject and prosthesis device under consideration. This optimization framework naturally allows constraints related to human-likeness, comfort, and physical limitations to be incorporated in trajectory design. Additionally, these trajectories can be optimally chosen to reduce the mechanical cost of transport of the robotic human-prosthesis model. This strategy also generalizes to realize different behaviors, such as stair-climbing [203]. A challenge with this approach is the dependency on the human model—including the expected motion prescribed to the human in the optimization. The validity of the stability guarantees depend on this model. One other requirement to maintain these stability guarantees is a tracking controller with convergence guarantees to ensure adherence to the stable periodic orbits. The next section will discuss different types of tracking controllers, including a control Lyapunov function approach which provides such a convergence certificate.

Tracking Controllers

After a reference trajectory is determined for a particular task and gait phase, the controller will compute a torque to track these trajectories.

PID Control with Feedforward Terms

A standard control method for trajectory tracking is proportional-integral-derivative (PID) control. This control law is defined by the positional errors, the integral of the positional errors, and the derivative of the positional errors (i.e. the velocity errors) and a tuned gain on each form of error to provide a corrective action to the system. For prosthesis reference trajectory tracking, researchers most commonly choose a

form of a PID controller, sometimes with the addition of a feedforward term u_{ff} :

$$u_p = k(y^a(q_p) - y^d(\tau_{q,t})) + k_i \int_0^t (y^a(q_p) - y^d(\tau_{q,t})) dt \\ + b(\dot{y}_a(q_p) - \dot{y}_d(\tau_{q,t})) + u_{ff}(\tau_{q,t}).$$

Here k_i is the gain on the integral term. It is interesting to note that PID control is a form of impedance control, as described in 2.6. Typically prosthesis control literature considers “impedance control” to be used with a single reference set-point, and “PID control” to be used with a reference trajectory. However, both use tuned parameters to effectively create a spring-damper behavior around a reference.

[65] used a PD controller to approximate a partial feedback linearizing controller to enforce effective shape outputs. [158] and [160] also tracked output trajectories with PD control, but in [158], a damping term was added to the actual velocity of the joints, as opposed to the velocity output tracking error to create a smoother behavior. This desired torque was commanded directly of the knee, but was provided as an input to an ankle control loop. In this loop, a couple torque laws were summed for the ankle. First, a friction compensator was used to reduce the ball screw transmission effects. Second a proportional-integral (PI) controller was used on the error between the measured torque, determined by a uniaxial force sensor and the ankle joint forward kinematics, and the desired torque. [92] used a PID controller to track the speed and incline-specific reference trajectories, that were modulated by the global thigh angle of the residual limb as the phase variable. This approach only required a dozen tunable parameters that were tuned once during level ground walking, and resulted in the prosthesis joint trajectories resembling human kinematic trends for continuously varying speeds and inclines.

Some researchers add a feedforward term to a PD controller based on human data or the physical parameters of the prosthesis to reduce tracking error. [76] added a feedforward torque based on the human torque control surface to a PD controller formed with the desired joint angles and velocities from control surfaces formed with human kinematics. [73] added a feedforward term based on inertia, gravity, and friction to a PD controller tracking the generated minimum jerk swing trajectory.

PID control provides a simple way to realize a desired trajectory. There are typically fewer gains to tune than an FSM with multiple impedance laws, and these gains can often be used for multiple behaviors and subjects. While PID control generally achieves good tracking for the ballistic motion of prosthesis swing phases, tracking

errors are generally present in stance phases. During stance phase, a prosthesis bears the weight of the user and high gains are required in order for a PID controller to produce a large enough torque to compensate for the moment produced by the user's dynamic load. However, when the prosthesis is no longer supporting the human's weight in subsequent gait phases, these high gains can cause oscillations and aggressive motions. This motivates the need for more sophisticated controllers, such as Control Lyapunov Functions as discussed next.

Control Lyapunov Functions

To account for the user's dynamic load, researchers have investigated how to apply model-based methods from bipedal robots to prostheses. One model-based tracking approach bipedal control researchers use is control Lyapunov functions (CLFs) [199]. CLFs provide a sufficient convergence rate to guarantee stability to the hybrid periodic orbits generated through HZD. A CLF, V , is a positive definite function that can be formed with the vector of outputs y and their derivatives \dot{y} . Using $\eta = (y^T, \dot{y}^T)^T$, we have,

$$c_1 \|\eta\|^2 \leq V(\eta) \leq c_2 \|\eta\|^2 \quad (2.4)$$

$$\dot{V}(\eta, \mu) \leq -c_3 V(\eta), \quad (2.5)$$

where c_1, c_2, c_3 are positive constants. Taking the derivative of the CLF, $V(\eta)$, brings in the output dynamics, which includes an auxiliary control input μ , to the expression of $\dot{V}(\eta, \mu)$. It is through this auxiliary control input that the CLF derivative, $\dot{V}(\eta, \mu)$, can be ensured to be less than the quantity $-c_3 V(\eta)$ to guarantee system stability. This auxiliary input is formed through the following,

$$\mu = \dot{J}_y \dot{q}_p + J_y \ddot{q}_p,$$

where J_y and \dot{J}_y are partial derivatives of the outputs y . For details, see [77]. Here, μ is a function of the accelerations of the system, \ddot{q}_p , determined through the prosthesis modeled dynamics, given by the Euler-Lagrange equation [204],

$$\ddot{q}_p = D_p^{-1}(q_p)(-H_p(q_p, \dot{q}_p) + J_{c,p}^T(q_p)\lambda_{c,p} + J_{f,p}^T(q_p)F_f + B_p u_p).$$

Here, D_p is the inertia matrix; H_p contains the Coriolis, centrifugal, and gravity terms; $J_{c,p}$ is the partial derivative of the holonomic ground contact constraints that are enforced through the constraint wrench forces and moments $\lambda_{c,p}$; $J_{f,p}$ projects the interaction forces F_f between the human and the prosthesis measured by a force

sensor; and B_p is the actuation matrix that projects the torque vector u_p . Through this chain of equations, one can see how the CLF stability condition (2.5) is a function of the control input torque vector u_p . Hence, the torques can be selected to satisfy the CLF inequality to guarantee stability. Often times, this CLF stability condition is placed as a constraint in a quadratic program (QP). The QP then determines the torques that optimally satisfy this constraint while minimizing a given cost.

These CLFs rely on a model of the full-order system, and in the case of a prosthesis, the human dynamics are unknown. To address this, [35] constructed a CLF just on the outputs, such that the controller was model-independent. To provide some model information to the system, impedance control laws were provided as a feed-forward term. The impedance parameters were obtained through a least squares error problem [205], designed to match the impedance control law to the human-inspired controller [195] constructed with the desired trajectories. This systematic approach allowed direct implementation on a prosthetic device with minimal human-in-the-loop tuning. This optimization-based controller improved tracking performance and decreased net mechanical work of a powered knee-ankle prosthesis compared to impedance control and PD control methods. Using a multi-domain hybrid system model, [36] extended this work to the multi-contact case to realize prosthesis ankle push-off.

One specific instance of a model-based CLF controller used for bipedal robots is the feedback linearizing controller. [152] constructed a feedback linearizing controller for a human model, and applied it in simulation to the human portion of a human-prosthesis system, while a PD controller controlled the prosthesis. The work of [65] constructed a feedback linearizing controller for the prosthesis portion utilizing the interaction force between the human and the prosthesis. This work was extended in [206] by constructing feedback linearizing controllers for the human and prosthesis using only their respective locally available information and demonstrating stability and robustness in simulation. Building off of this, other researchers developed a general framework for constructing feedback linearizing controller for subsystems that are separable from the rest of the system [207]. This work also formally proved this approach yields equivalent subsystem controllers to those generated by feedback linearization on the full-order system, meaning it has the same formal guarantees of stability. To provide more model-based controller options, [208] developed a generalize class of stabilizing controllers using CLFs in this separable subsystem framework. By designing trajectories through the asymmetric multi-domain HZD

method in 2.7 to match height and weight-specific able-bodied walking data, stable periodic orbits are found for the prosthesis system. Assuming the human follows a stable limit cycle [209], any controller in this subsystem class guarantees full-order system stability. Specifically for the prosthesis, this class of controllers only requires a load cell and an IMU at the human-prosthesis interface, in addition to prosthesis joint encoders, to realize model-based control and guarantee stability of the human-prosthesis system.

A controller of this class was realized through an online-optimization based approach with force estimation in [210] and real-time force sensing at both the socket and the ground in [97]. Most recently, this controller was extended to the case of multi-contact walking to emulate the heel-toe roll observed in human walking, generating ankle push-off behavior [77]. This controller was demonstrated on two able-bodied subjects that wore a knee-ankle prosthesis through a bypass adapter. The reference trajectories generated through HZD were modulated by the linearized hip position as the phase variable in stance phase, and by time in swing. This systematic methodology generates and realizes height and weight-matched healthy human kinematic trends, without tuning between subjects. This control method achieved better tracking performance than a traditional PD controller, enabling better replication of human kinematic trajectories.

As opposed to PID control, this model-based strategy allows the prosthesis to dynamically sense the human's load, enabling the prosthesis to leverage these dynamics or compensate for this load to achieve its desired motion. Additionally, this CLF approach provides a convergence certificate, that when paired with stable hybrid periodic orbits generated with HZD, provides formal guarantees of stability for the whole system. The optimization-based implementation of CLFs allows additional constraints and optimality criteria to be incorporated in the framework.

2.8 User-Specific Customization

As discussed throughout the review so far, a particular challenge of prosthesis control is customizing the locomotion for every individual user to optimize for various metrics aimed at naturalness, efficiency, and responsiveness. While some methods of control require less customization because they are able to generalize across users, experimental results have largely demonstrated that user-specific customization yields improved performance [51], [147], [211]. This motivates the need for fast and intuitive methods of user-customization that can be applied to a wide va-

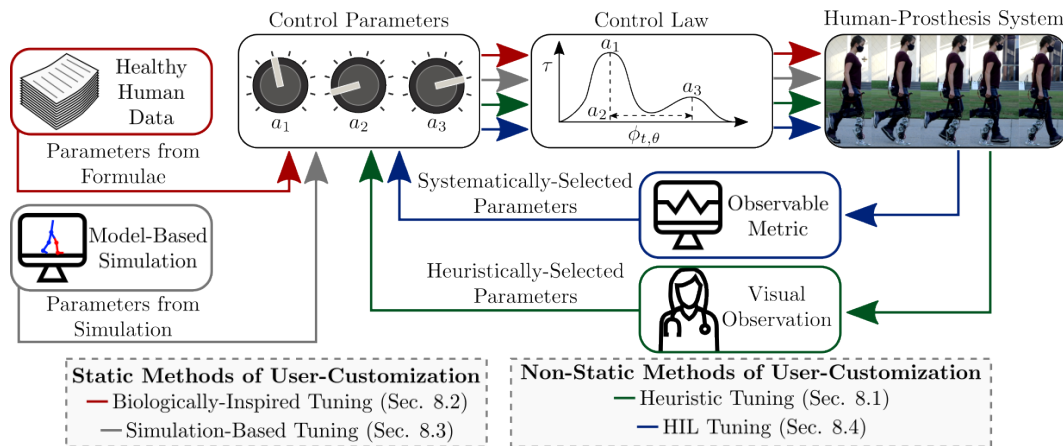


Figure 2.6: Methods of User-Specific Customization. We present four methods of customization, each illustrated using a different color: (red) biologically-inspired tuning which leverages relationships derived from biological systems and data; (grey) simulation-based tuning which leverages computer-based environments to predict which parameters would result in optimal behavior; (green) heuristic tuning which selects new parameters in each experimental iteration based on a clinician or user’s observations; and (blue) human-in-the-loop tuning which assigns numerical metrics to the experimentally-obtained prosthesis walking and uses algorithmic tools to predict new parameters to try in the subsequent iteration.

riety of control techniques. To date, four methods of user-customization have been explored: heuristic tuning performed by either a domain-expert or driven by feedback from the human user; automatic parameter selection based on biological data; parameter optimization using simulation-based software; and systematic tuning via human-in-the-loop testing.

Heuristic Tuning via Trial & Error

The oldest and most common method of user-customization for prosthesis control is to manually adjust various control parameters using the clinician (or an expert operator) perception of the walking [147], [212]. Note that while patient preference has always been taken into account during the tuning process, recent research has also begun formally accounting for user preference to study the underlying correlates [213] of user-preferred prosthesis control.

While heuristic tuning is straightforward, it requires onerous testing with the prosthesis user and a technical expert (typically an engineer or a clinician). For instance, the process of tuning impedance parameters and FSM thresholds has been shown to take several hours for each prosthesis user [31], [147]. This long tuning time is

widely referenced as one of the reasons why dual-actuated powered prostheses have not yet been commercialized for clinical use [51].

One potential solution for reducing the clinical time required for heuristic user customization is to make the tuning process more intuitive. For example, [51] conducted a case study on the use of an intuitive clinical control interface. The results found that through the intuitive interface, the tuning process was reduced to less than 10 minutes.

Another solution is to reduce the number of parameters that require tuning. Notably, recent work found that only 2-3 coefficients required subject-specific tuning per ambulation mode [214] for a powered knee-ankle prosthesis. This tuning process took approximately 30-40 minutes per subject. Specifically, this work attributes the success to the pairing of the impedance-based controller with a finite state machine and the translatability of impedance settings.

Biologically-Inspired Parameter Selection

Another method for reducing the time required for user customization is to set certain control parameters using physiological values measured from biological systems. For example, previous research has discovered formulas to automatically tune several parameters of impedance control [147]. One such formula, taken from [215], related the impedance stiffness parameter for the ankle joint $k_{ankle} \in \mathbb{R}$ to be a function of the user's body mass $W \in \mathbb{R}$ and the angle of the ankle joint $q_{ankle} \in \mathbb{R}$:

$$k_{ankle} = W(0.237q_{ankle} + 0.028). \quad (2.6)$$

This stiffness expression was found by characterizing the impedance of the ankle in a perturbation study.

Another way to leverage trends from human locomotion to automatically set impedance control parameters was introduced in Section 2.6. Specifically, quasi-stiffness control uses biological relationships observed in human walking between joint torque and joint angle to determine impedance parameters. Effectively, this method aims to emulate the same quasi-stiffness of a biological joint on a prosthesis joint. Thus, a similar method for automatically determining impedance parameters is to directly estimate human joint impedance [177], [216].

Lastly, researchers have leveraged human joint torque profiles to design variable impedance control laws [161]. Specifically, this work optimized coefficients for

phase-based polynomials to define an impedance control model that fit the able-bodied dataset.

Simulation-Based Optimization

The third method of user customization is to optimize the control parameters using simulated results from simulation environments. A simulation environment commonly used in lower-limb prosthesis control is OpenSim [217], [218]. This simulation environment allows operators to study human biomechanics resulting from prosthesis control. However, a known limitation is that it does not accurately capture human adaptation or disturbances.

Other simulation environments have also been created using musculoskeletal model dynamics. For example, [70] created a neuromuscular model for the full prosthesis-side limb (residual thigh and prosthesis) and included models of the prosthesis series elastic actuators. Fifty-three parameters defined this neuromuscular control model. This set of parameters were determined through a 2-stage optimization that first aimed to minimize cost of transport and in the second stage, aimed to maximum distance traveled over uneven terrain. For this optimization, the researchers created an amputee-prosthesis model by modeling the amputee with a neuromuscular model, modeling the residual thigh as a severed limb, and by modeling the prosthesis as a rigid-body with the physical parameters of the given device.

Lastly, simulation environments can be created using the rigid body dynamics of a human-prosthesis model. For example, [34] developed a method to determine impedance parameters through an ODE parameter estimation algorithm that aimed to match healthy human kinematic trajectories for a bipedal model built with physical parameters of a given prosthesis device and of average human data. Similarly, [77], [86] developed a human-prosthesis model to determine parameters of an HZD optimization framework [195], [198] that defined prosthesis trajectories that satisfied stability guarantees for the human-prosthesis model. This provides an automatic way to generate kinematic reference trajectories for a given prosthesis device and in a height- and weight- specific way for a subject. Similarly, [87] leveraged an HZD optimization framework with the addition of a musculoskeletal model to systematically optimize the prosthesis trajectories to match healthy myoelectric patterns.

Human-in-the-loop Tuning

The final method of user customization leverages human-in-the-loop (HILO) testing to systematically optimize specific parameters for specific objective metrics. One commonly utilized HILO framework is reinforcement learning [219]–[221]. For example, [222] developed a reinforcement learning (RL) framework to automatically tune 12 impedance control parameters (3 parameters in each of the 4 FSM states) with the goal of generating normative target knee kinematics. Similarly, [223] also demonstrated reinforcement learning towards tuning 12 impedance control parameters, but instead the tuning objective was to mimic the motion of the intact knee.

The advantage of RL-based control designs is that this method of tuning is particularly successful towards non-intuitive control parameters. However, the main limitation is that it relies on subjectively determining the corresponding performance measures. This is especially challenging since it is not clear which numerical metrics are most important for prosthetic walking.

To address this challenge, some researchers have also utilized inverse reinforcement learning to first automatically obtain performance measures, which can then be used in a reinforcement learning framework [211]. They argue that joint impedance parameters in a finite state impedance setting require manual tuning to provide personalized gait assistance. They also argue that a limitation of their previous work with model-free RL [219]–[221] towards automatically tuning 12 impedance control parameters is that prescribing knee movement profiles for each user and each task is not feasible. Thus, they reformulate the target movement profiles to mimic the contralateral joint of the intact leg.

Another common strategy is to frame the HILO problem as an online-learning problem. In particular, [224] framed the optimization problem as a dueling bandits problem to automatically select which parameter set (out of 9 potential parameter sets) a prosthesis subject most preferred. Notably, this strategy addressed the problem of high-dimensional parameter spaces by using an offline optimization step (conducted using the Covariance Matrix Adaptation Strategy [225]) to optimize 43 neuromuscular control policy parameters using existing gait data from 9 human subjects. In total, this tuning procedure consisted of approximately 45 minutes of walking, with 15 minutes of hand-tuning required prior to the Bayesian optimization procedure. Notably, this work is one of the first to formally incorporate subjective assessments of user preference for lower-limb prostheses using HILO.

Lastly, [84] utilized a Covariance Matrix Adaptation Evolution Strategy to optimize parameters of an ankle prosthesis torque profile for metabolic rate. The authors chose to use this optimization strategy since gradient descent is inherently sensitive to measurement noise and Bayesian optimization is not robust to human adaptation over time.

2.9 Discussion

As control of prostheses becomes more complex, so does the task of user-specific tuning. Thus, future research is needed towards creating control architectures that can generalize across prosthesis users and conditions, as well as towards creating intuitive methods of user customization. To bring these devices into the real-world, there remain several items that need to be addressed. In this section, we will highlight and discuss a few of these items, separated into open problems and practical considerations.

Open Problems

There are several remaining *open problems* in the field of powered prosthesis control that need to be addressed for commercial viability.

Open Problem 1: Creating prosthesis controllers that generalize across subjects and tasks

As discussed, achieving natural, efficient, and responsive prosthesis performance with state-of-the-art control methods requires extensive tuning, which can be especially arduous for multi-joint prostheses. Hence, there is a discerning need for control methods that generalize easily across tasks and users. Such prosthesis controllers would significantly reduce the amount of user-customization required in a clinical setting, improving the commercial viability of powered prostheses.

One existing approach for developing prosthesis task and gait phase estimators that generalize across users is the development of user-independent machine learning classifiers [90], [133]. However, to expand these classifiers to a wider variety of locomotion modes and users, the collection of larger and more diverse data sets is required [226]. While this entails an extensive amount of human-subject experimentation and data collection, the obtained data sets would be extremely valuable training data for classifiers.

Second, an approach to realize mid-level controllers that retain clinical benefits across a variety of prosthesis users is to develop controllers that account for subject-specific differences and adapt to the human's real-time motion. Model-based approaches, such as HZD and neuromuscular model control, utilize analytical models of the human-prosthesis system. These models can account for subject-specific differences such as weight, height, and limb length. If these models were improved to capture additional subject-specific differences, such as muscle strength, and to better predict a human's motion, they could be leveraged to systematically generate prosthesis controllers in a subject-specific way. Control strategies that utilize external sensors, such as phase-based approaches and heuristic algorithms, have demonstrated adaptability to an individual's real-time motion. Exploring ways to integrate real-time human sensing into model-based control strategies could build adaptive capabilities into these systematic methods.

Ideally, by developing both of these techniques (user-independent task estimation and subject-specific mid-level controllers), no additional tuning would be required. However, if there still existing parameters that require tuning, it is important that these parameters be designed such that they can either be automatically tuned using self-tuning algorithms, or that the parameters are clinically friendly. Examples of clinically intuitive parameters are the amount of knee flexion and ankle push-off, and the transition point for ankle push-off, as used in [227]. These chosen parameters allowed a prosthetic clinician to tune a knee-ankle prosthesis controller for an amputee subject in 10 minutes. Similar parameters were used in [160] where subjects were able to walk comfortably with the default parameters of their controller but the parameters could be tuned to accommodate different walking styles. Overall, to bring the achievements realized in lab settings discussed in this review to the daily lives of a large population of amputees, we see the answer to be a control method that both generalizes between users and contains clinically intuitive tunable parameters.

Open Problem 2: Ensuring user safety

Beyond realizing the current achievements in the real-world, an open problem in prosthesis control is ensuring user safety through fault prevention. This relies on both understanding conditions of failure to enable quick fault detection as well as the development of active control strategies for mitigating faults. Compared to passive prostheses, powered prostheses have a unique capability for active fault prevention. This includes preventing stumbles due to obstacles or external perturbations. How-

ever, as powered prostheses become more complex, this also introduces additional opportunities for internal faults. Thus, powered prostheses also have a growing need for control schemes that are robust to control faults.

The first component of fault prevention research includes studying the biomechanic response of human-prosthesis balance recovery. Existing research towards this includes simulating uneven terrains [228], [229], introducing obstacles during prosthesis locomotion [230], [231] and applying external forces to the human pelvis [232], [233]. Notably, [234] developed a predictive targeting algorithm that determines the timing of disturbances to the swing foot caused from obstacles, allowing for more systematic studies of stumble recovery with respect to the timing of the perturbation during swing phase.

Similarly, research towards transfemoral prosthesis fault prevention also includes identifying common conditions that contribute user falls. For example, [149] identified two failure conditions: skipped transitions in the controller's FSM; and foot scuffing in swing. Notably, unexpected transitions in an FSM have been shown to lead to sudden, large torque changes [76]. Additionally, [235] observed that falls were commonly caused when the sound limb failed to clear obstacles and when the prosthesis-size limb failed to initiating swing or failed to land after a swing step.

By understanding the conditions that cause user falls, researchers have recently had success towards detecting and mitigating failures. Towards detecting failures, there are two existing approaches: model-based and data-driven. Model-based approaches predict the response of the human-prosthesis system in order to detect abnormalities. However, a criticism of model-based methods is that models are likely not precise enough to accurately predict faults. Alternatively, data-driven methods use machine learning algorithms instead of models to identify abnormal behaviors. For example, [236] adopted novelty outlier detection (semi-supervised recognition) to identify abnormal interactions during level-ground walking. The results found that subject-specific models were required to characterize faulty interactions.

Towards mitigating failures, researchers have developed several failure-specific approaches. For example, to address missed transitions, [76] proposed using a continuous phase-variable approach. For foot scuffing, [237] developed a control approach that learns online to recognize a user's intent to avoid an obstacle and modifies the swing trajectory accordingly to avoid a trip. In [116], they fused data from a laser range finder and an IMU to estimate the prosthetic limb pose, used sparse GP's to predict the user's future hip angles and heights, and updated prosthesis joint desired

trajectories to avoid foot scuffing and early landing. Lastly, [235] propose that the prosthesis should aid in ankle push-off (to aid the sound leg's ability to clear obstacles) and initiate a swing step in response to a stumble and provide more robust stance support.

Lastly, research on fault prevention also includes the study of *internal* faults, a growing concern as powered prostheses become more complex and incorporate additional sensors. Towards this, [238] studied the biomechanics of a human-prosthesis system reacting to internal sensor errors and observed two balance recovery strategies: regulating trunk and intact leg angular momentum, and delaying the loading of body weight.

Open Problem 3: Achieving volitional control without degrading healthy biomechanical performance

Another approach towards improving the responsiveness of powered prostheses is enabling the sensation of volitional control. Researchers have achieved volitional control for single-actuated prostheses using direct proportional EMG control, but using EMG sensors introduces many complications, as described in 2.3. Additionally, since the muscles used for intent detection of ankle joints are removed in a transfemoral amputation, researchers have looked for alternative means to give the human volitional control for multi-joint prostheses. Typically external mechanical sensors are chosen and have been used to demonstrate continuous adaptation behavior with a small number of tuning parameters, as described in Sections 2.5 and 2.7. However, in state-based phase variable methods, limits of a human's volitional control have been observed. When the prosthesis foot is flat on the ground, the global hip angle, which is used in the phase variables of [77], [160], is fully determined by the prosthesis knee and ankle joints, meaning the human has little volitional control of their own phase variable here. Additionally, [160], [161] observed a slow ankle push-off when state-based phase control was used. The researchers mitigated this issue by using feedforward phase progression in this phase, but this also removes human volitional control. Further investigation needs to be conducted between the trade-offs of state-based and time-based control. Going forward, there is a need to create consistent means of human volitional control so prosthesis devices feel more responsive to users.

Open Problem 4: Formulating device-level control objectives and improving human models to advance human-prosthesis-level performance

Throughout this survey, we have discussed various methods of prosthesis control aimed at optimizing for the control objectives presented in Sec. 2.2. In general, these control objectives are captured using performance outcome measures such as reductions in metabolic expenditure [14], improved gait symmetry (both kinematic and kinetic) [219], and total mechanical work of intact joints [239]. However, it is important to note that it is still unclear which performance measures most closely align with *healthy* human-prosthesis walking as evaluated by a clinician. Thus, more research is needed towards identifying clear and agreed-upon performance outcome measures corresponding to clinically healthy prosthesis walking.

Assuming that there exist appropriate performance measures, as discussed in Sec. 2.8, there exist both offline and online methods for customizing prosthesis controllers to optimize for these performance measures. The offline approach is to compute the performance measures after executing various prosthesis controllers and collecting human-subject data. Then, based on these observations, the controller is modified in attempt to improve this performance. While this approach can eventually lead to improved prosthesis performance, it is heuristic in nature and there is a long time-scale between trials and improvements. In comparison, the online approach computes the performance measures using real-time data and then systematically optimizes the performance measures using human-in-the-loop optimization. However, this process requires several iterations to optimize the prosthesis locomotion and typically requires episodic data collection to compute the measures. Both this online and the offline approach demand large amounts of testing time from subjects. Thus, the final open problem for powered prosthesis control is to develop methods for optimizing performance measures directly, without relying on heuristic tuning and human-in-the-loop optimization. To accomplish this, we propose two approaches.

The first approach is to design device-level control objectives that correspond to optimal performance outcomes. There are currently some device-level metrics researchers use, however these do not necessarily lead to improved human-prosthesis walking. For example, one of the most commonly used device-level metrics, known as profile matching, compares the difference between the kinematic and kinetic behavior of the prosthetic limb to an able-bodied leg. While matching kinematic and kinetic trends provides a sensible first-pass evaluation of how the prosthetic leg

compares to able-bodied behavior, there are physical reasons this may not accurately emulate a human leg. Given a prosthesis with different physical properties than those of an intact leg, matching torque trends will not result in similar kinematics, and vice versa. As detailed in [206], [207], the prosthesis only affects the human through the interaction forces at the socket and the position and velocity changes at this socket interface. As such, different prosthetic devices following the same kinematic trajectories or torque profiles will produce different socket forces than each other and a biological leg, hence affecting the human dynamics in different manners. For these reasons, prostheses that only aim to emulate the kinematic and kinematic behavior of human legs will have a different dynamic effect on the human than a biological leg and the overall walking will differ from able-bodied walking. While bearing some visual resemblance to biological walking seems important for social reasons, purely imitating kinematic or kinetic behavior seems misaimed for restoring emulative function of a lower-limb to an amputee.

A second example of a device-level metric, is the magnitude of ankle pushoff. It was long believed that prosthesis ankle pushoff was correlated with metabolic reduction of the human user [240], however this does not always hold true [85]. These mismatches in device-level metrics used in the field of prosthesis control and their resulting effect on a prosthesis user highlights that a better understanding is needed regarding the coupling between the dynamics of the prosthesis joints and the intact joints. If researchers could identify clear relationships between device-level outcomes and human-prosthesis performance metrics, then it would be possible to target the design of prosthesis controllers to achieve these device-level control objectives.

The second approach for directly optimizing for performance measures is to develop more accurate human-prosthesis system models. This would allow for a more systematic approach towards offline optimization. Specifically, a human-prosthesis model could account for both subject-specific differences and the physical parameters of the device and could provide a prediction of how the prosthesis motion will influence the overall human-prosthesis motion. Then, by encoding the human-prosthesis performance metrics as cost functions in simulation, prosthesis control parameters could be optimized with respect to this metric. While some researchers already use model-based optimization approaches [36], [70], [77], discrepancies exist between their human model and a real human user. Because the controller is optimized for a given human-prosthesis model, the method may not prove to be

optimal for a real human user because of the ways the human's behavior differs from the model's. Building a more sophisticated human model would minimize these differences and allow prosthesis controllers to be directly optimized for human locomotion objectives.

Practical Considerations

Finally, we will discuss *practical considerations* of translating powered prostheses from research settings into the real world. In contrast to open problems, these considerations are not things which remain to be *achieved* but instead are simply important to *consider* when developing and evaluating powered prostheses.

Practical Consideration 1: Prosthesis design plays a critical role in translating powered prostheses to the real world.

While we have not discussed prosthetic design in this review, it is important to note that design considerations play a key role in the development and realization of prosthesis controllers. From a design perspective, a large limiting factor in developing commercial dual-actuated powered prostheses is the large weight and size that accompanies actuation and power requirements. Part of this challenge could be addressed through control. By developing control strategies that minimize energy usage, like the effort in [35], smaller actuators and power sources could be used, reducing the size and weight of a device and extending battery life.

Other ways to improve the energy efficiency of the device could be addressed through the mechanical design. For example, incorporating passive components, such as dampers and springs, could provide some compliance for energy absorption as well as capture and recover energy inputted to the device, as done in [148], [241]–[244]. However, incorporating this compliance into the system would increase controller complexity and the chance for model uncertainty in model-based control methods. Additionally, series-elastic-actuators, used in [15], [24], for example, decrease the bandwidth of the controller but allow a means to obtain torque feedback enabling closed loop torque control. A different approach to improve energy efficiency through design is by selecting low impedance actuators such that a prosthesis leg could swing forward with less or no actuation in swing phase, as done in [23], [157]. This would increase the passive responsiveness of a device to a user's residual limb. As discussed in Open Problem 3, this influence on the human's volitional control over the prosthesis should be considered. Another benefit of this design choice is

that the low impedance also enables open-loop torque control by minimizing the effect of unmodeled actuator dynamics.

Aside from energy efficiency, prosthesis design choices also influence the performance and measured success of a given control method. For example, the location of the center of mass of a powered prosthesis has been shown to influence the metabolic efficiency of an amputee [245]. Since controls researchers consider metabolic cost as a control objective, the influence design plays in this measure will affect the evaluation of a given control method, preventing direct observation of the controller's performance based on this metric.

To decouple the mechanical design factor from the control problem, some researchers have developed testbeds or "emulators" that provide external assistance to a human, as a prosthesis would, without the use of a portable prototype [246], [247]. This reduces the time and expertise generally required to develop a specialized prosthesis prototype while allowing experimentation of various control algorithms. The power and actuation for the system are kept off board, such that these typical design factors for compact devices do not limit the control capabilities. This freedom in control design allows researchers to evaluate control strategies before making compromises because of design limitations. While the challenge of design and its influence on control capabilities must be confronted to realize powered prostheses in the real world, developing and evaluating control approaches in ideal conditions could shape what design features to prioritize in device development as well as uncover underlying principles that influence a prosthesis controller's efficacy.

Practical Consideration 2: To realize the benefits of powered prostheses, prosthesis user training is likely required.

Lastly, it is important to consider the level of training each prosthesis user has obtained when evaluating the performance of prosthesis controllers. As noted in [147], teaching amputees how to ambulate on powered prostheses is critical to achieving positive outcomes. For example, [46], [67] required several training sessions before being able to demonstrate improvements in biomechanical gait of amputees using a powered prosthesis. Hence, training amputees to walk with prosthesis devices in a biomechanically healthy manner is likely required in order to achieve an optimal walking pattern and fully exploit the benefits powered prostheses can offer.

One important aspect of this consideration is the tradeoff between short-term user comfort and long-term biomechanic advantages. Specifically, while it is well-understood that user preference is an important consideration in prosthesis control (i.e., researchers have shown that user preference is correlated with positive reception of passive prostheses by consumers [248]), following user preference does not necessarily converge to biomechanically optimal walking in the short run. For example, transfemoral amputees tend to avoid stance knee flexion with their prosthesis because it feels like buckling. They have been conditioned to keep their prosthetic leg straight to not feel like they are falling. From biomechanics, though, we know that knee flexion is important for weight acceptance and to reduce the impact effects from foot strike [74]. Here, a user's initial preference leads to a behavior that is biomechanically disadvantageous and longer term training may be required for individuals with amputation to adapt to control schemes that provide stance phase knee flexion.

With training, users can learn to walk in ways that are more biomechanically healthy. For example, [249] showed that prior to training, prosthesis users self-selected walking gait was asymmetric. However, by using visual feedback for the human users during the gait tuning process, all subjects significantly increased their stance time (1.15 ± 0.1 sec for able-bodied (AB) participants and 1.06 ± 0.1 sec for transfemoral amputee (TFA) participants) and decreased their stance time asymmetry ($23\% \pm 7\%$ for AB participants and $19\% \pm 5\%$ for TFA participants). To this end, it will be important to distinguish between user preferences to accommodate in control methods and user experiences that amputees should be trained to become comfortable with and adapt correctly to.

2.10 Conclusion

Overall, powered prostheses have promising potential to achieve natural, efficient, and responsive locomotion for individuals with lower-limb amputations. Throughout this survey, we introduce the state-of-the-art control strategies across varying levels of control: high-level task estimation, mid-level desired torque computation, and low-level torque realization. These methods have demonstrated various improvements to prosthesis performance with respect to naturalness of motion, efficiency of gait, and responsiveness to the user. Developing control methods that generalize across users and can be customized for users in a straight-forward manner could enable realization of these benefits for a wider population of users. This widespread applicability in addition to improvements in ensuring user safety, hu-

man volitional control, and the overall health of a the resultant human-prosthesis gait could make these devices clinically viable to be used by people with lower-limb amputations in everyday life, motivating pursuit of future research.

Chapter 3

PRELIMINARIES

This chapter will present the preliminary theoretical background to provide the fundamental groundwork for the theoretical developments in this thesis. All of the theory presented here is based on previous work and is not part of the author’s original contributions for her PhD.

The text for this chapter was adapted from:

R. Gehlhar, J. Reher, and A. D. Ames. “Control of Separable Subsystems with Application to Prostheses”. In: *arXiv preprint arXiv:1909.03102*, 2019.

R. Gehlhar and A. D. Ames. “Separable Control Lyapunov Functions With Application to Prostheses”. In: *IEEE Control Systems Letters*, 5.2, 2021, pp. 559–564.

R. Gehlhar and A. D. Ames. “Estimate-to-state stability for hybrid human-prosthesis systems”. In: *2021 60th IEEE Conference on Decision and Control (CDC)*, IEEE, 2021, pp. 705–712.

R. Gehlhar and A. D. Ames. “Model-dependent prosthesis control with interaction force estimation”. In: *2021 IEEE International Conference on Robotics and Automation (ICRA)*. IEEE, 2021, pp. 3226–3232.

R. Gehlhar and A. D. Ames. “Emulating Human Kinematic Behavior on Lower-Limb Prostheses via Multi-Contact Models and force-sensor-based Nonlinear Control”. In: *Submitted to 2023 IEEE International Conference on Robotics and Automation (ICRA)*. IEEE, 2022.

3.1 Background Nonlinear Control Theory

Hybrid Control System

During stance and swing phases of bipedal walking, the dynamics of the system are continuous. For these continuous dynamics we consider the following general affine control system,

$$\dot{x} = f(x) + g(x)u, \tag{3.1}$$

with states $x \in X \subset \mathbb{R}^n$ and control inputs $u \in \mathbb{R}^m$, where $m \leq n$. When the foot strikes the ground in walking, it causes a discrete jump in velocities. We consider the following for these impact dynamics,

$$x^+ = \Delta_X(x^-),$$

where x^+ indicates post-impact states, and x^- , pre-impact states. To model these phases of dynamics, we employ a hybrid system,

$$\mathcal{H}\mathcal{C}_x = \begin{cases} \dot{x} = f(x) + g(x)u & \text{if } (x) \in \mathcal{D} \setminus S \\ x^+ = \Delta_X(x^-) & \text{if } (x^-) \in S. \end{cases} \quad (3.2)$$

The functions f , g , Δ_X are locally Lipschitz continuous in their arguments, meaning given an initial condition $x_0 = x(t_0)$, there exists a unique solution $x(t)$ for some time. For simplicity we assume forward completeness, i.e. solutions exist for all time.

The admissible states during a phase of continuous dynamics exist in a domain \mathcal{D} ,

$$\mathcal{D} = \{(x) \in X : \ell(x) \geq 0\}, \quad (3.3)$$

a closed subset of X . The transitions between these domains are initiated by a guard (switching surface) $S \subset \mathcal{D}$,

$$S = \{(x) \in X : \ell(x) = 0 \text{ and } \dot{\ell}(x) < 0\}, \quad (3.4)$$

which is a co-dimension one submanifold of \mathcal{D} . Here the continuously differentiable function $\ell : X \rightarrow \mathbb{R}$ yields $L_g \ell = 0$. This guard S defines the states of the system when the conditions $\ell(x) = 0$ and $\dot{\ell}(x) < 0$ are reached. When this guard is reached, the impact dynamics map the system back to the domain of continuous dynamics \mathcal{D} .

We can stabilize the affine control system 3.1 by constructing a *feedback linearizing* control law for u , which cancels out the nonlinear dynamics of the system and applies a linear controller to stabilize the resultant linear system.

Feedback Linearization

To begin construction of u for the affine control system (3.1), we define linearly independent outputs $y : \mathbb{R}^n \rightarrow \mathbb{R}^m$ so that the system has the same number of outputs as inputs. These outputs are of valid vector relative degree $\vec{\gamma} = (\gamma_1, \gamma_2, \dots, \gamma_m)$ [39]. We define the vector of partial derivatives of the $\gamma_i - 1$ *Lie derivatives* [38], [39] of the $y_i(x)$ outputs with respect to the dynamic drift vector $f(x)$ for $i = 1, \dots, m$ as follows:

$$\frac{\partial L_f^{\vec{\gamma}-1} y(x)}{\partial x} \triangleq \begin{bmatrix} \frac{\partial L_f^{\gamma_1-1} y_1(x)}{\partial x} \\ \frac{\partial L_f^{\gamma_2-1} y_2(x)}{\partial x} \\ \vdots \\ \frac{\partial L_f^{\gamma_m-1} y_m(x)}{\partial x} \end{bmatrix}.$$

Then, we define the vector of γ_i Lie derivatives with respect to drift vector $f(x)$ and control matrix $g(x)$, respectively:

$$L_f^{\vec{\gamma}} y(x) \triangleq \frac{\partial L_f^{\vec{\gamma}-1} y(x)}{\partial x} f(x),$$

$$L_g L_f^{\vec{\gamma}-1} y(x) \triangleq \frac{\partial L_f^{\vec{\gamma}-1} y(x)}{\partial x} g(x).$$

With these Lie derivatives, we write the vector of the γ_i^{th} derivatives of the outputs,

$$y^{(\vec{\gamma})} \triangleq \begin{bmatrix} y_1^{(\gamma_1)} \\ y_2^{(\gamma_2)} \\ \vdots \\ y_m^{(\gamma_m)} \end{bmatrix} = L_f^{\vec{\gamma}} y(x) + L_g L_f^{\vec{\gamma}-1} y(x) u. \quad (3.5)$$

From this, we construct a feedback linearizing controller,

$$u(x) = - \underbrace{(L_g L_f^{\vec{\gamma}-1} y(x))^{-1}}_{A(x)} \underbrace{(L_f^{\vec{\gamma}} y(x) - \mu)}_{L_f^* y(x)} \quad (3.6)$$

$$= -A^{-1}(x)(L_f^* y(x) - \mu),$$

where $\mu \in \mathbb{R}^m$ is the auxiliary control input the user defines to render the linearized system stable. See [39] or [38] for details. Note that $A(x)$ is invertible because the outputs are linearly independent and the system is square [39, p. 407], since the number of inputs equals the number of outputs. Applying this controller to the output dynamics of (3.5) yields,

$$y^{(\vec{\gamma})} = \mu, \quad (3.7)$$

such that we can prescribe a desired behavior of the output dynamics through our design of μ .

Coordinate Transformation to Normal Form

With these outputs we can perform a coordinate transformation to normal form to obtain a system in terms of our controllable (output) states and the uncontrollable states. Any partially feedback linearizable system can be converted to normal form per methods introduced in [39, pp. 407-411]. For each output i , we define the

following output coordinates,

$$\eta_i = \begin{bmatrix} \eta_i^{(1)} \\ \eta_i^{(2)} \\ \vdots \\ \eta_i^{(\gamma_i)} \end{bmatrix} = \begin{bmatrix} y_i(x) \\ L_f y_i(x) \\ \vdots \\ L_f^{\gamma_i-1} y_i(x) \end{bmatrix}.$$

This gives a total of $\gamma := \sum_{i=1}^m \gamma_i$ output coordinates:

$$\eta = \begin{bmatrix} \eta_1 \\ \eta_2 \\ \vdots \\ \eta_m \end{bmatrix} \in \mathbb{R}^\gamma.$$

We then define $n - \gamma$ zero dynamics coordinates,

$$z = \begin{bmatrix} z_1(x) \\ z_2(x) \\ \vdots \\ z_{n-\gamma}(x) \end{bmatrix} \in \mathbb{R}^{n-\gamma}.$$

With this, we define the diffeomorphism,

$$\Phi(x) = \begin{bmatrix} \eta \\ z \end{bmatrix},$$

where $\Phi(x) : \mathbb{R}^n \rightarrow \mathbb{R}^n$. To determine the output dynamics, we write the derivatives of each output coordinate,

$$\dot{\eta}_i = \begin{bmatrix} \eta_i^{(2)} \\ \eta_i^{(3)} \\ \vdots \\ L_f^{\gamma_i} y_i(\Phi^{-1}(\eta, z)) + L_g L_f^{\gamma_i-1} y_i(\Phi^{-1}(\eta, z))u \end{bmatrix} \triangleq \begin{bmatrix} \eta_i^2 \\ \eta_i^3 \\ \vdots \\ a_i(\eta, z) + b_i(\eta, z)u. \end{bmatrix}$$

The dynamics of the output states are then,

$$\dot{\eta} = \begin{bmatrix} \dot{\eta}_1 \\ \dot{\eta}_2 \\ \vdots \\ \dot{\eta}_m \end{bmatrix} \triangleq f_\eta(\eta, z) + g_\eta(\eta, z)u. \quad (3.8)$$

Feedback Linearization via Normal Form

With the system in normal form, we can show how feedback linearization transforms the output dynamics into a linear system.

$$\begin{aligned} \dot{\eta}^{(\bar{y})} = \begin{bmatrix} \dot{\eta}_1^{(\gamma_1)} \\ \dot{\eta}_2^{(\gamma_2)} \\ \vdots \\ \dot{\eta}_m^{(\gamma_m)} \end{bmatrix} &= \begin{bmatrix} a_1(\eta, z) + b_1(\eta, z)u \\ a_2(\eta, z) + b_2(\eta, z)u \\ \vdots \\ a_m(\eta, z) + b_m(\eta, z)u \end{bmatrix} = L_f^{\bar{y}}y(\Phi^{-1}(\eta, z)) + L_gL_f^{\bar{y}-1}y(\Phi^{-1}(\eta, z)) \\ &\triangleq a(\eta, z) + b(\eta, z)u. \end{aligned}$$

With this, we construct a feedback linearizing controller:

$$u = -b^{-1}(\eta, z)(a(\eta, z) - \mu),$$

with auxiliary control input μ . Note this controller is equivalent to the feedback linearizing controller in (3.6), the only difference is this expression is given in terms of η and z instead of x . Here $b(\eta, z)$ is invertible because the outputs are linearly independent and the system is square. Applying this controller results in $\dot{\eta}^{(\bar{y})} = \mu$ and we rewrite our linearized output dynamics:

$$\dot{\eta}_i = \underbrace{\begin{bmatrix} 0 & I_{\gamma_i-1 \times \gamma_i-1} \\ 0 & 0 \end{bmatrix}}_{F_i} \eta_i + \underbrace{\begin{bmatrix} 0_{\gamma_i-1 \times 1} \\ 1 \end{bmatrix}}_{G_i} \mu_i, \quad (3.9)$$

$$\dot{\eta} = F\eta + G\mu,$$

where $\mu = (\mu_1^T, \mu_2^T, \dots, \mu_m^T)^T$, and,

$$\begin{aligned} F &= \text{diag}(F_1, F_2, \dots, F_m) \in \mathbb{R}^{n \times n}, \\ G &= \text{diag}(G_1, G_2, \dots, G_m) \in \mathbb{R}^{n \times m}, \end{aligned} \quad (3.10)$$

where $\text{diag}()$ notates a block diagonal matrix of listed elements. This F and G yield a full rank controllability matrix enabling CLF construction with a continuous-time Algebraic Riccati equation (CARE), which we will present in 3.2.

Hybrid Control System for Outputs and Zero Dynamics

For these controlled (output) states $\eta \in \mathcal{N} \subset \mathbb{R}^y$ and uncontrolled states, $z \in Z \subset \mathbb{R}^{n-y}$, we define the following hybrid control system,

$$\mathcal{HC} = \begin{cases} \begin{cases} \dot{\eta} = f_\eta(\eta, z) + g_\eta(\eta, z)u \\ \dot{z} = \Psi(\eta, z) \end{cases} & \text{if } \Phi^{-1}(\eta, z) \in \mathcal{D} \setminus S \\ \begin{cases} \eta^+ = \Delta_{\mathcal{N}}(\eta^-, z^-) \\ z^+ = \Delta_Z(\eta^-, z^-) \end{cases} & \text{if } \Phi^{-1}(\eta^-, z^-) \in S. \end{cases} \quad (3.11)$$

Here, we assume $f_\eta(0, z) = 0$ and $\Delta_{\mathcal{N}}(0, z) = 0$, yielding the surface Z defined by $\eta = 0$ with dynamics $\dot{z} = \Psi(0, z)$ as invariant for the continuous and discrete dynamics. This yields the hybrid system for the hybrid zero dynamics:

$$\mathcal{H}|_Z = \begin{cases} \dot{z} = \Psi(0, z) & \text{if } z \in Z \setminus (S \cap Z) \\ z^+ = \Delta_Z(0, z^-) & \text{if } z^- \in S \cap Z. \end{cases}$$

Control Lyapunov Functions

To construct a control input u that stabilizes the output dynamics of (3.11), a control Lyapunov function (CLF) can be used. A CLF for the continuous output dynamics of (3.11) is a positive definite function with positive constants $c_1, c_2, c_3 > 0$ such that for all $(\eta, z) \in \mathcal{N} \times Z$,

$$c_1 \|\eta\|^2 \leq V(\eta) \leq c_2 \|\eta\|^2 \quad (3.12)$$

$$\inf_{u \in U} [L_{f_\eta} V(\eta, z) + L_{g_\eta} V(\eta, z)u + c_3 V(\eta)] \leq 0, \quad (3.13)$$

where $L_{f_\eta} V$ and $L_{g_\eta} V$ denote the Lie derivatives [250]. The following set consists of control values that yield $\dot{V}(\eta, z, u) < -c_3 V(\eta)$, i.e. satisfy (3.13):

$$K(\eta, z) = \{u \in U : L_{f_\eta} V(\eta, z) + L_{g_\eta} V(\eta, z)u + c_3 V(\eta) \leq 0\}.$$

While a control input $u \in K$ is sufficient to guarantee exponential stability of the continuous output dynamics of (3.11), the impacts in the hybrid system (3.11) require stronger convergence guarantees. For this reason, the notion of a rapidly exponentially stabilizing CLF (RES-CLF) was developed in [199] to provide such guarantees.

RES-CLF. A RES-CLF for the continuous dynamics of (3.11) is a function with positive constants $c_1, c_2, c_3 > 0$ such that for all $0 < \varepsilon < 1$ and $(\eta, z) \in \mathcal{N} \times Z$,

$$c_1 \|\eta\|^2 \leq V_\varepsilon(\eta) \leq \frac{c_2}{\varepsilon^2} \|\eta\|^2 \quad (3.14)$$

$$\inf_{u \in U} [L_{f_\eta} V_\varepsilon(\eta, z) + L_{g_\eta} V_\varepsilon(\eta, z)u + \frac{c_3}{\varepsilon} V_\varepsilon(\eta)] \leq 0. \quad (3.15)$$

The following set consists of control values that yield $\dot{V}_\varepsilon(\eta, z, u) < -\frac{c_3}{\varepsilon} V_\varepsilon(\eta)$, i.e. satisfy (3.15):

$$K_\varepsilon(\eta, z) = \{u \in U : L_{f_\eta} V_\varepsilon(\eta, z) + L_{g_\eta} V_\varepsilon(\eta, z)u + \frac{c_3}{\varepsilon} V_\varepsilon(\eta) \leq 0\}.$$

With $u^\varepsilon(\eta, z) \in K_\varepsilon(\eta, z)$ for all $\eta \in \mathcal{N} \times Z$ the closed-loop system of the continuous dynamics of (3.2) becomes:

$$\mathcal{H}_\varepsilon = \begin{cases} \dot{\eta} = f_\eta(\eta, z) + g_\eta(\eta, z)u^\varepsilon(\eta, z) & \text{if } \Phi^{-1}(\eta, z) \in \mathcal{D} \setminus S \\ \dot{z} = \Psi(\eta, z) & \\ \eta^+ = \Delta_{\mathcal{N}}(\eta^-, z^-) & \\ z^+ = \Delta_Z(\eta^-, z^-) & \text{if } \Phi^{-1}(\eta^-, z^-) \in S. \end{cases} \quad (3.16)$$

We are specifically interested in systems with periodic orbits because of the periodic nature of walking. So, for the continuous dynamics of (3.16), let $\varphi_t(\eta, z)$ be its periodic flow and \mathcal{O} its corresponding periodic orbit. For the zero dynamics $\dot{z} = \Psi(0, z)$ with periodic flow φ_t^z , let \mathcal{O}_Z be its corresponding periodic orbit. Because of the invariance of the zero dynamics surface Z assumption (i.e. $f_\eta(0, z) = 0$ and $\Delta_{\mathcal{N}}(0, z) = 0$), a periodic orbit for the zero dynamics \mathcal{O}_Z corresponds to a periodic orbit for the full-order dynamics, $\mathcal{O} = \iota_0(\mathcal{O}_Z)$, where $\iota_0 : Z \rightarrow \mathcal{N} \times Z$ is the canonical embedding $\iota_0(z) = (0, z)$. We saw in [199] how the existence of a RES-CLF guaranteed for an exponentially stable periodic orbit \mathcal{O}_Z for the zero dynamics $\mathcal{H}|_Z$ transverse to $S \cap Z$, the corresponding periodic orbit of the full-order dynamics $\mathcal{O} = \iota_0(\mathcal{O}_Z)$ is exponentially stable.

Trajectory Generation

In order to shape the output dynamics of (3.11) such that an exponentially stable periodic orbit \mathcal{O}_Z will exist in the zero dynamics, we enforce certain constraints in an optimization problem that solves for parameters α to define the outputs,

$$y(x) = y_a(x) - y_d(\tau, \alpha).$$

Here y_a is the actual output of the system and y_d is the desired output trajectory defined by α and modulated by τ , which could be a time- or state-based phase variable [153], [154].

The goal of control is to drive these outputs to 0. Then since $f_\eta(0, z) = 0$ and $\Delta_{\mathcal{N}}(0, z) = 0$, the hybrid system (3.11) is reduced to a lower-dimensional manifold, or the *zero dynamics surface* [195]:

$$Z_\alpha = \{x \in \mathcal{D} : y_v(x, \alpha) = 0, \dot{y}(x, \alpha) = 0\}. \quad (3.17)$$

To ensure that the system remains on the zero dynamics surface even through impact, such that the zero dynamics surface is invariant through impact, we enforce

the following condition in trajectory generation,

$$\Delta(S \cap Z) \subseteq Z. \quad (3.18)$$

In other words, when the system evolving on the zero dynamics surface Z reaches the guard S , the impact Δ will map the system back to the zero dynamics surface.

To develop periodic orbits, we enforce the following periodicity condition,

$$(\eta_0, z_0) = \Delta(\varphi_T(\eta_0, z_0)),$$

where η_0 and z_0 are the initial conditions. This condition means that, for the initial condition (η_0, z_0) , after the continuous dynamics flow for a period T , the impact dynamics Δ will map the system back to the same initial condition (η_0, z_0) .

We include these conditions in an optimization problem that solves for parameters α to define desired outputs $y_d(\tau, \alpha)$ of the system, such that when a control input u drives the actual outputs $y_a(x)$ to the desired outputs $y_d(\tau, \alpha)$, i.e. the outputs y are 0, there is an exponentially stable periodic orbit in the zero dynamics:

$$\begin{aligned} \{\alpha^*, C^*\} &= \operatorname{argmin}_{\alpha, C} \mathcal{J} \\ \text{s.t. } &\Delta(S \cap Z_\alpha) \subseteq Z_\alpha \\ &(\eta_0, z_0) = \Delta(\varphi_T(\eta_0, z_0)) \\ &C_{\min} \leq C_v \leq C_{\max}. \end{aligned} \quad (3.19)$$

The solution to this optimization problem includes the parameters α and the decision variables $C = (x_0, \dots, x_N, T)$, here x_i is the system state at the i^{th} discretization for the duration T . Upper and lower bounds for the decision variables, C_{\max} and C_{\min} , respectively, are enforced through the constraints. Here \mathcal{J} is the cost function. For bipedal robot systems, typical cost functions include mechanical cost of transport, torque squared, the difference between the desired outputs and human walking data, or a combination of these costs [195], [201].

Input to State Stability

One final piece of nonlinear control theory background we will introduce is input-to-state stability (ISS). We will present this construction for a general affine control system (3.1) and then in Chapter 6 we will relate a similar notion to a hybrid system with outputs and zero dynamics. For the affine control system (3.1), consider the case where it experiences a time-varying disturbance signal $d \in \mathbb{R}^m$ to the input u ,

$$\dot{x} = f(x) + g(x)(u + d). \quad (3.20)$$

While we could construct a control input u with a CLF to guarantee the system with zero disturbance, $d = 0$, is stable, with an unknown disturbance, stability can not be guaranteed. However, we could guarantee stability to a set. For disturbances in nonlinear systems, ISS [251], [252] can guarantee convergence to a set around the origin, with the bound in terms of $\|d\|_\infty$, where $\|d\|_\infty = \sup_{t \geq 0} \{|d(t)|\}$. Here we consider the conditions for exponential ISS. For the classical definition see [251]. The system (3.20) is *exponential input-to-state stable* (e-ISS) if there exists $\beta \in \mathcal{KL}_\infty$, $\iota \in \mathcal{K}_\infty$, and constant $c > 0$ such that

$$\|x(t, x_0, d)\| \leq \beta(\|x_0\|, t)e^{-ct} + \iota(\|d\|_\infty), \quad \forall x_0, d, \forall t \geq 0.$$

We can quantify e-ISS via Lyapunov functions. A continuously differentiable function $V : \mathbb{R}^n \rightarrow \mathbb{R}_{\geq 0}$ is an *e-ISS Lyapunov function* with constants $c_1, c_2, c_3 > 0$ and $\iota \in \mathcal{K}_\infty$ such that $\forall x \in \mathbb{R}^n, d \in \mathbb{R}^{n_d}$,

$$\begin{aligned} c_1\|x\|^2 &\leq V(x) \leq c_2\|x\|^2 \\ \|x\| \geq \iota(\|d\|_\infty) &\Rightarrow \dot{V}(x, d) \leq -c_3V(x). \end{aligned} \tag{3.21}$$

The background theory presented in this section will be used as a basis for the theoretical contributions of this thesis, developed in Chapters 4, 5, and 6. All of the novel theoretical constructions in this thesis are first developed in the context of general nonlinear control systems, and they are followed with applications to general robotic systems. We will now present the general constructions used for robotic systems.

3.2 Nonlinear Control of Robotic Systems

Robotic System

Consider an n_q DOF robotic system in ϑ -dimensional space. The coordinates $q \in \mathbb{R}^{n_q}$ define the robot's configuration space \mathcal{Q} . The dynamics of the robotic system are given by the classical Euler-Lagrangian equation [204],

$$D(q)\ddot{q} + H(q, \dot{q}) = Bu + J^T(q)\lambda. \tag{3.22}$$

Here $D(q) \in \mathbb{R}^{n_q \times n_q}$ is the inertial matrix. $H(q, \dot{q}) = C(q, \dot{q}) + G(q) \in \mathbb{R}^{n_q}$, a vector of centrifugal and Coriolis forces and a vector containing gravity forces, respectively. The actuation matrix $B \in \mathbb{R}^{n_q \times m}$ contains the gear-reduction ratio of the actuated joints and is multiplied by the control inputs $u \in \mathbb{R}^m$, where m denotes the number of control inputs. The wrenches $\lambda \in \mathbb{R}^{n_h}$ enforce the n_h holonomic

constraints. The Jacobian matrix of the holonomic constraints $J(q) = \frac{\partial h}{\partial q} \in \mathbb{R}^{n_h \times n_q}$ enforces the holonomic constraints by:

$$\dot{J}(q, \dot{q})\dot{q} + J(q)\ddot{q} = 0. \quad (3.23)$$

Solving (3.22) and (3.23) simultaneously yields the *constrained dynamics*.

To relate this to the continuous dynamics of the hybrid control system of (3.2), we write the following ODE,

$$\dot{x} = \frac{d}{dt} \begin{bmatrix} q \\ \dot{q} \end{bmatrix} = \underbrace{\begin{bmatrix} \dot{q} \\ D^{-1}(q)(-H(q, \dot{q}) + J^T(q)\lambda) \end{bmatrix}}_{f(x)} + \underbrace{\begin{bmatrix} 0 \\ D^{-1}(q)B \end{bmatrix}}_{g(x)} u.$$

The discrete dynamics Δ_X of (3.2) are determined by assuming a perfectly plastic impact. See [253], [254] for details.

Bipedal Robot Gait Generation

Multi-Domain Hybrid System. To have bipedal walking emulate human heel-toe roll, multiple contact points need to be accounted for. As the contact points change, the different holonomic constraints change the continuous dynamics, requiring multiple domains in a hybrid system. To model this multi-domain hybrid system, we use a directed graph $\Gamma = (V, E)$ with vertices $v \in V$ that connect edges $\{e = \{v \rightarrow v^+\}\}_{v \in V} = E$, where v^+ is the subsequent vertex of v in the directed graph. For each vertex v , there is a domain \mathcal{D}_v (3.3) and control input u_v . On \mathcal{D}_v , there is a control system (f_v, g_v) , that define the continuous dynamics $\dot{x} = f_v(x) + g_v(x)u_v$ for each $x \in \mathcal{D}_v$ and $u_v \in \mathcal{U}$. The transition point between one domain \mathcal{D}_v and the next \mathcal{D}_{v^+} in the directed cycle is defined by the guard S_e . The guard triggers the reset map, $\Delta_e : S_e \subset \mathcal{D}_v \rightarrow \mathcal{D}_{v^+}$, giving the postimpact states of the system: $x^+ = \Delta_e(x)$, where $x \in \mathcal{D}_v$ and $x^+ \in \mathcal{D}_{v^+}$.

With the sets of each of these objects, $\mathcal{D} = \{\mathcal{D}_v\}_{v \in V}$, $\mathcal{U} = \{u_v\}_{v \in V}$, $S = \{S_e\}_{e \in E}$, $\Delta = \{\Delta_e\}_{e \in E}$, and $FG = \{(f_v, g_v)\}_{v \in V}$, we define this *multi-domain hybrid control system* as a tuple [255], [256]:

$$\mathcal{H}\mathcal{C}_{\text{md}} = (\Gamma, \mathcal{D}, \mathcal{U}, S, \Delta, FG). \quad (3.24)$$

Gait Generation. To prescribe outputs to this multi-domain hybrid control system, typically relative degree 1 and 2 outputs are used for walking robots and respectively

defined as,

$$y_{1,v}(q, \dot{q}) = y_{1,v}^a(q, \dot{q}) - y_{1,v}^d, \quad (3.25)$$

$$y_{2,v}(q) = y_{2,v}^a(q) - y_{2,v}^d(\tau_v, \alpha_v). \quad (3.26)$$

While the phase variable τ_v can be time- or state-based, for more robust control, a state-based phase variable $\tau(q)$ is used [154] and is typically defined as follows,

$$\tau(q)_v = \frac{p_v(q) - p_{0,v}}{p_{f,v} - p_{0,v}}. \quad (3.27)$$

Here $p_v(q)$ is a state-dependent function that is monotonic in \mathcal{D}_v and $p_{0,v}$ and $p_{f,v}$ are the initial and final values of this function in this domain. For walking, previous work found the forward progression of the stance hip to be monotonic during a human gait cycle [150]. This qualifies it to be used as $p_v(q)$ for the phase variable.

As described previously in Subsection 3.1, a control input u is designed to drive these outputs to 0. We previously discussed how this results in the system evolving on the zero dynamics surface 3.17. However, when a relative degree 1 output $y_{1,v}$ is used, the zero dynamics cannot necessarily remain invariant through impacts. In fact, enforcing impact invariance on the velocity-modulating output is too restrictive due to the jump of velocities by the impact map. Hence, we only enforce an impact invariance condition on the relative degree 2 outputs, resulting in *partial zero dynamics*:

$$PZ_{\alpha_v} = \{(q, \dot{q}) \in \mathcal{D}_v : y_{2,v}(q, \alpha_v) = 0, \dot{y}_{2,v}(q, \alpha_v) = 0\}.$$

For a domain where a relative degree 1 output is used, the optimization problem (3.19) uses this partial zero dynamics surface PZ_{α} instead of Z_{α} , as shown in the following domain-specific optimization problem:

$$\begin{aligned} \{\alpha_v^*, C_v^*\} &= \operatorname{argmin}_{\alpha_v, C_v} \mathcal{J}_v \\ \text{s.t. } \Delta_e(S_e \cap PZ_{\alpha_v}) &\subseteq PZ_{\alpha_{v+}} \\ (\eta_0, z_0) &= \varphi_T^{\mathcal{H}}(\eta_0, z_0), \\ C_{\min} &\leq C_v \leq C_{\max} \\ c_{\min} &\leq c_v(C_v) \leq c_{\max}, \end{aligned} \quad (3.28)$$

where $\varphi_T^{\mathcal{H}}$ is the hybrid periodic flow for the whole multi-domain hybrid system (3.24), and $c_v(C_v)$ enforce real-world constraints of the robot such as torque and

joint limits and contact conditions. To solve this optimization problem, we use a direct collocation based optimization algorithm, FROST [198].

The solution to the optimization provides the α parameters that define Bézier polynomials,

$$\mathbf{B}(\tau_v) = \sum_{i=0}^m \alpha_{v,i} \frac{m!}{(m-i)!i!} \tau_v^i (1-\tau_v)^{m-i}, \quad (3.29)$$

where m is the degree of the Bézier polynomial with coefficients $\alpha_v = \{\alpha_{v,i}\}_{i=1,\dots,m}$.

ID-CLF-QP

A RES-CLF, as described in Subsection 3.1, could be used to construct a control input u to track these generated trajectories.

We can use the linearized output dynamics (3.9) to construct a CLF for the robotic system. First, using F and G from (3.9), we solve the CARE equation,

$$F^T P + P F + P G G^T P + Q = 0,$$

for $P = P^T > 0$, with the user selected weighting matrix $Q = Q^T > 0$. From the method of [199], we construct a CLF by the following,

$$V(\eta) = \eta^T P \eta.$$

For this robotic system with relative degree 1 and 2 outputs, we define $\eta = (y_1^T, y_2^T, \dot{y}_2^T)^T$ and transform the CLF into a RES-CLF using the method in [199] with $0 < \varepsilon < 1$:

$$V_\varepsilon(\eta) = \eta^T \begin{bmatrix} I & 0 & 0 \\ 0 & \frac{1}{\varepsilon} I & 0 \\ 0 & 0 & I \end{bmatrix} P \begin{bmatrix} I & 0 & 0 \\ 0 & \frac{1}{\varepsilon} I & 0 \\ 0 & 0 & I \end{bmatrix} \eta =: \eta^T P^\varepsilon \eta.$$

To obtain the convergence constraint, we take the derivative,

$$\dot{V}_\varepsilon(\eta) = L_F V_\varepsilon(\eta) + L_G V_\varepsilon(\eta) \mu \leq -\frac{\lambda_{\min}(Q)}{\lambda_{\max}(P^\varepsilon)} V_\varepsilon(\eta),$$

with Lie derivatives along the linearized output dynamics as,

$$L_F V_\varepsilon(\eta) = \eta^T (F^T P^\varepsilon + P^\varepsilon F) \eta,$$

$$L_G V_\varepsilon(\eta) = 2\eta^T P^\varepsilon G,$$

and μ , as given by (3.6), is

$$\mu = L_f^* y(x) + A(x)u.$$

However, to implement a CLF on hardware, the feedback linearizing terms $L_f^* y(x)$ and $A(x)$ in (3.2) pose a challenge in that they require inversion of the inertia matrix $D(q)$ which is computationally expensive and can have numerical instability. To avoid this, [37] developed an inverse dynamics CLF quadratic program (ID-CLF-QP) that includes the CLF stability condition (3.2), the dynamics (3.22), and the holonomic constraints (3.23) as constraints in the QP. This way the QP can determine the control input u , accelerations \ddot{q} , and constraint wrenches λ simultaneously in a way that satisfies the stability constraint with respect to the dynamics and holonomic constraints.

To form this controller, we recall $\mu = (\dot{y}^T, \ddot{y}^T)^T$ and rewrite the outputs in terms of the robotic system's configuration coordinates q and velocities \dot{q} ,

$$\begin{bmatrix} \dot{y}_1 \\ \ddot{y}_2 \end{bmatrix} = \underbrace{\begin{bmatrix} \frac{\partial y_1}{\partial q} \\ \frac{\partial}{\partial q} \left(\frac{\partial y_2}{\partial q} \dot{q} \right) \end{bmatrix}}_{J_y(q, \dot{q})} \dot{q} + \underbrace{\begin{bmatrix} \frac{\partial y_1}{\partial \dot{q}} \\ \frac{\partial y_2}{\partial q} \end{bmatrix}}_{J_y(q)} \ddot{q}.$$

We will include these terms in the QP cost with the holonomic constraints, enforcing these as soft constraints, using,

$$J_{\text{qp}}(q) = \begin{bmatrix} J_y(q) \\ J(q) \end{bmatrix}, \quad \dot{J}_{\text{qp}}(q, \dot{q}) = \begin{bmatrix} \dot{J}_y(q, \dot{q}) \\ \dot{J}(q, \dot{q}) \end{bmatrix}.$$

With these terms we formulate our ID-CLF-QP:

$$\begin{aligned} \Upsilon^* &= \underset{\Upsilon \in \mathbb{R}^{n_{\text{qp}}}}{\text{argmin}} \left\| \dot{J}_{\text{qp}}(q, \dot{q}) \dot{q} + J_{\text{qp}}(q) \ddot{q} - v^{\text{pd}} \right\|^2 + \sigma W(\Upsilon) + \rho \zeta \\ &\text{s.t. } D(q) \ddot{q} + H(q, \dot{q}) = Bu + J^T(q) \lambda \\ &\quad L_F V(x) + L_G V(x) (\dot{J}_y(q, \dot{q}) \dot{q} + J_y(q) \ddot{q}) \leq -\frac{c}{\varepsilon} V(x) + \zeta \\ &\quad -u_{\max} \leq u \leq u_{\max}, \end{aligned} \tag{3.30}$$

with decision variables $\Upsilon = (\dot{q}^T, u^T, \lambda^T)^T$. Here $v^{\text{pd}} = (\mu_{\text{pd}}^T, 0^T)^T$, $W(\Upsilon)$ is a regularization term designed to make the system well-posed, σ and ρ are user-selected weights, ζ is a relaxation term to allow the torque bounds $(-u_{\max}, u_{\max})$ to be met.

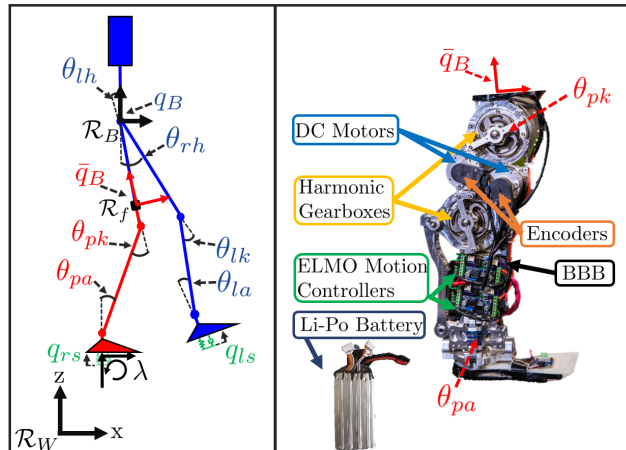


Figure 3.1: Human-Prosthesis Model and Platform. (Left) Human-prosthesis model with generalized coordinates. (Right) AMPRO3 powered prosthesis platform with components and coordinates labeled.

3.3 Human-Prosthesis Model and Powered Prosthesis Platform

Human-Prosthesis Model

We model the human-prosthesis system as a planar (2D) 12 DOF bipedal robot, comprised of 8 rigid links: torso, 2 human thighs, prosthesis partial thigh, a human and prosthesis calf, and a human and prosthesis foot. The parameter for the human limbs are estimated based on the user's total height and mass. The length, mass, and COM are calculated based on Plagenhoef's table of percentages [257]. The inertia of each limb is calculated based on Erdmann's table of radiuses of gyration [258]. The prosthesis parameters are based on a CAD model of AMPRO3 [19], a powered transfemoral prosthesis. We define the generalized coordinates as $q = (q_r^T, q_s^T)^T$, where q_s correspond to the prosthesis subsystem coordinates and q_r refers to the remaining coordinates for the human. We define the human coordinates q_r as $(q_B^T, \theta_{lh}, \theta_{lk}, \theta_{la}, \theta_{rh})^T$, where q_B denotes a 3 DOF floating base frame at the torso, and the other coordinates represent the left hip, knee, and ankle, and the right hip, respectively. The prosthesis coordinates q_s are $(\bar{q}_B^T, q_{pk}, q_{pa})^T$, where \bar{q}_B denote the 3 DOF floating base frame at socket attachment point and the other coordinates represent the prosthesis knee and ankle, respectively. We model the prosthesis floating base as rigidly attached to the distal end of the amputee's residual right thigh. This is shown in Figure 3.1. We include coordinates q_{rs} and q_{ls} in this figure since these are used to model a spring-damper ground contact in the gait generation of Chapter 9.

Powered Prosthesis Platform: AMPRO3

We use the transfemoral powered prosthesis platform AMPRO3 custom-built and introduced in [19]. The device has an iWalk adapter such that an able-bodied human can test the device. A different adapter can be used to connect this device directly into an amputee's socket. Two brushless DC motors (MOOG BN23) with 1 Nm peak torque actuate the knee and ankle pitch joints through interactions with their respective timing belt connected to each joint's harmonic gear box. This gear reduction system gives a 120:1 mechanical reduction for the knee and 175:1 for the ankle. The motors are controlled by 2 ELMO motion controllers (Gold Solo Whistle) which receive position and velocity feedback from 2 incremental encoders. These motion controllers in turn send this feedback to the microprocessor, a Beaglebone Black Rev C (BBB). The BBB returns a commanded torque to the motion controllers. The whole prosthesis system is powered by a 9-cell 4400 mAh Li-Po battery (Thunder Power RC). The components described here can be seen in Figure 3.1.

Chapter 4

SEPARABLE SUBSYSTEMS

Nonlinear control methodologies have successfully realized stable human-like walking on powered prostheses [34]–[36]. However, these methods are typically restricted to model independent controllers due to the unknown human dynamics acting on the prosthesis. The work in this chapters overcomes this restriction by introducing the notion of a *separable subsystem control law*, independent of the full-order system dynamics. By constructing an equivalent subsystem, we calculate the control law with local information. We build a subsystem model of a general open-chain manipulator to demonstrate the control method’s applicability. Employing these methods for an amputee-prosthesis model, we develop a *model-dependent* prosthesis controller that relies solely on measurable states and inputs but is equivalent to a controller developed with knowledge of the human dynamics and states. We demonstrate the results through simulating an amputee-prosthesis system and show the model dependent prosthesis controller performs identically to a feedback linearizing controller based on the whole system, confirming the equivalency.

This chapter was adapted from:

R. Gehlhar, J. Reher, and A. D. Ames. “Control of Separable Subsystems with Application to Prostheses”. In: *arXiv preprint arXiv:1909.03102*, 2019.

4.1 Introduction

To examine robotic systems influenced by human behavior, the methods in [259], [260] considered the interaction forces. This approach is part of a larger investigation of modeling and control of robots in contact with a dynamic environment, which Vukobratovic examined in many of his works, most comprehensively in [261]. However, these works remain focused on simple models and do not consider incorporating the interaction forces in general nonlinear control methods. The work of [262] incorporated the interaction forces between the amputee and prosthesis into the prosthesis dynamics to develop a feedback linearizing prosthesis controller. Considering this as a specific example of a subsystem controller, we develop a *general framework to control separable subsystems*.

In Section 4.2 we develop a feedback linearizing control law for a *separable subsystem*, a system independent of its full-order system dynamics. While this controller solely depends on the subsystem dynamics, we prove it is *equivalent* to one developed with the full-order system dynamics, hence guaranteeing full-order system stability. Second, we construct the control law using an *equivalent subsystem* with measurable inputs. In Section 4.3 we examine the application to robotic systems by outlining construction of a subsystem of a general open-chain manipulator. Following this framework, we model a powered prosthesis, Figure 4.1, as a subsystem in Section 4.4. By using the interaction forces and global orientation and velocities at the amputee's socket, we calculate our *separable subsystem control law*, independent of both the human dynamics and states. We demonstrate the application of these ideas with simulation results.

These novel methods hold potential to construct model dependent controllers for nonlinear subsystems where the dynamics of the full-order system are either unknown or computationally expensive. This ability could allow nonlinear control approaches to give formal guarantees on stability and safety to coupled subsystems. This chapter approaches subsystem controller construction in the context of both general nonlinear systems and robotic systems leading to two main contributions,

- (i) developing proofs of equivalency between a subsystem controller that relies solely on local information and the full-order system feedback linearizing controller, and
- (ii) providing a robotic decomposition method to apply these results to any open-chain robotic system.

We develop a prosthesis controller similar to [262] as a specific example.

4.2 Separable Subsystem Control

Constructing the feedback linearizing controller in (3.6) requires the dynamics of the full-order system. However, in the case of large dimensional systems, the full dynamics may be unknown or may become computationally expensive, inhibiting feedback linearization.

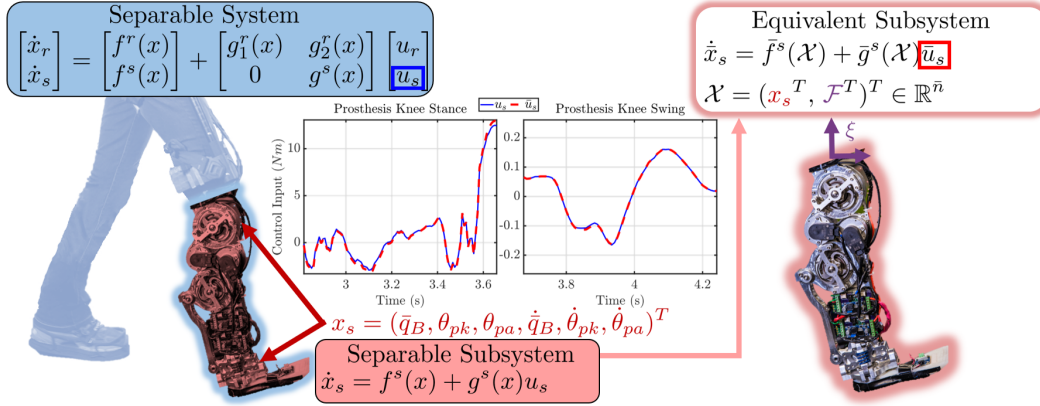


Figure 4.1: Amputee-Prosthesis Separable System and Equivalent Subsystem. (Left) Amputee-prosthesis separable system (blue), with separable prosthesis subsystem AMPRO3 (red). (Right) Equivalent prosthesis subsystem. (Middle) Control input from inverse dynamics of human-prosthesis motion capture walking data, determined with full-order system dynamics (blue) and with equivalent subsystem dynamics (red).

Control Law for Separable Subsystem

This section eliminates the need to know the full-order system dynamics for feedback linearization by constructing a *separable subsystem control law* that only depends on subsystem dynamics. We begin by defining a *separable control system*.

Definition 1: The affine control system (3.1) is a **separable control system** if it can be structured as

$$\begin{bmatrix} \dot{x}_r \\ \dot{x}_s \end{bmatrix} = \begin{bmatrix} f^r(x) \\ f^s(x) \end{bmatrix} + \begin{bmatrix} g_1^r(x) & g_2^r(x) \\ 0 & g^s(x) \end{bmatrix} \begin{bmatrix} u_r \\ u_s \end{bmatrix}, \quad (4.1)$$

$$x_r \in \mathbb{R}^{n_r}, \quad x_s \in \mathbb{R}^{n_s}, \quad u_r \in \mathbb{R}^{m_r}, \quad u_s \in \mathbb{R}^{m_s},$$

where $n_r + n_s = n$ and $m_r + m_s = m$.

Because of the structure of $g(x)$ in (4.1), u_r only acts on part of the system. This motivates defining a *separable subsystem* independent of u_r .

Definition 2: For a separable control system (4.1), its **separable subsystem** is defined as

$$\dot{x}_s = f^s(x) + g^s(x)u_s, \quad (4.2)$$

which depends on the full-order system states $x \in \mathbb{R}^n$.

Now, to construct a feedback linearizing control law for this separable subsystem, we construct output functions that solely depend on the subsystem states $x_s \in \mathbb{R}^{n_s}$ and whose Lie derivatives solely depend on the subsystem (4.2).

Definition 3: For a separable subsystem (4.2) of the separable control system (4.1), a set of linearly independent output functions with vector relative degree $\vec{\gamma}^s = (\gamma_1^s, \gamma_2^s, \dots, \gamma_{m_s}^s)$ with respect to (4.1) are **separable subsystem outputs** if they only depend on $x_s \in \mathbb{R}^{n_s}$,

$$y^s(x_s) \in \mathbb{R}^{m_s}, \quad (4.3)$$

and meet the following cross-term cancellation conditions for $j = 1, \dots, \gamma_i^s - 1$ and $i = 1, \dots, m_s$:

$$\frac{\partial L_{f_s}^j y^s(x)}{\partial x_r} f^r(x) = 0, \quad (D3.1)$$

$$\frac{\partial L_{f_s}^{\gamma_i^s - 1} y^s(x)}{\partial x_r} \begin{bmatrix} g_1^r(x) & g_2^r(x) \end{bmatrix} = \begin{bmatrix} 0 & 0 \end{bmatrix}. \quad (D3.2)$$

We use these outputs to introduce a *separable subsystem control law* in terms of the subsystem (4.2) alone.

Definition 4: For a separable subsystem (4.2) with separable subsystem outputs (4.3), we define a **separable subsystem control law** as the feedback linearizing control law

$$\begin{aligned} u_{\text{ssc}}(x) &\triangleq - \underbrace{(L_{g^s} L_{f_s}^{\vec{\gamma}^s - \mathbf{1}} y^s(x))^{-1}}_{A_s(x)} \underbrace{(L_{f_s}^{\vec{\gamma}^s} y^s(x) - \mu_s)}_{L_{f_s}^* y^s(x)} \\ &= -A_s^{-1}(x) (L_{f_s}^* y^s(x) - \mu_s). \end{aligned} \quad (4.4)$$

This control law is independent of the rest of the system dynamics $f^r(x)$, $g_1^r(x)$, and $g_2^r(x)$, but still depends on the full-order system states x . We will address this dependence in subsequent results to develop an implementable form of this control law solely dependent on subsystem states and measurable inputs.

To compare this control law $u_{\text{ssc}}(x)$ to $u_s(x)$, we construct *separable outputs* for the full-order system that include the separable subsystem outputs $y^s(x_s)$ used for (4.4).

Definition 5: For a separable control system, a set of linearly independent output functions with vector relative degree $\vec{\gamma}$ are **separable outputs** if they are structured

as

$$y(x) = \begin{bmatrix} y^r(x) \\ y^s(x_s) \end{bmatrix}, \quad y^r(x) \in \mathbb{R}^{m_r}, \quad y^s(x_s) \in \mathbb{R}^{m_s}, \quad (4.5)$$

and $y^s(x_s)$ are separable subsystem outputs with vector relative degree $\bar{\gamma}^s$. The remaining outputs $y^r(x)$ have vector relative degree $\bar{\gamma}^r$ and can depend on any of the system states x . The number of subsystem outputs m_s and the number of the rest of the outputs m_r sums to m , and $\bar{\gamma} = (\bar{\gamma}^r, \bar{\gamma}^s)$.

For the following theorem, we define the auxiliary control input μ as divided in the following form:

$$\mu = \begin{bmatrix} \mu_r \\ \mu_s \end{bmatrix}, \quad \mu_r \in \mathbb{R}^{m_r}, \quad \mu_s \in \mathbb{R}^{m_s}. \quad (4.6)$$

Theorem 1: For a separable control system (4.1), if the control law $u(x) = (u_r(x)^T, u_s(x)^T)^T$ (3.6) is constructed with separable outputs (4.5) and auxiliary control input (4.6), then $u_s(x) = u_{\text{ssc}}(x)$.

Proof: We begin by relating the 3 components $(A^{-1}(x), L_f^*y(x), \mu)$ of $u(x)$ to the components of $u_{\text{ssc}}(x)$, $(A_s^{-1}(x), L_{f_s}^*y^s(x), \mu_s)$. We are given $\mu = \begin{bmatrix} \star \\ \mu_s \end{bmatrix}$ by (4.6). With condition (D3.2), we show:

$$\begin{aligned} A(x) &= \left(\begin{bmatrix} \frac{\partial L_f^{\bar{\gamma}^r-1} y^r(x)}{\partial x_r} & \frac{\partial L_f^{\bar{\gamma}^r-1} y^r(x)}{\partial x_s} \\ \frac{\partial L_{f_s}^{\bar{\gamma}^s-1} y^s(x)}{\partial x_r} & \frac{\partial L_{f_s}^{\bar{\gamma}^s-1} y^s(x)}{\partial x_s} \end{bmatrix} \begin{bmatrix} g_1^r(x) & g_2^r(x) \\ 0 & g^s(x) \end{bmatrix} \right) \\ &= \begin{bmatrix} \star & \star \\ 0 & \frac{\partial L_{f_s}^{\bar{\gamma}^s-1} y^s(x)}{\partial x_s} g^s(x) \end{bmatrix} = \begin{bmatrix} \star & \star \\ 0 & A_s(x) \end{bmatrix}, \\ A(x)^{-1} &= \begin{bmatrix} \star & \star \\ 0 & A_s(x)^{-1} \end{bmatrix}, \end{aligned}$$

where the final step is true because of the 0 corner block and properties of block matrix inversion. Similarly, we show:

$$\begin{aligned} L_f^*y(x) &= \begin{bmatrix} \frac{\partial L_f^{\bar{\gamma}^r-1} y^r(x)}{\partial x_r} & \frac{\partial L_f^{\bar{\gamma}^r-1} y^r(x)}{\partial x_s} \\ \frac{\partial L_{f_s}^{\bar{\gamma}^s-1} y^s(x)}{\partial x_r} & \frac{\partial L_{f_s}^{\bar{\gamma}^s-1} y^s(x)}{\partial x_s} \end{bmatrix} \begin{bmatrix} f^r(x) \\ f^s(x) \end{bmatrix} \\ &= \begin{bmatrix} \star & \star \\ \frac{\partial L_{f_s}^{\bar{\gamma}^s-1} y^s(x)}{\partial x_s} f^s(x) \end{bmatrix} = \begin{bmatrix} \star \\ L_{f_s}^*y^s(x) \end{bmatrix}. \end{aligned}$$

Putting these components together to construct $u(x)$ yields

$$\begin{aligned} u(x) &= - \begin{bmatrix} \star & \star \\ 0 & A_s^{-1}(x) \end{bmatrix} \left(\begin{bmatrix} \star \\ L_{f^s}^* y^s(x) \end{bmatrix} - \begin{bmatrix} \star \\ \mu_s \end{bmatrix} \right) \\ &= \begin{bmatrix} \star \\ -A_s^{-1}(x)(L_{f^s}^* y^s(x) - \mu_s) \end{bmatrix} = \begin{bmatrix} \star \\ u_{\text{ssc}}(x) \end{bmatrix}, \end{aligned}$$

showing $u_s(x) = u_{\text{ssc}}(x)$ as defined in (4.4).

By Theorem 1, we can construct a stabilizing controller (4.4) for the subsystem independent of the rest of the system dynamics, identical to the portion of the controller constructed with the full-order system dynamics acting on the subsystem. In the case of full-state feedback linearizable systems [39], this guarantees full-order system stability when (3.6) is applied to the rest of the system. This enables construction of stable *model dependent* controllers for separable subsystems without knowledge of the full-order system dynamics.

Equivalency of Subsystems

Although we now have a subsystem control law independent of the rest of the system dynamics, it still depends on the full-order system states $x \in \mathbb{R}^n$. Consider the case where the states $x_r \in \mathbb{R}^{n_r}$ cannot be measured. If we could construct an equivalent subsystem whose dynamics are a function of the subsystem states $x_s \in \mathbb{R}^{n_s}$, and measurable inputs $\mathcal{F} \in \mathbb{R}^{n_f}$, we could calculate the subsystem control law *independent of the full-order system states*.

Consider another subsystem,

$$\begin{aligned} \dot{\bar{x}}_s &= \bar{f}^s(\mathcal{X}) + \bar{g}^s(\mathcal{X})\bar{u}_s \\ \mathcal{X} &= \begin{bmatrix} \bar{x}_s \\ \mathcal{F} \end{bmatrix} = \begin{bmatrix} x_s \\ \mathcal{F} \end{bmatrix} \in \mathbb{R}^{\bar{n}}, \end{aligned} \tag{4.7}$$

where \mathcal{X} is the state vector $\bar{x}_s = x_s$ augmented with an input \mathcal{F} . Using the same *separable subsystem outputs* as (4.3), we define a control law $\bar{u}_s(\mathcal{X})$ for the subsystem as:

$$\begin{aligned} \bar{u}_s(\mathcal{X}) &\triangleq - \underbrace{(L_{\bar{g}^s} L_{\bar{f}^s}^{\gamma_s - 1} y^s(\mathcal{X}))^{-1}}_{\bar{A}_s(\mathcal{X})} \underbrace{(L_{\bar{f}^s}^{\gamma_s} y^s(\mathcal{X}) - \mu_s)}_{L_{\bar{f}^s}^* y^s(\mathcal{X})} \\ &= -\bar{A}_s^{-1}(\mathcal{X})(L_{\bar{f}^s}^* y^s(\mathcal{X}) - \mu_s). \end{aligned} \tag{4.8}$$

Theorem 2: For the subsystems (4.2) and (4.7), if $\exists T : \mathbb{R}^n \rightarrow \mathbb{R}^{\bar{n}}$ s.t. $T(x) = \mathcal{X}$ and the following conditions hold,

$$\begin{aligned} f^s(x) &= \bar{f}^s(\mathcal{X}), \\ g^s(x) &= \bar{g}^s(\mathcal{X}), \end{aligned} \tag{T2}$$

then $u_s(x) = \bar{u}_s(\mathcal{X})$. Applying these to (4.2) and (4.7), respectively, results in dynamical systems such that given the same initial condition $\begin{bmatrix} x_{r0} \\ x_{s0} \end{bmatrix} = \begin{bmatrix} x_r(t_0) \\ x_s(t_0) \end{bmatrix}$ yields solutions $x_s(t) = \bar{x}_s(t) \forall t \geq t_0$.

Proof. Since the subsystems have the same dynamics and outputs, the Lie derivatives comprising their control laws are also the same, hence

$$\begin{aligned} u_s(x) &= -A_s^{-1}(x)(L_{f^s}^* y^s(x) - \mu_s) \\ &= -\bar{A}_s^{-1}(\mathcal{X})(L_{\bar{f}^s}^* y^s(\mathcal{X}) - \mu_s) = \bar{u}_s(\mathcal{X}). \end{aligned}$$

With the same control law and dynamics, the closed-loop dynamics of the subsystems are the same:

$$\begin{aligned} \dot{x}_s &= f^s(x) + g^s(x)u_s(x) \\ &= \bar{f}^s(\mathcal{X}) + \bar{g}^s(\mathcal{X})\bar{u}_s(\mathcal{X}) = \dot{\bar{x}}_s. \end{aligned}$$

Hence, given the same initial condition $\begin{bmatrix} x_{r0} \\ x_{s0} \end{bmatrix} = \begin{bmatrix} x_r(t_0) \\ x_s(t_0) \end{bmatrix}$, they have the same solution $x_s(t) = \bar{x}_s(t) \forall t \geq t_0$.

By Theorems 1 and 2, we can construct a stabilizing *model dependent* controller, namely (4.8), for the subsystem (4.2) independent of the rest of the system dynamics and with measurable inputs.

Zero Dynamics. For full-state feedback linearizable systems, this control method will stabilize the full-order system. For partially feedback linearizable systems, we can apply this method to the feedback linearizable portion of the system. If the zero dynamics are stable, then we can guarantee full-order system stability, which will be proved through Lyapunov methods in the next chapter, Chapter 5.

4.3 Separable Robotic Control Systems

This method of subsystem control for separable systems applies to robotic control systems. While a robotic system may not initially be in the form of (4.1), one can construct an equivalent model by dividing the model into 2 subsystems and constraining them to each other through a holonomic constraint [204]. For a model in ϑ -dimensional space, one can consider this holonomic constraint as a $n_f := \frac{\vartheta(\vartheta+1)}{2}$

DOF fixed joint. Now, the control inputs of one subsystem only affect the other subsystem through the *constraint wrench*. This construction hence decouples the dynamics of one subsystem from the control input of the other so the robotic system can be in separable system form (4.1).

Robotic System in Separable Form

For an open-chain robotic system, consider decomposing this robotic system into 2 subsystems, with the subsystem under consideration denoted with coordinates $q_s \in \mathbb{R}^{n_{q,s}}$ and the remaining subsystem denoted with coordinates $q_r \in \mathbb{R}^{n_{q,r}}$. The floating base coordinates $q_B \in \mathbb{R}^{n_f}$ for the full robotic system are contained in q_r , i.e. $q_B \subset q_r$. We consider another floating base with coordinates $\bar{q}_B \in \mathbb{R}^{n_f}$ at the attachment point between the subsystem denoted with coordinates q_s and the rest of the system. A n_f DOF holonomic constraint models this attachment as a fixed joint, as previously described. These coordinates are part of q_s , i.e. $\bar{q}_B \subset q_s$, and can be determined for any robotic system by q_r through the forward kinematics [204], meaning one does not need to directly sense these subsystem floating base coordinates when they have knowledge of the rest of the system with coordinates q_r . An example of this configuration for an amputee-prosthesis system is shown in Figure 4.2.

The dynamics for the remaining system and the subsystem of focus are given, respectively, by the classical Euler-Lagrangian equation [204],

$$D_r(q_r)\ddot{q}_r + H_r(q_r, \dot{q}_r) = B_r u_r + J_{c,r}^T(q_r)\lambda_r + J_{f,r}^T F_f, \quad (4.9)$$

and

$$D_s(q_s)\ddot{q}_s + H_s(q_s, \dot{q}_s) = B_s u_s + J_{c,s}^T(q_s)\lambda_s + J_{f,s}^T F_f, \quad (4.10)$$

with respective holonomic constraint equations,

$$\dot{J}_{c,r}(q_r, \dot{q}_r)\dot{q}_r + J_{c,r}(q_r)\ddot{q}_r = 0,$$

and,

$$\dot{J}_{c,s}(q_s, \dot{q}_s)\dot{q}_s + J_{c,s}(q_s)\ddot{q}_s = 0, \quad (4.11)$$

where $J_{c,r}$ and $J_{c,s}$ are the Jacobians of the $n_{c,r}$ and $n_{c,s}$ holonomic constraints, respectively, for the contacts of the respective subsystems with respective contact wrenches λ_r and λ_s , and $J_{f,r}$ and $J_{f,s}$ are the fixed joint constraint Jacobians for the respective subsystems with fixed joint constraint wrench F_f . Together these

second subsystem through these interaction forces and the global coordinates and velocities. There is not another way one subsystem can affect the other except through this interface.

Robotic System in Nonlinear Form. Using the notation from Section 4.2, $x_s = (q_s^T, \dot{q}_s^T)^T \in \mathbb{R}^{n_s}$ will denote the states of the subsystem under consideration for control, and $x_r = (q_r^T, \dot{q}_r^T)^T \in \mathbb{R}^{n_r}$ will denote the states of the remaining system. We also define the control input $u = (u_r^T, u_s^T)^T$, where $u_r \in \mathbb{R}^{m_r}$ and $u_s \in \mathbb{R}^{m_s}$, and construct the robotic system in nonlinear form with $x = (x_r^T, x_s^T)^T$:

$$\begin{aligned} \dot{x} = \begin{bmatrix} \dot{x}_r \\ \dot{x}_s \end{bmatrix} &= f(x) + g(x)u \\ &= \underbrace{\begin{bmatrix} \dot{q}_r \\ D_r^{-1}(-H_r + J_{c,r}^T \lambda_{c,r} + J_{f,r}^T F_f) \\ \dot{q}_s \\ D_s^{-1}(-H_s + J_{c,s}^T \lambda_{c,s} + J_{f,s}^T F_f) \end{bmatrix}}_{f(x)} + \underbrace{\begin{bmatrix} D_r^{-1}B_r & 0 \\ 0 & D_s^{-1}B_s \end{bmatrix}}_{g(x)} \underbrace{\begin{bmatrix} u_r \\ u_s \end{bmatrix}}_u \quad (4.12) \\ &\triangleq \begin{bmatrix} f^r(x) \\ f^s(x) \end{bmatrix} + \begin{bmatrix} g_1^r(x) & g_2^r(x) \\ 0 & g^s(x) \end{bmatrix} \begin{bmatrix} u_r \\ u_s \end{bmatrix}, \end{aligned}$$

and we see that our robotic system can be written as a *separable control system* (4.1).

Remark 2. By Theorem 1, for any *separable subsystem outputs* $y^s(x_s)$, a feedback linearizing control law $u_s(x)$ (4.4) can be constructed. Typically, we calculate $u(x)$ with λ in terms of u by solving (3.22) for \ddot{q} and substituting it into (3.23). Solving for λ yields

$$\begin{aligned} \lambda(q, \dot{q}, u) &= (JD^{-1}J^T)^{-1}(JD^{-1}(H - Bu) - \dot{J}\dot{q}) \\ &\triangleq \lambda_f + \lambda_g u. \end{aligned} \quad (4.13)$$

When λ_f and λ_g are included in $f(x)$ and $g(x)$, respectively, the system does not yield a separable form. However, it calculates the same $u(x)$, hence Theorem 1 still applies.

Equivalent Robotic Subsystem and Controller

The advantage of constructing a robotic system in the form (4.1) is applying Theorem 2 to construct an equivalent control law for a robotic subsystem without knowledge of the full system dynamics and states. For the full robotic system, the subsystem base coordinates \bar{q}_B can be determined through forward kinematics with q_r and

the fixed joint forces and moments F_f can be determined through the holonomic constraints with expression for the constraint wrenches (4.13). However, to obtain the subsystem dynamics independent of the coordinates of the rest of the system, additional sensing is required. When we can directly measure these subsystem base coordinates \bar{q}_B and the forces and moments F_f at the fixed joint, the robotic separable subsystem dynamics of (4.10) becomes our equivalent robotic subsystem.

Transformation for Subsystem States and Inputs. Using the notation from Section 4.2, with x_s from the full-order system, $x_s = (q_s^T, \dot{q}_s^T)^T \in \mathbb{R}^{n_s}$ and $\mathcal{F} = F_f \in \mathbb{R}^{n_f}$, we construct the robotic subsystem in nonlinear form. We relate the subsystem's augmented state vector \mathcal{X} to the full-order system states x . To obtain an expression for F_f based on the equation for $\lambda(q, \dot{q}, u)$ given in (4.13), we define the transformation $\iota : \mathbb{R}^{n_h} \rightarrow \mathbb{R}^{n_f}$ where $\iota_f(\lambda) = \iota_f(\lambda \supset F_f) = F_f$. Hence the transformation $T(x) = \mathcal{X}$ is defined as:

$$T(x) \triangleq \begin{bmatrix} x_s \\ \iota_f(\lambda(q, \dot{q}, u)) \end{bmatrix} = \begin{bmatrix} x_s \\ F_f \end{bmatrix} = \mathcal{X}.$$

Robotic Subsystem in Nonlinear Form. We construct the equivalent robotic subsystem as in (4.7):

$$\begin{aligned} \dot{\bar{x}}_s &= \begin{bmatrix} \dot{q}_s \\ D_s^{-1}(-H_s + J_{c,s}^T \lambda_{c,s} + J_{f,s}^T F_f) \end{bmatrix} + \begin{bmatrix} 0 \\ D_s^{-1}B \end{bmatrix} \bar{u}_s \\ &\triangleq \bar{f}^s(\mathcal{X}) + \bar{g}^s(\mathcal{X})\bar{u}_s. \end{aligned} \quad (4.14)$$

Remark 3. With condition (T2) met, Theorem 2 applies, enabling users to construct controllers for a robotic subsystem, without knowledge of the full dynamics and states, given the constraint forces and moments F_f at the fixed joint and its global coordinates \bar{q}_B and velocities $\dot{\bar{q}}_B$. This control law yields the same evolution of subsystem states x_s as those of the full-order system under the control law $u(x)$.

To support our arguments for robotic system separability and subsystem equivalency with experimental data, we examined human-prosthesis motion capture walking data [263] and computed the control input with inverse dynamics. With position and time data, we computed discrete accelerations. By averaging these over a time window we obtain accelerations for computing the inverse dynamics with the full-order system dynamics (3.22) and equivalent subsystem dynamics (4.10). This yielded identical prosthesis control inputs. See Figure 4.1.

4.4 Amputee-Prosthesis Application

To demonstrate these results the human-prosthesis model described in 3.3 is constructed according to the method described for a separable robotic system in 4.3 for a 65.8 kg and 1.73 m female. Two domains are considered, one for prosthesis stance \mathcal{D}_{ps} , and one for prosthesis swing \mathcal{D}_{pns} . For each domain, a 3 DOF holonomic constraint is used to model the foot contact points present in human walking behavior [254]. The height of the swing leg is the unilateral condition $\ell(x)$ used as the guard condition in (3.4). For this system, $m_s = 2$ for the number of actuated joints in the prosthesis subsystem $(\theta_{pk}, \theta_{pa})$, and $m_r = 4$ for the rest of the of actuated joints $(\theta_{lh}, \theta_{lk}, \theta_{la}, \theta_{rh})$.

In practice, an IMU on the socket attached to the amputee's residual thigh can give the global rotation and velocities required to determine \bar{q}_B . The global cartesian positions are not required since they do not appear in the dynamics. A load cell at the socket interface could measure the interaction forces F_f .

For the relative degree 1 output (3.25), we use the linearized forward hip velocity for $y_{1,v}^d$, which appeared approximately constant in human locomotion data [195]. For the relative degree 2 outputs (3.26), we define $y_{2,v}^d(\tau_v, \alpha_v)$ with a 6th order Bézier polynomial (3.29). The values $y_{1,v}^d$ and α_v are determined through the optimization described in 3.2 with torque squared as the cost function.

Phase Variable. The linearized forward hip position is used as $p(x)$ for the phase variable (3.27). In the prosthesis stance domain \mathcal{D}_{ps} , the phase variable τ_{ps} is a function of the prosthesis states q_{pk} and q_{pa} , but in the prosthesis swing domain \mathcal{D}_{pns} , it needs IMUs on the human's stance leg to measure the phase variable in real-time. It can differentiate this signal to calculate the time derivatives $\dot{\tau}_{pw}$ and $\ddot{\tau}_{pw}$.

Separable Outputs. To design *separable outputs* to enable separable subsystem control, we define the actual outputs y_v^a :

- hip velocity: $y_{1,v}^{a, \text{hip}} = r_v^{\text{sk}} \dot{\theta}_v^{\text{sk}} + (r_v^{\text{sk}} + r_v^{\text{sa}}) \dot{\theta}_v^{\text{sa}}$
- stance calf: $y_{2,v}^{a, \text{sc}} = -\theta_v^{\text{sk}} - \theta_v^{\text{sa}},$
- stance hip: $y_{2,v}^{a, \text{sh}} = -\theta_v^{\text{sh}},$
- non-stance hip: $y_{2,v}^{a, \text{nsh}} = -\theta_v^{\text{nsh}},$
- non-stance knee: $y_{2,v}^{a, \text{nsk}} = \theta_v^{\text{nsk}},$

- non-stance ankle: $y_{2,v}^{a,nsa} = \theta_v^{nsa}$.

Here r_v^{sk} and r_v^{sa} are the stance knee and ankle limb lengths, respectively. The angle labels prefaced with “s” signify “stance” side joint angles for a given domain, and the labels prefaced with “ns” denote the “nonstance” angles. The *separable subsystem outputs* are defined as $y_{ps}^s(x_s) = (y_{1,ps}^{hip}, y_{2,ps}^{sc})$ for \mathcal{D}_{ps} and $y_{pns}^s(x_s) = (y_{2,pns}^{nsk}, y_{2,pns}^{nsa})$ for \mathcal{D}_{pns} . In \mathcal{D}_{ps} , we have $\tau_{ps}(x_s)$ and hence $y_{1,ps}^{hip}$ satisfies (D3.2) because clearly $\frac{\partial y_1^s(x_s)}{\partial x_r} = 0$ and (D3.1) does not apply since its relative degree γ_1^s is 1. Because the relative degree 2 outputs are based on position and also the signal τ_{pns} in \mathcal{D}_{pns} , their Lie derivatives are the velocities of the specified prosthesis joints, meaning $\frac{\partial L_{f^s} y_2^s(x)}{\partial x_r} = 0$, satisfying (D3.1) and (D3.2). The remaining outputs for each domain define $y_{r,ps}(x)$ and $y_{r,pns}(x)$, respectively.

Prosthesis State-based Control

Since τ_{ps} is a function of x , x is the only time dependent variable in the output functions $y_{ps}(x)$, meaning a control law for the full-order system $u_{ps}(x) = (u_{r,pns}(x)^T, u_{s,ps}(x)^T)^T$ can be defined by (3.6) and for the subsystem $\bar{u}_{s,ps}(\mathcal{X})$ by (4.8). By Theorems 1 and 2, $u_{s,ps}(x) = \bar{u}_{s,ps}(\mathcal{X})$.

For \mathcal{D}_{pns} , τ_{pns} is measured and hence not a function of x , so we define the control laws slightly differently to account for the time dependency of τ_{pns} ,

$$u_{pns}(x, \mathcal{T}) = \begin{bmatrix} u_{r,pns}(x, \mathcal{T}) \\ u_{s,pns}(x, \mathcal{T}) \end{bmatrix} = -A(x)^{-1} (L_f^* y(x) - \begin{bmatrix} \dot{y}_{1,pns}^d \\ \ddot{y}_{2,pns}^d \end{bmatrix} - \mu), \quad (4.15)$$

where $\mathcal{T} = (\tau_{pns}, \dot{\tau}_{pns}, \ddot{\tau}_{pns})$, $A(x)$ and $L_f^* y(x)$ from (3.6), and

$$\begin{bmatrix} \dot{y}_{1,pns}^d \\ \ddot{y}_{2,pns}^d \end{bmatrix} = \begin{bmatrix} \frac{\partial y_{1,pns}^d(\tau_{pns}, \alpha_{pns})}{\partial \tau_{pns}} \dot{\tau}_{pns} \\ \frac{\partial^2 y_{2,pns}^d(\tau_{pns}, \alpha_{pns})}{\partial \tau_{pns}^2} \dot{\tau}_{pns}^2 + \frac{\partial y_{2,pns}^d(\tau_{pns}, \alpha_{pns})}{\partial \tau_{pns}} \ddot{\tau}_{pns} \end{bmatrix}.$$

Note the Lie derivatives of $y_{pns}(x)$ result in only being with respect to $y_{pns}^a(x)$ since $y_{pns}^d(\tau, \alpha)$ is not a function of x . A feedback linearizing controller for the subsystem is given by

$$\bar{u}_{s,pns}(\mathcal{X}, \mathcal{T}) = -A_s^{-1}(\mathcal{X}) (L_{f^s}^* y^s(\mathcal{X}) - \ddot{y}_{pns}^{s,d} - \mu_s), \quad (4.16)$$

where $A_s(\mathcal{X})$ and $L_{f^s}^* y(\mathcal{X})$ are defined as in (4.8) and

$$\ddot{y}_{2,pns}^{s,d} = \frac{\partial^2 y_{2,pns}^{s,d}(\tau_{pns}, \alpha_{pns})}{\partial \tau_{pns}^2} \dot{\tau}_{pns}^2 + \frac{\partial y_{2,pns}^{s,d}(\tau_{pns}, \alpha_{pns})}{\partial \tau_{pns}} \ddot{\tau}_{pns}.$$

Here also, the Lie derivatives of $y_{\text{pns}}^s(x_s)$ result in only being with respect to $y_{\text{pns}}^{s,a}$ since $y_{\text{pns}}^{s,d}$ is not a function of x .

Proposition 1: For a separable control system (4.1) with separable outputs (4.5), if the control input $u_{\text{pns}}(x, \mathcal{T}) = (u_{r,\text{pns}}(x, \mathcal{T})^T, u_{s,\text{pns}}(x, \mathcal{T})^T)^T$ is constructed as a feedback linearizing controller of the form (4.15) with μ structured as (4.6), then $u_{s,\text{pns}}(x, \mathcal{T}) = \bar{u}_{s,\text{pns}}(\mathcal{X}, \mathcal{T})$.

Proof: Extending Theorem 1's proof, we need only show

$$\begin{bmatrix} \dot{y}_{1,\text{pns}}^d \\ \ddot{y}_{2,\text{pns}}^d \end{bmatrix} = \begin{bmatrix} \dot{y}_{1,\text{pns}}^d \\ \ddot{y}_{2,\text{pns}}^{r,d} \\ \ddot{y}_{2,\text{pns}}^{s,d} \end{bmatrix} = \begin{bmatrix} \star \\ \ddot{y}_{2,\text{pns}}^{s,d} \end{bmatrix}.$$

Including this component with the 3 components given in Theorem 1's proof yields $u_{\text{pns}}(x, \mathcal{T}) = [\bar{u}_{s,\text{pns}}^\star]$, showing $u_{s,\text{pns}}(x, \mathcal{T}) = \bar{u}_{s,\text{pns}}(\mathcal{X}, \mathcal{T})$.

Prosthesis Result. Feedback linearization can be performed on the prosthesis subsystem with limited information of the human system and yield the *same* control law as when a controller is constructed for the prosthesis with full knowledge of the human dynamics and states, yielding full-order system stability. Although the domains are fully-actuated, zero dynamics exist due to the relative degree 1 output. Since we constructed the outputs to satisfy PHZD conditions, the zero dynamics are stable. Hence, the theorems presented in this chapter apply.

Simulation Results

The hybrid system (3.24) was simulated for 100 steps with $u_{\text{ps}}(x)$ and $u_{\text{pns}}(x, \mathcal{T})$ acting on the full-order system for \mathcal{D}_{ps} and \mathcal{D}_{pns} , respectively. The gaits were simulated again for 100 steps with $u_{r,\text{ps}}(x)$ and $\bar{u}_{s,\text{ps}}(\mathcal{X})$ acting on the human and prosthesis joints, respectively, for \mathcal{D}_{ps} , and $u_{r,\text{pns}}(x, \mathcal{T})$ and $\bar{u}_{s,\text{pns}}(\mathcal{X}, \mathcal{T})$ for \mathcal{D}_{pns} . Figure 4.3 depicts the prosthesis control inputs for each simulation, showing they match identically, demonstrating Theorem 1 and 2. The control laws enforced the trajectories found from the optimization and yielded stable amputee-prosthesis walking in simulation, as can be seen in the supplementary video [264].

The prosthesis subsystem was simulated for the continuous domains with values of \bar{q}_B , $\dot{\bar{q}}_B$, and F_f obtained from the full-order system simulation. Additionally, during \mathcal{D}_{pns} , τ_{pns} , $\dot{\tau}_{\text{pns}}$, and $\ddot{\tau}_{\text{pns}}$ from the full-order system were fed to the prosthesis simulation. These subsystem states from the prosthesis simulation and full-order

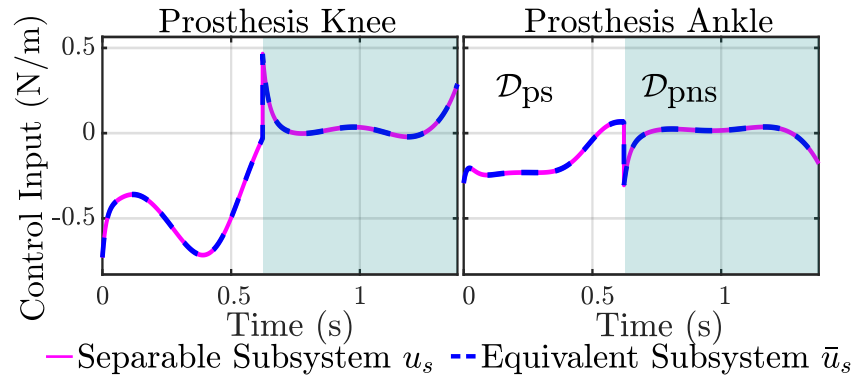


Figure 4.3: Control inputs of prosthesis knee (left) and prosthesis ankle (right) for subsystem control law u_s and \bar{u}_s over stance and non-stance domains.

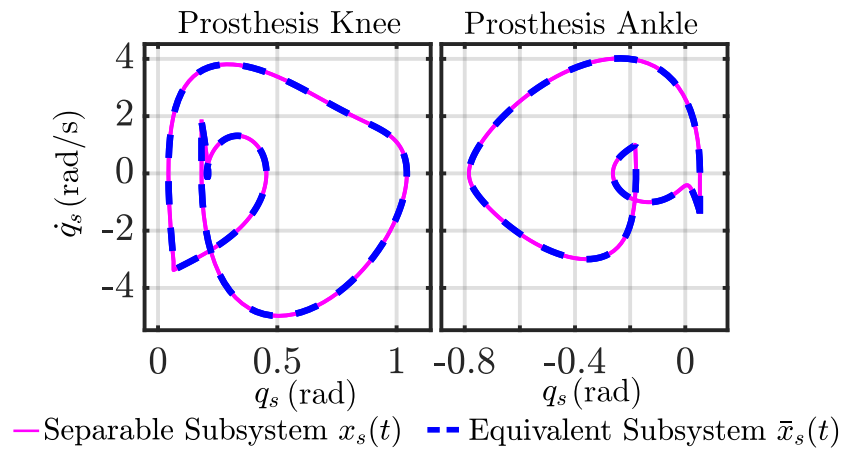


Figure 4.4: Phase portraits of prosthesis knee (left) and prosthesis ankle (right) for stance and non-stance domains.

system simulation are shown in Figure 4.4, again showing they match, demonstrating Theorem 2. These phase portraits also show the prosthesis followed stable periodic orbits. A second model was modified with human parameters increased by 24.9 kg and simulated using the same trajectories. Since the prosthesis only relies on the force measurement and global position and velocities, it still achieved perfect tracking of the outputs, shown in Figure 4.5.

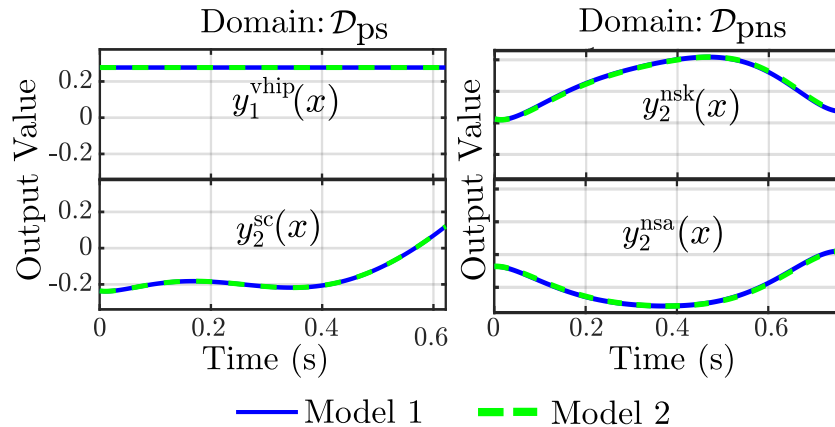


Figure 4.5: Output functions of prosthesis knee and ankle for \mathcal{D}_{ps} (right) and \mathcal{D}_{pns} (left) for 65.8 kg Model 1 and 90.7 kg Model 2.

4.5 Conclusion

This chapter presented a novel framework for controlling separable systems, resulting in a controller for the subsystem, equivalent to a controller with knowledge of the full-order states and dynamics. This formulation enables users to develop model dependent controllers for subsystems with limited information of the full-order system, with the same full-order system stability guarantees. Further, we outlined how to isolate a subsystem from an open-chain manipulator. This decomposition allows control of robotic modules without knowledge of its full system and provides a modeling method for robots that interact with another dynamic system.

We demonstrated these methods on a prosthesis and showed that the prosthesis was able to achieve its desired behavior with two different human models acting on it. This suggests this model-based approach could generalize across subjects since it reacts in real-time to an individual's varying dynamic load. In fact, this result extends beyond simulation results in this thesis. The separable subsystem framework developed in this chapter leads to the formation of an entire class of subsystem controllers with formal guarantees of stability in the next chapter. It is controllers of this very class that then realize a similar result experimentally in Chapters 8 and 9, where the prosthesis achieves its desired motion with two different subjects while it has no knowledge of the change of user.

SEPARABLE CONTROL LYAPUNOV FUNCTIONS

This chapter extends the work of the previous chapter by further translating bipedal trajectory tracking methods to prostheses to enable construction of a class of model-dependent prosthesis controllers using locally available sensor information. While the previous chapter could establish stability guarantees for full-state feedback linearizable systems with a single form of subsystem controller, this chapter creates an entire class of subsystem controllers that guarantee full-order system stability even when there are uncontrollable dynamics (zero dynamics). The *rapidly exponentially stabilizing control Lyapunov functions* (RES-CLFs) developed for bipedal robots guarantee stability of the *hybrid zero dynamics* in the presence of impacts that occur in walking [199]. These methods cannot be directly applied to prostheses because of the unknown human dynamics. We overcome this challenge with two RES-CLFs, one for the prosthesis subsystem and another for the remaining human system. Further, we outline a method to construct these RES-CLFs for this type of *separable system* by first constructing separable CLFs for partially feedback linearizable systems. This work develops a class of separable subsystem controllers that rely only on local information but provide formal guarantees of stability for the full-order hybrid system with zero dynamics.

This chapter was adapted from:

R. Gehlhar and A. D. Ames. “Separable Control Lyapunov Functions With Application to Prostheses”. In: *IEEE Control Systems Letters*, 5.2, 2021, pp. 559–564.

5.1 Introduction

In developing a class of controllers for bipedal robots, researchers looked to establish stability given the impacts and zero dynamics present in walking. Using a RES-CLF, they extended the stability of periodic orbits in the hybrid zero dynamics to the full-order dynamics [199]. This method was applied in experiment to establish stable walking of an under-actuated five-link robot subject to impact dynamics at foot strike. CLFs also proved useful for robotic walking on hardware when formulated as quadratic programs (QPs) [37], [265]. To apply this powerful nonlinear control technique to powered prostheses, we view the human-prosthesis system as

a separable system [207], where a subsystem, namely the prosthesis, is separable from the system since it is not a function of the control input of the remaining system, the human. We examine separating RES-CLFs for separable systems to construct a RES-CLF based on the prosthesis alone with the same stability guarantees established in [199]. Separable Lyapunov functions were termed in [266] to describe stability analysis methods for interconnected nonlinear systems, such as in [267]. Here we construct separable RES-CLFs to define a class of controllers to render provably stable hybrid periodic orbits of nonlinear separable systems with zero dynamics.

The main contributions of this chapter are

- (i) establishing stability guarantees of a hybrid dynamical system with zero dynamics through a subsystem controller relying solely on local information, and
- (ii) providing a method to synthesize such controllers.

This work enables construction of a class of model-dependent prosthesis controllers, bringing the human in the loop of prosthesis control with strong formal guarantees of stability. Section 5.2 establishes that a composite CLF for a separable system guarantees stability of a hybrid periodic orbit. Section 5.3 outlines construction of CLFs for partially feedback linearizable systems that yield a separable form to construct RES-CLFs for separable systems. Section 5.4 describes the amputee-prosthesis model used to demonstrate the results in simulation.

5.2 Composite RES-CLF for Separable Systems

In this section we extend exponential stability of a hybrid periodic orbit in the zero dynamics to the full-order dynamics with two RES-CLFs for a separable system, the form of the human-prosthesis system, shown in Figure 5.1. As discussed in the previous chapter, we can construct an equivalent prosthesis subsystem, independent of the human, using inputs available from a force sensor and IMU in practice. A RES-CLF for this equivalent subsystem, allows independent construction of the separable subsystem control law relying only on local information and stabilizes the full-order system when the remaining system is known to stabilize itself.

To construct CLFs for each system, we begin by constructing separable outputs $y^r(x)$ and $y^s(x_s)$ 4.5 and transforming the separable system into normal form through the

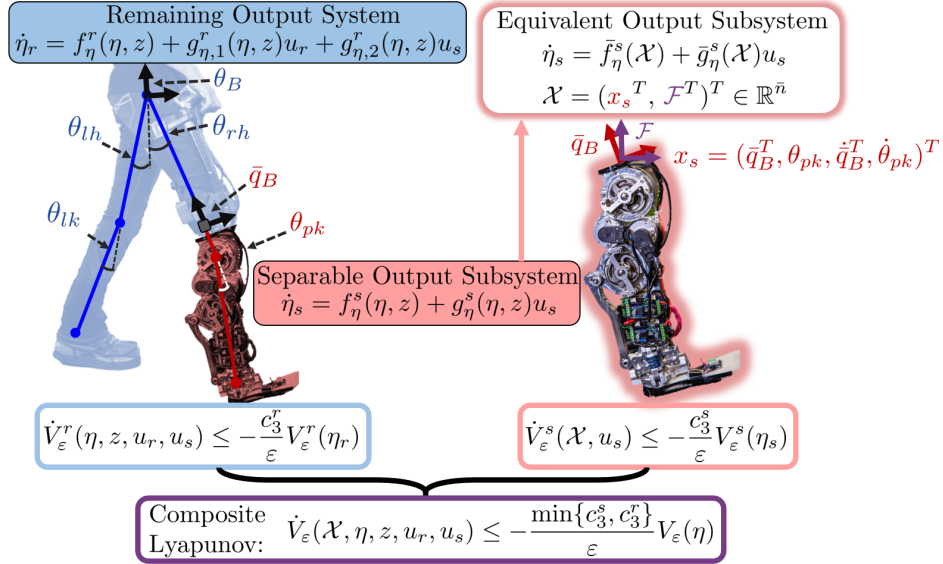


Figure 5.1: Human-prosthesis separable system (left) with separable prosthesis subsystem (red) and remaining human system (blue). Equivalent prosthesis subsystem (right) with base coordinates and interaction force inputs \mathcal{F} . The composite CLF of the remaining system RES-CLF (blue) and equivalent subsystem RES-CLF (red) yields a RES-CLF for the whole system (purple).

process outlined in Subsection 3.1. The output dynamics (3.8) result in a separable subsystem form (4.1),

$$\begin{bmatrix} \dot{\eta}_r \\ \dot{\eta}_s \end{bmatrix} = \begin{bmatrix} f_{\eta}^r(\eta, z) \\ f_{\eta}^s(\eta, z) \end{bmatrix} + \begin{bmatrix} g_{\eta,1}^r(\eta, z) & g_{\eta,2}^r(\eta, z) \\ 0 & g_{\eta}^s(\eta, z) \end{bmatrix} + \begin{bmatrix} u_r \\ u_s \end{bmatrix}, \quad (5.1)$$

since $\eta_s^{\bar{y}_s} = L_{f_s}^* y^s(x) + A_s(x)u$ is independent of u_r , as shown in the proof of Theorem 1, and the 1st to $(\bar{y}_s - \mathbf{1})^{\text{th}}$ derivatives of η_s are a linear relationship with η_s and hence are also independent of u_r . We consider the bottom row as the separable output subsystem, and the top row as the remaining output system. The separable subsystem output dynamics can equivalently be written in terms of \mathcal{X} since they are either functions of only x_s or functions of the partial derivatives of the subsystem outputs and the subsystem dynamics, which can both be equivalently written in terms of \mathcal{X} . Hence we can equivalently define the output dynamics as,

$$\dot{\eta}_s = \bar{f}_{\eta}^s(\mathcal{X}) + \bar{g}_{\eta}^s(\mathcal{X})u_s. \quad (5.2)$$

We now use these outputs dynamics to construct a RES-CLF for each system. We begin by assuming there exists a RES-CLF $V_\varepsilon^s(\eta_s)$ for the equivalent subsystem,

$$c_1^s \|\eta_s\|^2 \leq V_\varepsilon^s(\eta_s) \leq \frac{c_2^s}{\varepsilon^2} \|\eta_s\|^2 \quad (5.3)$$

$$\inf_{u_s \in \mathbb{R}^{m_s}} [L_{\bar{f}_\eta^s} V_\varepsilon^s(\mathcal{X}) + L_{\bar{g}_\eta^s} V_\varepsilon^s(\mathcal{X}) u_s] \leq -\frac{c_3^s}{\varepsilon} V_\varepsilon^s(\eta_s),$$

where c_1^s , c_2^s , and c_3^s are positive constants. Here $V_\varepsilon^s(\eta_s)$ is only a function of the separable subsystem states η_s and its derivative $\dot{V}_\varepsilon^s(\mathcal{X}, u_s)$ is based solely on local information since we use the equivalent output dynamics given in (5.2). The following set consists of all control values u_s that satisfy $\dot{V}_\varepsilon^s(\mathcal{X}, u_s) \leq -\frac{c_3^s}{\varepsilon} V_\varepsilon^s(\eta_s)$:

$$K_\varepsilon^s(\mathcal{X}) = \{u_s \in \mathbb{R}^{m_s} : L_{\bar{f}_\eta^s} V_\varepsilon^s(\mathcal{X}) + L_{\bar{g}_\eta^s} V_\varepsilon^s(\mathcal{X}) u_s \leq -\frac{c_3^s}{\varepsilon} V_\varepsilon^s(\eta_s)\}.$$

Let us also assume there exists a RES-CLF $V_\varepsilon^r(\eta_r)$ for the remaining system such that, given a $u_s \in K_\varepsilon^s(\mathcal{X})$,

$$c_1^r \|\eta_r\|^2 \leq V_\varepsilon^r(\eta_r) \leq \frac{c_2^r}{\varepsilon^2} \|\eta_r\|^2 \quad (5.4)$$

$$\begin{aligned} \inf_{u_r \in \mathbb{R}^{m_r}} [L_{f^r} V_\varepsilon^r(\eta, z) + L_{g_1^r} V_\varepsilon^r(\eta, z) u_r \\ + L_{g_2^r} V_\varepsilon^r(\eta, z) u_s] \leq -\frac{c_3^r}{\varepsilon} V_\varepsilon^r(\eta_r), \end{aligned}$$

where c_1^r , c_2^r , and c_3^r are positive constants. Here $V_\varepsilon^r(\eta_r)$ is only a function of the remaining states η_r and its derivative $\dot{V}_\varepsilon^r(\eta, z, u)$ depends on both control inputs (u_r, u_s) . The following set consists of all control values u_r that satisfy $\dot{V}_\varepsilon^r(\eta, z, u) \leq -\frac{c_3^r}{\varepsilon} V_\varepsilon^r(\eta_r)$ for $u_s \in K_\varepsilon^s(\mathcal{X})$:

$$\begin{aligned} K_\varepsilon^r(\eta, z) = \{u_r \in \mathbb{R}^{m_r} : L_{f^r} V_\varepsilon^r(\eta, z) + L_{g_1^r} V_\varepsilon^r(\eta, z) u_r \\ + L_{g_2^r} V_\varepsilon^r(\eta, z) u_s \leq -\frac{c_3^r}{\varepsilon} V_\varepsilon^r(\eta_r)\} |_{u_s \in K_\varepsilon^s(\mathcal{X})}. \end{aligned}$$

Theorem 3: Let \mathcal{O}_Z be an exponentially stable periodic orbit of the hybrid zero dynamics $\mathcal{H}|_Z$ transverse to $S \cap Z$ and assume there exists RES-CLFs $V_\varepsilon^s(\eta_s)$ and $V_\varepsilon^r(\eta_r)$ for the equivalent output subsystem (5.2) and remaining system (5.1), respectively, of the continuous dynamics of $\mathcal{H}\mathcal{C}$ (3.11). Then there exists an $\bar{\varepsilon} > 0$ such that for all $0 < \varepsilon < \bar{\varepsilon}$ and for all Lipschitz continuous $u_s^\varepsilon(\mathcal{X}) \in K_\varepsilon^s(\mathcal{X})$ and respective $u_r^\varepsilon(\eta, z) \in K_\varepsilon^r(\eta, z) |_{u_s \in \bar{K}_\varepsilon^s(\mathcal{X})}$, $\mathcal{O} = \iota_0(\mathcal{O}_Z)$ is an exponentially stable hybrid periodic orbit of \mathcal{H}_ε with $u^\varepsilon(\mathcal{X}, \eta, z) = (u_r^{\varepsilon T}(\eta, z), u_s^{\varepsilon T}(\mathcal{X}))^T$.

Proof: We show the conditions listed above are within the conditions of Theorem 2 of [199], so the same result holds. First we show that given a RES-CLF for the equivalent subsystem and remaining system, there exists a RES-CLF for the whole system. Consider the composite Lyapunov function:

$$V_\varepsilon(\eta) = V_\varepsilon^s(\eta_s) + V_\varepsilon^r(\eta_r) \leq \frac{\max\{c_2^s, c_2^r\}}{\varepsilon^2} \|\eta\|^2.$$

Similarly $V_\varepsilon(\eta) \geq \min\{c_1^s, c_1^r\} \|\eta\|^2$, satisfying (3.14). For (3.15),

$$\begin{aligned} \dot{V}_\varepsilon(\mathcal{X}, \eta, z, u_r, u_s) &= \dot{V}_\varepsilon^s(\mathcal{X}, u_s) + \dot{V}_\varepsilon^r(\eta, z, u_r) \\ &\leq -\frac{\min\{c_3^s, c_3^r\}}{\varepsilon} V_\varepsilon(\eta), \end{aligned}$$

establishing $V_\varepsilon(\eta)$ as a RES-CLF of the continuous dynamics of (3.11). Dropping the arguments (\mathcal{X}, u_s) and (η, z, u_r) for simplicity's sake, we next show for $u^\varepsilon = (u_r^{\varepsilon T}, u_s^{\varepsilon T})^T$, where $u_r^\varepsilon \in K_\varepsilon^r$ and $u_s^\varepsilon \in K_\varepsilon^s$, that $u^\varepsilon \in K_\varepsilon$ by ensuring $\dot{V}_\varepsilon \leq -\frac{\min\{c_3^s, c_3^r\}}{\varepsilon} V_\varepsilon(\eta)$. Using this u_r^ε and u_s^ε and building on what was shown above,

$$\begin{aligned} \dot{V}_\varepsilon &= \dot{V}_\varepsilon^s + \dot{V}_\varepsilon^r \\ &= (L_{\bar{f}_\eta^s} V_\varepsilon^s + L_{\bar{g}_\eta^s} V_\varepsilon^s u_s^\varepsilon) + (L_{f^r} V_\varepsilon^r + L_{g_1^r} V_\varepsilon^r u_r^\varepsilon + L_{g_2^r} V_\varepsilon^r u_s^\varepsilon) \\ &\leq \left(-\frac{c_3^s}{\varepsilon} V_\varepsilon^s(\eta_s)\right) + \left(-\frac{c_3^r}{\varepsilon} V_\varepsilon^r(\eta_r)\right) \\ &\leq -\frac{\min\{c_3^s, c_3^r\}}{\varepsilon} V_\varepsilon(\eta), \end{aligned}$$

hence $u^\varepsilon = (u_r^{\varepsilon T}, u_s^{\varepsilon T})^T \in K_\varepsilon(\eta, z)$. Since these conditions fit within the conditions of Theorem 2 of [199], the same result applies: $\mathcal{O} = \iota_0(\mathcal{O}_Z)$ is exponentially stable for \mathcal{H}_ε . \square

Remark 4. In Section 5.4, we prescribe limit cycle motion matching human data to the human model with a RES-CLF controller. Research on central pattern generators suggest biological walkers such as humans exhibit stable rhythmic behavior, meaning they have limit cycles [209]. Thus we do not make biomechanical claims of the human's control method, but instead prescribe a stable limit cycle to approximate human walking. Our class of RES-CLF controllers encompasses all controllers that stabilize these hybrid limit cycles; for control purposes we find it reasonable to assume the human's effective control input is within our class of control laws for the remaining system. Then by Theorem 3, a RES-CLF prosthesis subsystem controller with only local information will guarantee the entire system is stable.

5.3 Separable CLF Construction

To obtain RES-CLFs for separable systems, we begin with constructing CLFs for partially feedback linearizable systems, an idea introduced in [250, pp. 160-172]. Our construction yields a separable form that allows us to independently stabilize each output while guaranteeing full-order system stability. This method also provides a basis to construct separable RES-CLFs for separable systems.

Separable CLFs. We start with the hybrid system (3.11) of our output states η and uncontrollable states z . This system is in normal form, as explained in 3.1. To enable independent controller construction for the human and prosthesis subsystems, we construct a CLF that we can separate for each output η_i , starting with a lemma on the structure of the CARE solution.

Lemma 1: For any F and G of the form (3.10) and weight matrix $Q = \text{diag}(Q_1, \dots, Q_m)$, where $Q_i \in \mathbb{R}^{\gamma_i \times \gamma_i}$, a solution to the CARE equation,

$$F^T P + PF + PGG^T P + Q = 0, \quad (5.5)$$

is a block diagonal positive definite matrix $P = \text{diag}(P_1, \dots, P_m)$ with elements $\{P_i \in \mathbb{R}^{\gamma_i \times \gamma_i}\}_{i=1, \dots, m}$.

Proof: Let us assume P is of the given form, this would yield the left side of (5.5) to be a block diagonal matrix of the following set of components:

$$\{F_i^T P_i + P_i F_i + P_i G_i G_i^T P_i + Q_i\}_{i=1 \dots m},$$

where the right side of (5.5) equates each of these components to 0. This takes the form of CARE and since F_i and G_i of the form (3.10) yield a full rank controllability matrix, there exists a solution P_i for $i = 1 \dots k$. Hence this block diagonal structure of P satisfies (5.5) and is therefore a solution. \square

We know from [199] that for a P from CARE, $V(\eta) = \eta^T P \eta$ is a CLF satisfying

$$\inf_{\mu} [L_F V(\eta) + L_G V(\eta) \mu] \leq -\frac{\lambda_{\min}(Q)}{\lambda_{\max}(P)} V(\eta), \quad (5.6)$$

where $L_F V(\eta) = \eta(F^T P + PF)\eta$ and $L_G V(\eta) = 2\eta^T P G$. Based on this construction, we can separate our CLF such that for each output η_i we can define a CLF $V^i(\eta_i)$, or *sub-CLF*, with sub-components from our *separable CLF* $V(\eta)$.

Definition 6: A *separable CLF* is a CLF $V_{\text{sep}}(\eta) = \eta^T P \eta$ with P of the form in Lemma 1, satisfying (5.5) for F and G of (3.10) and Q of the form in Lemma 1, where $k \geq 2$.

Definition 7: A *sub-CLF* is a function $V_{\text{sub}}(\eta_{\text{sub}})$:

$$V_{\text{sub}}(\eta_{\text{sub}}) := V^i(\eta_i) = \eta_i^T P_i \eta_i, \quad (5.7)$$

$$\inf_{\mu \in \mathbb{R}} [L_F V^i(\eta_i) + L_G V^i(\eta_i) \mu] \leq -\frac{\lambda_{\min}(Q_i)}{\lambda_{\max}(P_i)} V^i(\eta_i),$$

where $L_F V^i(\eta_i) = \eta_i (F_i^T P_i + P_i F_i) \eta_i$ and $L_G V^i(\eta_i) = 2\eta_i^T P_i G_i$. for $i \in \{1 \dots k\}$ for a separable CLF $V_{\text{sep}}(\eta)$.

Based on these definitions, we now establish constructing the auxiliary control inputs μ_i to satisfy their sub-CLF conditions will yield a μ satisfying the separable CLF condition.

Theorem 4: Given a separable CLF $V_{\text{sep}}(\eta)$, if for all $i \in \{1 \dots k\}$, μ_i satisfies its sub-CLF condition (5.7), then $\mu = [\mu_1^T, \mu_2^T, \dots, \mu_m^T]^T$ satisfies (5.6) for $V_{\text{sep}}(\eta)$.

Proof: Since P in $V_{\text{sep}}(\eta)$ is the specified block diagonal structure in Lemma 1 and satisfies (5.5), each P_i must satisfy:

$$F_i^T P_i + P_i F_i + P_i G_i G_i^T P_i + Q_i = 0,$$

and hence forms a CLF satisfying the sub-CLF conditions (5.7). We write $V_{\text{sep}}(\eta)$ as a composite CLF of sub-CLFs:

$$V_{\text{sep}}(\eta) = \eta_1^T P_1 \eta_1 + \eta_2^T P_2 \eta_2 + \dots + \eta_m^T P_m \eta_m = \sum_{i=1}^m V^i(\eta_i),$$

where $V^i(\eta_i) = \eta_i^T P_i \eta_i$. Taking the infimum of the derivative, we bound the separable CLF in terms of the sub-CLFs:

$$\begin{aligned} \inf_{\mu \in \mathbb{R}^m} [L_F V_{\text{sep}}(\eta) + L_G V_{\text{sep}}(\eta) \mu] &= \sum_{i=1}^m \inf [L_F V^i(\eta_i) + L_G V^i(\eta_i) \mu_i] \\ &\leq \sum_{i=1}^m -\frac{\lambda_{\min}(Q_i)}{\lambda_{\max}(P_i)} V^i(\eta_i). \end{aligned}$$

Comparing the elements in this bound to the separable CLF bound in (5.6), we note $V_{\text{sep}}(\eta) = \sum_{i=1}^m V^i(\eta_i)$, $\lambda_{\min}(Q_i) \geq \lambda_{\min}(Q)$, and $\lambda_{\max}(P_i) \leq \lambda_{\max}(P)$ for all $i = 1, \dots, m$. Hence:

$$\sum_{i=1}^m -\frac{\lambda_{\min}(Q_i)}{\lambda_{\max}(P_i)} V^i(\eta_i) \leq -\frac{\lambda_{\min}(Q)}{\lambda_{\max}(P)} V_{\text{sep}}(\eta).$$

Therefore any set $\{\mu_i \in \mathbb{R}\}_{i=1,\dots,m}$ that satisfies each respective sub-CLF condition (5.7), will also satisfy the CLF condition (5.6) for the separable CLF. \square

This CLF construction allows us to develop μ_i with only knowledge of η_i to stabilize each output while guaranteeing stability of the whole system. For the human-prosthesis system, we can construct these inputs separately for the human and prosthesis. To apply Theorem 3, we now extend this method to develop RES-CLFs for separable systems.

Separable RES-CLFs for Separable Systems. For a system with m relative degree 2 outputs, common in mechanical systems, we can transform each sub-CLF to a sub-RES-CLF following the method in [199] with $0 < \varepsilon < 1$:

$$V_\varepsilon^i(\eta) = \eta_i^T \begin{bmatrix} \frac{1}{\varepsilon}I & 0 \\ 0 & I \end{bmatrix} P_i \begin{bmatrix} \frac{1}{\varepsilon}I & 0 \\ 0 & I \end{bmatrix} \eta_i =: \eta_i^T P_i^\varepsilon \eta_i. \quad (5.8)$$

By Theorem 3's proof constructions, we conclude the summation of sub-RES-CLFs yields a RES-CLF for the whole system. Repeating Theorem 4's proof would establish the same result for this separable RES-CLF. By summing the sub-RES-CLFs for the separable subsystem outputs we attain a RES-CLF $V_\varepsilon^s(\eta_s) = \eta_s^T P_s^\varepsilon \eta_s$ for the equivalent subsystem (4.7) and with the remaining outputs a RES-CLF $V_\varepsilon^r(\eta_r) = \eta_r^T P_r^\varepsilon \eta_r$ for the remaining system (4.1), where P_r^ε and P_s^ε are diagonal matrices of elements P_i^ε for their respective outputs.

To find a subsystem control law in $K_\varepsilon^s(\mathcal{X})$, we use the subsystem output dynamics (5.2) to formulate a QP for the subsystem control law u_s without knowledge of the rest of the system:

$$u_s^* = \underset{u_s \in \mathbb{R}^{m_s}}{\operatorname{argmin}} u_s^T \bar{g}_\eta^s(\mathcal{X})^T \bar{g}_\eta^s(\mathcal{X}) u_s + \bar{f}_\eta^s(\mathcal{X}) u_s \quad (5.9)$$

$$\text{s.t. } L_{F_s} V_\varepsilon^s(\eta_s) + L_{G_s} V_\varepsilon^s(\eta_s) (\bar{g}_\eta^s(\mathcal{X}) u_s + \bar{f}_\eta^s(\mathcal{X})) \leq -\frac{\lambda_{\min}(Q_s)}{\varepsilon \lambda_{\max}(P_s)} V_\varepsilon^s(\eta_s),$$

where again F_s , G_s , Q_s , and P_s are diagonal matrices of the elements F_i , G_i , Q_i , and P_i , respectively, for the subsystem outputs. These constructions work for any separable system with separable outputs, since its normal form is also separable. Inherently F and G of (3.10) comply with separable form and the feedback linearizing terms of (5.1) are separable, as shown in the proof of Theorem 1.

This subsystem control law relies solely on local information and guarantees stability of a hybrid periodic orbit of the zero dynamics in the full-order dynamics when the remaining system is stable. This QP formulation allows torque bounds and model-based constraints to be added, as in [37], [265].

5.4 Amputee-Prosthesis Application

We apply the controller (5.9) to the amputee-prosthesis model described in 3.3, but we omit the ankles for simplicity and model the feet as point contacts. The torso is not actuated, introducing zero dynamics into the system. In practice, we can emulate a point foot model on a transfemoral prosthesis by treating the ankle as a passive spring-damper. For the hybrid system (3.24), we model two domains, one for prosthesis stance and one for prosthesis non-stance (swing), and use the height of the non-stance foot as the guard. For separable outputs (4.5), we define the prosthesis knee for the separable subsystem output and the human's left hip, left knee, and right hip as the remaining system outputs. In the gait generation optimization (3.28), the Bézier polynomials (3.29) are designed to match human walking data [263] through the cost function. The impact invariance constraint of (3.18), ensures the hybrid periodic trajectories satisfy the assumption of Theorem 3.

Results. To encode the human-like walking trajectories in the human simulation, we use the feedback linearizing controller (3.6) where $\mu = (\mu_r^T, \mu_s^T)^T$, with μ_s as the min-norm controller satisfying the RES-CLF condition for $V_\varepsilon^s(\eta_s)$, and

$$\mu_r = -\frac{1}{\varepsilon^2}y_v^r(\eta) - \frac{1}{\varepsilon}\dot{y}_v^r(\eta),$$

which indeed yields a RES-CLF as shown in [199] for this remaining system. The prosthesis tracks its trajectory with the subsystem controller (5.9), which yields the same μ_s used for the remaining system controller. Simulating this system for 20 steps starting at a perturbed initial condition the prosthesis (subsystem) states settle into a stable periodic orbit, shown in Figure 5.2a, demonstrating the rapid convergence of this controller. This figure also depicts the stable periodic orbit of the zero dynamics, demonstrating the exact result of Theorem 3: a stable hybrid periodic orbit of the zero dynamics is guaranteed exponentially stable in the full-order dynamics for controllers of their respective RES-CLF controller classes. Figure 5.2b shows the output tracking of the prosthesis controller and its relation to human knee data with respect to a state-based parameterization of time [207]. Figure 5.3a depicts the RES-CLF derivatives for the subsystems and full-order system, with the full-order system's bound. This demonstrates Theorem 4 by showing the auxiliary control inputs for the remaining system and separable subsystem that satisfy their respective sub-CLF conditions also satisfy the CLF condition for the full-order system. Figure 5.3b shows the prosthesis control input from (5.9) is smooth for each domain and

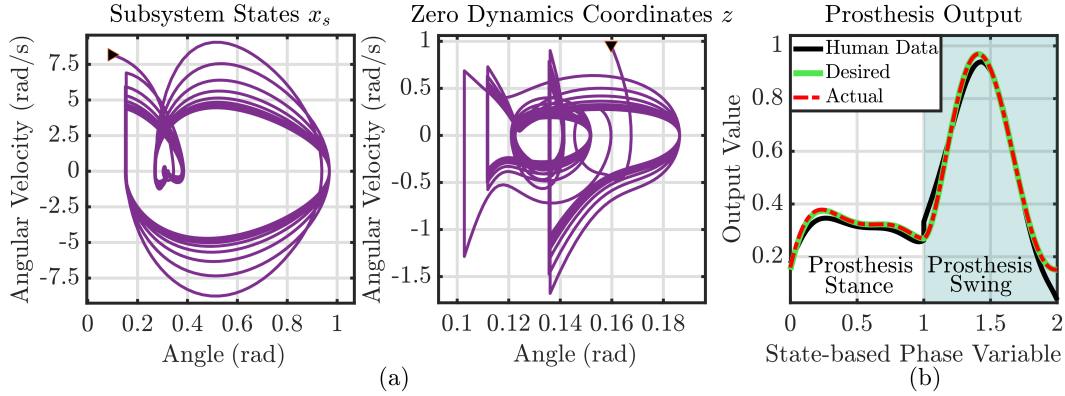


Figure 5.2: Phase Portraits and Output Tracking Simulation Results. (a) Phase portraits of subsystem states (left) and zero dynamics coordinates (right) showing stability for 20 steps with perturbed initial condition (triangle). (b) Actual output prosthesis trajectory $y_v^{a,s}$ tracking desired trajectory $y_v^{d,s}$, designed to match human data.

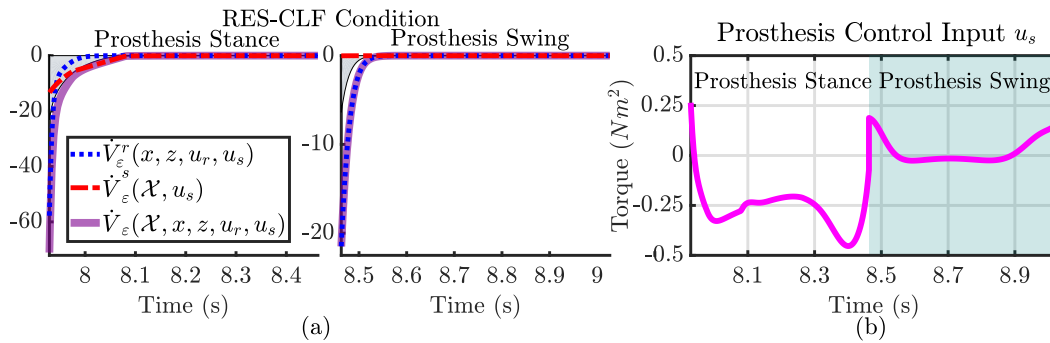


Figure 5.3: RES-CLF Convergence and Control Input Simulation Results. (a) RES-CLF derivatives for remaining system (blue) and subsystem (red) show convergence for prosthesis stance domain (left) and prosthesis swing (right) and yield a RES-CLF for the full-order system (purple) satisfying its RES-CLF bound (gray). (b) Prosthesis control input from CLF-QP.

remains in a reasonable range. Figure 5.4 shows gait tiles of the human-prosthesis system walking in simulation.

5.5 Conclusion

This chapter extended RES-CLFs to separable systems to establish exponential stability of a hybrid periodic orbit of the zero dynamics in the full-order dynamics with a subsystem controller constructed solely with local information. Following, we developed a method to construct such RES-CLFs for separable systems. This method also outlined constructing CLFs for linearized systems to stabilize each

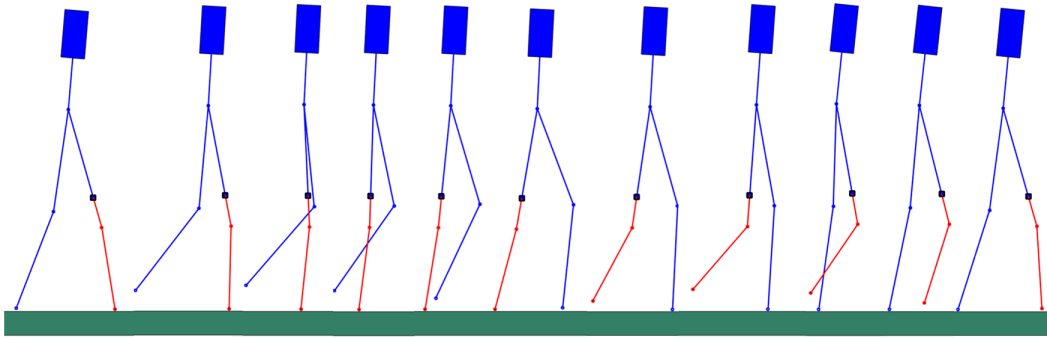


Figure 5.4: Gait tiles of human-prosthesis system, prosthesis in red, demonstrating human-like walking in simulation.

output independent of the rest of the system, while guaranteeing stability of the whole system. This work is significant since it enables construction of a class of model-dependent prosthesis controllers using only locally available sensor information. With the assumption the human can stabilize itself, these controllers provide formal guarantees of exponential stability for a hybrid human-prosthesis system with zero dynamics. This class of controllers gives freedom to design controllers with fast convergence in the presence of disturbances to be physically realizable. Controllers of this class are realized on a powered knee-ankle prosthesis in Chapters 7, 8, and 9. But first, we will prove the formal guarantees of stability established in this chapter still hold when there is uncertainty in the interaction force estimate used to complete the prosthesis subsystem dynamics model.

Chapter 6

ESTIMATE-TO-STATE STABILITY

The model-dependent prosthesis control methods developed in the previous chapter yield a wider range of stability properties compared to model-independent methods, but require knowledge of the interaction force between the human and prosthesis. Any error in force estimation compromise the formal guarantees. This chapter addresses this uncertainty by formalizing the stability of the human-prosthesis system subject to force estimation error. A novel notion of *estimate-to-state stability* is introduced and provides a means to guarantee exponential convergence of the prosthesis to a set when the controller’s model contains estimation error. Conditions are established to ensure input-to-state stability for the human’s hybrid periodic orbits when subject to disturbances from the prosthesis control action deviating from its nominal control law. A class of estimate-to-state stable prosthesis controllers is proposed and implemented in simulation, demonstrating how the human-prosthesis system converges to a tube around the desired trajectory resulting in stable walking.

This chapter was adapted from:

R. Gehlhar and A. D. Ames. “Estimate-to-state stability for hybrid human-prosthesis systems”. In: *2021 60th IEEE Conference on Decision and Control (CDC)*, IEEE, 2021, pp. 705–712.

6.1 Introduction

Model-dependent prosthesis controllers depend on the interaction forces between the human and prosthesis as well as the ground reaction forces on the prosthesis [208]. Because they directly measure the effects of the subject’s weight, theoretically, less tuning should be required to adjust to varying weight between subjects. However, any inaccuracy or time delay from a force estimate or measurement could introduce error into the model dynamics used for control. Since an error in the force enters the dynamics at the acceleration level, the torque control input is sensitive to this disturbance.

To develop a controller robust to these disturbances, we take inspiration from input-to-state stable (ISS) methods [251] which have been used to establish stability to set guarantees of nonlinear systems subject to input disturbances [252], [268]–[270].

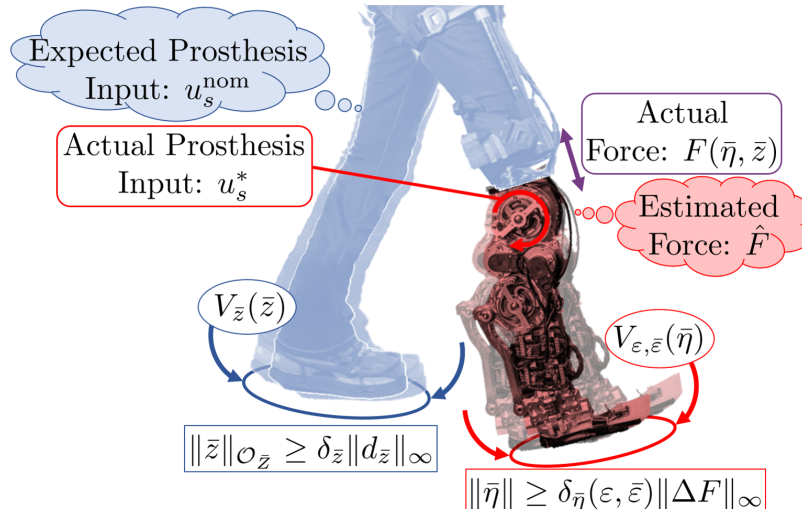


Figure 6.1: Human-prosthesis system. Prosthesis exponentially converges according to CLF $V_{\epsilon, \bar{\epsilon}}$ to a set bounded by force estimation error ΔF . Human exponentially converges according to zero dynamics Lyapunov function $V_{\bar{z}}$ to a set bounded by a disturbance created by the deviation of the prosthesis control input u_s^* from expected control law $u_p^{\text{nom}}(\bar{\eta}, \bar{z})$.

Most closely related to our application, [271] developed a special form of ISS control Lyapunov function (ISS-CLF) to establish ISS for a bipedal robot with hybrid zero dynamics. The work of [262] used local ISS to establish that the prosthesis system is robust to human-like kinematic variation in walking. In this chapter, we develop *formal guarantees of exponential ISS (e-ISS) of the whole human-prosthesis hybrid system with zero dynamics* when the prosthesis controller depends on a force estimate prone to error and deviates from the control law the human expects. We guarantee this stability through a class of novel estimate-to-state stable (ESS) CLF for which we construct a hardware implementable form using the work of [37].

In this chapter, Section 6.2 establishes ESS-CLFs. Section 6.3 introduces the hybrid system to represent the human-prosthesis system, Figure 6.1. This section also presents our main result, establishing input-to-state stability of the hybrid periodic orbit of the zero dynamics in the full-order dynamics in the presence of estimation error. To apply these concepts to the human-prosthesis system, we model a robotic system in Section 6.4 and develop an exponential ESS-CLF for it. Following, simulation results using this controller demonstrate the main results of this chapter:

- (i) a class of model-dependent controllers that reduce the effect of estimation uncertainty,

- (ii) establishing stability to a set for the hybrid periodic orbits of the zero dynamics in the full-order dynamics in the presence of force estimation uncertainty, and
- (iii) development of a hardware implementable form of a controller that reduces estimation uncertainty for a robotic system.

6.2 ISS and Estimate to State Stability

Estimate to State Stability. Consider the general affine control system (3.1) with an additional dynamics component $F(x)$ that can be estimated and is projected into the control system through a function $g_F(x)$,

$$\dot{x} = f(x) + g(x)u + g_F(x)F(x). \quad (6.1)$$

To construct a stabilizing controller u for this system, we define a continuously differentiable function $V : \mathbb{R}^n \rightarrow \mathbb{R}_{\geq 0}$ as an *exponentially stabilizing CLF* for the system (3.1):

$$\begin{aligned} c_1 \|x\|^2 &\leq V(x) \leq c_2 \|x\|^2 \\ \inf_{u \in \mathbb{R}^m} [L_f V(x) + L_g V(x)u + L_{g_F} V(x)F] &\leq -c_3 V(x), \end{aligned}$$

where $c_1, c_2, c_3 > 0$ are constants. This CLF yields the class of exponentially stabilizing controllers,

$$K(x) \triangleq \{u \in \mathbb{R}^m : \dot{V}(x, u) \leq -c_3 V(x)\}.$$

Any controller in this set, $u = k(x) \in K(x)$, is a state-feedback controller that exponentially stabilizes (6.1).

This controller relies on true knowledge of $F(x)$. Consider the case where we only have an estimate available, \hat{F} , our estimated model becomes,

$$\dot{x} = f(x) + g(x)u + g_F(x)\hat{F},$$

where \hat{F} is a time-varying signal given as input to our estimated dynamics. We denote the error between the true dynamics $F(x)$ and estimated dynamics \hat{F} as $\Delta F := F(x) - \hat{F}$. If we construct a controller \hat{u} that satisfies the following,

$$L_f V(x) + L_g V(x)\hat{u} + L_{g_F} V(x)\hat{F} \leq -c_3 V(x),$$

\hat{u} may not exponentially stabilize (6.1), i.e. $\hat{u} \notin K(x)$, but we may be exponentially stable to a region around the origin bounded by $\|\Delta F\|_\infty$. This motivates the following definition.

Definition 8: The system (6.1) is **exponential estimate-to-state stable** (*e-ESS*) with respect to the estimate \hat{F} if there exists $\beta \in \mathcal{KL}_\infty$, $\iota \in K_\infty$, and constant $c > 0$ such that,

$$\|x(t, x_0)\| \leq \beta(\|x_0\|, t)e^{-ct} + \iota(\|\Delta F\|_\infty), \quad \forall x_0, \forall t \geq 0. \quad (6.2)$$

We propose a Lyapunov function to certify e-ESS of (6.1).

Definition 9: The continuously differentiable function $V : \mathbb{R}^n \rightarrow \mathbb{R}_{\geq 0}$ is an **exponential estimate-to-state stabilizing Lyapunov function** (*e-ESS-Lyapunov function*) for (6.1) with estimate \hat{F} for $F(x)$,

$$\begin{aligned} c_1\|x\|^2 &\leq V(x) \leq c_2\|x\|^2 \\ \|x\| \geq \iota(\|\Delta F\|_\infty) &\Rightarrow \dot{V}(x, u) \leq -c_3V(x), \end{aligned} \quad (6.3)$$

where $c_1, c_2, c_3 > 0$ are constants and $\iota \in K_\infty$.

Lemma 2: A system (6.1) with estimate \hat{F} for $F(x)$ that admits an *e-ESS-Lyapunov function* is *e-ESS*.

The proof follows the ISS-Lyapunov proof of [251].

Definition 10: The continuously differentiable function $V : \mathbb{R}^n \rightarrow \mathbb{R}_{\geq 0}$ is an **exponential estimate-to-state stabilizing CLF** (*e-ESS-CLF*) for (6.1) with estimate \hat{F} for $F(x)$,

$$\begin{aligned} c_1\|x\|^2 &\leq V(x) \leq c_2\|x\|^2 \\ \|x\| \geq \iota(\|\Delta F\|_\infty) &\Rightarrow \\ \inf_{u \in \mathbb{R}^m} [L_f V(x) + L_g V(x)u + L_{g_F} V(x)\hat{F}] &\leq -c_3V(x), \end{aligned} \quad (6.4)$$

where $c_1, c_2, c_3 > 0$ are constants.

An e-ESS-CLF yields convergence to a set around the origin, dependent on the estimation error ΔF . To reduce this set size, we propose the following e-ESS-CLF, inspired by the e-ISS-CLF of [271].

Theorem 5: The continuously differentiable function $V_{\bar{\varepsilon}} : \mathbb{R}^n \rightarrow \mathbb{R}_{\geq 0}$ defined for constants $c_{1,\bar{\varepsilon}}, c_{2,\bar{\varepsilon}}, c_{3,\bar{\varepsilon}} > 0$,

$$\begin{aligned} c_{1,\bar{\varepsilon}}\|x\|^2 &\leq V(x) \leq c_{2,\bar{\varepsilon}}\|x\|^2 \\ \inf_{u \in \mathbb{R}^m} [L_f V(x) + L_g V(x)u + L_{g_F} V(x)\hat{F}] &\leq -c_{3,\bar{\varepsilon}}V(x) - \frac{1}{\bar{\varepsilon}}L_{g_F} V(x)L_{g_F} V(x)^T, \end{aligned} \quad (6.5)$$

is an ϵ -ESS-CLF of (6.1) $\forall \bar{\epsilon} > 0$, and a control input u in the class,

$$K^\epsilon(x) = \{u \in \mathbb{R}^m : L_f V(x) + L_g V(x)u L_{g_F} V(x) \hat{F} \leq -c_3 V(x) - \frac{1}{\bar{\epsilon}} L_{g_F} V(x) L_{g_F} V(x)^T\}, \quad (6.6)$$

converges to a set proportional to $\sqrt{\bar{\epsilon}}$ such that decreasing $\bar{\epsilon}$ decreases the set size.

Proof: Since $L_{g_F} V(x) \in \mathbb{R}^{1 \times m}$, $L_{g_F} V L_{g_F} V^T = |L_{g_F} V|^2 \geq 0$. Taking the derivative of $V_{\bar{\epsilon}}(x)$ along (6.1) yields,

$$\begin{aligned} \dot{V}_{\bar{\epsilon}}(x, \hat{u}) &= L_f V_{\bar{\epsilon}}(x) + L_g V_{\bar{\epsilon}}(x)u + L_{g_F} V_{\bar{\epsilon}}(x) \Delta F \\ &\leq -c_{3,\bar{\epsilon}} V_{\bar{\epsilon}}(x) - \frac{1}{\bar{\epsilon}} |L_{g_F} V_{\bar{\epsilon}}(x)|^2 + L_{g_F} V_{\bar{\epsilon}}(x) \Delta F \\ &\leq -c_{3,\bar{\epsilon}} V_{\bar{\epsilon}}(x) - \left(\frac{1}{\sqrt{\bar{\epsilon}}} |L_{g_F} V_{\bar{\epsilon}}(x)| - \frac{\sqrt{\bar{\epsilon}} \|\Delta F\|_\infty}{2} \right)^2 + \frac{\bar{\epsilon} \|\Delta F\|_\infty^2}{4} \\ &= -c_{3,\bar{\epsilon}} \lambda_{\bar{\epsilon}} V_{\bar{\epsilon}}(x) - c_{3,\bar{\epsilon}} (1 - \lambda_{\bar{\epsilon}}) V_{\bar{\epsilon}}(x) + \frac{\bar{\epsilon} \|\Delta F\|_\infty^2}{4}, \end{aligned}$$

with $\lambda_{\bar{\epsilon}} \in (0, 1)$. Setting $-c_{3,\bar{\epsilon}} (1 - \lambda_{\bar{\epsilon}}) V(x) + \frac{\bar{\epsilon} \|\Delta F\|_\infty^2}{4} \leq 0$, yields exponential convergence $\dot{V}_{\bar{\epsilon}}(x, \hat{u}) \leq -c_{3,\bar{\epsilon}} \lambda_{\bar{\epsilon}} V_{\bar{\epsilon}}(x)$ for,

$$\|x\| \geq \frac{1}{2} \sqrt{\frac{\bar{\epsilon}}{c_2 c_3 (1 - \lambda_{\bar{\epsilon}})}} \|\Delta F\|_\infty. \quad (6.7)$$

This takes the form of (6.4) and the set size can be decreased by choosing a smaller $\bar{\epsilon}$. \square

This result is important in the context of prosthesis control because the force between a human and prosthesis is a function of both of their states, meaning the prosthesis cannot determine this force on its own. For model-dependent prosthesis control, the prosthesis must measure or estimate this interaction force. We utilize these ϵ -ESS constructions in the rest of the chapter to guarantee exponential stability to a bounded region for the prosthesis when the controller includes force estimation error.

6.3 ISS and ESS Hybrid Control Systems

To model an amputee-prosthesis system, we employ a hybrid control system. From the prosthesis' perspective, the human is uncontrollable, hence we consider the zero dynamics in our hybrid system to represent the human. Since the human expects a certain control action from the prosthesis, when the prosthesis control law is based on estimated dynamics, its deviation from the nominal acts as a disturbance to the human. We show there exists conditions such that the human is ϵ -ISS to these input

disturbances. Because of the discrete dynamics, these conditions are only defined locally, so we additionally show the prosthesis stays within this bounded region.

Hybrid Control Systems

Consider a hybrid control system,

$$\mathcal{H}\mathcal{C}_{\bar{\eta}\bar{z}} = \begin{cases} \dot{\bar{\eta}} = \bar{f}(\bar{\eta}, \bar{z}) + \bar{g}(\bar{\eta}, \bar{z})\bar{u} + \bar{g}_F(\bar{\eta}, \bar{z})F(\bar{\eta}, \bar{z}) \\ \dot{\bar{z}} = \bar{\Psi}(\bar{\eta}, \bar{z}) + \bar{\Psi}_d(\bar{\eta}, \bar{z})d_{\bar{z}} \\ \bar{\eta}^+ = \Delta_{\bar{N}}(\bar{\eta}^-, \bar{z}^-) \\ \bar{z}^+ = \Delta_{\bar{Z}}(\bar{\eta}^-, \bar{z}^-) \end{cases} \begin{array}{l} \text{if } \Phi^{-1}(\bar{\eta}, \bar{z}) \in \bar{\mathcal{D}} \setminus \bar{\mathcal{S}} \\ \\ \\ \text{if } \Phi^{-1}(\bar{\eta}^-, \bar{z}^-) \in \bar{\mathcal{S}}, \end{array} \quad (6.8)$$

where $\bar{\eta} \in \bar{\mathcal{N}} \subset \mathbb{R}^{\bar{n}}$ are controlled (output) states, $\bar{z} \in \bar{\mathcal{Z}} \subset \mathbb{R}^{\bar{n}_z}$ uncontrolled states, $\bar{U} \subset \mathbb{R}^{\bar{m}}$ is a set of admissible control inputs for \bar{u} , and $d_{\bar{z}} \in \mathbb{R}^{n_d}$ is an input disturbance in the uncontrolled dynamics. The functions \bar{f} , \bar{g} , \bar{g}_F , F , $\bar{\Psi}$, $\bar{\Psi}_d$, $\Delta_{\bar{N}}$, and $\Delta_{\bar{Z}}$ are locally Lipschitz in their arguments. There exists a constant $c_{\bar{\Psi}_d} > 0$ such that $\|\bar{\Psi}_d(0, \bar{z})\| \leq c_{\bar{\Psi}_d}$, $\forall \bar{z} \in \bar{\mathcal{Z}}$. The domain $\bar{\mathcal{D}}$ is a closed subset of $\bar{\mathcal{N}} \times \bar{\mathcal{Z}}$, the guard or switching surface $\bar{\mathcal{S}} \subset \bar{\mathcal{D}}$ is a co-dimension one submanifold of $\bar{\mathcal{D}}$, respectively defined as

$$\begin{aligned} \bar{\mathcal{D}} &= \{(\bar{\eta}, \bar{z}) \in \bar{\mathcal{N}} \times \bar{\mathcal{Z}} : \bar{\ell}(\bar{\eta}, \bar{z}) \geq 0\}, \\ \bar{\mathcal{S}} &= \{(\bar{\eta}, \bar{z}) \in \bar{\mathcal{N}} \times \bar{\mathcal{Z}} : \bar{\ell}(\bar{\eta}, \bar{z}) = 0, \dot{\bar{\ell}}(\bar{\eta}, \bar{z}) < 0\}, \end{aligned} \quad (6.9)$$

where the continuously differentiable function $\bar{\ell} : \bar{\mathcal{N}} \times \bar{\mathcal{Z}} \rightarrow \mathbb{R}$ yields $L_{\bar{g}}\bar{\ell} = L_{\bar{g}_d}\bar{\ell} = 0$. We assume $\bar{f}(0, \bar{z}) = \bar{g}(0, \bar{z}) = \bar{g}_F(0, \bar{z}) = \Delta_{\bar{N}}(0, \bar{z}) = 0$ such that the surface $\bar{\mathcal{Z}}$ defined by $\bar{\eta} = 0$ with $d_{\bar{z}} = 0$, $\dot{\bar{z}} = \bar{\Psi}(0, \bar{z})$, is invariant for the continuous and discrete dynamics. The hybrid system for the hybrid zero dynamics is,

$$\mathcal{H}|_{\bar{\mathcal{Z}}} = \begin{cases} \dot{\bar{z}} = \bar{\Psi}(0, \bar{z}) & \text{if } \bar{z} \in \bar{\mathcal{Z}} \setminus (\bar{\mathcal{S}} \cap \bar{\mathcal{Z}}) \\ \bar{z}^+ = \Delta_{\bar{Z}}(0, \bar{z}^-) & \text{if } \bar{z}^- \in \bar{\mathcal{S}} \cap \bar{\mathcal{Z}}. \end{cases} \quad (6.10)$$

RES-CLFs. As discussed in 3.1 a RES-CLF, developed in [199], guarantees stability of a hybrid periodic orbit of the zero dynamics in the full-order dynamics. For the continuous output dynamics of (6.8), the continuously differentiable function $V_\varepsilon : \mathbb{R}^{\bar{n}} \rightarrow \mathbb{R}_{\geq 0}$ with constants $c_1, c_2, c_3 > 0$ is a RES-CLF, such that for all $0 < \varepsilon < 1$ and $(\bar{\eta}, \bar{z}) \in \bar{\mathcal{N}} \times \bar{\mathcal{Z}}$,

$$\begin{aligned} c_1 \|\bar{\eta}\|^2 &\leq V_\varepsilon(\bar{\eta}) \leq \frac{c_2}{\varepsilon^2} \|\bar{\eta}\|^2 \\ \inf_{\bar{u} \in \bar{U}} [L_{\bar{f}}V_\varepsilon(\bar{\eta}, \bar{z}) + L_{\bar{g}}V_\varepsilon(\bar{\eta}, \bar{z})\bar{u} + L_{\bar{g}_F}V_\varepsilon(\bar{\eta}, \bar{z})] &\leq \frac{c_3}{\varepsilon} V_\varepsilon(\bar{\eta}). \end{aligned} \quad (6.11)$$

The following set contains all control inputs that satisfy (6.11),

$$K_\varepsilon(\bar{\eta}, \bar{z}) = \{\bar{u} \in \bar{U} : L_{\bar{f}}V_\varepsilon(\bar{\eta}, \bar{z}) + L_{\bar{g}}V_\varepsilon(\bar{\eta}, \bar{z})\bar{u} + L_{\bar{g}_F}V_\varepsilon(\bar{\eta}, \bar{z}) \leq -\frac{c_3}{\varepsilon}V_\varepsilon(\bar{\eta})\}.$$

Note while this formulation appears slightly different from that proposed in [199] which did not have $\bar{g}_F(\bar{\eta}, \bar{z})F(\bar{\eta}, \bar{z})$ in the system dynamics, we can equivalently write the formulation given here with $\tilde{f}(\bar{\eta}, \bar{z}) := \bar{f}(\bar{\eta}, \bar{z}) + \bar{g}_F(\bar{\eta}, \bar{z})F(\bar{\eta}, \bar{z})$, resulting in the same form as in [199].

A $\bar{u}_\varepsilon(\bar{\eta}, \bar{z}) \in K_\varepsilon(\bar{\eta}, \bar{z})$ for all $(\bar{\eta}, \bar{z}) \in \bar{\mathcal{N}} \times \bar{\mathcal{Z}}$, with zero disturbance input ($d_{\bar{z}} = 0$), gives the closed-loop hybrid system of (6.8):

$$\mathcal{H}_{\bar{\eta}\bar{z}, \varepsilon} = \begin{cases} \begin{cases} \dot{\bar{\eta}} = \tilde{f}(\bar{\eta}, \bar{z}) + \bar{g}(\bar{\eta}, \bar{z})\bar{u}_\varepsilon(\bar{\eta}, \bar{z}) + \bar{g}_F(\bar{\eta}, \bar{z})F(\bar{\eta}, \bar{z}) \\ \dot{\bar{z}} = \bar{\Psi}(\bar{\eta}, \bar{z}) \end{cases} & \text{if } \Phi^{-1}(\bar{\eta}, \bar{z}) \in \bar{\mathcal{D}} \setminus \bar{\mathcal{S}} \\ \begin{cases} \bar{\eta}^+ = \Delta_{\bar{\mathcal{N}}}(\bar{\eta}^-, \bar{z}^-) \\ \bar{z}^+ = \Delta_{\bar{\mathcal{Z}}}(\bar{\eta}^-, \bar{z}^-) \end{cases} & \text{if } \Phi^{-1}(\bar{\eta}^-, \bar{z}^-) \in \bar{\mathcal{S}}. \end{cases} \quad (6.12)$$

Re-ESS-CLF. We assumed we have a RES-CLF controller \bar{u}_ε acting on our controllable dynamics. However we cannot perfectly determine a $\bar{u} \in K_\varepsilon(\bar{\eta}, \bar{z})$ when we only have access to \hat{F} and not $F(\bar{\eta}, \bar{z})$. Hence, we employ the e-ESS constructions of Section 6.2 to construct a *rapidly exponentially estimate-to-state stabilizing CLF* (Re-ESS-CLF).

Corollary 1: *The continuously differentiable function $V_{\varepsilon, \bar{\varepsilon}} : \mathbb{R}^{\bar{n}} \rightarrow \mathbb{R}_{\geq 0}$ defined for constants $c_1, c_2, c_3 > 0$,*

$$\begin{aligned} c_1 \|\bar{\eta}\|^2 &\leq V_{\varepsilon, \bar{\varepsilon}}(\bar{\eta}) \leq \frac{c_2}{\varepsilon^2} \|\bar{\eta}\|^2 \\ \inf_{\bar{u} \in \mathbb{R}^{\bar{m}}} [L_{\bar{f}}V_{\varepsilon, \bar{\varepsilon}}(\bar{\eta}, \bar{z}) + L_{\bar{g}}V_{\varepsilon, \bar{\varepsilon}}(\bar{\eta}, \bar{z})\bar{u} + L_{\bar{g}_F}V_{\varepsilon, \bar{\varepsilon}}(\bar{\eta}, \bar{z})\hat{F}] & \quad (6.13) \\ &\leq -\frac{c_3}{\varepsilon}V_{\varepsilon, \bar{\varepsilon}}(\bar{\eta}) - \frac{1}{\bar{\varepsilon}}L_{\bar{g}_F}V_{\varepsilon, \bar{\varepsilon}}(\bar{\eta}, \bar{z})L_{\bar{g}_F}VV_{\varepsilon, \bar{\varepsilon}}(\bar{\eta}, \bar{z})^T, \end{aligned}$$

is Re-ESS-CLF of the continuous $\bar{\eta}$ dynamics of (6.8), and a control input \bar{u} in the class,

$$\begin{aligned} K_{\varepsilon, \bar{\varepsilon}}(\bar{\eta}, \bar{z}, \hat{F}) &= \{\bar{u} \in \mathbb{R}^{\bar{m}} : L_{\bar{f}}V_{\varepsilon, \bar{\varepsilon}}(\bar{\eta}, \bar{z}) + L_{\bar{g}}V_{\varepsilon, \bar{\varepsilon}}(\bar{\eta}, \bar{z})\bar{u} \\ &+ L_{\bar{g}_F}V_{\varepsilon, \bar{\varepsilon}}(\bar{\eta}, \bar{z})\hat{F} \leq -\frac{c_3}{\varepsilon}V_{\varepsilon, \bar{\varepsilon}}(\bar{\eta}, \bar{z}) - \frac{1}{\bar{\varepsilon}}L_{\bar{g}_F}V_{\varepsilon, \bar{\varepsilon}}(\bar{\eta}, \bar{z})L_{\bar{g}_F}V_{\varepsilon, \bar{\varepsilon}}(\bar{\eta}, \bar{z})^T\}, \end{aligned} \quad (6.14)$$

converges to a set proportional to $\sqrt{\bar{\varepsilon}}$ such that decreasing $\bar{\varepsilon}$ decreases the set size $\bar{\eta}$ converges to.

Proof: The first part of the proof is similar to that of Theorem 5 resulting in $\dot{V}_{\varepsilon, \bar{\varepsilon}}(\bar{\eta}, \bar{z}, \bar{u}) \leq -\frac{c_3}{\varepsilon} V_{\varepsilon, \bar{\varepsilon}}(\bar{\eta})$ for,

$$\|\bar{\eta}\| \geq \frac{\varepsilon}{2} \sqrt{\frac{\bar{\varepsilon}\varepsilon}{c_2 c_3 (1-\lambda)}} \|\Delta F\|_{\infty} := \delta_{\bar{\eta}}(\varepsilon, \bar{\varepsilon}) \|\Delta F\|_{\infty}, \quad (6.15)$$

with $\lambda \in (0, 1)$ and constant $\delta_{\bar{\eta}} > 0$, dependent on $\varepsilon, \bar{\varepsilon}$. \square

We give the convergence rate of $\bar{\eta}$ for future use,

$$\|\bar{\eta}\| \leq \frac{1}{\varepsilon} \sqrt{\frac{c_2}{c_1}} e^{-\frac{c_3}{2\varepsilon} \lambda t} \|\bar{\eta}(0)\|. \quad (6.16)$$

Note, to have exponential stability closer to the origin, we can decrease $\delta_{\bar{\eta}}$ in (6.15) by decreasing $\bar{\varepsilon}$ without affecting the convergence rate here.

Periodic Orbits. Let the periodic flow of the continuous dynamics of (6.12) be $\varphi_t(\bar{\eta}, \bar{z})$. We assume the fixed point $(\bar{\eta}^*, \bar{z}^*)$ is in the switching surface, $(\bar{\eta}^*, \bar{z}^*) \in \bar{S}$. We consider the flow φ_t to be hybrid periodic with period $T > 0$ if $\varphi_T(\Delta(\bar{\eta}^*, \bar{z}^*)) = (\bar{\eta}^*, \bar{z}^*)$, with $\Delta_{\bar{\eta}\bar{z}}(\bar{\eta}, \bar{z}) = (\Delta_{\bar{N}}(\bar{\eta}, \bar{z}), \Delta_{\bar{Z}}(\bar{\eta}, \bar{z}))$. Let \mathcal{O} be the associated periodic orbit where $\mathcal{O} = \{\varphi_t(\Delta(\bar{\eta}^*, \bar{z}^*)) : 0 \leq t \leq T\}$. Corresponding to this periodic orbit an considering \bar{S} as the Poincaré section, we have the Poincaré map $P : \bar{S} \rightarrow \bar{S}$, a partial function:

$$P(\bar{\eta}, \bar{z}) = \varphi_{T_P(\bar{\eta}, \bar{z})}(\Delta_{\bar{\eta}\bar{z}}(\bar{\eta}, \bar{z})).$$

Here the time-to-impact function $T_P : \bar{S} \rightarrow \bar{\mathcal{D}}$ is,

$$T_P(\bar{\eta}, \bar{z}) = \inf\{t \geq 0 : \varphi_t(\Delta_{\bar{\eta}\bar{z}}(\bar{\eta}, \bar{z})) \in \bar{S}\}.$$

By the implicit function theorem, this function T_P is well-defined in a neighborhood of $(\bar{\eta}^*, \bar{z}^*)$ [199] and hence $T_P(\bar{\eta}^*, \bar{z}^*) = T$ and $P(\bar{\eta}^*, \bar{z}^*) = (\bar{\eta}^*, \bar{z}^*)$. Since $\varphi_t(\bar{\eta}, \bar{z})$ is Lipschitz continuous, so is T_P . We can divide the Poincaré map into the $\bar{\eta}$ -component $\mathcal{P}_{\bar{\eta}}$ and the \bar{z} -component $\mathcal{P}_{\bar{z}}$, i.e. $\mathcal{P} = (\mathcal{P}_{\bar{\eta}}, \mathcal{P}_{\bar{z}})$.

We similarly define the periodic flow of the continuous zero dynamics of (6.10) as φ_t^z and its corresponding hybrid periodic orbit as $\mathcal{O}_{\bar{z}}$. We call the associated Poincaré map $\rho : \bar{S} \cap \bar{Z} \rightarrow \bar{S} \cap \bar{Z}$ the restricted Poincaré map. Here this partial function is,

$$\rho(\bar{z}) = \varphi_{T_\rho(\bar{z})}^z(\Delta_{\bar{Z}}(0, \bar{z})). \quad (6.17)$$

Here $T_\rho(\bar{z})$ is the restricted time-to-impact function, defined as $T_\rho(\bar{z}) := T_P(0, \bar{z})$. The period is $T^* = T_\rho(0)$. Because we assume the zero dynamics surface \bar{Z} is

invariant, for a periodic orbit for the zero dynamics $\mathcal{O}_{\bar{z}}$ there exists a corresponding periodic orbit for the full-order dynamics, $\mathcal{O} = \iota_0(\mathcal{O}_{\bar{z}})$. Here $\iota_0 : \bar{Z} \rightarrow \bar{N} \times \bar{Z}$ is the canonical embedding $\iota_0(\bar{z}) = (0, \bar{z})$. From this we assume $\bar{x}^* = 0$ and without loss of generality we assume $\bar{z}^* = 0$ too.

We assume the norm on $\bar{N} \times \bar{Z}$ is constructed as $\|(\bar{\eta}, \bar{z})\| = \|\bar{\eta}\| + \|\bar{z}\|$ without losing generality. Then the distance from a periodic orbit \mathcal{O} to a point $(\bar{\eta}, \bar{z})$ is,

$$\begin{aligned} \|(\bar{\eta}, \bar{z})\|_{\mathcal{O}} &= \inf_{(x', \bar{z}') \in \mathcal{O}} \|(\bar{\eta}, \bar{z}) - (x', \bar{z}')\| \\ &= \inf_{\bar{z}' \in \mathcal{O}_{\bar{Z}}} \|\bar{z} - \bar{z}'\| + \|x - 0\| = \|\bar{z}\|_{\mathcal{O}_{\bar{Z}}} + \|\bar{\eta}\|. \end{aligned}$$

Zero Dynamics Lyapunov Function. To establish e-ISS of the full hybrid system (6.12), we construct a Lyapunov function for the stable hybrid periodic orbit $\mathcal{O}_{\bar{z}}$ of the zero dynamics. By [272], since $\mathcal{O}_{\bar{z}}$ is exponentially stable, there exists a Lyapunov function $V_{\bar{z}} : \bar{Z} \rightarrow \mathbb{R}_{\geq 0}$ for a neighborhood $\setminus B_r(\mathcal{O}_{\bar{z}})$ with $r > 0$ of $\mathcal{O}_{\bar{z}}$ such that,

$$c_{1,\bar{z}} \|\bar{z}\|_{\mathcal{O}_{\bar{Z}}}^2 \leq V_{\bar{z}}(\bar{z}) \leq c_{2,\bar{z}} \|\bar{z}\|_{\mathcal{O}_{\bar{Z}}}^2 \quad (6.18)$$

$$\frac{\partial V_{\bar{z}}}{\partial \bar{z}} \bar{\Psi}(0, \bar{z}) \leq -c_{3,\bar{z}} \|\bar{z}\|_{\mathcal{O}_{\bar{Z}}}^2 \quad (6.19)$$

$$\left\| \frac{\partial V_{\bar{z}}}{\partial \bar{z}} \right\| \leq c_{4,\bar{z}} \|\bar{z}\|_{\mathcal{O}_{\bar{Z}}}, \quad (6.20)$$

with constants $c_{1,\bar{z}}, c_{2,\bar{z}}, c_{3,\bar{z}}, c_{4,\bar{z}} > 0$. Since $\bar{\Psi}_d(0, \bar{z})$ is upper bounded by c_{Ψ_d} , then with a disturbance $d_{\bar{z}}$, our system has an e-ISS-Lyapunov function,

$$\begin{aligned} &\frac{\partial V_{\bar{z}}}{\partial \bar{z}} (\bar{\Psi}(0, \bar{z}) + \bar{\Psi}_d(0, \bar{z}) d_{\bar{z}}) \\ &\leq -c_{3,\bar{z}} \|\bar{z}\|_{\mathcal{O}_{\bar{Z}}}^2 + \frac{\partial V_{\bar{z}}}{\partial \bar{z}} \bar{\Psi}_d(0, \bar{z}) d_{\bar{z}} \\ &\leq -c_{3,\bar{z}} \|\bar{z}\|_{\mathcal{O}_{\bar{Z}}}^2 + c_{4,\bar{z}} \|\bar{z}\|_{\mathcal{O}_{\bar{Z}}} c_{\bar{\Psi}_d} \|d_{\bar{z}}\|_{\infty}. \end{aligned}$$

Similarly to Theorem 5, we use $\lambda_{\bar{z}} \in (0, 1)$ to establish exponential convergence at a rate $-\frac{c_{3,\bar{z}}}{2} \lambda_{\bar{z}}$ for,

$$\|\bar{z}\|_{\mathcal{O}_{\bar{Z}}} \geq \frac{c_{4,\bar{z}} c_{\bar{\Psi}_d}}{c_{3,\bar{z}} (1 - \lambda_{\bar{z}})} \|d_{\bar{z}}\|_{\infty} := \delta_{\bar{z}} \|d_{\bar{z}}\|_{\infty}. \quad (6.21)$$

Main Result

We now establish the main system result of the chapter: guaranteeing e-ISS of the hybrid periodic orbit of the zero dynamics $\mathcal{O}_{\bar{z}}$ with our Re-ESS-CLF of (6.13). To

establish bounds on the Poincaré maps and their time-to-impact functions, we give a proof sketch for a lemma due to space constraints. A similar proof can be found in Lemma 1 of [199] and Lemma 2 of [270]. Following, a theorem proves the main result. The basic method for the proof follows closely to that of Theorem 2 of [199] and Theorem 2 of [270]. These proofs are unique since they are developed for the hybrid system (6.8) which has a disturbance $d_{\bar{z}}$ with input matrix $\bar{\Psi}_d(\bar{\eta}, \bar{z})$ in the zero dynamics and whose control input \bar{u} may not be a RES-CLF controller in $K_\varepsilon(\bar{\eta}, \bar{z})$ but rather depends on force estimate \hat{F} . We highlight where the differences for our system come into these proofs.

Lemma 3: *Given the hybrid system (6.8) with input disturbance and $d_{\bar{z}}$, control input $\bar{u}(\bar{\eta}, \bar{z}) \in K_{\varepsilon, \bar{\varepsilon}}(\bar{\eta}, \bar{z}, \hat{F})$ (6.14), and periodic orbit $\mathcal{O}_{\bar{z}}$ of the hybrid zero dynamics $\mathcal{H}|_{\bar{z}}$ (6.10) transverse to $\bar{S} \cap \bar{Z}$, for $r > 0$ such that $(\bar{\eta}, \bar{z}) \in \setminus B_r(0, 0)$, and $\|\bar{\eta}\| \geq \delta_{\bar{\eta}}(\varepsilon, \bar{\varepsilon})\|\Delta F\|_\infty$ (6.15), there exists finite constants $A_{T\bar{\eta}}, A_{Td_{\bar{z}}}, A_{P\bar{\eta}}, A_{Pd_{\bar{z}}} > 0$ such that,*

$$\|T_P(\bar{\eta}, \bar{z}) - T_\rho(\bar{z})\| \leq A_{T\bar{\eta}}\|\bar{\eta}\| + A_{Td_{\bar{z}}}\|d_{\bar{z}}\|_\infty, \quad (6.22)$$

$$\|\mathcal{P}_{\bar{z}}(\bar{\eta}, \bar{z}) - \rho(\bar{z})\| \leq A_{P\bar{\eta}}\|\bar{\eta}\| + A_{Pd_{\bar{z}}}\|d_{\bar{z}}\|_\infty. \quad (6.23)$$

Proof Sketch: We construct an auxiliary time-to-impact function, T_B , to relate to both T_ρ and T_P , such that we can then relate T_ρ to T_P . The difference between T_B and T_ρ is bounded by a Lipschitz constant. Bounds of T_P are found which are valid for $(\bar{\eta}, \bar{z}) \in \setminus B_r(0, 0)$. For a given solution, $T_B = T_P$ because these are locally unique solutions in \bar{S} . To bound a solution $x(t)$ of $\varphi_t(\Delta(\bar{\eta}, \bar{z}))$, the initial condition is bounded with the Lipschitz constant of $\Delta_{\bar{N}}$ which is used in the bound of (6.16) with the T_P bounds and $\|\bar{\eta}\|$. Note this bound only holds for $\|\bar{\eta}\| \geq \delta_{\bar{\eta}}\|\Delta F\|_\infty$, a specific element of this proof. Using a Gronwall-Bellman argument similar to that in [199], we bound the difference between a solution $\bar{z}(t)$ for the full-order dynamics and zero dynamics. This bound again includes $\|\bar{\eta}\|$ as well as $\|d_{\bar{z}}\|_\infty$, another unique element of this proof. Grouping terms gives (6.22). Using the maximum of $\bar{\Psi}(0, \bar{z}(t))$ for a given solution $\bar{z}(t)$ and (6.22), we arrive at (6.23). \square

Theorem 6: *Given the hybrid system (6.8) with input disturbance $d_{\bar{z}}$, control input $\bar{u} \in K_{\varepsilon, \bar{\varepsilon}}(\bar{\eta}, \bar{z}, \hat{F})$, and periodic orbit $\mathcal{O}_{\bar{z}}$ of the hybrid zero dynamics $\mathcal{H}|_{\bar{z}}$ (6.10) transverse to $\bar{S} \cap \bar{Z}$, for $r > 0$ such that $(\bar{\eta}, \bar{z}) \in \setminus B_r(0, 0)$, there exists $\delta > 0$ such that for all $\|d_{\bar{z}}\|_\infty < \delta$ the periodic orbit $\mathcal{O} = \iota_0(\mathcal{O}_{\bar{z}})$ is e-ISS.*

Proof: Since the ISS stability of a hybrid periodic orbit can be analyzed via its Poincaré map [269], we seek to establish e-ISS of the Poincaré map. We aim to find a Lyapunov function $V_P(\bar{\eta}, \bar{z})$ for the discrete dynamics of the Poincaré map P that satisfies this discrete-time e-ISS Lyapunov condition with $\iota \in K_\infty$:

$$\begin{aligned} V_P(\mathcal{P}(\bar{\eta}, \bar{z})) - V_P(\bar{\eta}, \bar{z}) \\ \leq -\kappa(\|\bar{\eta}\|^2 + \|\bar{z}\|^2) + \iota(\|d_{\bar{z}}\|_\infty). \end{aligned} \quad (6.24)$$

For the zero dynamics on the switching surface \bar{S} , we establish a Lyapunov function. There exists an $r_{\bar{z}} > 0$ such that $\rho : B_{r_{\bar{z}}}(0) \cap (\bar{S} \cap \bar{Z}) \rightarrow B_{r_{\bar{z}}}(0) \cap (\bar{S} \cap \bar{Z})$ is well defined for all $z \in B_{r_{\bar{z}}}(0) \cap (\bar{S} \cap \bar{Z})$ and $\bar{z}_{k+1} = \rho(\bar{z}_k)$ is locally exponentially stable. By the converse Lyapunov theorem for discrete-time systems, there exists a Lyapunov function V_ρ defined on $B_{r_{\bar{z}}}(0) \cap (\bar{S} \cap \bar{Z})$ for some $r_{\bar{z}} > \kappa_k \|d_{\bar{z}}\|_\infty$ and constants $c_{1,\rho}, c_{2,\rho}, c_{3,\rho}, c_{4,\rho} > 0$ such that,

$$\begin{aligned} c_{1,\rho} \|\bar{z}\|^2 &\leq V_\rho(\bar{z}) \leq c_{2,\rho} \|\bar{z}\|^2 \\ V_\rho(\rho(\bar{z})) - V_\rho(\bar{z}) &\leq -c_{3,\rho} \|\bar{z}\|^2 \\ |V_\rho(\bar{z}) - V_\rho(\bar{z}')| &\leq c_{4,\rho} \|\bar{z} - \bar{z}'\| (\|\bar{z}\| + \|\bar{z}'\|). \end{aligned}$$

To obtain a Lyapunov function for the $\bar{\eta}$ dynamics in \bar{S} , we define our Re-ISS-CLF $V_{\varepsilon, \bar{\varepsilon}}$ restricted to the switching surface by, $V_{\varepsilon, \bar{\varepsilon}}^{\bar{S}}(\bar{\eta}) := V_{\varepsilon, \bar{\varepsilon}}|_{\bar{S}}(\bar{\eta})$. We define a composite Lyapunov function on $\setminus B_r(0, 0) \cap \bar{S}$,

$$V_P(\bar{\eta}, \bar{z}) = V_\rho(\bar{z}) + \sigma V_{\varepsilon, \bar{\varepsilon}}^{\bar{S}}(\bar{\eta}),$$

with constant $\sigma > 0$, which we define later, lower bound $\min\{c_{1,\rho}, \sigma c_1\} \|(\bar{\eta}, \bar{z})\|^2$, and upper bound $\max\{c_{2,\rho}, \sigma \frac{c_2}{\varepsilon^2}\} \|(\bar{\eta}, \bar{z})\|^2$. To satisfy (6.24), we first establish,

$$\begin{aligned} V_\rho(\mathcal{P}_{\bar{z}}(\bar{\eta}, \bar{z})) - V_\rho(\bar{z}) \\ = V_\rho(\mathcal{P}_{\bar{z}}(\bar{\eta}, \bar{z}) - \rho(\bar{z})) + V_\rho(\rho(\bar{z})) - V_\rho(\bar{z}) \\ \leq c_{4,\rho} \|\mathcal{P}_{\bar{z}}(\bar{\eta}, \bar{z}) - \rho(\bar{z})\| (\|\mathcal{P}_{\bar{z}}(\bar{\eta}, \bar{z})\| \\ + \|\rho(\bar{z})\|) - c_{3,\rho} \|\bar{z}\|^2. \end{aligned} \quad (6.25)$$

Using (6.23) and the Lipschitz constant L_ρ of $\rho(\bar{z})$, (6.17), gives,

$$\begin{aligned} \|\mathcal{P}_{\bar{z}}(\bar{\eta}, \bar{z})\| &= \|\mathcal{P}_{\bar{z}}(\bar{\eta}, \bar{z}) - \rho(\bar{z}) + \rho(\bar{z}) - \rho(0)\| \\ &\leq A_{P\bar{\eta}} \|\bar{\eta}\| + A_{Pd_{\bar{z}}} \|d_{\bar{z}}\|_\infty + L_\rho \|\bar{z}\| \\ \|\rho(\bar{z})\| &= \|\rho(\bar{z}) - \rho(0)\| \leq L_\rho \|\bar{z}\|, \end{aligned}$$

yielding known finite bounds along with those of (6.23) for (6.25). Because (6.23) is a unique development of this work from Lemma 3, this theorem proof is unique since it uses (6.23) and carries out the following steps with it. We next establish for $\|\bar{\eta}\| \geq \delta_{\bar{\eta}} \|\Delta F\|_\infty$, a unique bound in this proof,

$$\begin{aligned} V_{\varepsilon, \bar{\varepsilon}}^{\bar{S}}(\mathcal{P}_{\bar{\eta}}(\bar{\eta}, \bar{z})) - V_{\varepsilon, \bar{\varepsilon}}^{\bar{S}}(\bar{\eta}) &\leq e^{-\frac{c_3}{\varepsilon} \lambda t} V_{\varepsilon, \bar{\varepsilon}}(\Delta_{\bar{N}}(\bar{\eta}, \bar{z})) - c_1 \|\bar{\eta}\|^2 \\ &\leq \underbrace{\left(\frac{c_2}{\varepsilon^2} L_{\Delta_{\bar{N}}}^2 e^{-\frac{c_3}{\varepsilon} \lambda c_T T^*} - c_1 \right)}_{A_{V\bar{\eta}}(\varepsilon)} \|\bar{\eta}\|^2, \end{aligned} \quad (6.26)$$

where $A_{V\bar{\eta}}$ is a constant dependent on ε . Since $A_{V\bar{\eta}}(0^+) := \lim_{\varepsilon \rightarrow 0^+} A_{V\bar{\eta}}(\varepsilon) = 0$, there exists an $\tilde{\varepsilon}$ such that $A_{V\bar{\eta}}(\varepsilon) < c_1$, $\forall 0 < \varepsilon < \tilde{\varepsilon}$ such that (6.26) is negative definite.

The discrete-time Lyapunov condition (6.24) becomes,

$$\begin{aligned} V_\rho(\mathcal{P}_{\bar{z}}(\bar{\eta}, \bar{z})) - V_\rho(\bar{z}) + \sigma(V_{\varepsilon, \bar{\varepsilon}}^{\bar{S}}(\mathcal{P}_{\bar{\eta}}(\bar{\eta}, \bar{z})) - V_{\varepsilon, \bar{\varepsilon}}^{\bar{S}}(\bar{\eta})) &\leq c_{4,\rho}(A_{P\bar{\eta}}\|\bar{\eta}\| + A_{Pd_{\bar{z}}}\|d_{\bar{z}}\|_\infty)(A_{P\bar{\eta}}\|\bar{\eta}\| + A_{Pd_{\bar{z}}}\|d_{\bar{z}}\|_\infty \\ &\quad + 2L_\rho\|\bar{z}\|) - c_{3,\rho}\|\bar{z}\|^2 + \sigma(A_{V\bar{\eta}}(\varepsilon) - c_1)\|\bar{\eta}\|^2 \\ &= - \left[\|\bar{\eta}\| \quad \|\bar{z}\| \right] \Lambda(\varepsilon) \begin{bmatrix} \|\bar{\eta}\| \\ \|\bar{z}\| \end{bmatrix} + A_{Pd_{\bar{z}}}^2 \|d_{\bar{z}}\|_\infty^2 \\ &\quad + 2c_{4,\rho} A_{P\bar{\eta}} A_{Pd_{\bar{z}}} \|\bar{\eta}\| \|d_{\bar{z}}\|_\infty + 2A_{Pd_{\bar{z}}} L_\rho \|\bar{z}\| \|d_{\bar{z}}\|_\infty, \end{aligned}$$

where,

$$\Lambda(\varepsilon) = \begin{bmatrix} -c_{4,\rho} A_{P\bar{\eta}}^2 + \sigma(c_1 - A_{V\bar{\eta}}(\varepsilon)) & -c_{4,\rho} A_{P\bar{\eta}} L_\rho \\ -c_{4,\rho} A_{P\bar{\eta}} L_\rho & c_{3,\rho} \end{bmatrix}.$$

To yield positive definiteness of $\Lambda(\varepsilon)$, we choose $\bar{\sigma} > 0$ such that for $\sigma > \bar{\sigma}$ and $\varepsilon < \tilde{\varepsilon}$, $\det(\Lambda(\varepsilon)) > 0$:

$$\det(\Lambda(\varepsilon)) = -c_{4,\rho} A_{P\bar{\eta}}^2 + \sigma(c_1 - A_{V\bar{\eta}}(\varepsilon)) c_{3,\rho} - 2c_{4,\rho} A_{P\bar{\eta}} L_\rho.$$

We select,

$$\bar{\sigma} := \frac{c_{4,\rho} A_{P\bar{\eta}}^2 + 2c_{4,\rho} A_{P\bar{\eta}} L_\rho}{(c_1 - A_{V\bar{\eta}}(\varepsilon)) c_{3,\rho}},$$

where $\bar{\sigma} > 0$ for all $0 < \varepsilon < \tilde{\varepsilon}$. We choose $\kappa = \lambda_{\min}(\Lambda(\varepsilon))$, the minimum eigenvalue of $\Lambda(\varepsilon)$. As in Theorem 5, we again split the derivative with $\lambda_P \in (0, 1)$,

$$\begin{aligned} V_P(\mathcal{P}_{\bar{z}}(\bar{\eta}, \bar{z})) - V_P(\bar{\eta}, \bar{z}) &\leq -\lambda_{\min}(\Lambda(\varepsilon)) \lambda_P \|(\bar{\eta}, \bar{z})\|^2 - \lambda_{\min}(\Lambda(\varepsilon)) (1 - \lambda_P) \|(\bar{\eta}, \bar{z})\|^2 \\ &\quad + A_{\bar{\eta}\bar{z}} \|(\bar{\eta}, \bar{z})\| \|d_{\bar{z}}\|_\infty + A_{Pd_{\bar{z}}}^2 \|d_{\bar{z}}\|_\infty^2, \end{aligned} \quad (6.27)$$

with $A_{\bar{\eta}\bar{z}} = \max\{2c_{4,\rho}A_{P\bar{\eta}}A_{Pd\bar{z}}, 2A_{Pd\bar{z}}L_\rho\}$. This satisfies the discrete time e-ISS Lyapunov condition (6.24). Setting the last 3 terms of (6.27) ≤ 0 and solving for the positive root of the resultant quadratic equation, we establish exponential convergence at a rate of $-\lambda_{\min}(\Lambda(\varepsilon))\lambda_P$ to the set,

$$\|(\bar{\eta}, \bar{z})\| \leq \frac{A_{\bar{\eta}\bar{z}} + \sqrt{A_{\bar{\eta}\bar{z}}^2 + 4\lambda_{\min}(\Lambda(\varepsilon))(1 - \lambda_P)A_{Pd\bar{z}}^2}}{2\lambda_{\min}(\Lambda(\varepsilon))(1 - \lambda_P)} \|d_{\bar{z}}\|_\infty.$$

We require this bound to be less than $r_{\bar{z}}$, yielding,

$$\delta_P := \frac{2r_{\bar{z}}\lambda_{\min}(\Lambda(\varepsilon))(1 - \lambda_P)}{A_{\bar{\eta}\bar{z}} + \sqrt{A_{\bar{\eta}\bar{z}}^2 + 4\lambda_{\min}(\Lambda(\varepsilon))(1 - \lambda_P)A_{Pd\bar{z}}^2}}.$$

To also ensure the continuous dynamics of \bar{z} remain bounded by $r_{\bar{z}}$, we require $\|d_{\bar{z}}\|_\infty < \delta := \min\{\delta_P, \frac{r_{\bar{z}}}{\delta_{\bar{z}}}\}$, unique to this proof, and hence establishing e-ISS of \mathcal{O} for $\|d_{\bar{z}}\|_\infty < \delta$. \square

6.4 ESS-ID-CLF-QP for Human-Prosthesis System

To apply these results, we use the human-prosthesis model described in 3.3, but omit the ankles for simplicity, as we did in 5.4. To connect this model to the hybrid system (6.8), we define the human remaining system states as the uncontrollable states $\bar{z} = (q_r^T, \dot{q}_r^T)^T$. We define 1 separable subsystem output (4.3) $y^s(q_s)$ to form controllable states $\bar{\eta} = (y^{sT}, \dot{y}^{sT})^T$. We solve the dynamics (4.3) and (3.23) for λ ,

$$\lambda(q, \dot{q}, u_r, u_s) = (JD^{-1}J^T)^{-1}(JD^{-1}(H - B \begin{bmatrix} u_r \\ u_s \end{bmatrix}) - J\dot{q}). \quad (6.28)$$

The human assumes a nominal control input of $u_s^{\text{nom}}(q_s, \dot{q}_s)$ for the prosthesis, while the actual control input is $u_s^{\text{act}}(q_s, \dot{q}_s)$. Using (6.28), we obtain the uncontrollable dynamics of (6.8),

$$\begin{aligned} \dot{\bar{z}} = & \underbrace{\begin{bmatrix} \dot{q}_r \\ D_r^{-1}(-H_r + B_r u_r + \begin{bmatrix} J_{c,r}^T & J_{f,h}^T & 0 \end{bmatrix} \lambda(q, \dot{q}, u_r, u_s^{\text{nom}})) \end{bmatrix}}_{\bar{\Psi}(\bar{\eta}, \bar{z})} \\ & - \underbrace{\begin{bmatrix} 0 \\ D_r^{-1} \begin{bmatrix} J_{c,r}^T & J_{f,h}^T & 0 \end{bmatrix} (JD^{-1}J^T)^{-1} JD^{-1} B \end{bmatrix}}_{\bar{\Psi}_d(\bar{\eta}, \bar{z})} \underbrace{\begin{bmatrix} 0 \\ u_s^{\text{act}} - u_s^{\text{nom}} \end{bmatrix}}_{d_{\bar{z}}}, \end{aligned} \quad (6.29)$$

where arguments q and \dot{q} are suppressed for simplicity. The difference between u_s^{act} and u_s^{nom} perturbs the uncontrollable human dynamics. With the human-prosthesis

interaction force F_f from $\lambda(q, \dot{q}, u_r, u_s^{\text{act}})$ (6.28), we obtain the controllable dynamics of (6.8),

$$\begin{aligned} \dot{\bar{\eta}} &= \underbrace{\begin{bmatrix} \frac{\partial y^s}{\partial q_s} \dot{q}_s \\ f_2(q_s, \dot{q}_s) \end{bmatrix}}_{\bar{f}(\bar{\eta}, \bar{z})} + \underbrace{\begin{bmatrix} 0 \\ g_2(q_s, \dot{q}_s) \end{bmatrix}}_{\bar{g}(\bar{\eta}, \bar{z})} \underbrace{u_s}_u + \underbrace{\begin{bmatrix} 0 \\ g_{F,2}(q_s, \dot{q}_s) \end{bmatrix}}_{\bar{g}_F(\bar{\eta}, \bar{z})} \underbrace{J_{f,s} F_f}_{F(\bar{\eta}, \bar{z})} \\ f_2 &:= \frac{\partial}{\partial q_s} \left(\frac{\partial y^s}{\partial q_s} \dot{q}_s \right) \dot{q}_s + \frac{\partial y^s}{\partial q_s} D_s^{-1} (-H_s + \lambda_{s,f}) \\ g_2 &:= \frac{\partial y^s}{\partial q_s} D_s^{-1} (B_s - J_{c,s}^T \lambda_{s,g}) \\ g_{F,2} &:= \frac{\partial y^s}{\partial q_s} D_s^{-1} (1 - J_{c,s}^T \lambda_{s,g_F}) \end{aligned} \quad (6.30)$$

where $\lambda_{s,f}$, $\lambda_{s,g}$, and λ_{s,g_F} are defined by,

$$\begin{aligned} \lambda_s(q, \dot{q}, \bar{F}, u_s) &= \underbrace{(J_{c,s} D_s^{-1} J_{c,s}^T)^{-1}}_{\mathcal{X}_p} (J_{c,s} D_s^{-1} (H_s - B_s u_s - \bar{F}) - \dot{J}_{c,s} \dot{q}_s) \\ &= \underbrace{\mathcal{X}_p (J_{c,s} D_s^{-1} H_s - \dot{J}_{c,s} \dot{q}_s)}_{\lambda_{s,f}} - \underbrace{\mathcal{X}_p J_{c,s} D_s^{-1} \bar{F}}_{\lambda_{s,g_F}} - \underbrace{\mathcal{X}_p J_{c,s} D_s^{-1} B_s u_s}_{\lambda_{s,g}}, \end{aligned}$$

where the argument \bar{F} can either be the actual projected force $J_{f,s}(q_s)F_f(q, \dot{q})$ or the estimated force \hat{F} .

For this hybrid system (3.24), two domains are considered, one for prosthesis stance, and another for prosthesis non-stance. The guard condition $\ell(\bar{\eta}, \bar{z})$ (6.9) is the height of the swing foot. The desired output trajectories are determined through the optimization (3.28) with the cost function designed to match human motion capture data. The following impact invariance constraint is enforced: $\Delta(\bar{S} \cap \bar{Z}) \subset \bar{Z}$ [195]. This satisfies our assumption for (6.8), $\bar{f}(0, \bar{z}) = \bar{g}(0, \bar{z}) = \bar{g}_F(0, \bar{z}) = \Delta_{\bar{X}}(0, \bar{z}) = 0$.

ESS-ID-CLF-QP. Since our output coordinates here, $\bar{\eta}$, are the same as our separable subsystem output coordinates, η_s , we can use our separable subsystem RES-CLF (5.3). To implement a controller of this class, we use the form of an ID-CLF-QP [37], described in 3.2. Developing this for our subsystem, we feedback linearize the separable subsystem to arrive at linearized subsystem output dynamics,

$$\dot{\bar{\eta}} = \dot{\eta}_s = F_s \eta_s + G_s \mu_s,$$

where,

$$\mu_s = \ddot{y}^s = \underbrace{\frac{\partial}{\partial q_s} \left(\frac{\partial y^s}{\partial q_s} \dot{q}_s \right)}_{J_{y^s}(q_s, \dot{q}_s)} \dot{q}_s + \underbrace{\frac{\partial y^s}{\partial q_s}}_{J_{y^s}(q_s)} \ddot{q}_s. \quad (6.31)$$

which is the bottom row of (6.30) Solving the algebraic Riccati equation gives a matrix P_s which we use with ε to form our RES-CLF: $V_\varepsilon^s = \bar{\eta}^T P_s^\varepsilon \bar{\eta}$. The CLF condition is,

$$\dot{V}_\varepsilon(\bar{\eta}, \mu_s) = L_{F_s} V_\varepsilon^s(\bar{\eta}) + L_{G_s} V_\varepsilon^s(\bar{\eta}) \mu_s \leq -\frac{1}{\varepsilon} \underbrace{\frac{\lambda_{\min}(Q_s)}{\lambda_{\max}(P_s)}}_{c_3} V(\bar{\eta}), \quad (6.32)$$

with weight matrix Q_s , $c_1 = \lambda_{\min}(P_s)$, $c_2 = \lambda_{\max}(P_s)$, $L_{F_s} V_\varepsilon^s(\bar{\eta}) = \bar{\eta} (F_s^T P_s^\varepsilon + P_s^\varepsilon F_s) \bar{\eta}$, and $L_{G_s} V_\varepsilon^s(\bar{\eta}) = 2\bar{\eta}^T P_s^\varepsilon G_s$.

The work of [37] developed an inverse dynamics CLF quadratic program (ID-CLF-QP) to solve for control inputs that satisfied a CLF condition without inverting dynamic components of the robotic system to make it computationally faster and more numerically stable to implement on hardware, as explained in Section 3.2. Using the prosthesis dynamics and constraints, output acceleration expression (6.31), and the RES-CLF condition (6.32) with an additional term to form an Re-ESS-CLF condition, we construct an *ESS-ID-CLF-QP*:

$$\begin{aligned} \Upsilon^* &= \operatorname{argmin}_{\Upsilon \in \mathbb{R}^{n_{\text{qp}}}} \left\| J_{y^s} \dot{q}_s + J_{y^s} \ddot{q}_s - \mu_s^{\text{pd}} \right\|^2 \\ &\text{s.t. } D_s \ddot{q}_s + H_s = B_s u_s + J_{c,s}^T \lambda_s + \hat{F} \\ &\quad J_{c,s} \ddot{q}_s + \dot{J}_{c,s} \dot{q}_s = 0 \\ &\quad L_{F_s} V_\varepsilon^s(\bar{\eta}) + L_{G_s} V_\varepsilon^s(\bar{\eta}) \mu_{y^s} \leq -\frac{c_3^s}{\varepsilon} V_\varepsilon^s(\bar{\eta}) - \frac{1}{\varepsilon} |L_{G_s} V_\varepsilon^s(\bar{\eta}) J_{y^s} \bar{\kappa}|^2, \end{aligned} \quad (6.33)$$

where $\Upsilon = [\ddot{q}_s^T, u_s^T, \lambda_s^T]^T$, $\mu_{y^s} = J_{y^s} \dot{q}_s + J_{y^s} \ddot{q}_s$, and $\mu_s^{\text{pd}} := K_s y^s(q_s) + K_d \dot{y}^s(q_s)$ such that the control input u is close to a feedback linearizing controller with PD gains on the outputs. Here $J_{f,s} F_f$ is replaced by an estimate \hat{F} . Here $\bar{\kappa} \geq \|\kappa(q_s)\| \forall q_s$, where,

$$\kappa(q_s) = D_s^{-1} (1 - J_{c,s}^T (J_{c,s} D_s^{-1} J_{c,s}^T)^{-1} J_{c,s} D_s^{-1}). \quad (6.34)$$

A $\bar{\kappa} \geq \|\kappa(q_s)\|$ exists since D_s is bounded [273] as well as $J_{c,s}$ since $h_{c,p}(q_s)$ are degree one functions of q_s . This bound can be determined offline such that this controller can be run online without inverting these matrices.

Theorem 7: *Given the hybrid system (6.8) with input disturbance $d_{\bar{z}}$, controllable dynamics (6.30), uncontrollable dynamics (6.29), respective impact dynamics for the robotic model, the solution $u_s^* \in \Upsilon^*$ to the ESS-ID-CLF-QP as the control input u , and periodic orbit $\mathcal{O}_{\bar{z}}$ of the hybrid zero dynamics $\mathcal{H}|_{\bar{z}}$ (6.10) transverse to $S \cap \bar{Z}$,*

for $r > 0$ such that $(\bar{\eta}, \bar{z}) \in \setminus B_r(0, 0)$, there exists $\delta > 0$ such that for all $\|d_{\bar{z}}\|_\infty < \delta$ the periodic orbit $\mathcal{O} = \iota_0(\mathcal{O}_{\bar{z}})$ is e-ISS.

Proof: The work of [274] proved the solution to the ID-CLF-QP gives a control input $u_s^* \in K_\varepsilon$. Following a similar method we show the inclusion of $\frac{1}{\varepsilon}|L_{G_s}V_\varepsilon^s(\bar{\eta})J_{y^s}\bar{\kappa}|^2$ gives a u_s^* that yields ESS. By construction, our CLF satisfies the RES-CLF conditions. By solving the prosthesis dynamics and holonomic constraint equation in the ESS-ID-CLF-QP for \ddot{q}_s and substituting this into the CLF equation,

$$\begin{aligned} L_{F_s}V_\varepsilon^s + L_{G_s}V_\varepsilon^s(\dot{J}_{y^s}\dot{q}_s + J_{y^s}(f_2 + g_2u_s + g_{F,2}\hat{F})) \\ \leq -\frac{c_3^s}{\varepsilon}V_\varepsilon^s(\bar{\eta}) - \frac{1}{\varepsilon}|L_{G_s}V_\varepsilon^s(\bar{\eta})J_{y^s}\bar{\kappa}|^2, \end{aligned}$$

we see the QP solves for u that satisfies this CLF, and $L_{g_F}V_\varepsilon(\bar{\eta}, \bar{z})\hat{F}$ of (6.13) equates to,

$$L_{g_F}V_\varepsilon^s(\bar{\eta}, \bar{z})\hat{F} = L_{G_s}V_\varepsilon^s(\bar{\eta})J_{y^s} \underbrace{D_s^{-1}(1 - J_{c,s}^T\bar{\lambda}_r^{g_F})}_{\kappa(q_s)} \hat{F}.$$

While Theorem 5 was proved using the actual value of $L_{g_F}V_\varepsilon^s$, it could just as easily be done with an upper bound of this term, such as $L_{G_s}V_\varepsilon^s(\bar{\eta})J_{y^s}\bar{\kappa}$, to show a CLF satisfying this condition yields e-ESS. Hence, the results of Theorem 6 hold, establishing e-ISS of $\mathcal{O} = \iota_0(\mathcal{O}_{\bar{z}})$. \square

Since humans are thought to exhibit limit cycles [209], i.e. periodic orbits, we assume they are stable within a neighborhood of these orbits and hence, as the zero dynamics in this system, contain e-ISS hybrid periodic orbits. Therefore, this ESS-ID-CLF-QP prosthesis controller guarantees e-ISS of the hybrid periodic orbits of the human-prosthesis system.

Simulation Results. A feedback linearizing controller enforced the human trajectories. The ESS-ID-CLF-QP (6.33) controlled the prosthesis using values of $\bar{\varepsilon} = 100, 50, 25,$ and 10 . (The holonomic constraints were included as soft constraints in the cost and a regularization term was also included in the cost to make the problem well-posed [37].) To create an estimated force \hat{F} , we multiplied $J_{f,s}^T$ with true F_f values, perturbed to emulate disturbances seen on force sensors available for AMPRO3, a pressure sensor and load cell. True F_f values from 5 ms prior emulated the time-delay on the pressure sensor. White Gaussian noise with a variance of 1 was added to this F_f to model load cell variance. To account for the load on the load cell when tared on the prosthesis, an offset is added to the force measurements.

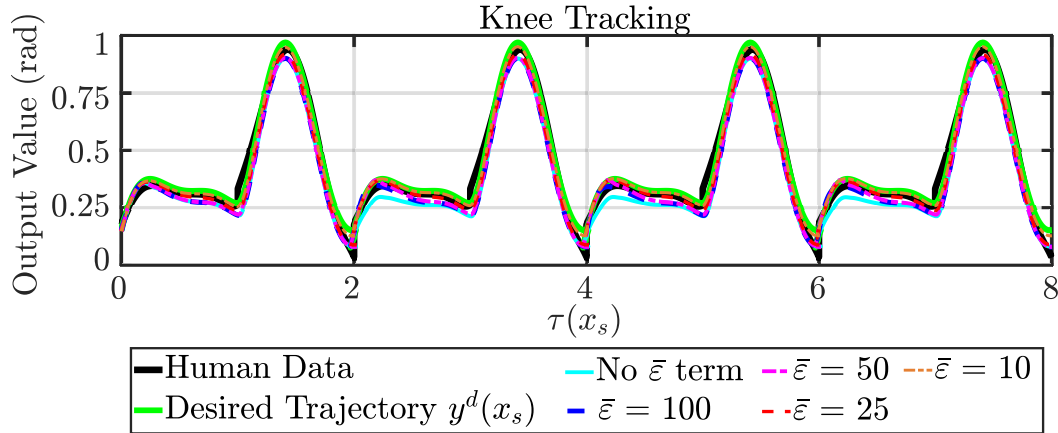


Figure 6.2: Four step cycles of prosthesis knee output tracking for ESS-ID-CLF-QP with different values of $\bar{\varepsilon}$ compared to the human data the desired trajectory was generated to match, the desired trajectory, and the output when no $\frac{1}{\bar{\varepsilon}}|L_{G_s}V_{\bar{\varepsilon}}^s(\bar{\eta})J_{y^s}\bar{k}|^2$ term is used in the CLF constraint.

Here we added an offset of -16 N, -62 N, and -5 Nm (10% of the minimum F_f seen) to F_f to test the controller's robustness to offset measurement error.

Figure 6.2 depicts the result of Theorem 5, prosthesis outputs converging closer to the desired trajectories with decreasing values of $\bar{\varepsilon}$. Figure 6.2 shows not using an $\bar{\varepsilon}$ term yields the largest tracking error, demonstrating using an e-ESS control law is advantageous. Decreasing $\bar{\varepsilon}$ comes at the cost of creating a more aggressive controller that can yield a non-smooth control input and create chatter on hardware. Figure 6.3 depicts the results of Theorem 6, e-ISS hybrid periodic orbits of the human and prosthesis system for 10 step cycles when subject to force estimation error in the controller. Using 5x the disturbance, the controller still achieved stability, demonstrating its robustness. Using 10x the disturbance led to instability, showing the controller's limitations.

6.5 Conclusion

This chapter presented the novel method of estimate-to-state stability to establish formal guarantees of stability to a set for the prosthesis in the presence of force estimation error. Further, through analysis of the Poincaré map of the hybrid periodic orbits, we established conditions for input-to-state stability of the human subject to the prosthesis' deviations from the nominal control law. These constructions formalize stability guarantees for the amputee-prosthesis system in the presence of inevitable uncertainty and disturbance. Now that we have established these

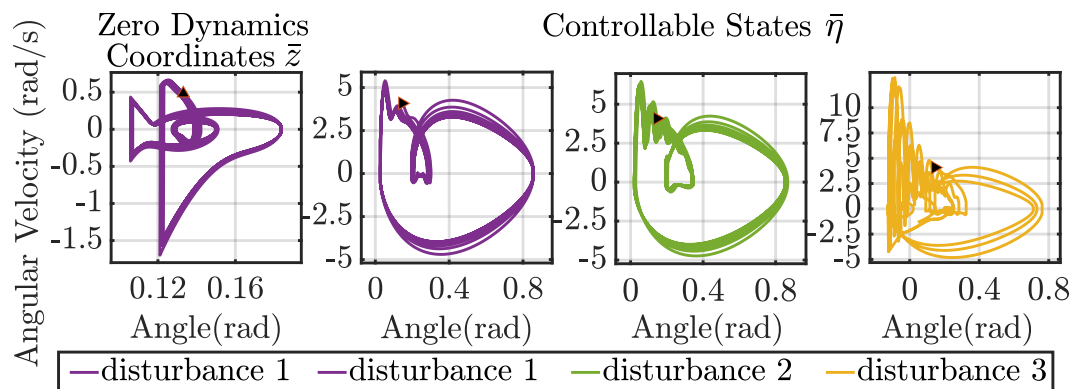


Figure 6.3: Phase portraits of unactuated human torso (left purple) and prosthesis knee (right purple) from simulation using ESS-ID-CLF-QP with $\bar{\epsilon} = 10$. (green) Prosthesis knee stability with 5x the disturbance. (yellow) Prosthesis knee instability with 10x the disturbance.

guarantees, the next chapter will implement a controller of the separable subsystem CLF class (5.2) on hardware, similar to the ID-CLF-QP in this paper (6.33), to realize the first model-based lower-limb prosthesis controller.

*Chapter 7***MODEL-BASED PROSTHESIS CONTROL REALIZATION
WITH FORCE ESTIMATION**

After developing subsystem controllers in Chapters 4 and 5 and establishing stability guarantees in the presence of force estimation error in 6, this chapter brings these theoretical constructions to hardware realization. This chapter utilizes RES-CLFs together with force estimation to construct model-based optimization-based controllers for the prosthesis. These are experimentally realized on hardware with onboard sensing and computation. This hardware demonstration has formal guarantees of stability, utilizes the natural dynamics of the system, and achieves superior tracking to other prosthesis trajectory tracking control methods.

This chapter was adapted from:

R. Gehlhar and A. D. Ames. “Model-dependent prosthesis control with interaction force estimation”. In: *2021 IEEE International Conference on Robotics and Automation (ICRA)*. IEEE, 2021, pp. 3226–3232.

7.1 Introduction

Quadratic programs (QPs) provide a means to implement a CLF constraint while optimizing a cost and provide a flexible framework to incorporate feasibility constraints such as torque bounds. CLFs in QPs have been realized in simulation in various works [208], [275]–[277], but few to date on hardware [265]. One difficulty in implementing these controllers on hardware is the typical required inversion of the inertia matrix, which is computationally expensive and prone to numerical instability. An alternative CLF-QP was developed in [37] using an inverse dynamics (ID) approach to overcome this challenge and achieved dynamic crouching behavior in experiment on a 3D underactuated compliant bipedal robot. This ID-CLF-QP provides the starting basis for developing an implementable CLF-QP on our robotic prosthesis.

While [278] applied a CLF-QP to a prosthesis, this was done in a model-independent fashion and required a feed-forward impedance control input term to overcome the limitations of the model-independent nature. Implementing a model-based prosthesis controller introduces an additional challenge: *it requires knowledge of*

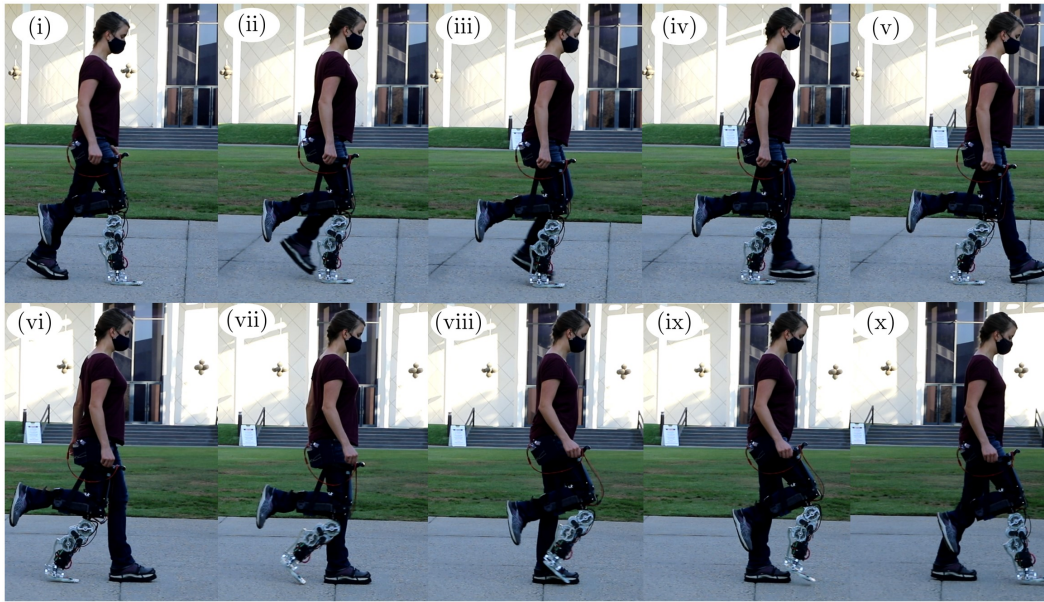


Figure 7.1: Gait tiles of powered prosthesis AMPRO3 worn by able-bodied human user walking with model-dependent prosthesis controller. Top shows prosthesis stance, bottom shows prosthesis non-stance. Numbers align with phases of gait trajectory shown in Figure 7.4.

the interaction force between the human and the prosthesis. Since integrating a force sensor into the prosthesis platform would require modifications of the platform, this chapter develops an algorithm to estimate the interaction forces, as a first pass, to implement a model-dependent prosthesis controller.

In this chapter, we leverage RES-CLFs and their formal guarantees in the context of the ID-CLF-QP framework. The unknown dynamics of the human enter the prosthesis dynamics via interaction forces, so we estimate these forces to complete the model-dependent nature. Inspired by the average acceleration discrete algorithm in [279], we developed a force estimation method with on-board velocity measurements. To demonstrate these results, we realize the controller on-board the AMPRO3 prosthesis [19], shown in Figure 7.1. In particular, we demonstrate that the model-based ID-CLF-QP results in accurate tracking. More generally, we are thus able to transfer the formal guarantees afforded by RES-CLFs to hardware, with the result being stable prosthesis locomotion in practice.

In this chapter, Section 7.2 lays out our specific controller construction for a robotic subsystem. This section describes the discrete force estimation method and how the controller is respectively formed to be incorporate this estimate. The force estimate

completes the prosthesis subsystem dynamics to enable model-dependent prosthesis control which we demonstrate in simulation in 7.3 and experiment in 7.4, yielding provably stable human-prosthesis walking. The main contributions of this chapter are,

- (i) the synthesis of model-dependent controllers using force estimation and
- (ii) the first realization of fully model-dependent prosthesis control, bringing the human into the loop of prosthesis control with strong formal guarantees of stability.

7.2 Controller Realization for Hardware

Implementing a model-based subsystem controller of the class (5.2) on hardware requires knowledge of the interaction force F_f . Since a force sensor was not available on the prosthesis platform we developed a method to estimate the interaction force using discrete calculations of acceleration. We include this estimated term in the dynamics of an ID-CLF-QP and realize this QP at sample time to implement on hardware.

Force Estimation. We estimate the joint acceleration \ddot{q}_s^{est} based on the discrete velocity measurements and time,

$$\ddot{q}_{s,k-1}^{\text{est}} = \frac{\dot{q}_{s,k} - \dot{q}_{s,k-1}}{t_k - t_{k-1}},$$

where k represents the current time step and $k - 1$ represents the previous time step. Finding the difference between our estimated acceleration and the expected acceleration based on the dynamics from the previous time step,

$$\ddot{q}_{s,k-1}^{\text{exp}} = D_s(q_{s,k-1})^{-1} \left(-H_s(q_{s,k-1}, \dot{q}_{s,k-1}) + B_s u_{s,k-1} + J_{c,s}^T(q_{s,k-1}) \bar{\lambda}_{h,k-1} \right), \quad (7.1)$$

we multiply this by the inertia matrix of the previous time step to obtain what we consider the *residual dynamics* \hat{F}_{k-1} :

$$\hat{F}_{k-1} = D_s(q_{s,k-1}) (\ddot{q}_{s,k-1}^{\text{est}} - \ddot{q}_{s,k-1}^{\text{exp}}). \quad (7.2)$$

We essentially back-calculate the interaction force that caused the acceleration difference. Note (7.2) cancels $D_s(q_{s,k-1})$ in (7.1), such that inertia matrix inversion is not required. To obtain a smoother signal, we average the residual dynamics measurements for N time steps:

$$\hat{F}_{k-1}^{\text{avg}} = \frac{1}{N} \sum_{i=1}^N \hat{F}_{k-i}. \quad (7.3)$$

By calculating the force projected into joint space, we are smoothing the exact signal we input to the dynamics and do not need a pseudo-inverse of $J_{f,s}$.

ID-CLF-QP+ \hat{F}^{est} . To formulate an ID-CLF-QP with this force estimate, we first introduce the following terms,

$$J_{\text{qp}}(q_s) = \begin{bmatrix} J_{y^s}(q_s) \\ J_{c,s}(q_s) \end{bmatrix} \quad \dot{J}_{\text{qp}}(q_s, \dot{q}_s) = \begin{bmatrix} \dot{J}_{y^s}(q_s, \dot{q}_s) \\ \dot{J}_{c,s}(q_s, \dot{q}_s) \end{bmatrix}.$$

With these terms we will include the holonomic constraints as soft constraints in the QP since they are difficult to satisfy exactly on hardware. To find a control input u_s close to the feedback linearizing controller (4.8) with PD gains on our output accelerations,

$$\mu_s = K_p y^s(x_s) + K_d \dot{y}^s(x_s) := \mu_{\text{pd}}, \quad (7.4)$$

we minimize the difference between (6.31) and μ_{pd} in our QP cost. We replace $J_{f,s}^T F_f$ in the robotic subsystem dynamics (4.10) with $\hat{F}_{k-1}^{\text{avg}}$ and evaluate the QP at sample time:

$$\begin{aligned} \Upsilon_k^* &= \underset{\Upsilon_k \in \mathbb{R}^{n_\nu}}{\text{argmin}} \left\| \dot{J}_{\text{qp}}(q_s, \dot{q}_{s,k}) \dot{q}_{s,k} + J_{\text{qp}}(q_s) \ddot{q}_{s,k} - \nu^{\text{pd}} \right\|^2 + \sigma W(\Upsilon_k) + \rho \zeta \\ \text{s.t. } & D_s(q_{s,k}) \ddot{q}_{s,k} + H_s(q_{s,k}, \dot{q}_{s,k}) = B_s u_{s,k} + J_{c,s}^T(q_{s,k}) \lambda_{c,s,k} + \hat{F}_{k-1}^{\text{avg}} \\ & L_{F_s} V_\varepsilon^s(\mathcal{X}_k) + L_{G_s} V_\varepsilon^s(\mathcal{X}_k) \mu_{y^s,k} \leq -\frac{\lambda_{\min}(Q_s)}{\varepsilon \lambda_{\max}(P_s)} V_\varepsilon^s(\mathcal{X}_k) + \zeta_k. \\ & -u_{\max} \leq u_s \leq u_{\max}, \end{aligned} \quad (7.5)$$

where $\Upsilon = [\ddot{q}_s^T, u_s^T, \lambda_{c,s}^T, \zeta]^T \in \mathbb{R}^{n_{\text{qp}}}$, with $n_{\text{qp}} = n_{q,s} + m_s + n_{c,s} + 1$. Here $\nu^{\text{pd}} = (\mu_{\text{pd}}^T, 0^T)^T$, $W(\Upsilon)$ is a regularization term to make the problem well posed, σ and ρ are weighting terms, ζ is a relaxation term such that the torque bounds $(-u_{\max}, u_{\max})$ can always be met, and $\mu_{y^s,k} = \dot{J}_{y^s,k}(q_s, \dot{q}_s) \dot{q}_{s,k} + J_{y^s,k}(q_s) \ddot{q}_{s,k}$. This controller selects the joint accelerations \ddot{q}_s , control input u_s , and holonomic constraint wrench $\lambda_{c,s}$ to satisfy the robotic subsystem dynamics (4.10) and the subsystem RES-CLF (5.3) while optimally aiming to satisfy the holonomic constraints (4.11) and smoothly track the desired trajectories. Although we use the residual dynamics estimate from the previous time step to model the dynamics at the current time step, when run in a controller at a high enough frequency this method should capture the residual dynamics well enough.

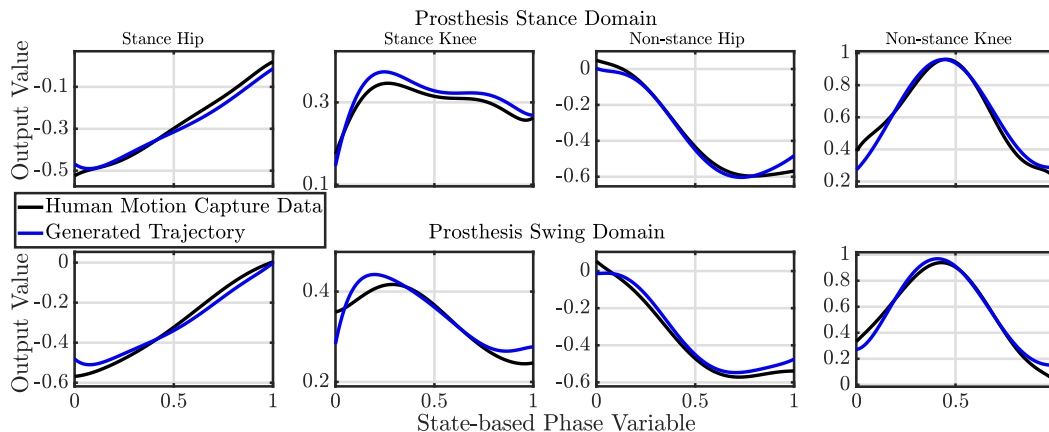


Figure 7.2: Joint outputs from optimization (blue) align closely with human motion capture data (black) showing the trajectories we use to test the human-prosthesis model in simulation and implement on the prosthesis device are human-like.

7.3 Human-Prosthesis Simulation

To demonstrate this ID-CLF-QP+ \hat{F}^{est} we first apply it to a prosthesis model in simulation while the human portion of the system is controlled by a method unknown to the prosthesis. The accuracy of the force estimation is also tested.

We use the human-prosthesis model described in Section 3.3, but omit the ankles in trajectory generation and simulation because it is more comfortable for the human user to have the prosthesis ankle have varying set point PD control instead of following a trajectory. For the hybrid system (3.24), we consider two continuous domains, \mathcal{D}_{ps} for prosthesis stance and \mathcal{D}_{pns} for prosthesis non-stance. To find a human-like walking trajectory for the model, human walking motion capture data is taken and Bézier polynomials are fit to the joint trajectories through the cost function of the optimization problem in (3.28). Figure 7.2 shows the resulting trajectories match the human data well. By finding a prosthesis knee trajectory similar to a human’s knee trajectory and is provably stable when the rest of the system is following the human-like trajectories, we assume the human can still stabilize itself with the prosthesis. Hence the condition required for our main theoretical idea is satisfied.

Simulation Results. We restrict our attention to implementing the proposed controller in the stance domain \mathcal{D}_{ps} where the interaction force is the largest and the prosthesis’ stability is critical as it supports the human. In practice we calculate the base coordinates \bar{q}_B , base velocities $\dot{\bar{q}}_B$, and phase variable $\tau(x_s)$ with inverse kinematics using the knee and ankle data and assuming the foot is flat on the ground.

The swing domain \mathcal{D}_{pns} requires an IMU to provide information about this domain's main unknown, the base coordinates. This is realized in the next chapter.

We prescribe a feedback linearizing control law to the human side to closely track the human-like trajectories in simulation. Variations of the ID-CLF-QP controller are implemented on the prosthesis in stance and a feedback linearizing control law in swing to enforce the subsystem output (4.3), where $y_s^a(x_s) = \theta_{pk}$. The ID-CLF-QP+ F_f is implemented with the exact interaction force F_f calculated with (4.13), since $F_f \in \lambda$, based on a feedback linearizing control law u (3.6). The ID-CLF-QP+ \hat{F}^{est} used the force estimator (7.3) with $N = 1$ since averaging is unnecessary in simulation. Finally the ID-CLF-QP was used without any interaction force information.

The resultant control inputs are shown in Figure 7.3a and tracking results in Figure 7.4. The ID-CLF-QP+ F_f and ID-CLF-QP+ \hat{F}^{est} achieved practically exact tracking results and had very similar control inputs. This suggests the force estimator estimates the force well enough to give similar performance as when using the exact force. The ID-CLF-QP with no consideration of the interaction force outputs a very different control input and had terrible tracking, indicating the significance of accounting for the force. To compare the force estimate with the actual computed force, the summation of the constraint wrenches and interaction force projected into joint space is taken since the constraint wrench calculation for the subsystem controller (7.5) is coupled with the interaction force estimate and hence they cannot be individually compared with the constraint forces and interaction force calculated with the full-order dynamics (3.22). Figure 7.3b compares the actual force components calculated by $\begin{bmatrix} J_{c,s}^T(q_s) & J_{f,s}^T(q_s) \end{bmatrix} \begin{bmatrix} \lambda_{c,s}^T & F_f^T \end{bmatrix}^T$ to the estimated force components $J_{f,s}^T(q_s)\lambda_{c,s} + \hat{F}$, showing the force estimation works with high accuracy.

7.4 Human-Prosthesis Experimentation

The platform used to demonstrate the model-based control method is described in Section 3.3. Here we present the experimental results of the proposed controller. The results verify this controller meets our formal condition for exponential stability and it outperforms the less model-dependent controllers.

Hardware Results. The ID-CLF-QP+ \hat{F}^{est} was implemented on the prosthesis platform in stance (with $N = 10$ in (7.3)) and superior trajectory convergence and tracking were achieved compared to a model-independent PD controller and the ID-CLF-QP controller without consideration for the force. A 1.7 m, 62 kg able-bodied

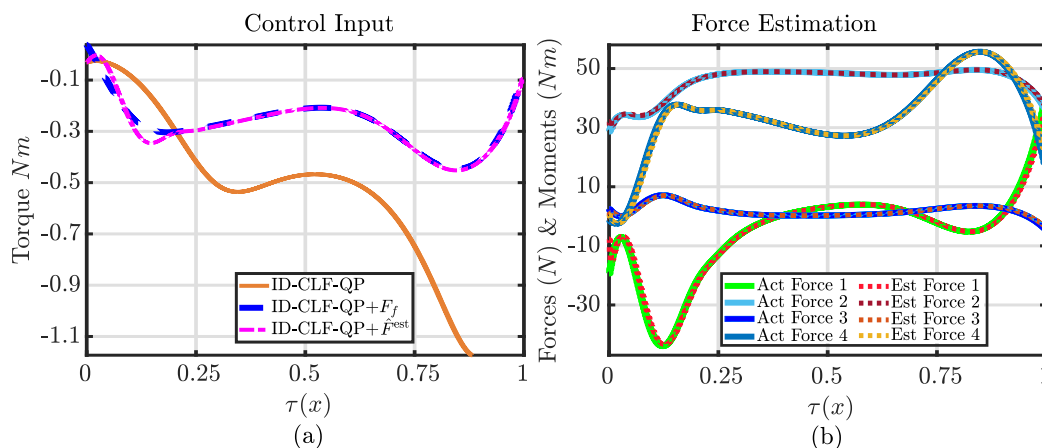


Figure 7.3: Control Input and Force Estimation Simulation Results. (a) Prosthesis stance control input for the knee from 3 simulations of the human-prosthesis model walking with variations of the ID-CLF-QP applied to the prosthesis. (b) The summation of the constraint forces and interaction forces projected into joint space.

human tested the device in walking for over 20 consecutive steps with each controller. The experimental results are shown in the supplemental video [280]. The ankle had a PD controller with varying set point. A PD controller was applied to the knee in swing, but did not perfectly converge to the trajectory. Hence the output starts off the trajectory in stance, explaining the jump present in the desired trajectory in Figure 7.4. However, the ID-CLF-QP+ \hat{F}^{est} recovers from this disturbance and converges to the trajectory, demonstrating the advantage of the exponential convergence of a model-based RES-CLF. Figure 7.5 also shows the significant tracking improvement exhibited by the ID-CLF-QP+ \hat{F}^{est} in stance compared to the other controllers. The rapid convergence and superior tracking are two important results of this work.

Main Result. The primary result of this work is implementing a model-dependent controller on a prosthesis with formal guarantees of stability. Figure 7.5 shows this result where the CLF derivative is plotted with its stability bound, indicating the prosthesis satisfies this formal guarantee of stability. (The slight breaking of the bound is due to the relaxation term in the CLF-QP). When the CLF condition is well below its bound, the control input, shown in the bottom of Figure 7.5, has a small magnitude because the controller is letting the natural dynamics of the system bring it to its desired trajectory. This effect is especially significant considering the prosthesis starts off the trajectory at the beginning of the stance phase and this precisely demonstrates the advantage of model-dependent control over model-independent control. A controller without model information would respond to the

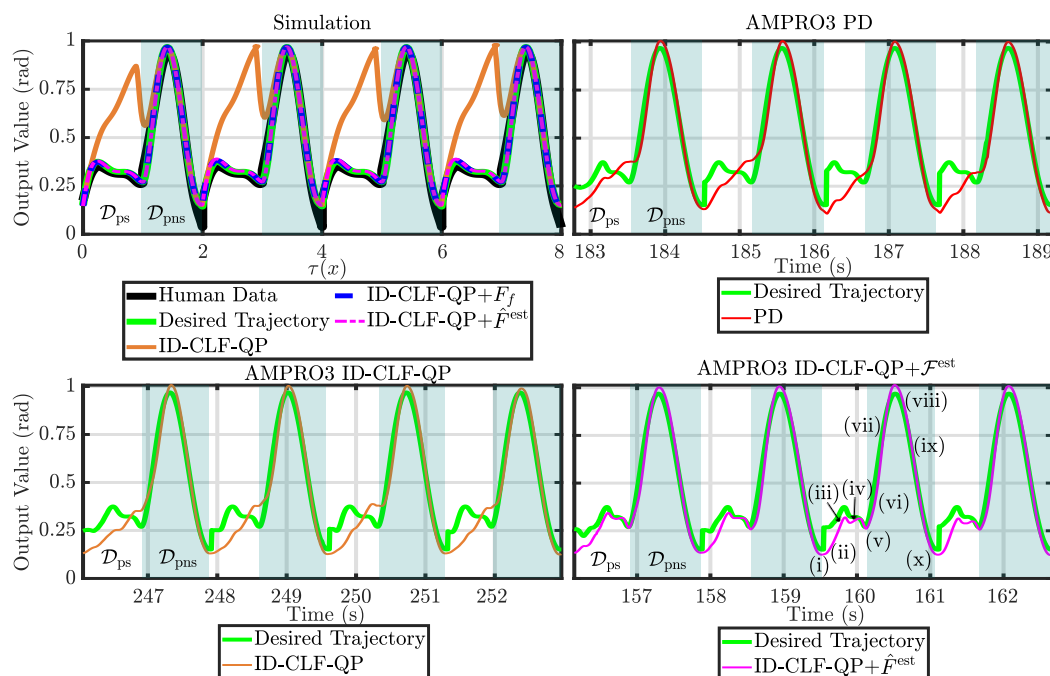


Figure 7.4: Simulation and Experimental Output Tracking Results. (Top left) Output tracking from 3 simulations with variations of the ID-CLF-QP on the prosthesis in stance plotted with the desired trajectory and the human data with respect to the phase variable. Experiment output tracking with the PD controller (top right), ID-CLF-QP (bottom left), and ID-CLF-QP+ \hat{F}^{est} (bottom right) applied in stance plotted with the desired trajectory in time. \mathcal{D}_{ps} white, \mathcal{D}_{pns} shaded. Numbers in bottom right plot indicate phase of gait corresponding to gait tiles in Figure 7.1

large error with a large torque which would require more energy and the sudden movement could cause discomfort to the user. This model-dependent controller, on the other hand, allows the natural dynamics of the system to bring the prosthesis to its desired trajectory without using more energy and yielding a less aggressive movement for the user.

(Note: Due to COVID-19 restrictions, the results of this study were restricted to one subject. The next two chapters demonstrate the control method on more subjects.)

7.5 Conclusion

In this work, the novel methodology of developing RES-CLFs for separable systems [207], [208] is realized on a prosthesis platform, demonstrating the first experimental realization of a model-dependent prosthesis controller that accounts for interaction forces. As such, this is the first instance of realizing prosthesis control with formal guarantees of stability for the full-order hybrid system with zero dynamics. These

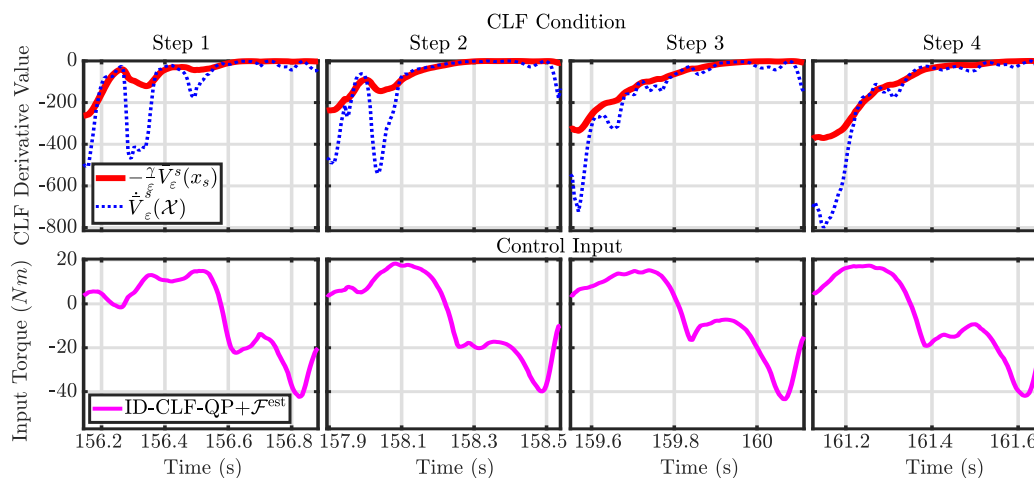


Figure 7.5: Results of four phases of stance from experiment. (Top) The RES-CLF derivative (blue) plotted against its bound (red). (Bottom) The prosthesis knee control input.

guarantees with consideration for the interaction forces ensure safety of the user and a responsiveness to the real-time dynamics are novel relative to existing prosthesis control methods. Being able to implement model-dependent controllers on a prosthesis platform opens the door to applying various nonlinear control techniques to prostheses and other robotic subsystems, thereby improving performance.

The next chapter applies this control method in the swing phase by incorporating an IMU into the prosthesis platform. This next approach also includes a force sensor at the human adapter attachment point to measure the interaction force in real-time.

*Chapter 8***MODEL-BASED PROSTHESIS CONTROL REALIZATION
WITH REAL-TIME FORCE SENSING**

This chapter realizes the first model-dependent prosthesis knee controller that uses in-the-loop on-board real-time force sensing at the interface between the human and prosthesis and at the ground. The result is an optimization-based control methodology that formally guarantees stability while enabling human-prosthesis walking on a variety of terrain types. Experimental results demonstrate this force-sensor-based controller outperforms similar controllers not using force sensors, improving tracking across 4 terrain types.

This chapter was adapted from:

R. Gehlhar, J.-h. Yang, and A. D. Ames. “Powered Prosthesis Locomotion on Varying Terrains: Model-Dependent Control With Real-Time Force Sensing”. In: *IEEE Robotics and Automation Letters* 7.2, 2022, pp. 5151–5158.

8.1 Introduction

The previous chapter realized the first model-dependent prosthesis controller in stance with consideration for the forces—however, as a first pass, these forces were estimated rather than sensed. Holonomic constraints were used to determine the ground reaction forces and moment and force estimation for the socket interaction forces and moment. (For simplicity we refer to these as “GRFs” and “socket forces”.) The lack of real-time force sensing, therefore, necessitated the assumption of rigid contact with the ground (via the use of holonomic constraints). This inaccurately represents many real-life scenarios where the terrain deforms under a load, like granular media [281]. Developing control methods accounting for non-rigid terrain is especially important for prostheses to enable amputees to walk stably on a variety of surfaces present in daily life. Additionally, estimating (not sensing) the socket forces may not accurately capture the varying load a user applies during stance. To more accurately account for the interactions between the user and the prosthesis, and the prosthesis and the environment, it is necessary to integrate real-time force sensing into the model-based controller.

The main contributions of this chapter are:

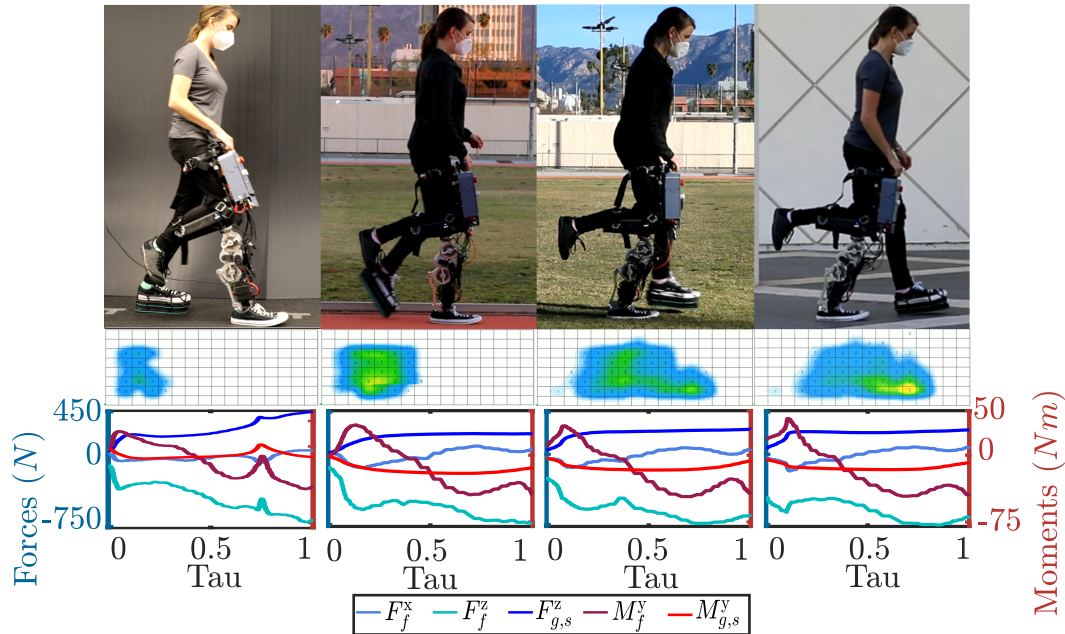


Figure 8.1: Gait Tiles of Experimental Results with Force Sensor Measurements. (top) Gait tiles of human subject walking with model-dependent prosthesis knee controller using real-time force sensing on four terrains: rubber floor, outdoor track, grass, and sidewalk. (middle) Insole pressure sensor maps in the stance phases of a walking cycle. (bottom) Measured socket and ground force profiles during stance for respective terrain.

- (i) realizing the first model-dependent prosthesis knee controller that uses real-time force sensing at the ground and socket and
- (ii) demonstrating improved tracking performance with the proposed control method across 4 terrains and for 2 subjects.

To achieve this result, we integrate a load cell, insole pressure sensor, and an inertial measurement unit (IMU) on a transfemoral powered prosthesis platform (shown in Figure 8.1). To leverage these sensors, we use an optimization-based controller utilizing RES-CLFs, developed in the previous chapters. This time, the controller previously presented directly accounts for the force sensing in real-time, i.e., the sensed forces are utilized to “complete the model” of the human-prosthetic system and thereby determine the next control action. The insole pressure sensor, therefore, allows for the control actions to be dynamically modulated based upon the sensed terrain type (removing the need to assume locomotion on a non-deformable surface). The load cell quantifies the interaction between the human and prosthesis allowing the prosthesis to compensate for this dynamic load in real-time and achieve its

desired behavior in the presence of these large external forces. This framework is demonstrated experimentally on the prosthesis shown in Figure 8.1, resulting in stable human-prosthesis walking with 2 subjects. Walking is also achieved on 4 different terrain types with the proposed controller demonstrating improved tracking performance across all terrains.

It is important to note that force sensing has long been utilized in prosthesis control, although not in the context of realizing model-based controllers via real-time force sensing. Load cells have been incorporated into powered prosthesis platforms to detect ground contact, GRFs, and center of pressure (CoP) [282]–[284]. The work of [282] used GRF sensing capability to determine motion intent to trigger transitions between gait phases of finite-state based impedance control. The work of [283] used the CoP to encode and modulate virtual constraints for prosthesis control. However, to date, GRF and socket force measurements have not been included in the modeled dynamics to achieve model-dependent prosthesis control. Additionally, to the best of the authors’ knowledge, GRFs and CoP measurements from an insole plantar pressure sensor have not been utilized as real-time feedback in prosthesis control [285].

The chapter is structured in the following manner. Section 8.2 constructs the controller of focus in this chapter that utilizes real-time force and IMU measurements. Following, Section 8.3 presents the pressure sensor used in this study and the additions made to the powered transfemoral prosthesis platform, AMPRO3, to integrate the force sensors and IMU. The experimental set-up and results in Section 8.4 show the improved knee tracking performance with this real-time force feedback for 4 types of terrain and for 2 subjects on a single terrain type.

8.2 Controller Realization for Hardware

While [210] realized a variation of the ID-CLF-QP, this method was only applied in stance, relied on a force estimation method for F_f , and used the holonomic constraint wrench $\lambda_{c,p}$ for the GRFs. This rigid-contact model used for the GRFs does not hold for a foot contacting a variety of real-world non-rigid terrains. To overcome these limitations, we incorporated an IMU, load cell, and insole pressure sensor into the prosthesis platform.

Sensor Measurements to Complete Dynamics. While the floating base positions and velocities can still be obtained in stance by inverse kinematics with the prosthesis joint positions and velocities, we use an IMU on the human leg adapter to measure

the floating base y-rotation and angular velocity in swing. These measurements with the kinematics give the x- and z-Cartesian velocities. The x- and z-Cartesian positions do not affect the dynamics and hence are not required. The work in this chapter employed a 6-axis load cell to directly measure the interaction forces F_f between the human and prosthesis and an insole pressure sensor, detailed in Section 8.3, to determine the vertical GRF F_g^z and pitch ground reaction moment M_g^y . The only remaining unknown force is the horizontal GRF. We solve for the wrench $\lambda_{h,x} \in \mathbb{R}^1$ through a holonomic constraint, assuming the foot does not slip on the ground.

Force Sensing ID-CLF-QP. The final controller formulation is

$$\begin{aligned} \Upsilon^* = \operatorname{argmin}_{\Upsilon \in \mathbb{R}^{n_{\text{qp}}}} & \left\| \dot{J}_{\text{qp}}(q_s, \dot{q}_s) \dot{q}_s + J_{\text{qp}}(q_s) \ddot{q}_s - v^{\text{pd}} \right\|^2 + \sigma W(\Upsilon) + \rho \zeta \\ \text{s.t. } & D_s(q_s) \ddot{q}_s + H_s(q_s, \dot{q}_s) = B_s u_s + J_{c,s}^T(q_s) \tilde{F}_g + J_{f,s}^T(q_s) F_f \\ & L_{F_s} V_\varepsilon^s(\mathcal{X}) + L_{G_s} V_\varepsilon^s(\mathcal{X}) (J_{y^s} \dot{q}_s + J_{y^s} \ddot{q}_s) \leq -\frac{\lambda_{\min}(Q_s)}{\varepsilon \lambda_{\max}(P_s)} V_\varepsilon^s(\mathcal{X}) + \zeta \\ & -u_{\max} \leq u_s \leq u_{\max}, \end{aligned} \tag{8.1}$$

with modified set of decision variables $\Upsilon = (\ddot{q}_s^T, u_s^T, \lambda_{c,s}^x, \zeta)^T \in \mathbb{R}^{n_{\text{qp}}}$ and $n_{\text{qp}} = n_{q,s} + m_s + 2$. The decision variable $\lambda_{c,s}^x$ is included with the measured GRFs F_g^z and M_g^y in $\tilde{F}_g = (\lambda_{c,s}^x, F_g^z, M_g^y)^T$.

The same outputs generated in the last chapter were used for in this work as well. For this initial realization of a force sensing model-dependent prosthesis controller, we limit the scope to a knee controller. We use the given model in the ID-CLF-QP to generate a knee torque, but predefine a torque for the ankle based on a varying set point PD controller. Since we do not enforce an ankle trajectory, we generate a prosthesis knee trajectory for the prosthesis using the full system model without ankles. The next chapter realizes this force sensing ID-CLF-QP controller on both the knee and ankle for a more complex gait that emulates human heel-toe roll.

8.3 Prosthesis Platform for Controller Realization

We integrated a pressure sensor, a load cell, and IMU into the powered prosthesis platform, described in 3.3, to achieve model-based prosthesis control with real-time in-the-loop forcing sensing. First, we will describe the pressure sensor selection and use due to the novelty of incorporating plantar pressure data as real-time force input to a model-dependent controller.

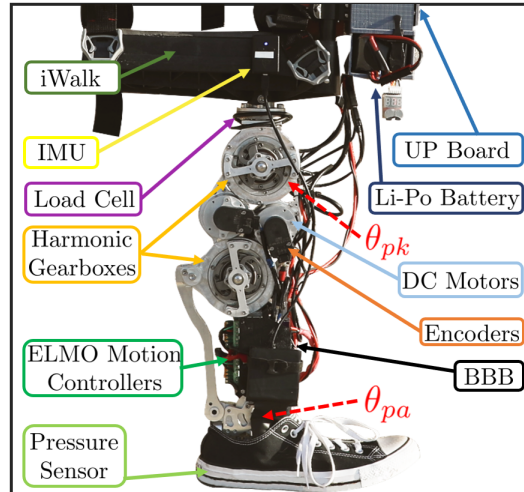


Figure 8.2: Transfemoral powered prosthesis AMPRO3 with labeled hardware components, including newly integrated force sensors (load cell and pressure sensor).

Pressure Sensor. The pressure sensor used for this study met the restrictive real-time control requirements for our application. Most commercially available insole pressure sensors are designed for recording data for offline gait analysis and are incompatible with our application. The sensor for this study is \$2.5-3k and a company-provided API returns the raw data in real-time over a USB connection.

The pressure sensor used is a SensorProd Inc. Tactilus Foot Insole Sensor System, High-Performance V Series (SP049). Made of a piezoresistive sensor array, the insole pressure sensor can sense up to 206.8 kPa at 101 separate points per foot. The sensor provides a resolution of $\pm 1 \mu\text{Pa}$, along with an accuracy of $\pm 10\%$, repeatability of $\pm 2\%$, and a hysteresis of $\pm 5\%$. To interface with the pressure sensor, we use an UP Board (02/32), a small x86 single-board computer.

We incorporated the Tactilus API, a precompiled C++ Windows Library from SensorProd Inc., into a Windows C++ program which scanned the pressure readings in real time at about 200 Hz with the UP Board through a USB connection. We applied a Gaussian smoothing filter and simple moving average filter to the sensor element pressure readings. With the sensor element pressure, surface area, and displacement from the ankle's center of rotation we calculate the vertical GRF F_g^z and ground reaction moment M_g^y .

Prosthesis Platform AMPRO3. The controller algorithms run on the Beaglebone Black Rev C (BBB) microprocessor at 166Hz and are coded in C++ packages with ROS. The coded force sensing ID-CLF-QP is based on code from [37].

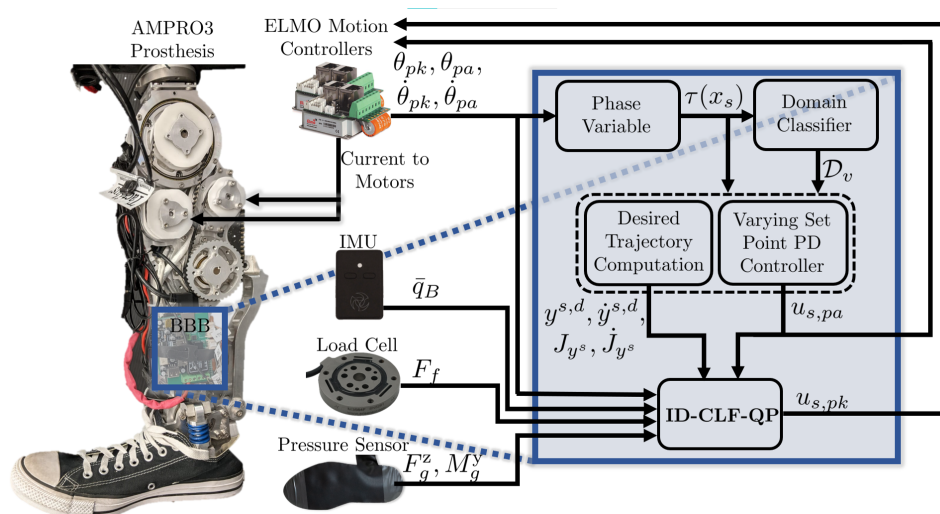


Figure 8.3: Block diagram depicting how the Beaglebone microprocessor, motion controllers, IMU, load cell, and pressure sensor are involved in the control scheme.

The insole sensor is physically integrated into the prosthetic system through placement over the insole of a shoe worn by the prosthesis foot. The sensor connects to the UP Board through USB, and sends force and moment measurements to the BBB through UDP over Ethernet. There is a 5 ms time delay between when the sensor is read and the BBB receives the data caused largely by the time it takes the Windows program to receive all the data from the sensor.

A Yost Labs 3-Space™ Sensor USB/RS232 IMU is mounted to the side of the human leg adapter on the prosthesis platform. This connects to the BBB via USB and streams data at 750 Hz. A 6-axis load cell (M3564F, Sunrise Instruments) is mounted at the interface between the proximal end of the prosthesis knee joint and distal end of the human leg adapter with custom designed aluminum parts. The load cell can measure forces/moments along the x and y-axes up to 2500 N/200 Nm and z-axis up to 5000 N/100 Nm. A signal conditioning box (M8131 Sunrise Instruments) connects to the BBB with a custom-designed cape and sends data and sends new data via CAN communication once every control loop. A newly designed electronics box mounted on the iWalk houses the load cell box, UP Board, and a 9-cell 4400 mAh Li-Po battery (Thunder Power RC) which powers the whole system. Figure 8.2 shows AMPRO3 with the aforementioned components labeled and Figure 8.3 shows a control block diagram with the sensors. The prosthesis weighs 5.95 kg on its own, and totals 10.54 kg with the iWalk, electronics box, battery, and sensors.

8.4 Human-Prosthesis Experimentation

On this prosthesis platform, we realize our model-dependent force sensing knee controller, resulting in stable human-prosthesis walking. We present the results here.

Experimental Procedure. A 1.7 m, 62 kg non-amputee human subject (Subject 1) and a 1.8 m, 75 kg non-amputee subject (Subject 2) tested the prosthesis device with an iWalk adapter. The iWalk allows a subject's bent right leg to be strapped to the device for walking as shown in Figure 5.4. A foam shoe lift strapped to the bottom of their left leg's shoe evens the length difference between their own left leg and their right leg with the prosthesis. We applied the proposed controller to the knee in both stance and non-stance phase. A PD controller with varying set-point was applied to the prosthesis ankle. Both subjects walked with the prosthesis for at least 30 steps with 4 different controllers on a rubber floor. Gait tiles of an experiment are shown in Figure 8.4. Subject 1 walked with the prosthesis with 2 of these controllers on an additional 3 terrains: an outdoor track, grass, and a sidewalk.

The first controller is the force sensing ID-CLF-QP (8.1), the controller of focus in this chapter, using the pressure sensor to obtain F_g^z , M_g^y , the load cell to obtain F_f , and the IMU in swing for \bar{q}_B and $\dot{\bar{q}}_B$. For comparison, we tested an ID-CLF-QP without including the measurements from the pressure sensor and load cell to see the effect the force sensor measurements have on the controller performance. Here the GRFs were determined with the holonomic constraints (4.11) but the fixed joint forces F_f were considered 0. Thirdly, we compared the performance to the previous force estimating ID-CLF-QP in [210], where the holonomic constraints are again used to determine the GRFs and the effect of the socket forces is estimated with a force estimator with a moving average time window of 30. Here the time window was increased to yield a smooth torque response when using the same gains K_P , K_D in v_{pd} as those selected for the force sensing ID-CLF-QP. The gains v_{pd} and all other user-selected terms in the QP were kept consistent between controllers. Finally, we compared the performance to a traditional PD controller, which is used in other prosthesis control methods [283], [286]. The experimental results are shown in the supplemental video [287].

Hardware Results. The knee phase portrait of Figure 8.5 a. shows the stability of this main controller for 18 steps on a sidewalk. Figure 8.5 b. depicts the CLF derivative with its upper CLF stability bound for the first 4 steps. While the derivative occasionally exceeds the bound because of the relaxation term in the QP



Figure 8.4: Gait tiles of 2 subjects walking on a rubber floor with the force sensing ID-CLF-QP prosthesis controller.

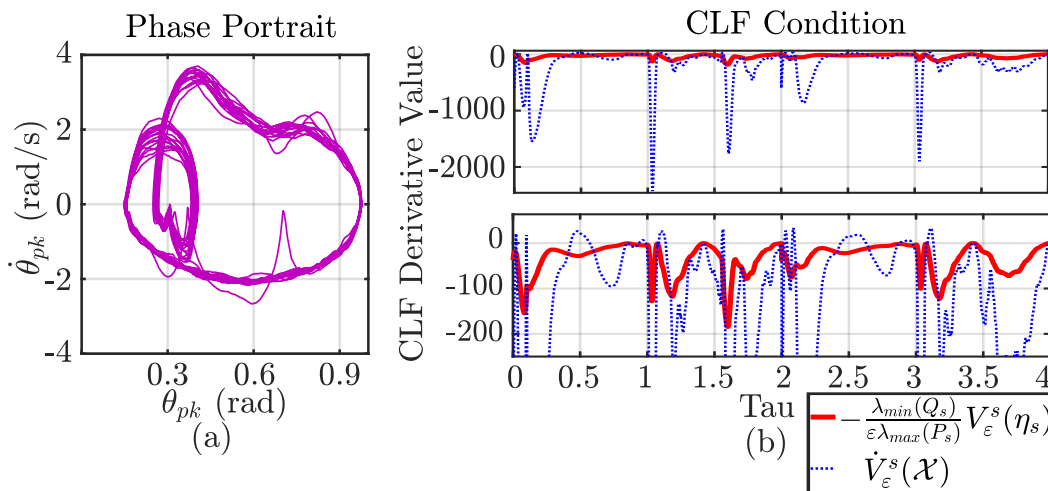


Figure 8.5: Phase Portrait and CLF Convergence Experimental Results. (a) Phase portrait of first 18 steps using the force sensing ID-CLF-QP controller (8.1) on a sidewalk, showing the system yields a stable periodic orbit. (b) (top) CLF bound and derivative for first 4 steps of the same experiment, showing the prosthesis usually satisfies the stability condition, (bottom) magnified plot of the CLF bound, w.r.t. phase variable $\tau(x_s)$.

(8.1), the overall human-prosthesis system can still be input-to-state stable as proved in [288]. Additionally, although the force measurements may have error from sensor noise and time delay, the work of [288] showed for a bounded error in the force measurement the prosthesis will still be stable to a set and conditions exist such that the human will remain exponential input-to-state stable [251] when the prosthesis deviates from its nominal control law.

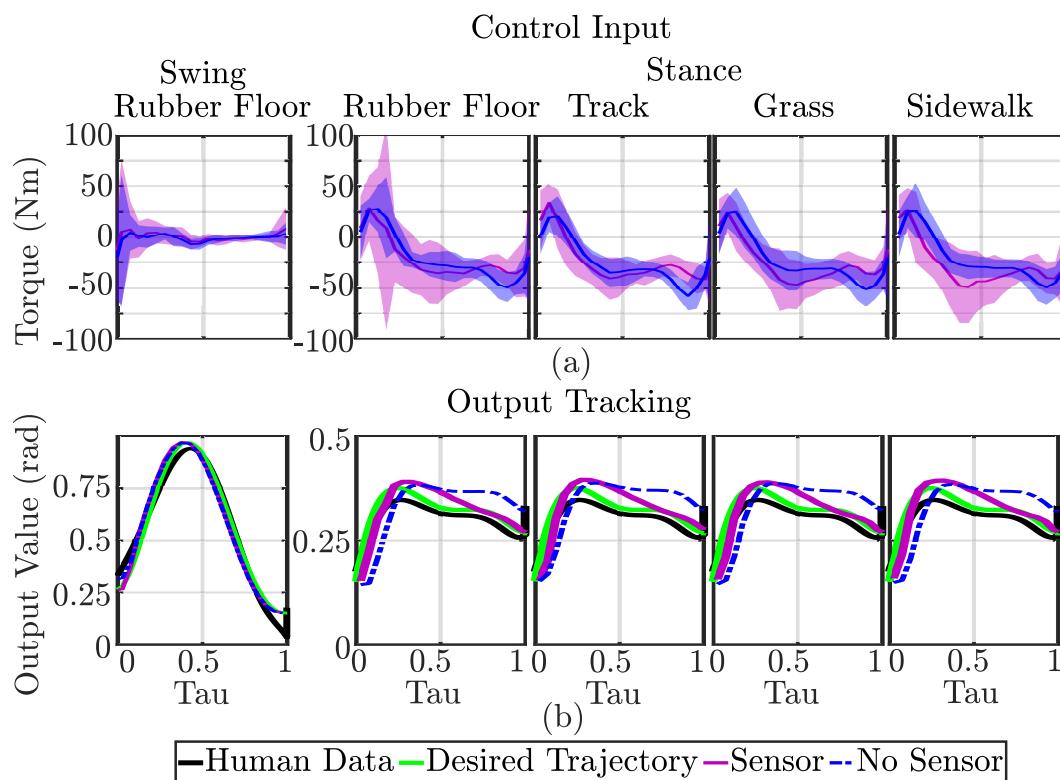


Figure 8.6: Control Input and Output Tracking Experimental Results for Four Terrains. (a) Control input (mean and 3 standard deviations) and (b) output tracking with force sensing ID-CLF-QP and the ID-CLF-QP without force sensors for four different terrains for 11 step cycles, w.r.t. to phase variable $\tau(x_s)$.

Figure 8.6 a. shows the mean torque inputs with 3 standard deviations of the first two controllers for 11 step cycles on 4 different terrains. (Note the standard deviations overlap appears as purple.) Both controllers exhibit variation between steps on a given terrain and variation across terrains, however the variation in the force sensing ID-CLF-QP leads to better tracking performance. Figure 8.6 b. depicts the tracking performance with the mean. The human motion capture data used to generate the desired trajectory is also depicted. The swing tracking is similar for all controllers, so only one example is shown. The force sensing ID-CLF-QP achieves better tracking in stance than the ID-CLF-QP without force sensors on all terrains. Table 8.1 shows the root mean square error (RMSE) of the force sensing ID-CLF-QP (“Sensor”) over 11 step cycles is lower than the ID-CLF-QP with no force sensors (“No Sensor”) in stance for all four terrains.

Figure 8.7 shows that the torque and tracking results for the four controllers for 2 subjects. The stance tracking results show better tracking performance from the

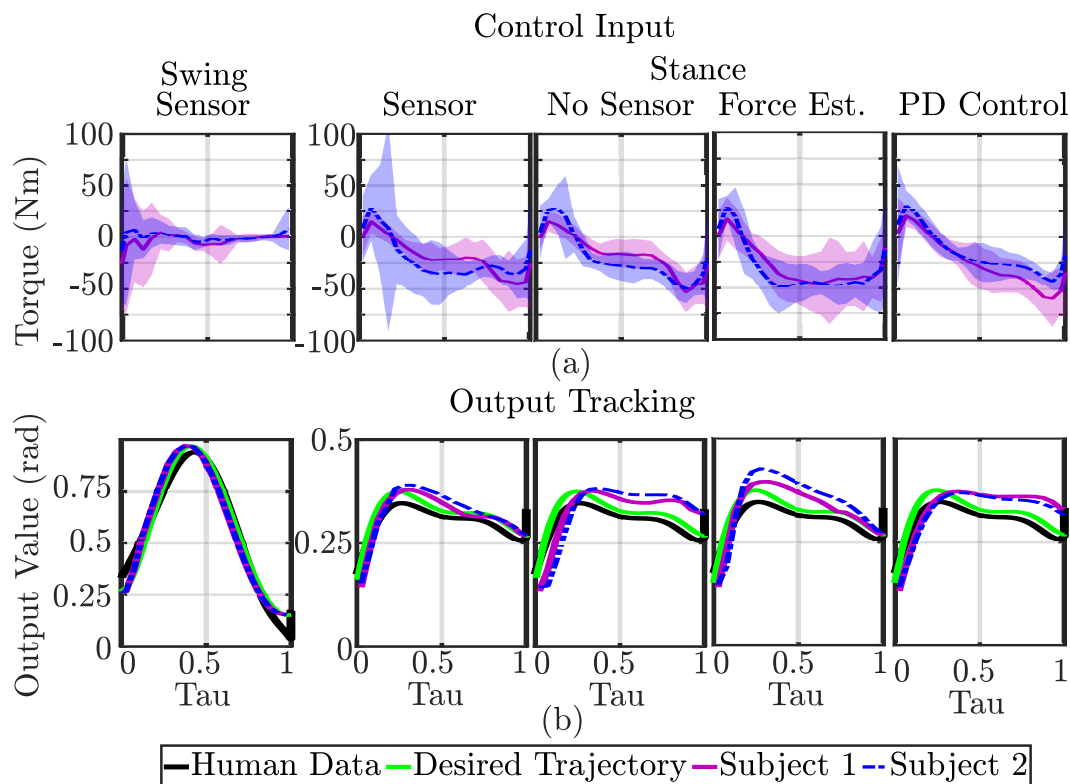


Figure 8.7: Control Input and Output Tracking Experimental Results for Four Controllers. (a) Control input (mean and 3 standard deviations) and (b) output tracking (mean) with force sensing ID-CLF-QP, no sensor ID-CLF-QP, force estimating ID-CLF-QP, and PD controller for 11 step cycles, w.r.t. phase variable $\tau(x_s)$.

force sensing ID-CLF-QP for both subjects compared to the 3 other controllers. Table 8.2 shows the RMSE of the tracking performance over 11 step cycles where the force sensing ID-CLF-QP has the lowest RMSE out of all of the controllers in stance for both subjects. The greater difference between RMSE values for the stance phase makes sense since this is when the prosthesis undergoes loading from the user and our controllers' vary in their response to these interaction forces. The force sensing ID-CLF-QP's better tracking for both subjects without tuning in between suggests this control method is more transferrable across subjects, meaning it could lend a method that works for multiple subjects without hours of expert tuning for each subject, as is currently required by impedance control methods [33]. Future work will test this control method on more subjects to further investigate its transferability across subjects.

These results show the force sensing ID-CLF-QP can achieve better tracking utilizing force sensors than without, suggesting that accounting for the forces in the dynamics

Table 8.1: Tracking RMSE of 4 Terrains for 2 Controllers

| | Stance RMSE (θ) | | Swing RMSE (θ) | |
|------------|--------------------------|-----------|-------------------------|-----------|
| | Sensor | No Sensor | Sensor | No Sensor |
| Rubber Fl. | 0.0409 | 0.0797 | 0.0341 | 0.0349 |
| Track | 0.0460 | 0.0662 | 0.0302 | 0.0297 |
| Grass | 0.0398 | 0.0740 | 0.0328 | 0.0307 |
| Sidewalk | 0.0380 | 0.0763 | 0.0331 | 0.0295 |

Table 8.2: Tracking RMSE of 4 Controllers for 2 Subjects

| | Stance RMSE (θ) | | Swing RMSE (θ) | |
|------------|--------------------------|-----------|-------------------------|-----------|
| | Subject 1 | Subject 2 | Subject 1 | Subject 2 |
| Sensor | 0.0237 | 0.0409 | 0.0331 | 0.0341 |
| No Sensor | 0.0455 | 0.0797 | 0.0372 | 0.0349 |
| Force Est | 0.0357 | 0.0552 | 0.0409 | 0.0401 |
| PD Control | 0.0484 | 0.0522 | 0.0464 | 0.0427 |

allows this model-dependent controller to respond to its real-time loading conditions to achieve good tracking. This also suggests the improvement in model accuracy allows this model-dependent controller to better capture the nonlinearities of a trajectory, motivating the use of model-dependent prosthesis controllers to achieve more dynamic behaviors.

8.5 Conclusion

The work in this chapter achieved the first experimental realization of a model-dependent prosthesis knee controller in both stance and swing using real-time in-the-loop force measurements to complete the dynamics through integration of an insole pressure sensor, load cell, and IMU in the prosthesis platform, resulting in stable human-prosthesis walking. By directly measuring the forces from the human and ground with the load cell and pressure sensor, we enable the prosthesis to account for its real-world conditions. These sensing methods increase the validity of our human-prosthesis stability guarantees and could empower a variety of amputees to walk in varying ways across changing terrain.

This controller achieved better tracking on 4 types of terrain compared to its counterpart without force sensors. Additionally this controller outperformed its counterpart with force estimation and a traditional PD controller on 2 subjects. These results demonstrate the controller's robustness and ability to adapt to varying external forces from the user and the ground. Its improved performance on 2 subjects without tuning in between suggests the real-time force response could replace the need to tune

many parameters for every user and behavior, as is required in typical impedance prosthesis control methods [33]. Since this control method relies on real-time dynamic force sensing, as opposed to static tuned parameters, to respond to the forces induced by the user and the terrain, it could provide a more transferable method across users and behaviors, reducing the time amputees spend in a tuning session.

In the next chapter, this controller will be applied to the ankle in addition to the knee for a more complex multi-contact gait [36] that emulates human heel-toe roll, to achieve a more natural and efficient gait.

*Chapter 9***MODEL-BASED MULTI-CONTACT PROSTHESIS WALKING**

Ankle push-off largely contributes to limb energy generation in human walking, leading to smoother and more efficient locomotion. Because of these benefits, this chapter aims to replicate this ankle push-off behavior with a powered prosthesis. This work uses multi-contact models of locomotion together with force-sensor-based nonlinear optimization-based controllers to achieve human-like kinematic behavior, including ankle push-off, on a powered transfemoral prosthesis for 2 subjects. The proposed controller is implemented on a prosthesis for two subjects without tuning between subjects, emulating subject-specific human kinematic trends on the prosthesis joints. These experimental results demonstrate that our force-sensor-based nonlinear control approach achieves better tracking of human kinematic trajectories than traditional methods.

This chapter was adapted from:

R. Gehlhar and A. D. Ames. “Emulating Human Kinematic Behavior on Lower-Limb Prostheses via Multi-Contact Models and force-sensor-based Nonlinear Control”. In: *Submitted to 2023 IEEE International Conference on Robotics and Automation (ICRA)*. IEEE. 2022.

9.1 Introduction

In human walking, ankles contribute the most positive work of trailing leg joints in forward rocking [289] and contribute up to 60% of the total energy generated by a limb during a gait cycle [40]. Ankle push-off specifically contributes to the forward acceleration of the body [75] and also greatly smooths the transition from double support to swing phase in human gait [290]. Researchers showed for a simple powered walking model, that toe push-off can supply energy to the system at a quarter of the cost of applying a hip torque because this toe push-off reduces the collision energy loss at heel strike [291]. For amputees specifically, increase in prosthetic ankle push-off reduces the loading impulse of the intact limb and the risk of knee osteoarthritis for amputees [47].

The HZD framework we have used to generate walking trajectories for the prosthesis also allows modeling of multiple domains of continuous dynamics to model

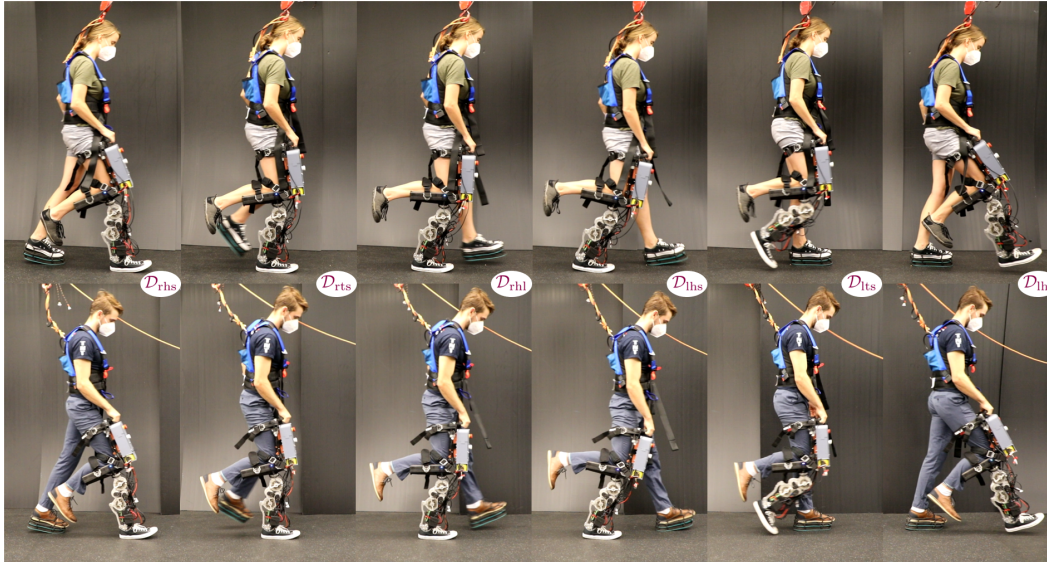


Figure 9.1: (top) Subject 1 and (bottom) Subject 2 walking with powered prosthesis controlled by multi-domain model-based prosthesis controller with real-time force sensing following provably stable human-like walking trajectories. Labels indicate the respective domain the human-prosthesis is in in the multi-domain hybrid-system graph shown in Figure 9.2

multi-contact behavior occurring in heel-toe roll used for ankle push-off. With this trajectory generation method, other works have realized multi-contact walking through model-independent tracking methods on bipedal robots [256], [292] and a powered prosthesis [36]. In order to retain stability guarantees online, this chapter implements the separable subsystem CLF controller to realize multi-contact behavior on a prosthesis following a human-like trajectory generated through HZD methods. This work differs from [36] in both method and results, using a formally grounded force-sensor-based controller to achieve human-like walking, verified through the kinematics. This chapter extends the work of the previous chapters with 3 main contributions:

- (i) we simultaneously apply the first model-based lower-limb prosthesis controller with real-time force sensing to the ankle in addition to the knee of a transfemoral prosthesis,
- (ii) we expand this model-based controller to a 6-domain hybrid system framework to emulate human multi-contact behavior (heel-toe roll),
- (iii) we demonstrate this new controller on 2 subjects with 2 different subject-specific prescribed walking gaits, and compare it to two other control methods.

In this chapter, Section 9.2 describes the domains and ground model used in a multi-domain hybrid system to model multi-contact behavior. This section also describes the separable output functions used, where we can use a subset of these outputs to construct a controller for the prosthesis. We then discuss how we use human motion capture data to generate the desired outputs to match this kinematic data while also satisfying stability guarantees for the human-prosthesis system. To implement these trajectories, we construct our control method in Section 9.3. In Section 9.4 we describe the powered prosthesis platform we implement the controller on. We realize this controller on 2 subjects, shown in Figure 9.1, and present the resultant human-like joint trajectories on the prosthesis along with comparisons to 2 other tested control methods.

9.2 Generating Subject-Specific Human-Inspired Walking Trajectories

Multi-Domain Hybrid System. We consider 3 phases per step for human walking: heel strike (*hs*) when the swinging foot’s heel reaches the ground, toe strike (*ts*) when that foot’s toe reaches the ground, and heel lift (*hl*) when the other foot’s heel lifts off of the ground and becomes the swinging leg. We omit a fourth phase of the toe lifting between toe strike and heel lift because it is a very short phase. Since a human walking with a prosthesis is an asymmetric system, we consider separate phases for the right and left leg, prefacing the abbreviations with “*r*” and “*l*” respectively, giving a total of 6 phases. The vertices for (3.24) are $V = \{rhs, rts, rhl, lhs, ltl, lhl\}$. The current phase of the system is dictated by the foot contacts present. The set of all contact points is given by $C = \{rh, rt, lh, lt\}$ signifying the right heel, right toe, left heel, and left toe. Figure 9.2 shows the contact points present for each phase, or *domain*, of walking.

Compliant Ground Model. To account for the compliance the prosthesis foot and human foot experience in ground contact with their shoes, we include a spring-damper at the base of each foot in our robot model for trajectory generation to serve as a “ground model”, as shown in Figure 3.1 We use a spring stiffness of $60,000N/m$ and a damping coefficient of $600Ns/m$ [86], [293]. These prismatic joints have coordinates q_{rs} and q_{ls} for the right and left spring, respectively. This allows us to generate model-based trajectories with more realistic impact dynamics. Since on hardware the prosthesis is measuring the forces at the level of the shoe

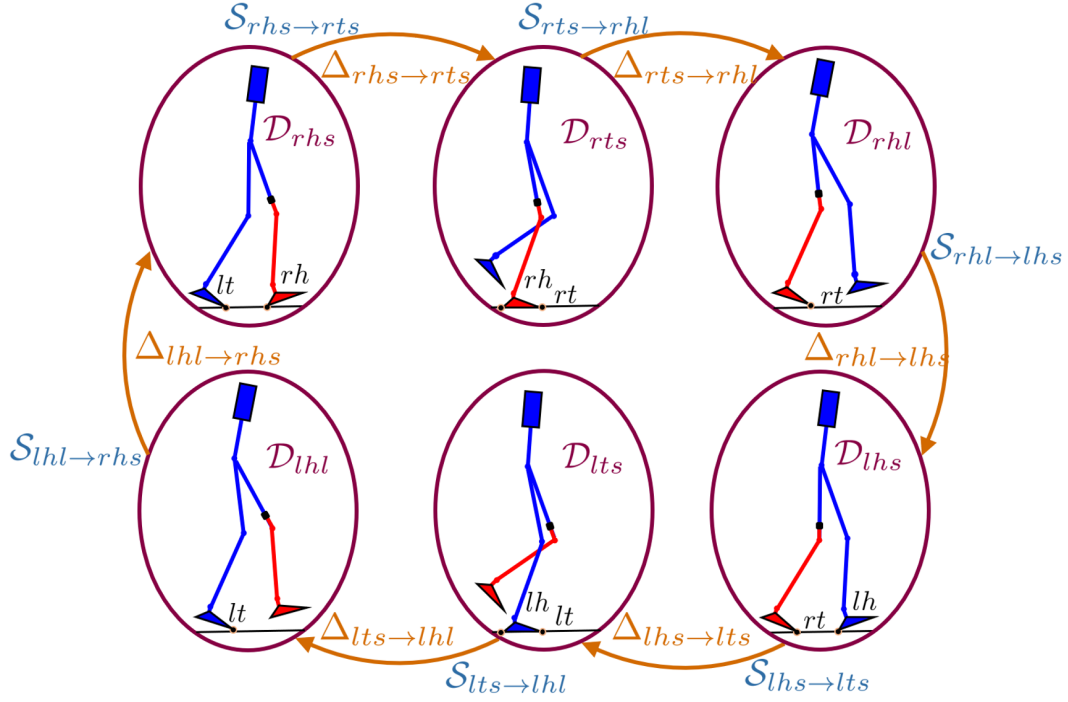


Figure 9.2: Six-domain directed graph of human-prosthesis hybrid system, modeling respective foot contact points for different phases of walking.

insole, instead of the forces beneath the shoe, we do not include this ground model in our prosthesis subsystem.

Separable Output Construction. To develop a controller for the subsystem (4.7), we select *separable outputs* $y_v(x) = (y_v^r(x), y_v^s(x_s))^T$, such that outputs for the subsystem $y_v^s(x_s)$ and their Lie derivatives [250] do not require information about the remaining system [207]. By selecting outputs that are either functions of the prosthesis joints or human joints, we can define the following separable subsystem outputs from this set.

$$y_{s,v}^a(x_s)|_{v \in \{rhs, rhl, lhs, ltl, lhl\}} = [\theta_{pk}, \theta_{pa}]^T,$$

$$y_{s,rts}^a(x_s) = [v_{rhip}, \theta_{pk}]^T,$$

with,

$$v_{rhip}(x_s) = (\bar{r}_B + r_{pk})\dot{\theta}_{pk} + (\bar{r}_B + r_{pa})\dot{\theta}_{pa},$$

where r_{\square} is the length between the joint specified in the subscript and the following distal joint, and \bar{r}_B is the length between the prosthesis base frame and the prosthesis knee.

To do state-based control for the first four domains, we define,

$$\begin{aligned}\delta_{rhs}(x_s) &= \bar{\theta}_{By}, \\ \delta_v(x_s)|_{v \in \{rts, rhl, lhs\}} &= \bar{r}_B \bar{\theta}_{By} + r_{pk} \theta_{pk} + r_{pa} \theta_{pa}.\end{aligned}$$

For \mathcal{D}_{lts} and \mathcal{D}_{lhl} we calculate τ_v based on the current time and predicted time duration from trajectory generation.

Human-Like Trajectories. We used the average human relative joint trajectories from the motion capture data set of [226]. For each of our subjects, we selected a data set obtained with subjects with similar height and mass. To divide the data into segments for each domain, we used gait cycle percentage estimates of walking phases from [294]. We used the first 12% of the data points for \mathcal{D}_{rhs} ; the next 19% for \mathcal{D}_{rts} ; the next 19% for \mathcal{D}_{rtl} ; and the final 12%, 19%, and 19% for \mathcal{D}_{lhs} , \mathcal{D}_{lts} , and \mathcal{D}_{lhl} , respectively. For each segment of data for a given domain, we fit Bézier polynomials to the data using fit in MATLAB. However, since there is not an impact causing discrete dynamics between the *ts* and *hl* domains, we have a single Bézier stretching across both domains. Because we wanted to generate periodic gaits and the average data trajectories had a large gap between end points, we included the first data point again at the end of the data series so the Bézier polynomials would yield periodic trajectories. This process gave a set of Bézier coefficients α_v^H for each domain.

We included these Bézier coefficients in the cost function of the HZD trajectory optimization (3.28). We built a human model for the optimization built for each subject based on their height, weight, and sex, such that we designed trajectories to match subject-specific data and satisfy stability guarantees for a subject-specific model.

9.3 Controller Realization

To enforce these trajectories on the prosthesis subsystem, we employ a rapidly exponentially stabilizing control Lyapunov function (RES-CLF), following the construction method in [199].

Force Sensing ID-CLF-QP. To develop a hardware implementable form of a RES-CLF, we construct a variation of the inverse dynamics CLF quadratic program (ID-CLF-QP), introduced in [37], that was developed for the prosthesis subsystem in [97]. To prescribe a desired behavior to our output dynamics $(\dot{y}_{1,v}^{sT}, \ddot{y}_{2,v}^{sT}) = \mu_s$,

we define a desired auxiliary control input,

$$\mu_{\text{pd},v} := K_p y_{2,v}^s(x_s) + K_d \dot{y}_{2,v}^s(x_s) + K_{y^a} \dot{y}_{2,v}^{s,a}(x_s) + K_v y_{1,v}^s(x_s).$$

We added the $K_{y^a} \dot{y}_{2,v}^{s,a}(x_s)$ to the typical output PD law used [37], [199] to reduce oscillations observed on hardware. In our QP cost we will minimize the difference between our actual auxiliary control input μ_s and $\mu_{\text{pd},v}$. If we solved (4.8) for μ_s , the expression would involve computationally expensive matrix inversions prone to numerical error [37]. Instead we use $\mu_{s,v} = (\dot{y}_{1,v}^{sT}, \dot{y}_{2,v}^{sT})^T$ and rewrite our outputs in terms of the subsystem configuration coordinates q_s and velocities \dot{q}_s :

$$\begin{bmatrix} \dot{y}_{1,v}^s \\ \dot{y}_{2,v}^s \end{bmatrix} = \underbrace{\begin{bmatrix} \frac{\partial y_{1,v}^s}{\partial q_s} \\ \frac{\partial}{\partial q_s} \left(\frac{\partial y_{2,v}^s}{\partial q_s} \dot{q}_s \right) \end{bmatrix}}_{J_{y^s,v}(q_s, \dot{q}_s)} \dot{q}_s + \underbrace{\begin{bmatrix} \frac{\partial y_{1,v}^s}{\partial \dot{q}_s} \\ \frac{\partial y_{2,v}^s}{\partial \dot{q}_s} \end{bmatrix}}_{J_{y^s,v}(q_s)} \ddot{q}_s.$$

We will include these terms in the QP cost with the holonomic constraints, enforcing these as soft constraints, using,

$$J_{\text{qp},v}(q_s) = \begin{bmatrix} J_{y^s,v}(q_s) \\ J_{c,s,v}(q_s) \end{bmatrix}, \quad \dot{J}_{\text{qp},v}(q_s, \dot{q}_s) = \begin{bmatrix} \dot{J}_{y^s,v}(q_s, \dot{q}_s) \\ \dot{J}_{c,s,v}(q_s, \dot{q}_s) \end{bmatrix}.$$

Here the holonomic constraint terms are domain specific, as indicated by subscript v , since the number of contact points changes between domains. With these terms, we formulate our ID-CLF-QP,

$$\begin{aligned} \Upsilon_v^* &= \underset{\Upsilon \in \mathbb{R}^{n_v}}{\text{argmin}} \left\| \dot{J}_{\text{qp},v}(q_s, \dot{q}_s) \dot{q}_s + J_{\text{qp},v}(q_s) \ddot{q}_s - v_v^{\text{pd}} \right\|^2 + \sigma W(\Upsilon) + \rho \zeta \\ \text{s.t. } & D_s(q_s) \ddot{q}_s + H_s(q_s, \dot{q}_s) = B_s u_s + J_{c,s,v}^T(q_s) \tilde{F}_{g,v} + J_{f,s}^T(q_s) F_f \\ & L_{F_s} V_{\varepsilon,v}^s(\mathcal{X}) + L_{G_s} V_{\varepsilon,v}^s(\mathcal{X}) (J_{y^s,v} \dot{q}_s + J_{y^s,v} \ddot{q}_s) \\ & \leq -\frac{\lambda_{\min}(Q_{s,v})}{\varepsilon \lambda_{\max}(P_{s,v})} V_{\varepsilon,v}^s(\mathcal{X}) + \zeta \\ & -u_{\max} \leq u_s \leq u_{\max}, \end{aligned} \quad (9.1)$$

with decision variables $\Upsilon_v = (\dot{q}_s^T, u_s^T, \bar{\lambda}_{h,x,v}, \zeta)^T$ and $v_v^{\text{pd}} = (\mu_{\text{pd},v}^T, 0^T)^T$. The GRFs $\tilde{F}_{g,v}$ contain the GRFs present for \mathcal{D}_v . We obtain the vertical GRF F_g^z and pitch moment M_g^y from a pressure sensor and the QP solves for x-component of the holonomic constraint $\lambda_{c,s}^x$. Even though the desired auxiliary control law $\mu_{\text{pd},v}$ differs from (7.4) which guarantees stability of the linearized system (3.9), we still have stability guarantees since the QP selects values that satisfy the CLF constraint.

Table 9.1: Tracking RMSE of 3 Controllers for 2 Subjects

| | Knee RMSE (rad) | | Ankle RMSE (rad) | |
|------------|-----------------|-----------|------------------|-----------|
| | Subject 1 | Subject 2 | Subject 1 | Subject 2 |
| Sensor | 0.0228 | 0.0230 | 0.0179 | 0.0150 |
| No Sensor | 0.0334 | 0.0315 | 0.0270 | 0.0306 |
| PD Control | 0.0242 | 0.0250 | 0.0494 | 0.0316 |

The dimensions and components of this controller are domain-dependent since the outputs change with domain as well as the contact points, which changes the type of GRFs applied and computed.

9.4 Multi-Contact Model-Based Controller Realization

We realize this model and force-sensor-based multi-domain controller on our powered prosthesis platform for 2 subjects, resulting in human-like multi-contact behavior.

Experimental Set-up. Two non-amputee subjects wore the prosthesis device through an iWalk adapter. Subject 1 was a 1.7 m, 66 kg female and Subject 2 was a 1.8 m 75 kg male. Both subjects wore a shoe lift on their left leg to even out the limb length difference when wearing the prosthesis. The subjects were allowed a chance to walk with the device before data recording started. Then they walked with each of the 3 controllers for at least 4 sets of 8 step cycles, taking a short break between controllers. The controllers included the ID-CLF-QP with force sensing (9.1) (“sensor” controller), the ID-CLF-QP with no force sensing (“no sensor” controller), and a PD controller ¹. When no force sensing was used, all of the GRFs were calculated through the holonomic constraints in the ID-CLF-QP. The weights and regularization terms in the ID-CLF-QP and the gains in v_{pd} were kept consistent for all tests. We set $v_{hip,v}^d = 0$ to allow the human to dictate the velocity of their stance progression instead of prescribing a set velocity. The experimental results can be seen in the supplemental video [295].

Experimental Results. Figure 9.3 shows the phase portraits of the prosthesis joints for 8 continuous step cycles with the ID-CLF-QP (9.1). The velocity varies between steps since it is modulated by a state-based phase variable. Figure 9.4 (a) shows the vertical GRF and pitch moment measured by the pressure sensor and horizontal

¹A small mechanical issue was present in the PD controller test with Subject 2. Because the tracking results were comparable to the PD controller test with Subject 1 we consider the effect of the mechanical issue to be minor and included the results for completeness.

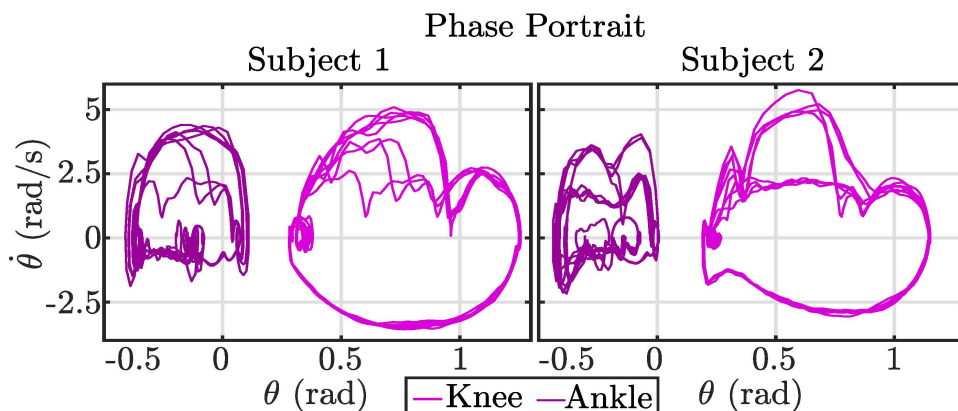


Figure 9.3: Phase portraits of the knee and ankle for 2 subjects for 8 continuous steps cycles using the ID-CLF-QP.

GRF calculated by the QP (9.1) during 1 step of walking with (9.1). For each controller, we computed the mean of the actual trajectories, for a set of 8 continuous step cycles, and plotted these against the desired trajectories and the subject-specific average human joint data [226] in Figure 9.4 (b). Here the ID-CLF-QP with force sensing (9.1) exhibits tight tracking to the desired trajectory, especially compared to the other controllers for the ankle. This tracking performance is quantified by the root-mean-square error (RMSE) in Table 9.1 showing it outperforms the other controllers for both joints and both subjects. More importantly, the ID-CLF-QP with force sensing matches the subject-specific human joint patterns most closely, demonstrating we can emulate this human-like behavior in a systematic way that does not involve tuning between subjects.

9.5 Conclusion

This work achieved human-like multi-contact human-prosthesis walking on 2 subjects using a model-based multi-domain controller with real-time force sensing, with no tuning between subjects. This approach provides a formally based, systematic method to generate and realize human-like motion on lower-limb powered prostheses. In terms of tracking, this controller outperformed its counterpart without force sensors and a standard PD controller on both subjects. Being able to realize multi-contact behavior on prostheses without tuning for each subject could bring the benefits of smoother and more energy efficient gait to amputees, restoring natural and healthy locomotion.

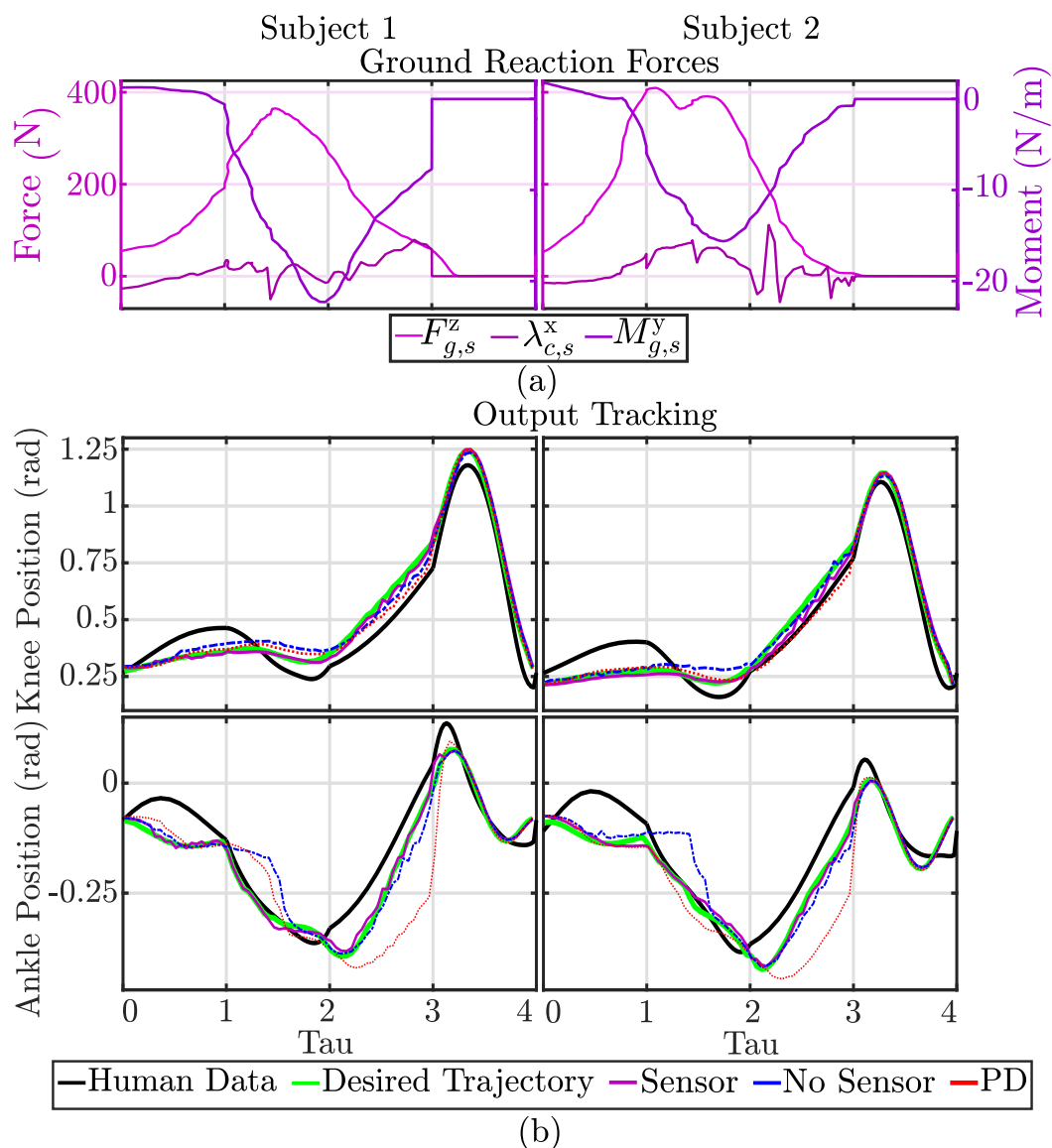


Figure 9.4: Ground Reaction Forces and Output Tracking Experimental Results. (a) The vertical GRF F_g^z and moment M_g^y measured by the pressure sensor and horizontal GRF $\bar{\lambda}_{g,x}$ during one step of walking with the ID-CLF-QP (9.1). (b) The mean of the actual outputs of the knee and ankle for 2 subjects and 3 controllers for 8 continuous step cycles plotted against the desired trajectory and the averaged human joint data.

Chapter 10

CONCLUSION

Motivated by the large number of lower-limb amputees, the draw-backs of passive prostheses, and the limitations of current prosthesis control methods, this thesis investigated model-based control approaches with the aim of developing a prosthesis control method that generalizes between users. By synthesizing control Lyapunov functions in a separable subsystem framework and integrating real-time force sensing into prosthesis control, this work bridged the gap between bipedal control theory and prosthesis hardware realization. Overall the result of this thesis is a formally-based systematic approach to generate and realize stable human-prosthesis walking that generalizes across users and is robust to various terrains.

The main contributions of this thesis are:

1. **Development of a class of nonlinear model-based subsystem controllers.** Through developing a separable subsystem framework in Chapter 4, the work of this thesis enabled synthesis of model-based subsystem controllers that solely rely on locally available subsystem information and proved equivalency to a controller developed with full-order system knowledge. Chapter 5 extended these constructions by developing an entire class of model-based subsystem controllers.
2. **Formal proofs that guarantee full-order system stability with these subsystem controllers.** Chapter 5 proved full-order system stability with the subsystem controllers, when the rest of the system can stabilize itself, as is the case for a human using a prosthesis. Chapter 6 established these stability guarantees are maintained even when the subsystem controller is subject to force estimation error, as the case would be in a real-world application.
3. **First and only experimental realization of model-based lower-limb prosthesis control that accounts for the human-prosthesis interaction force.** Chapter 7 realizes a model-based subsystem controller of the class developed in Chapter 5 on a powered prosthesis platform through developing a method to estimate the forces between the human and the prosthesis. Chapter 8 integrated real-time force sensing into the prosthesis control method

through sensor selection, mechanical design, software development, and the aforementioned theoretical constructions. This work then realized this control method with in-the-loop real-time force sensing on a powered prosthesis, demonstrating stable human-prosthesis walking that is robust to 4 different terrains and generalizes across 2 subjects. Finally, Chapter 9 extends this model-based control method to a multi-domain hybrid system to model the changing contact points occurring in human heel-toe roll. This work realizes subject-specific human-like walking behavior on a prosthesis for 2 subjects, improving tracking performance compared to traditional control methods with less model information.

10.1 Future Work

1. **Translate Nonlinear Control Methods to Robotic Assistive Devices.** By bridging the gap between bipedal control theory and prosthesis hardware realization, we have opened the door to leverage other advancements in nonlinear control methods for prostheses. One example of a recent advancement is the work of [296] that demonstrates bipedal walking that is robust to disturbances in terrain. This approach adjusts the walking gait based on desired step size and could lead to natural gait transitions and nonperiodic walking. Translating these strategies to powered prostheses could allow gait adaptation to increase versatility of locomotive patterns in response to the human, while guaranteeing stability.
2. **Emulate Biomechanical Features to Recover Natural Behavior.** While nonlinear control could provide guarantees of walking stability, to assess the health of a gait, we should look to biomechanics. Nonlinear control methods provide a framework in which biomechanical metrics can naturally be integrated. Encoding biomechanical principles as control objectives would allow us to directly improve upon those metrics. Emulating biomechanical features through nonlinear control could improve the naturalness of a prosthesis user's walking gait. One motivating example of this is our work in [87] where we incorporated human muscle models into the HZD gait generation method with the aim of achieving more natural walking prosthesis motion. The walking gaits generated with this addition led to human muscle activation patterns that more closely resembled that of healthy human walking. The results can be viewed in this video [297].

- 3. Infer Motion Intent to Determine Responsive Behavior.** To synergize this stable and natural motion with a human's desired motion, wearable sensors and machine learning techniques could be used to infer the human's motion intent and determine a responsive behavior. Wearable sensors could detect a human's motion, and machine learning techniques could decode all this sensory information to identify a pattern. A motivating example of wearable sensors' ability to detect human motion is the electronic skin sensor developed in [298] which we used to initiate one prosthesis step forward, as shown in this video [299]. The complexity of machine learning algorithms makes them difficult to run online on-board a small microprocessor, preventing them from being physically feasible for prosthetic applications. However, in a recent collaboration, we achieved the first instance of using a hardware-accelerated RNN for real-time prosthesis control [300], as shown in this video [301]. This opens the door to being able to decode complex human sensory information online to bring the human into the loop of prosthesis control.

BIBLIOGRAPHY

- [1] K. Ziegler-Graham, E. J. MacKenzie, P. L. Ephraim, T. G. Trivison, and R. Brookmeyer, "Estimating the prevalence of limb loss in the united states: 2005 to 2050," *Archives of Physical Medicine and Rehabilitation*, vol. 89, no. 3, pp. 422–429, 2008, ISSN: 0003-9993.
- [2] P. DeVita, J. Helseth, and T. Hortobagyi, "Muscles do more positive than negative work in human locomotion," *The Journal of experimental biology*, vol. 210, pp. 3361–73, Oct. 2007.
- [3] D. A. Winter, "Energy generation and absorption at the ankle and knee during fast, natural, and slow cadences.," *Clinical orthopaedics and related research*, vol. 175, pp. 147–54, 1983.
- [4] E. R. Esposito, K. M. Rodriguez, C. A. Rábago, and J. M. Wilken, "Does unilateral transtibial amputation lead to greater metabolic demand during walking," *J Rehabil Res Dev*, vol. 51, no. 8, pp. 1287–96, 2014.
- [5] N. H. Molen, "Energy/speed relation of below-knee amputees walking on a motor-driven treadmill," *Internationale Zeitschrift für angewandte Physiologie einschließlich Arbeitsphysiologie*, vol. 31, pp. 173–185, 2004.
- [6] R. L. Waters and S. Mulroy, "The energy expenditure of normal and pathologic gait," *Gait & Posture*, vol. 9, no. 3, pp. 207–231, 1999, ISSN: 0966-6362.
- [7] R. L. Waters, J. Perry, D. J. Antonelli, and H. J. Hislop, "Energy cost of walking of amputees: The influence of level of amputation.," *The Journal of bone and joint surgery. American volume*, vol. 58 1, pp. 42–6, 1976.
- [8] R. Gailey, "Review of secondary physical conditions associated with lower-limb amputation and long-term prosthesis use," *The Journal of Rehabilitation Research and Development*, vol. 45, no. 1, pp. 15–30, Dec. 2008.
- [9] W. C. Miller, M. Speechley, and B. Deathe, "The prevalence and risk factors of falling and fear of falling among lower extremity amputees," *Archives of Physical Medicine and Rehabilitation*, vol. 82, no. 8, pp. 1031–1037, 2001, ISSN: 0003-9993.
- [10] E. L. Bukowski, "Atlas of Amputations and Limb Deficiencies: Surgical, Prosthetic, and Rehabilitation Principles, ed 3," *Physical Therapy*, vol. 86, no. 4, pp. 595–596, Apr. 2006, ISSN: 0031-9023.
- [11] E. C. Martinez/Villalpando, L. Mooney, G. Elliott, and H. Herr, "Antagonistic active knee prosthesis. a metabolic cost of walking comparison with a variable-damping prosthetic knee," in *2011 Annual International Conference of the IEEE Engineering in Medicine and Biology Society*, Aug. 2011, pp. 8519–8522.

- [12] S. K. Au, J. Weber, and H. Herr, “Powered ankle-foot prosthesis improves walking metabolic economy,” *IEEE Transactions on robotics*, vol. 25, no. 1, pp. 51–66, 2009.
- [13] H. Herr and A. Grabowski, “Bionic ankle-foot prosthesis normalizes walking gait for persons with leg amputation,” *Proceedings. Biological sciences / The Royal Society*, vol. 279, pp. 457–64, Jul. 2011.
- [14] E. D. Ledoux and M. Goldfarb, “Control and evaluation of a powered transfemoral prosthesis for stair ascent,” *IEEE Transactions on Neural Systems and Rehabilitation Engineering*, vol. 25, no. 7, pp. 917–924, 2017.
- [15] S. K. Au and H. M. Herr, “Powered ankle-foot prosthesis,” *IEEE Robotics & Automation Magazine*, vol. 15, no. 3, pp. 52–59, 2008.
- [16] Ossur, Reykjavik, Iceland, *The power knee*, 2018.
- [17] F. Sup, A. Bohara, and M. Goldfarb, “Design and control of a powered transfemoral prosthesis,” *The International Journal of Robotics Research*, vol. 27, no. 2, pp. 263–273, 2008, PMID: 19898683.
- [18] B. E. Lawson, J. Mitchell, D. Truex, A. Shultz, E. Ledoux, and M. Goldfarb, “A robotic leg prosthesis: Design, control, and implementation,” *IEEE Robotics & Automation Magazine*, vol. 21, no. 4, pp. 70–81, 2014.
- [19] H. Zhao, E. Ambrose, and A. D. Ames, “Preliminary results on energy efficient 3D prosthetic walking with a powered compliant transfemoral prosthesis,” in *Robotics and Automation (ICRA), 2017 IEEE International Conference on*, IEEE, 2017, pp. 1140–1147.
- [20] M. Cempini, L. J. Hargrove, and T. Lenzi, “Design, development, and benchtop testing of a powered polycentric ankle prosthesis,” in *2017 IEEE/RSJ International Conference on Intelligent Robots and Systems (IROS)*, 2017, pp. 1064–1069.
- [21] N. Thatte, “Design and Evaluation of Robust Control Methods for Robotic Transfemoral Prostheses,” Ph.D. dissertation, Carnegie Mellon University, USA, Jul. 2019.
- [22] M. Tran, L. Gabert, M. Cempini, and T. Lenzi, “A lightweight, efficient fully powered knee prosthesis with actively variable transmission,” *IEEE Robotics and Automation Letters*, vol. 4, no. 2, pp. 1186–1193, 2019.
- [23] T. Elery, S. Rezazadeh, C. Nesler, and R. D. Gregg, “Design and validation of a powered knee-ankle prosthesis with high-torque, low-impedance actuators,” *IEEE Transactions on Robotics*, vol. 36, no. 6, pp. 1649–1668, 2020.
- [24] A. F. Azocar, L. M. Mooney, J.-F. Duval, A. M. Simon, L. J. Hargrove, and E. J. Rouse, “Design and clinical implementation of an open-source bionic leg,” *Nature Biomedical Engineering*, vol. 4, pp. 941–953, 2020.

- [25] N. Hogan, "Impedance control: An approach to manipulation," in *1984 American Control Conference*, 1984, pp. 304–313.
- [26] B. E. Lawson, H. A. Varol, A. Huff, E. Erdemir, and M. Goldfarb, "Control of stair ascent and descent with a powered transfemoral prosthesis," *IEEE Transactions on Neural Systems and Rehabilitation Engineering*, vol. 21, no. 3, pp. 466–473, 2013.
- [27] K. Bhakta, J. Camargo, P. Kunapuli, L. Childers, and A. Young, "Impedance Control Strategies for Enhancing Sloped and Level Walking Capabilities for Individuals with Transfemoral Amputation Using a Powered Multi-Joint Prosthesis," *Military Medicine*, vol. 185, no. Supplement 1, pp. 490–499, Dec. 2019, ISSN: 0026-4075. DOI: 10.1093/milmed/usz229.
- [28] J. T. Lee and M. Goldfarb, "Effect of a swing-assist knee prosthesis on stair ambulation," *IEEE Transactions on Neural Systems and Rehabilitation Engineering*, vol. 29, pp. 2046–2054, 2021. DOI: 10.1109/TNSRE.2021.3116787.
- [29] M. E. Carney, T. Shu, R. Stolyarov, J.-F. Duval, and H. M. Herr, "Design and preliminary results of a reaction force series elastic actuator for bionic knee and ankle prostheses," *IEEE Transactions on Medical Robotics and Bionics*, vol. 3, no. 3, pp. 542–553, 2021. DOI: 10.1109/TMRB.2021.3098921.
- [30] F. Sup, H. A. Varol, and M. Goldfarb, "Upslope walking with a powered knee and ankle prosthesis: Initial results with an amputee subject," *IEEE Transactions on Neural Systems and Rehabilitation Engineering*, vol. 19, no. 1, pp. 71–78, 2011.
- [31] A. H. Shultz, B. E. Lawson, and M. Goldfarb, "Running with a powered knee and ankle prosthesis," *IEEE Transactions on Neural Systems and Rehabilitation Engineering*, vol. 23, no. 3, pp. 403–412, 2015.
- [32] B. E. Lawson, B. Ruhe, A. Shultz, and M. Goldfarb, "A powered prosthetic intervention for bilateral transfemoral amputees," *IEEE Transactions on Biomedical Engineering*, vol. 62, no. 4, pp. 1042–1050, 2015.
- [33] A. Simon, K. Ingraham, N. Fey, *et al.*, "Configuring a powered knee and ankle prosthesis for transfemoral amputees within five specific ambulation modes," *PloS one*, vol. 9, e99387, Jun. 2014. DOI: 10.1371/journal.pone.0099387.
- [34] N. Aghasadeghi, H. Zhao, L. J. Hargrove, A. D. Ames, E. J. Perreault, and T. Bretl, "Learning impedance controller parameters for lower-limb prostheses," in *Intelligent robots and systems (IROS), 2013 IEEE/RSJ international conference on*, IEEE, 2013, pp. 4268–4274.
- [35] H. Zhao, J. Horn, J. Reher, V. Paredes, and A. D. Ames, "First steps toward translating robotic walking to prostheses: A nonlinear optimization based control approach.," *Autonomous Robots*, vol. 41, no. 3, pp. 725–742, 2017.

- [36] H. Zhao, J. Horn, J. Reher, V. Paredes, and A. D. Ames, “Multicon-tact locomotion on transfemoral prostheses via hybrid system models and optimization-based control,” *IEEE Transactions on Automation Science and Engineering*, vol. 13, no. 2, pp. 502–513, Apr. 2016. doi: 10.1109/TASE.2016.2524528.
- [37] J. Reher, C. Kann, and A. D. Ames, “An inverse dynamics approach to control lyapunov functions,” in *2020 American Control Conference (ACC)*, 2020, pp. 2444–2451.
- [38] H. Khalil, *Nonlinear Systems*, ser. Pearson Education. Prentice Hall, 2002, ISBN: 9780130673893.
- [39] S. Sastry, *Nonlinear Systems: Analysis, Stability, and Control*, ser. Interdisci- plinary Applied Mathematics. Springer New York, 2013, ISBN: 9781475731088.
- [40] L. F. Teixeira-Salmela, S. Nadeau, M.-H. Milot, D. Gravel, and L. F. Requião, “Effects of cadence on energy generation and absorption at lower extremity joints during gait,” *Clinical Biomechanics*, vol. 23, no. 6, pp. 769–778, 2008, ISSN: 0268-0033.
- [41] L. Torburn, G. Schweiger, J. Perry, and C. Powers, “Below-knee amputee gait in stair ambulation: A comparison of stride characteristics using five different prosthetic feet,” *Clinical orthopaedics and related research*, pp. 185–92, Jul. 1994.
- [42] H. J. Vack, D. H. Nielsen, and D. G. Shurp, “Kinetic patterns during stair ascent in patients with transtibial amputations using three different prosthe- ses,” *Jpo Journal of Prosthetics and Orthotics*, vol. 11, pp. 57–62, 1999.
- [43] T. Schmalz, S. Blumentritt, and B. Marx, “Biomechanical analysis of stair ambulation in lower limb amputees,” *Gait & Posture*, vol. 25, no. 2, pp. 267– 278, 2007, ISSN: 0966-6362.
- [44] H. Hobara, Y. Kobayashi, T. Nakamura, *et al.*, “Lower extremity joint kine- matics of stair ascent in transfemoral amputees,” *Prosthetics and orthotics international*, vol. 35, pp. 467–72, Dec. 2011.
- [45] R. Riener, M. Rabuffetti, and C. Frigo, “Stair ascent and descent at different inclinations,” *Gait & Posture*, vol. 15, no. 1, pp. 32–44, 2002, ISSN: 0966- 6362.
- [46] A. Armannsdottir, R. Tranberg, G. Halldorsdottir, and K. Briem, “Frontal plane pelvis and hip kinematics of transfemoral amputee gait. effect of a prosthetic foot with active ankle dorsiflexion and individualized training – a case study,” *Disability and Rehabilitation: Assistive Technology*, vol. 13, no. 4, pp. 388–393, 2018, PMID: 28974119.

- [47] D. C. Morgenroth, A. D. Segal, K. E. Zelik, *et al.*, “The effect of prosthetic foot push-off on mechanical loading associated with knee osteoarthritis in lower extremity amputees,” *Gait & posture*, vol. 34, no. 4, pp. 502–507, 2011.
- [48] R. L. Waters, J. Perry, D. J. Antonelli, and H. J. Hislop, “Energy cost of walking of amputees: The influence of level of amputation.,” *The Journal of bone and joint surgery. American volume*, vol. 58 1, pp. 42–6, 1976.
- [49] F. Nowroozi, M. L. Salvaneli, and L. H. Gerber, “Energy expenditure in hip disarticulation and hemipelvectomy amputees.,” *Archives of physical medicine and rehabilitation*, vol. 64 7, pp. 300–3, 1983.
- [50] R. Browning, J. Modica, R. Kram, and A. Goswami, “The effects of adding mass to the legs on the energetics and biomechanics of walking,” *Medicine and science in sports and exercise*, vol. 39, pp. 515–25, Apr. 2007.
- [51] D. Quintero, E. Reznick, D. J. Lambert, S. Rezazadeh, L. Gray, and R. D. Gregg, “Intuitive clinician control interface for a powered knee-ankle prosthesis: A case study,” *IEEE journal of translational engineering in health and medicine*, vol. 6, pp. 1–9, 2018.
- [52] M. Tucker, J. Olivier, A. Pagel, *et al.*, “Control strategies for active lower extremity prosthetics and orthotics: A review,” *Journal of NeuroEngineering and Rehabilitation*, vol. 12, p. 1, Jan. 2015.
- [53] M. Windrich, M. Grimmer, O. Christ, S. Rinderknecht, and P. Beckerle, “Active lower limb prosthetics: A systematic review of design issues and solutions,” *BioMedical Engineering OnLine*, vol. 15, Dec. 2016.
- [54] M. A. Price, P. Beckerle, and F. C. Sup, “Design optimization in lower limb prostheses: A review,” *IEEE Transactions on Neural Systems and Rehabilitation Engineering*, vol. 27, no. 8, pp. 1574–1588, 2019.
- [55] A. S. Voloshina and S. H. Collins, “Lower limb active prosthetic systems—overview,” *Wearable robotics*, pp. 469–486, 2020.
- [56] G. R. B. Hurley, R. McKenney, M. Robinson, M. Zadavec, and M. R. Pierrynowski, “The role of the contralateral limb in below-knee amputee gait,” *Prosthetics and Orthotics International*, vol. 14, no. 1, pp. 33–42, 1990, PMID: 2192355.
- [57] A. Boonstra, J. Schrama, V. Fidler, and W. Eisma, “The gait of unilateral transfemoral amputees,” *Scandinavian journal of rehabilitation medicine*, vol. 26, pp. 217–23, Jan. 1995.
- [58] L. Nolan and A. Lees, “The functional demands on the intact limb during walking for active trans-femoral and trans-tibial amputees,” *Prosthetics and orthotics international*, vol. 24, pp. 117–25, Sep. 2000.

- [59] L. Nolan, A. Wit, K. Dudziński, A. Lees, M. Lake, and M. Wychowski, "Adjustments in gait symmetry in trans-femoral and trans-tibial amputees," *Gait & posture*, vol. 17, pp. 142–51, May 2003.
- [60] E. Isakov, H. Burger, J. Krajnik, M. Gregorič, and Č. Marinček, "Double-limb support and step-length asymmetry in below-knee amputees.," *Scandinavian journal of rehabilitation medicine*, vol. 29 2, pp. 75–9, 1997.
- [61] S. M. Jaegers, J. H. Arendzen, and H. J. de Jongh, "Prosthetic gait of unilateral transfemoral amputees: A kinematic study.," *Archives of physical medicine and rehabilitation*, vol. 76 8, pp. 736–43, 1995.
- [62] J. Engsborg, A. Lee, K. Tedford, and J. Harder, "Normative ground reaction force data for able-bodied and below-knee-amputee children during walking," *Journal of pediatric orthopedics*, vol. 13, pp. 169–73, Mar. 1993.
- [63] K. Suzuki, "Force plate study on the artificial limb gait," *J Jpn Orthop Assoc*, vol. 46, pp. 43–55, 1974.
- [64] M. Schmid, G. Beltrami, D. Zambarbieri, and G. Verni, "Centre of pressure displacements in trans-femoral amputees during gait," *Gait & posture*, vol. 21, pp. 255–62, May 2005.
- [65] R. D. Gregg, T. Lenzi, L. J. Hargrove, and J. W. Sensinger, "Virtual constraint control of a powered prosthetic leg: From simulation to experiments with transfemoral amputees," *IEEE Transactions on Robotics*, vol. 30, no. 6, pp. 1455–1471, 2014.
- [66] A. M. Simon, N. P. Fey, K. A. Ingraham, S. B. Finucane, E. G. Halsne, and L. J. Hargrove, "Improved weight-bearing symmetry for transfemoral amputees during standing up and sitting down with a powered knee-ankle prosthesis," *Archives of Physical Medicine and Rehabilitation*, vol. 97, no. 7, pp. 1100–1106, 2016, ISSN: 0003-9993.
- [67] C. Jayaraman, S. Hoppe-Ludwig, S. Deems-Dluhy, *et al.*, "Impact of powered knee-ankle prosthesis on low back muscle mechanics in transfemoral amputees: A case series," *Frontiers in Neuroscience*, vol. 12, 2018, ISSN: 1662-453X.
- [68] G. R. Hunt, S. Hood, and T. Lenzi, "Stand-up, squat, lunge, and walk with a robotic knee and ankle prosthesis under shared neural control," *IEEE Open Journal of Engineering in Medicine and Biology*, vol. 2, pp. 267–277, 2021.
- [69] M. F. Eilenberg, H. Geyer, and H. Herr, "Control of a powered ankle-foot prosthesis based on a neuromuscular model," *IEEE Transactions on Neural Systems and Rehabilitation Engineering*, vol. 18, no. 2, pp. 164–173, 2010.
- [70] N. Thatte and H. Geyer, "Toward balance recovery with leg prostheses using neuromuscular model control," *IEEE Transactions on Biomedical Engineering*, vol. 63, no. 5, pp. 904–913, 2015.

- [71] M. Latash and V. Zatsiorsky, "Joint stiffness: Myth or reality?" *Human Movement Science*, vol. 12, pp. 653–692, Dec. 1993.
- [72] E. J. Rouse, R. D. Gregg, L. J. Hargrove, and J. W. Sensinger, "The difference between stiffness and quasi-stiffness in the context of biomechanical modeling," *IEEE Transactions on Biomedical Engineering*, vol. 60, no. 2, pp. 562–568, 2013.
- [73] T. Lenzi, L. Hargrove, and J. Sensinger, "Speed-adaptation mechanism: Robotic prostheses can actively regulate joint torque," *IEEE Robotics & Automation Magazine*, vol. 21, no. 4, pp. 94–107, 2014.
- [74] S. Blumentritt, H. W. Scherer, U. Wellershaws, and J. W. Michael, "Design principles, biomechanical data and clinical experience with a polycentric knee offering controlled stance phase knee flexion: A preliminary report," *JPO Journal of Prosthetics and Orthotics*, vol. 9, pp. 18–24, 1997.
- [75] V. T. Inman, "Human locomotion," *Canadian Medical Association journal*, vol. 94 20, pp. 1047–54, 1966.
- [76] N. Thatte, T. Shah, and H. Geyer, "Robust and adaptive lower limb prosthesis stance control via extended kalman filter-based gait phase estimation," *IEEE Robotics and Automation Letters*, vol. 4, no. 4, pp. 3129–3136, 2019.
- [77] R. Gehlhar and A. D. Ames, "Emulating human kinematic behavior on lower-limb prostheses via multi-contact models and force-based nonlinear control," in *Submitted to 2023 IEEE International Conference on Robotics and Automation (ICRA)*, IEEE, 2022. [Online]. Available: <https://arxiv.org/abs/2209.13739>,
- [78] S. Hood, L. Gabert, and T. Lenzi, "Powered knee and ankle prosthesis with adaptive control enables climbing stairs with different stair heights, cadences, and gait patterns," *IEEE Transactions on Robotics*, vol. 38, no. 3, pp. 1430–1441, 2022.
- [79] S. Huang, J. P. Wensman, and D. P. Ferris, "An experimental powered lower limb prosthesis using proportional myoelectric control," *Journal of Medical Devices*, vol. 8, no. 2, 2014.
- [80] A. Brandt and H. H. Huang, "Effects of extended stance time on a powered knee prosthesis and gait symmetry on the lateral control of balance during walking in individuals with unilateral amputation," *Journal of neuroengineering and rehabilitation*, vol. 16, no. 1, pp. 1–11, 2019.
- [81] R. Bohannon, "Comfortable and maximum walking speed of adults aged 20-79 years: Reference values and determinants," *Age and ageing*, vol. 26, pp. 15–9, Jan. 1997.
- [82] H. J. Ralston, "Energy-speed relation and optimal speed during level walking," *Internationale Zeitschrift für angewandte Physiologie einschließlich Arbeitsphysiologie*, vol. 17, pp. 277–283, 2004.

- [83] D. Winter, *The Biomechanics and Motor Control of Human Gait: Normal, Elderly and Pathological*, 2nd. University of Waterloo Press, 1991, ISBN: 9780888981059.
- [84] C. G. Welker, A. S. Voloshina, V. L. Chiu, and S. H. Collins, “Shortcomings of human-in-the-loop optimization of an ankle-foot prosthesis emulator: A case series,” *Royal Society open science*, vol. 8, no. 5, p. 202 020, 2021.
- [85] R. E. Quesada, J. M. Caputo, and S. H. Collins, “Increasing ankle push-off work with a powered prosthesis does not necessarily reduce metabolic rate for transtibial amputees,” *Journal of Biomechanics*, vol. 49, no. 14, pp. 3452–3459, 2016.
- [86] H. Zhao, A. Hereid, E. Ambrose, and A. D. Ames, “3d multi-contact gait design for prostheses: Hybrid system models, virtual constraints and two-step direct collocation,” in *2016 IEEE 55th Conference on Decision and Control (CDC)*, 2016, pp. 3668–3674. DOI: 10.1109/CDC.2016.7798821.
- [87] K. Li, M. Tucker, R. Gehlhar, Y. Yue, and A. D. Ames, “Natural multicontact walking for robotic assistive devices via musculoskeletal models and hybrid zero dynamics,” *IEEE Robotics and Automation Letters*, vol. 7, no. 2, pp. 4283–4290, 2022. DOI: 10.1109/LRA.2022.3149568,
- [88] S. Fritz and M. Lusardi, “Walking speed: The sixth vital sign,” *J Geriatr Phys Ther*, vol. 32, pp. 46–49, Jan. 2009.
- [89] T. R. Clites, M. J. Carty, J. B. Ullauri, *et al.*, “Proprioception from a neurally controlled lower-extremity prosthesis,” *Science Translational Medicine*, vol. 10, no. 443, eaap8373, 2018.
- [90] A. J. Young and L. J. Hargrove, “A classification method for user-independent intent recognition for transfemoral amputees using powered lower limb prostheses,” *IEEE Transactions on Neural Systems and Rehabilitation Engineering*, vol. 24, no. 2, pp. 217–225, 2015.
- [91] J. Mendez, S. Hood, A. Gunnell, and T. Lenzi, “Powered knee and ankle prosthesis with indirect volitional swing control enables level-ground walking and crossing over obstacles,” *Science Robotics*, vol. 5, no. 44, eaba6635, 2020.
- [92] T. K. Best, K. R. Embry, E. J. Rouse, and R. D. Gregg, “Phase-variable control of a powered knee-ankle prosthesis over continuously varying speeds and inclines,” in *2021 IEEE/RSJ International Conference on Intelligent Robots and Systems (IROS)*, IEEE, 2021, pp. 6182–6189.
- [93] J. Kulkarni, S. Wright, C. Toole, J. Morris, and R. Hiron, “Falls in patients with lower limb amputations: Prevalence and contributing factors,” *Physiotherapy*, vol. 82, no. 2, pp. 130–136, 1996, ISSN: 0031-9406.
- [94] —, “Falls in patients with lower limb amputations: Prevalence and contributing factors,” English, *Physiotherapy*, vol. 82, no. 2, pp. 130–136, 1996.

- [95] W. C. Miller, A. B. Deathe, M. Speechley, and J. Koval, "The influence of falling, fear of falling, and balance confidence on prosthetic mobility and social activity among individuals with a lower extremity amputation," *Archives of physical medicine and rehabilitation*, vol. 82, no. 9, pp. 1238–1244, 2001.
- [96] C. K. Wong, J. Wilska, and M. Stern, "Balance, balance confidence, and falls using nonmicroprocessor and microprocessor knee prostheses: A case study after vascular amputation with 12-month follow-up," *JPO: Journal of Prosthetics and Orthotics*, vol. 24, no. 1, pp. 16–18, 2012.
- [97] R. Gehlhar, J.-h. Yang, and A. D. Ames, "Powered prosthesis locomotion on varying terrains: Model-dependent control with real-time force sensing," *IEEE Robotics and Automation Letters*, vol. 7, no. 2, pp. 5151–5158, 2022. DOI: 10.1109/LRA.2022.3154810,
- [98] A. Fleming, N. Stafford, S. Huang, X. Hu, D. P. Ferris, and H. H. Huang, "Myoelectric control of robotic lower limb prostheses: A review of electromyography interfaces, control paradigms, challenges and future directions," *Journal of neural engineering*, vol. 18, no. 4, p. 041004, 2021.
- [99] J. Sigurdardottir, "Emg as a control parameter in lower limb prosthetics: Surface vs. implanted electrodes," Ph.D. dissertation, Reykjavik University, 2015.
- [100] H. A. Dewald, P. Lukyanenko, J. M. Lambrecht, *et al.*, "Stable, three degree-of-freedom myoelectric prosthetic control via chronic bipolar intramuscular electrodes: A case study," *Journal of NeuroEngineering and Rehabilitation*, vol. 16, no. 1, pp. 1–13, 2019.
- [101] M. Ortiz-Catalan, R. Brånemark, B. Håkansson, and J. Delbeke, "On the viability of implantable electrodes for the natural control of artificial limbs: Review and discussion," *Biomedical engineering online*, vol. 11, no. 1, pp. 1–24, 2012.
- [102] P. F. Pasquina, M. Evangelista, A. J. Carvalho, *et al.*, "First-in-man demonstration of a fully implanted myoelectric sensors system to control an advanced electromechanical prosthetic hand," *Journal of neuroscience methods*, vol. 244, pp. 85–93, 2015.
- [103] A. K. Vaskov, P. P. Vu, N. North, *et al.*, "Surgically implanted electrodes enable real-time finger and grasp pattern recognition for prosthetic hands," *IEEE Transactions on Robotics*, 2022.
- [104] J. Wang, O. A. Kannape, and H. M. Herr, "Proportional emg control of ankle plantar flexion in a powered transtibial prosthesis," in *2013 IEEE 13th International Conference on Rehabilitation Robotics (ICORR)*, 2013, pp. 1–5.

- [105] X. Zhang and H. Huang, "A real-time, practical sensor fault-tolerant module for robust emg pattern recognition," *Journal of neuroengineering and rehabilitation*, vol. 12, no. 1, pp. 1–16, 2015.
- [106] J. W. Sensinger, B. A. Lock, and T. A. Kuiken, "Adaptive pattern recognition of myoelectric signals: Exploration of conceptual framework and practical algorithms," *IEEE Transactions on Neural Systems and Rehabilitation Engineering*, vol. 17, no. 3, pp. 270–278, 2009.
- [107] J. H. Hong and M. S. Mun, "Relationship between socket pressure and emg of two muscles in trans-femoral stumps during gait," *Prosthetics and orthotics international*, vol. 29, no. 1, pp. 59–72, 2005.
- [108] A. C. Myers, H. Huang, and Y. Zhu, "Wearable silver nanowire dry electrodes for electrophysiological sensing," *Rsc Advances*, vol. 5, no. 15, pp. 11 627–11 632, 2015.
- [109] S. H. Yeon, T. Shu, H. Song, *et al.*, "Acquisition of surface emg using flexible and low-profile electrodes for lower extremity neuroprosthetic control," *IEEE Transactions on Medical Robotics and Bionics*, vol. 3, no. 3, pp. 563–572, 2021.
- [110] S. Huang and D. P. Ferris, "Muscle activation patterns during walking from transtibial amputees recorded within the residual limb-prosthetic interface," *Journal of neuroengineering and rehabilitation*, vol. 9, no. 1, pp. 1–16, 2012.
- [111] E. C. Wentink, E. C. Prinsen, J. S. Rietman, and P. H. Veltink, "Comparison of muscle activity patterns of transfemoral amputees and control subjects during walking," *Journal of neuroengineering and rehabilitation*, vol. 10, no. 1, pp. 1–11, 2013.
- [112] A. G. Kurbis, B. Laschowski, and A. Mihailidis, "Stair recognition for robotic exoskeleton control using computer vision and deep learning," *bioRxiv*, 2022.
- [113] J. P. Diaz, R. L. da Silva, B. Zhong, H. H. Huang, and E. Lobaton, "Visual terrain identification and surface inclination estimation for improving human locomotion with a lower-limb prosthetic," in *2018 40th Annual International Conference of the IEEE Engineering in Medicine and Biology Society (EMBC)*, IEEE, 2018, pp. 1817–1820.
- [114] N. E. Krausz, T. Lenzi, and L. J. Hargrove, "Depth sensing for improved control of lower limb prostheses," *IEEE Transactions on Biomedical Engineering*, vol. 62, no. 11, pp. 2576–2587, 2015.
- [115] M. Liu, D. Wang, and H. Huang, "Development of an environment-aware locomotion mode recognition system for powered lower limb prostheses," *IEEE Transactions on Neural Systems and Rehabilitation Engineering*, vol. 24, no. 4, pp. 434–443, 2015.

- [116] N. Thatte, N. Srinivasan, and H. Geyer, “Real-time reactive trip avoidance for powered transfemoral prostheses,” *Robotics: Science and Systems XV*, 2019.
- [117] A. J. Young, A. M. Simon, N. P. Fey, and L. J. Hargrove, “Intent recognition in a powered lower limb prosthesis using time history information,” *Annals of biomedical engineering*, vol. 42, no. 3, pp. 631–641, 2014.
- [118] S. Culver, H. Bartlett, A. Shultz, and M. Goldfarb, “A stair ascent and descent controller for a powered ankle prosthesis,” *IEEE Transactions on Neural Systems and Rehabilitation Engineering*, vol. 26, no. 5, pp. 993–1002, 2018.
- [119] W. Svensson and U. Holmberg, “Foot and ground measurement using portable sensors,” in *9th International Conference on Rehabilitation Robotics, 2005. ICORR 2005.*, 2005, pp. 448–451.
- [120] W. S. Ulf Holmberg, “An autonomous control system for a prosthetic foot ankle,” *IFAC Proceedings Volumes*, vol. 39, no. 16, pp. 856–861, 2006, 4th IFAC Symposium on Mechatronic Systems, ISSN: 1474-6670.
- [121] E. Ceseracciu, M. Reggiani, Z. Sawacha, *et al.*, “Svm classification of locomotion modes using surface electromyography for applications in rehabilitation robotics,” in *19th International Symposium in Robot and Human Interactive Communication*, IEEE, 2010, pp. 165–170.
- [122] I. J. Myung, “Tutorial on maximum likelihood estimation,” *Journal of mathematical Psychology*, vol. 47, no. 1, pp. 90–100, 2003.
- [123] H. Huang, F. Zhang, L. J. Hargrove, Z. Dou, D. R. Rogers, and K. B. Englehart, “Continuous locomotion-mode identification for prosthetic legs based on neuromuscular–mechanical fusion,” *IEEE Transactions on Biomedical Engineering*, vol. 58, no. 10, pp. 2867–2875, 2011.
- [124] L. J. Hargrove, K. Englehart, and B. Hudgins, “A comparison of surface and intramuscular myoelectric signal classification,” *IEEE transactions on biomedical engineering*, vol. 54, no. 5, pp. 847–853, 2007.
- [125] A. V. Nefian, L. Liang, X. Pi, X. Liu, and K. Murphy, “Dynamic bayesian networks for audio-visual speech recognition,” *EURASIP Journal on Advances in Signal Processing*, vol. 2002, no. 11, pp. 1–15, 2002.
- [126] L. Peeraer, B. Aeyels, and G. Van der Perre, “Development of emg-based mode and intent recognition algorithms for a computer-controlled above-knee prosthesis,” *Journal of biomedical engineering*, vol. 12, no. 3, pp. 178–182, 1990.
- [127] H. Huang, T. A. Kuiken, R. D. Lipschutz, *et al.*, “A strategy for identifying locomotion modes using surface electromyography,” *IEEE Transactions on Biomedical Engineering*, vol. 56, no. 1, pp. 65–73, 2008.

- [128] L. J. Hargrove, A. M. Simon, A. J. Young, *et al.*, “Robotic leg control with emg decoding in an amputee with nerve transfers,” *New England Journal of Medicine*, vol. 369, no. 13, pp. 1237–1242, 2013.
- [129] D. Jin, J. Yang, R. Zhang, R. Wang, and J. Zhang, “Terrain identification for prosthetic knees based on electromyographic signal features,” *Tsinghua Science and Technology*, vol. 11, no. 1, pp. 74–79, 2006.
- [130] T. Hussain, N. Iqbal, H. F. Maqbool, M. Khan, M. I. Awad, and A. A. Dehghani-Sanij, “Intent based recognition of walking and ramp activities for amputee using semg based lower limb prostheses,” *Biocybernetics and biomedical engineering*, vol. 40, no. 3, pp. 1110–1123, 2020.
- [131] L. J. Hargrove, A. J. Young, A. M. Simon, *et al.*, “Intuitive Control of a Powered Prosthetic Leg During Ambulation: A Randomized Clinical Trial,” *JAMA*, vol. 313, no. 22, pp. 2244–2252, Jun. 2015, ISSN: 0098-7484.
- [132] F. Zhang and H. Huang, “Source selection for real-time user intent recognition toward volitional control of artificial legs,” *IEEE Journal of Biomedical and Health Informatics*, vol. 17, no. 5, pp. 907–914, 2013.
- [133] K. Bhakta, J. Camargo, L. Donovan, K. Herrin, and A. Young, “Machine learning model comparisons of user independent & dependent intent recognition systems for powered prostheses,” *IEEE Robotics and Automation Letters*, vol. 5, no. 4, pp. 5393–5400, 2020.
- [134] J. Camargo, W. Flanagan, N. Csomay-Shanklin, B. Kanwar, and A. Young, “A machine learning strategy for locomotion classification and parameter estimation using fusion of wearable sensors,” *IEEE Transactions on Biomedical Engineering*, vol. 68, no. 5, pp. 1569–1578, 2021.
- [135] K. Bhakta, J. Camargo, W. Compton, K. Herrin, and A. Young, “Evaluation of continuous walking speed determination algorithms and embedded sensors for a powered knee & ankle prosthesis,” *IEEE Robotics and Automation Letters*, vol. 6, no. 3, pp. 4820–4826, 2021.
- [136] K. Aminian, B. Najafi, C. Büla, P.-F. Leyvraz, and P. Robert, “Spatio-temporal parameters of gait measured by an ambulatory system using miniature gyroscopes,” *Journal of biomechanics*, vol. 35, no. 5, pp. 689–699, 2002.
- [137] B. Mariani, C. Hoskovec, S. Rochat, C. Büla, J. Penders, and K. Aminian, “3d gait assessment in young and elderly subjects using foot-worn inertial sensors,” *Journal of biomechanics*, vol. 43, no. 15, pp. 2999–3006, 2010.
- [138] Q. Li, M. Young, V. Naing, and J. Donelan, “Walking speed estimation using a shank-mounted inertial measurement unit,” *Journal of biomechanics*, vol. 43, no. 8, pp. 1640–1643, 2010.

- [139] J.-S. Hu, K.-C. Sun, and C.-Y. Cheng, “A kinematic human-walking model for the normal-gait-speed estimation using tri-axial acceleration signals at waist location,” *IEEE Transactions on Biomedical Engineering*, vol. 60, no. 8, pp. 2271–2279, 2013.
- [140] Z. He and W. Zhang, “Estimation of walking speed using accelerometer and artificial neural networks,” in *International Workshop on Computer Science for Environmental Engineering and EcoInformatics*, Springer, 2011, pp. 42–47.
- [141] H. Vathsangam, A. Emken, D. Spruijt-Metz, and G. S. Sukhatme, “Toward free-living walking speed estimation using gaussian process-based regression with on-body accelerometers and gyroscopes,” in *2010 4th International Conference on Pervasive Computing Technologies for Healthcare*, IEEE, 2010, pp. 1–8.
- [142] S. Zihajehzadeh and E. J. Park, “Regression model-based walking speed estimation using wrist-worn inertial sensor,” *PloS one*, vol. 11, no. 10, e0165211, 2016.
- [143] H. T. T. Vu, D. Dong, H.-L. Cao, *et al.*, “A review of gait phase detection algorithms for lower limb prostheses,” *Sensors*, vol. 20, no. 14, p. 3972, 2020.
- [144] D. Winter, *Biomechanics and Motor Control of Human Movement*. Wiley, 2009, ISBN: 9780470398180.
- [145] S. Au, M. Berniker, and H. Herr, “Powered ankle-foot prosthesis to assist level-ground and stair-descent gaits,” *Neural Networks*, vol. 21, no. 4, pp. 654–666, 2008, Robotics and Neuroscience, ISSN: 0893-6080.
- [146] R. Fluit, E. Prinsen, S. Wang, and H. Kooij, “A comparison of control strategies in commercial and research knee prostheses,” *IEEE transactions on bio-medical engineering*, vol. PP, Apr. 2019.
- [147] A. M. Simon, K. A. Ingraham, N. P. Fey, *et al.*, “Configuring a powered knee and ankle prosthesis for transfemoral amputees within five specific ambulation modes,” *PloS one*, vol. 9, no. 6, e99387, 2014.
- [148] S. C. Culver, L. G. Vailati, and M. Goldfarb, “A primarily-passive knee prosthesis with powered stance and swing assistance,” in *2022 International Conference on Rehabilitation Robotics (ICORR)*, 2022, pp. 1–6.
- [149] N. Thatte and H. Geyer, “Comparison of balance recovery among current control strategies for robotic leg prostheses,” in *Wearable Robotics: Challenges and Trends*, J. C. Moreno, J. Masood, U. Schneider, C. Maufroy, and J. L. Pons, Eds., Cham: Springer International Publishing, 2022, pp. 63–67, ISBN: 978-3-030-69547-7.

- [150] S. Jiang, S. Partrick, H. Zhao, and A. D. Ames, “Outputs of human walking for bipedal robotic controller design,” in *American Control Conference (ACC), 2012*, IEEE, 2012, pp. 4843–4848.
- [151] M. A. Holgate, T. G. Sugar, and A. W. Bohler, “A novel control algorithm for wearable robotics using phase plane invariants,” in *2009 IEEE International Conference on Robotics and Automation*, 2009, pp. 3845–3850.
- [152] R. W. Sinnet, H. Zhao, and A. D. Ames, “Simulating prosthetic devices with human-inspired hybrid control,” in *2011 IEEE/RSJ International Conference on Intelligent Robots and Systems*, IEEE, 2011, pp. 1723–1730.
- [153] E. R. Westervelt, J. W. Grizzle, and D. E. Koditschek, “Hybrid zero dynamics of planar biped walkers,” *IEEE Transactions on Automatic Control*, vol. 48, no. 1, pp. 42–56, Jan. 2003.
- [154] E. R. Westervelt, J. W. Grizzle, C. Chevallereau, J. H. Choi, and B. Morris, *Feedback control of dynamic bipedal robot locomotion*. CRC press, 2018.
- [155] D. J. Villarreal, H. A. Poonawala, and R. D. Gregg, “A robust parameterization of human gait patterns across phase-shifting perturbations,” *IEEE Transactions on Neural Systems and Rehabilitation Engineering*, vol. 25, no. 3, pp. 265–278, 2017.
- [156] D. Villarreal and R. Gregg, “Unified phase variables of relative degree two for human locomotion,” in *2016 38th Annual International Conference of the IEEE Engineering in Medicine and Biology Society (EMBC)*, IEEE, 2016, pp. 6262–6267.
- [157] H. L. Bartlett, S. T. King, M. Goldfarb, and B. E. Lawson, “Design and assist-as-needed control of a lightly powered prosthetic knee,” *IEEE Transactions on Medical Robotics and Bionics*, vol. 4, no. 2, pp. 490–501, 2022.
- [158] D. Quintero, D. J. Villarreal, D. J. Lambert, S. Kapp, and R. D. Gregg, “Continuous-phase control of a powered knee–ankle prosthesis: Amputee experiments across speeds and inclines,” *IEEE Transactions on Robotics*, vol. 34, no. 3, pp. 686–701, 2018.
- [159] D. J. Villarreal and R. D. Gregg, “A survey of phase variable candidates of human locomotion,” in *2014 36th Annual International Conference of the IEEE Engineering in Medicine and Biology Society*, 2014, pp. 4017–4021.
- [160] S. Rezazadeh, D. Quintero, N. Divekar, E. Reznick, L. Gray, and R. D. Gregg, “A phase variable approach for improved rhythmic and non-rhythmic control of a powered knee-ankle prosthesis,” *IEEE Access*, vol. 7, pp. 109 840–109 855, 2019.
- [161] T. Best, C. Welker, E. Rouse, and R. Gregg, “Data-Driven Variable Impedance Control of a Powered Knee-Ankle Prosthesis for Adaptive Speed and Incline Walking,” *techriv preprint techrxiv:19165895.v3*, Aug. 2022.

- [162] H. T. T. Vu, F. Gomez, P. Cherelle, D. Lefeber, A. Nowé, and B. Vanderborght, “Ed-fnn: A new deep learning algorithm to detect percentage of the gait cycle for powered prostheses,” *Sensors*, vol. 18, no. 7, p. 2389, 2018.
- [163] A. Mannini, V. Genovese, and A. M. Sabatini, “Online decoding of hidden markov models for gait event detection using foot-mounted gyroscopes,” *IEEE journal of biomedical and health informatics*, vol. 18, no. 4, pp. 1122–1130, 2013.
- [164] J. Taborri, E. Scalona, E. Palermo, S. Rossi, and P. Cappa, “Validation of inter-subject training for hidden markov models applied to gait phase detection in children with cerebral palsy,” *Sensors*, vol. 15, no. 9, pp. 24 514–24 529, 2015.
- [165] R. L. Evans and D. Arvind, “Detection of gait phases using orient specks for mobile clinical gait analysis,” in *2014 11th International Conference on Wearable and Implantable Body Sensor Networks*, IEEE, 2014, pp. 149–154.
- [166] J. Bae and M. Tomizuka, “Gait phase analysis based on a hidden markov model,” *Mechatronics*, vol. 21, no. 6, pp. 961–970, 2011.
- [167] M. D. Sánchez Manchola, M. J. P. Bernal, M. Munera, and C. A. Cifuentes, “Gait phase detection for lower-limb exoskeletons using foot motion data from a single inertial measurement unit in hemiparetic individuals,” *Sensors*, vol. 19, no. 13, p. 2988, 2019.
- [168] H. Zhao, Z. Wang, S. Qiu, *et al.*, “Adaptive gait detection based on foot-mounted inertial sensors and multi-sensor fusion,” *Information Fusion*, vol. 52, pp. 157–166, 2019.
- [169] N. Nazmi, M. A. A. Rahman, S.-I. Yamamoto, and S. A. Ahmad, “Walking gait event detection based on electromyography signals using artificial neural network,” *Biomedical Signal Processing and Control*, vol. 47, pp. 334–343, 2019.
- [170] M. Gadaleta, G. Cisotto, M. Rossi, R. Z. U. Rehman, L. Rochester, and S. Del Din, “Deep learning techniques for improving digital gait segmentation,” in *2019 41st Annual International Conference of the IEEE Engineering in Medicine and Biology Society (EMBC)*, IEEE, 2019, pp. 1834–1837.
- [171] M. Lempereur, F. Rousseau, O. Rémy-Néris, *et al.*, “A new deep learning-based method for the detection of gait events in children with gait disorders: Proof-of-concept and concurrent validity,” *Journal of biomechanics*, vol. 98, p. 109 490, 2020.
- [172] J. Taborri, E. Palermo, S. Rossi, and P. Cappa, “Gait partitioning methods: A systematic review,” *Sensors*, vol. 16, no. 1, p. 66, 2016.

- [173] N. Hogan, “Adaptive control of mechanical impedance by coactivation of antagonist muscles,” *IEEE Transactions on Automatic Control*, vol. 29, no. 8, pp. 681–690, 1984.
- [174] N. P. Fey, A. M. Simon, A. J. Young, and L. J. Hargrove, “Controlling knee swing initiation and ankle plantarflexion with an active prosthesis on level and inclined surfaces at variable walking speeds,” *IEEE Journal of Translational Engineering in Health and Medicine*, vol. 2, pp. 1–12, 2014.
- [175] W. Hong, V. Paredes, K. Chao, S. Patrick, and P. Hur, “Consolidated control framework to control a powered transfemoral prosthesis over inclined terrain conditions,” in *2019 International Conference on Robotics and Automation (ICRA)*, 2019, pp. 2838–2844.
- [176] H. Lee and N. Hogan, “Time-varying ankle mechanical impedance during human locomotion,” *IEEE Transactions on Neural Systems and Rehabilitation Engineering*, vol. 23, Aug. 2014.
- [177] E. J. Rouse, L. J. Hargrove, E. J. Perreault, and T. A. Kuiken, “Estimation of human ankle impedance during the stance phase of walking,” *IEEE Transactions on Neural Systems and Rehabilitation Engineering*, vol. 22, no. 4, pp. 870–878, 2014.
- [178] A. L. Shorter and E. J. Rouse, “Mechanical impedance of the ankle during the terminal stance phase of walking,” *IEEE Transactions on Neural Systems and Rehabilitation Engineering*, vol. 26, no. 1, pp. 135–143, 2018.
- [179] A. H. Hansen, D. S. Childress, S. C. Miff, S. A. Gard, and K. P. Mesplay, “The human ankle during walking: Implications for design of biomimetic ankle prostheses,” *Journal of Biomechanics*, vol. 37, no. 10, pp. 1467–1474, 2004, ISSN: 0021-9290.
- [180] B. E. Lawson, E. D. Ledoux, and M. Goldfarb, “A robotic lower limb prosthesis for efficient bicycling,” *IEEE Transactions on Robotics*, vol. 33, no. 2, pp. 432–445, 2017.
- [181] R. Baud, A. R. Manzoori, A. Ijspeert, and M. Bouri, “Review of control strategies for lower-limb exoskeletons to assist gait,” *Journal of NeuroEngineering and Rehabilitation*, vol. 18, no. 1, pp. 1–34, 2021.
- [182] J. Zhang, P. Fiers, K. A. Witte, *et al.*, “Human-in-the-loop optimization of exoskeleton assistance during walking,” *Science*, vol. 356, no. 6344, pp. 1280–1284, 2017.
- [183] J. L. van Leeuwen, “Muscle function in locomotion,” in *Mechanics of Animal Locomotion*. 1992, ch. 7, pp. 191–250.
- [184] H. Geyer and H. Herr, “A muscle-reflex model that encodes principles of legged mechanics produces human walking dynamics and muscle activities,” *IEEE Transactions on Neural Systems and Rehabilitation Engineering*, vol. 18, no. 3, pp. 263–273, 2010.

- [185] T. A. Kuiken, G. Dumanian, R. D. Lipschutz, L. Miller, and K. Stubblefield, "The use of targeted muscle reinnervation for improved myoelectric prosthesis control in a bilateral shoulder disarticulation amputee," *Prosthetics and orthotics international*, vol. 28, no. 3, pp. 245–253, 2004.
- [186] J. B. Hijjawi, T. A. Kuiken, R. D. Lipschutz, L. A. Miller, K. A. Stubblefield, and G. A. Dumanian, "Improved myoelectric prosthesis control accomplished using multiple nerve transfers," *Plastic and reconstructive surgery*, vol. 118, no. 7, pp. 1573–1578, 2006.
- [187] T. A. Kuiken, G. Li, B. A. Lock, *et al.*, "Targeted muscle reinnervation for real-time myoelectric control of multifunction artificial arms," *Jama*, vol. 301, no. 6, pp. 619–628, 2009.
- [188] T. Boretius, J. Badia, A. Pascual-Font, *et al.*, "A transverse intrafascicular multichannel electrode (time) to interface with the peripheral nerve," *Biosensors and Bioelectronics*, vol. 26, no. 1, pp. 62–69, 2010.
- [189] F. M. Petrini, M. Bumbasirevic, G. Valle, *et al.*, "Sensory feedback restoration in leg amputees improves walking speed, metabolic cost and phantom pain," *Nature medicine*, vol. 25, no. 9, pp. 1356–1363, 2019.
- [190] R. D. Gregg, E. J. Rouse, L. J. Hargrove, and J. W. Sensinger, "Evidence for a time-invariant phase variable in human ankle control," *PLOS ONE*, vol. 9, no. 2, pp. 1–13, Feb. 2014.
- [191] T. Flash and N. Hogan, "The coordination of arm movements: An experimentally confirmed mathematical model," *Journal of Neuroscience*, vol. 5, no. 7, pp. 1688–1703, 1985, ISSN: 0270-6474.
- [192] K. R. Embry, D. J. Villarreal, R. L. Macaluso, and R. D. Gregg, "Modeling the kinematics of human locomotion over continuously varying speeds and inclines," *IEEE Transactions on Neural Systems and Rehabilitation Engineering*, vol. 26, no. 12, pp. 2342–2350, 2018.
- [193] A. Hansen and D. Childress, "Investigations of roll-over shape: Implications for design, alignment, and evaluation of ankle-foot prostheses and orthoses," *Disability and rehabilitation*, vol. 32, pp. 2201–9, Jan. 2010.
- [194] A. Hansen, D. Childress, and E. Knox, "Roll-over shapes of human locomotor systems: Effects of walking speed," *Clinical biomechanics (Bristol, Avon)*, vol. 19, pp. 407–14, Jun. 2004.
- [195] A. D. Ames, "Human-inspired control of bipedal walking robots," *IEEE Transactions on Automatic Control*, vol. 59, no. 5, pp. 1115–1130, 2014.
- [196] A. Hof, M. Gazendam, and W. Sinke, "The condition for dynamic stability," *Journal of biomechanics*, vol. 38, pp. 1–8, Feb. 2005.
- [197] S. Bruijn, O. Meijer, P. Beek, and J. Van Dieen, "Assessing the stability of human locomotion: A review of current measures," *Journal of the Royal Society, Interface / the Royal Society*, vol. 10, p. 20120999, Oct. 2013.

- [198] A. Hereid, E. A. Cousineau, C. M. Hubicki, and A. D. Ames, “3D dynamic walking with underactuated humanoid robots: A direct collocation framework for optimizing hybrid zero dynamics,” in *Robotics and Automation (ICRA), 2016 IEEE International Conference on*, IEEE, 2016, pp. 1447–1454.
- [199] A. D. Ames, K. Galloway, K. Sreenath, and J. W. Grizzle, “Rapidly exponentially stabilizing control Lyapunov functions and hybrid zero dynamics,” *IEEE Transactions on Automatic Control*, vol. 59, no. 4, pp. 876–891, 2014.
- [200] K. Sreenath, H.-W. Park, I. Poulakakis, and J. Grizzle, “Embedding active force control within the compliant hybrid zero dynamics to achieve stable, fast running on mabel,” *The International Journal of Robotics Research*, vol. 32, no. 3, pp. 324–345, 2013.
- [201] J. P. Reher, A. Hereid, S. Kolathaya, C. M. Hubicki, and A. D. Ames, “Algorithmic foundations of realizing multi-contact locomotion on the humanoid robot durus,” in *Algorithmic Foundations of Robotics XII*, Springer, 2020, pp. 400–415.
- [202] W.-L. Ma, S. Kolathaya, E. R. Ambrose, C. M. Hubicki, and A. D. Ames, “Bipedal robotic running with durus-2d: Bridging the gap between theory and experiment,” in *Proceedings of the 20th International Conference on Hybrid Systems: Computation and Control*, ser. HSCC ’17, Pittsburgh, Pennsylvania, USA: Association for Computing Machinery, 2017, pp. 265–274, ISBN: 9781450345903.
- [203] H. Zhao, J. Reher, J. Horn, V. Paredes, and A. D. Ames, “Realization of stair ascent and motion transitions on prostheses utilizing optimization-based control and intent recognition,” in *Rehabilitation Robotics (ICORR), 2015 IEEE International Conference on*, IEEE, 2015, pp. 265–270.
- [204] R. M. Murray, S. S. Sastry, and L. Zexiang, *A Mathematical Introduction to Robotic Manipulation*, 1st. CRC Press, Inc., 1994, ISBN: 0849379814.
- [205] H. Zhao and A. D. Ames, “Quadratic program based control of fully-actuated transfemoral prosthesis for flat-ground and up-slope locomotion,” in *American Control Conference (ACC), 2014*, IEEE, 2014, pp. 4101–4107.
- [206] A. E. Martin and R. D. Gregg, “Stable, robust hybrid zero dynamics control of powered lower-limb prostheses,” *IEEE Transactions on Automatic Control*, vol. 62, no. 8, pp. 3930–3942, 2017.
- [207] R. Gehlhar, J. Reher, and A. D. Ames, “Control of separable subsystems with application to prostheses,” *arXiv preprint arXiv:1909.03102*, 2019. DOI: [10.48550/arXiv.1909.03102](https://doi.org/10.48550/arXiv.1909.03102),
- [208] R. Gehlhar and A. D. Ames, “Separable control lyapunov functions with application to prostheses,” *IEEE Control Systems Letters*, vol. 5, no. 2, pp. 559–564, 2021. DOI: [10.1109/LCSYS.2020.3004181](https://doi.org/10.1109/LCSYS.2020.3004181),

- [209] G. Taga, “A model of the neuro-musculo-skeletal system for human locomotion,” *Biol. Cybern.*, vol. 73, no. 2, pp. 113–121, Jul. 1995, ISSN: 0340-1200.
- [210] R. Gehlhar and A. D. Ames, “Model-dependent prosthesis control with interaction force estimation,” in *2021 IEEE International Conference on Robotics and Automation (ICRA)*, IEEE, 2021, pp. 3226–3232. DOI: 10.1109/ICRA48506.2021.9561250,
- [211] W. Liu, R. Wu, J. Si, and H. Huang, “A new robotic knee impedance control parameter optimization method facilitated by inverse reinforcement learning,” *IEEE Robotics and Automation Letters*, vol. 7, no. 4, pp. 10 882–10 889, 2022.
- [212] F. Sup IV, A. Varol, J. Mitchell, T. Withrow, and M. Goldfarb, “Preliminary evaluations of a self-contained anthropomorphic transfemoral prosthesis,” *IEEE/ASME transactions on mechatronics : a joint publication of the IEEE Industrial Electronics Society and the ASME Dynamic Systems and Control Division*, vol. 14, pp. 667–676, Dec. 2009.
- [213] T. R. Clites, M. K. Shepherd, K. A. Ingraham, L. Wontorcik, and E. J. Rouse, “Understanding patient preference in prosthetic ankle stiffness,” *Journal of neuroengineering and rehabilitation*, vol. 18, no. 1, pp. 1–16, 2021.
- [214] K. Bhakta, J. Camargo, P. Kunapuli, L. Childers, and A. Young, “Impedance control strategies for enhancing sloped and level walking capabilities for individuals with transfemoral amputation using a powered multi-joint prosthesis,” *Military medicine*, vol. 185, no. Supplement_1, pp. 490–499, 2020.
- [215] E. J. Rouse, L. J. Hargrove, E. J. Perreault, and T. A. Kuiken, “Estimation of human ankle impedance during walking using the perturber robot,” in *2012 4th IEEE RAS & EMBS International Conference on Biomedical Robotics and Biomechatronics (BioRob)*, 2012, pp. 373–378.
- [216] S. Pfeifer, H. Vallery, M. Hardegger, R. Riener, and E. J. Perreault, “Model-based estimation of knee stiffness,” *IEEE transactions on biomedical engineering*, vol. 59, no. 9, pp. 2604–2612, 2012.
- [217] S. L. Delp, F. C. Anderson, A. S. Arnold, *et al.*, “Opensim: Open-source software to create and analyze dynamic simulations of movement,” *IEEE transactions on biomedical engineering*, vol. 54, no. 11, pp. 1940–1950, 2007.
- [218] J. Camargo, K. Bhakta, J. Maldonado-Contreras, S. Zhou, K. Herrin, and A. Young, “Opensim model for biomechanical analysis with the open-source bionic leg,” in *2022 International Symposium on Medical Robotics (ISMR)*, IEEE, 2022, pp. 1–6.

- [219] Y. Wen, M. Li, J. Si, and H. Huang, "Wearer-prosthesis interaction for symmetrical gait: A study enabled by reinforcement learning prosthesis control," *IEEE transactions on neural systems and rehabilitation engineering*, vol. 28, no. 4, pp. 904–913, 2020.
- [220] M. Li, Y. Wen, X. Gao, J. Si, and H. Huang, "Toward expedited impedance tuning of a robotic prosthesis for personalized gait assistance by reinforcement learning control," *IEEE Transactions on Robotics*, vol. 38, no. 1, pp. 407–420, 2021.
- [221] X. Gao, J. Si, Y. Wen, M. Li, and H. Huang, "Reinforcement learning control of robotic knee with human-in-the-loop by flexible policy iteration," *IEEE Transactions on Neural Networks and Learning Systems*, 2021.
- [222] Y. Wen, J. Si, A. Brandt, X. Gao, and H. H. Huang, "Online reinforcement learning control for the personalization of a robotic knee prosthesis," *IEEE transactions on cybernetics*, vol. 50, no. 6, pp. 2346–2356, 2019.
- [223] R. Wu, M. Li, Z. Yao, W. Liu, J. Si, and H. Huang, "Reinforcement learning impedance control of a robotic prosthesis to coordinate with human intact knee motion," *IEEE Robotics and Automation Letters*, vol. 7, no. 3, pp. 7014–7020, 2022.
- [224] N. Thatte, H. Duan, and H. Geyer, "A method for online optimization of lower limb assistive devices with high dimensional parameter spaces," in *2018 IEEE International Conference on Robotics and Automation (ICRA)*, IEEE, 2018, pp. 5380–5385.
- [225] N. Hansen, "The cma evolution strategy: A comparing review," *Towards a new evolutionary computation*, pp. 75–102, 2006.
- [226] J. Camargo, A. Ramanathan, W. Flanagan, and A. Young, "A comprehensive, open-source dataset of lower limb biomechanics in multiple conditions of stairs, ramps, and level-ground ambulation and transitions," *Journal of Biomechanics*, p. 110320, 2021, ISSN: 0021-9290. DOI: <https://doi.org/10.1016/j.jbiomech.2021.110320>.
- [227] D. Quintero Maldonado, E. Reznick, D. Lambert, S. Rezazadeh, L. Gray, and R. Gregg, "Intuitive clinician control interface for a powered knee-ankle prosthesis: A case study," *IEEE Journal of Translational Engineering in Health and Medicine*, vol. PP, pp. 1–1, Nov. 2018.
- [228] J. A. Sturk, E. D. Lemaire, E. H. Sinitski, *et al.*, "Maintaining stable transfemoral amputee gait on level, sloped and simulated uneven conditions in a virtual environment," *Disability and Rehabilitation: Assistive Technology*, vol. 14, no. 3, pp. 226–235, 2019.
- [229] E. H. Sinitski, E. D. Lemaire, N. Baddour, M. Besemann, N. Dudek, and J. S. Hebert, "Maintaining stable transtibial amputee gait on level and simulated uneven conditions in a virtual environment," *Disability and Rehabilitation: Assistive Technology*, vol. 16, no. 1, pp. 40–48, 2021.

- [230] A. Vrieling, H. Van Keeken, T. Schoppen, *et al.*, “Obstacle crossing in lower limb amputees,” *Gait & posture*, vol. 26, no. 4, pp. 587–594, 2007.
- [231] C. T. Barnett, R. C. Polman, and N. Vanicek, “Longitudinal kinematic and kinetic adaptations to obstacle crossing in recent lower limb amputees,” *Prosthetics and Orthotics International*, vol. 38, no. 6, pp. 437–446, 2014.
- [232] A. Olenšek, M. Zadavec, H. Burger, and Z. Matjačić, “Dynamic balancing responses in unilateral transtibial amputees following outward-directed perturbations during slow treadmill walking differ considerably for amputated and non-amputated side,” *Journal of NeuroEngineering and Rehabilitation*, vol. 18, no. 1, pp. 1–11, 2021.
- [233] M. J. Major, C. K. Serba, and K. E. Gordon, “Perturbation recovery during walking is impacted by knowledge of perturbation timing in below-knee prosthesis users and non-impaired participants,” *Plos one*, vol. 15, no. 7, e0235686, 2020.
- [234] S. King, M. Eveld, A. Martínez, K. Zelik, and M. Goldfarb, “A novel system for introducing precisely-controlled, unanticipated gait perturbations for the study of stumble recovery,” *Journal of NeuroEngineering and Rehabilitation*, vol. 16, p. 69, Jun. 2019.
- [235] M. Eveld, S. King, K. Zelik, and M. Goldfarb, “Factors leading to falls in transfemoral prosthesis users: A case series of sound-side stumble recovery responses,” *Journal of NeuroEngineering and Rehabilitation*, vol. 19, Sep. 2022.
- [236] A. Naseri, M. Liu, I.-C. Lee, W. Liu, and H. Huang, “Characterizing prosthesis control fault during human-prosthesis interactive walking using intrinsic sensors,” *IEEE Robotics and Automation Letters*, vol. 7, no. 3, pp. 8307–8314, 2022.
- [237] M. Gordon, N. Thatte, and H. Geyer, “Online learning for proactive obstacle avoidance with powered transfemoral prostheses,” in *2019 International Conference on Robotics and Automation (ICRA)*, 2019, pp. 7920–7925.
- [238] I.-C. Lee, M. Liu, M. D. Lewek, X. Hu, W. G. Filer, and H. Huang, “Towards safe wearer-prosthesis interaction: Evaluation of gait stability and human compensation strategy under faults in robotic transfemoral prostheses,” *IEEE Transactions on Neural Systems and Rehabilitation Engineering*, 2022.
- [239] J. Camargo, K. Bhakta, K. Herrin, and A. Young, “Biomechanical evaluation of stair ambulation using impedance control on an active prosthesis,” *Journal of Biomechanical Engineering*, vol. 145, no. 2, p. 021 007, 2022.
- [240] J. M. Caputo and S. H. Collins, “Prosthetic ankle push-off work reduces metabolic rate but not collision work in non-amputee walking,” *Scientific reports*, vol. 4, no. 1, pp. 1–9, 2014.

- [241] E. J. Rouse, L. M. Mooney, and H. M. Herr, “Clutchable series-elastic actuator: Implications for prosthetic knee design,” *The International Journal of Robotics Research*, vol. 33, no. 13, pp. 1611–1625, 2014.
- [242] J. Lee and M. Goldfarb, “Swing-assist for enhancing stair ambulation in a primarily-passive knee prosthesis,” in *2020 IEEE International Conference on Robotics and Automation (ICRA)*, 2020, pp. 740–746.
- [243] H. L. Bartlett, S. T. King, M. Goldfarb, and B. E. Lawson, “A semi-powered ankle prosthesis and unified controller for level and sloped walking,” *IEEE Transactions on Neural Systems and Rehabilitation Engineering*, vol. 29, pp. 320–329, 2021.
- [244] J. T. Lee and M. Goldfarb, “Effect of a swing-assist knee prosthesis on stair ambulation,” *IEEE Transactions on Neural Systems and Rehabilitation Engineering*, vol. 29, pp. 2046–2054, 2021.
- [245] J. F. Lehmann, R. Price, R. Okumura, K. Questad, B. J. de Lateur, and A. Négretot, “Mass and mass distribution of below-knee prostheses: Effect on gait efficacy and self-selected walking speed,” *Archives of Physical Medicine and Rehabilitation*, vol. 79, no. 2, pp. 162–168, 1998, ISSN: 0003-9993.
- [246] W. Flowers and R. Mann, “An electrohydraulic knee-torque controller for a prosthesis simulator,” *Journal of biomechanical engineering*, vol. 99, no. 1, pp. 3–8, 1977.
- [247] J. M. Caputo and S. H. Collins, “A universal ankle–foot prosthesis emulator for human locomotion experiments,” *Journal of biomechanical engineering*, vol. 136, no. 3, 2014.
- [248] B. J. Hafner, J. E. Sanders, J. Czerniecki, and J. Fergason, “Energy storage and return prostheses: Does patient perception correlate with biomechanical analysis?” *Clinical Biomechanics*, vol. 17, no. 5, pp. 325–344, 2002.
- [249] B. L. Fylstra, I.-C. Lee, M. Li, M. Lewek, and H. Huang, *Human-prosthesis cooperation: Combining adaptive prosthesis control with visual feedback guided gait*, 2022.
- [250] A. Isidori, *Nonlinear Control Systems*. Springer London, 1995, ISBN: 9783540199168.
- [251] E. D. Sontag and Y. Wang, “On characterizations of the input-to-state stability property,” *Systems & Control Letters*, vol. 24, no. 5, pp. 351–359, 1995, ISSN: 0167-6911. DOI: [https://doi.org/10.1016/0167-6911\(94\)00050-6](https://doi.org/10.1016/0167-6911(94)00050-6).
- [252] E. Sontag, A. Agrachev, A. Morse, H. Sussmann, and V. Utkin, “Input to state stability: Basic concepts and results,” in Jan. 1970, vol. 1932, pp. 163–220, ISBN: 978-3-540-77644-4. DOI: [10.1007/978-3-540-77653-6_3](https://doi.org/10.1007/978-3-540-77653-6_3).
- [253] Y. Hurmuzlu and D. B. Marghitu, “Rigid body collisions of planar kinematic chains with multiple contact points,” *The International Journal of Robotics Research*, vol. 13, no. 1, pp. 82–92, 1994. DOI: [10.1177/027836499401300106](https://doi.org/10.1177/027836499401300106).

- [254] J. W. Grizzle, C. Chevallereau, R. W. Sinnet, and A. D. Ames, “Models, feedback control, and open problems of 3d bipedal robotic walking,” *Automatica*, vol. 50, no. 8, pp. 1955–1988, 2014, ISSN: 0005-1098.
- [255] A. D. Ames, R. Vasudevan, and R. Bajcsy, “Human-data based cost of bipedal robotic walking,” in *Proceedings of the 14th International Conference on Hybrid Systems: Computation and Control*, ser. HSCC ’11, Chicago, IL, USA: Association for Computing Machinery, 2011, pp. 153–162, ISBN: 9781450306294. DOI: 10.1145/1967701.1967725.
- [256] H. Zhao, A. Hereid, W.-l. Ma, and A. D. Ames, “Multi-contact bipedal robotic locomotion,” *Robotica*, vol. 35, no. 5, pp. 1072–1106, 2017. DOI: 10.1017/S0263574715000995.
- [257] S. Plagenhoef, F. G. Evans, and T. Abdelnour, “Anatomical data for analyzing human motion,” *Research Quarterly for Exercise and Sport*, vol. 54, no. 2, pp. 169–178, 1983.
- [258] W. Erdmann, “Geometry and inertia of the human body - review of research,” *Acta of Bioengineering and Biomechanics*, vol. 1, pp. 23–35, 1999.
- [259] A. De Luca and C. Manes, “Modeling of robots in contact with a dynamic environment,” *IEEE Transactions on Robotics and Automation*, vol. 10, no. 4, pp. 542–548, Sep. 1994, ISSN: 1042-296X. DOI: 10.1109/70.313104.
- [260] K. Khalaf, D. Gan, and H. Hemami, “Dynamics and control of separable coupled rigid body systems,” *Robotics and Biomimetics*, vol. 4, no. 1, p. 14, Nov. 2017, ISSN: 2197-3768. DOI: 10.1186/s40638-017-0068-0.
- [261] M. Vukobratovic, V. Matijevic, and V. Potkonjak, *Dynamics of Robots with Contact Tasks*, 1st. Springer-Science+Business Media, 2003. DOI: 10.1007/978-94-017-0397-0.
- [262] A. E. Martin and R. D. Gregg, “Stable, robust hybrid zero dynamics control of powered lower-limb prostheses,” *IEEE Transactions on Automatic Control*, vol. 62, no. 8, pp. 3930–3942, 2017. DOI: 10.1109/TAC.2017.2648040.
- [263] R. Gehlhar, Y. Chen, and A. D. Ames, “Data-driven characterization of human interaction for model-based control of powered prostheses,” in *2020 IEEE/RSJ International Conference on Intelligent Robots and Systems (IROS)*, 2020, pp. 4126–4133. DOI: 10.1109/IROS45743.2020.9341388,
- [264] https://youtu.be/eFZ2_s6FGUI.
- [265] K. Galloway, K. Sreenath, A. D. Ames, and J. W. Grizzle, “Torque saturation in bipedal robotic walking through control lyapunov function-based quadratic programs,” *IEEE Access*, vol. 3, pp. 323–332, 2015. DOI: 10.1109/ACCESS.2015.2419630.

- [266] A. Rantzer, B. S. Rüffer, and G. Dirr, “Separable lyapunov functions for monotone systems,” in *52nd IEEE Conference on Decision and Control*, Dec. 2013, pp. 4590–4594. DOI: [10.1109/CDC.2013.6760604](https://doi.org/10.1109/CDC.2013.6760604).
- [267] H. Ito, Z. Jiang, S. N. Dashkovskiy, and B. S. Rüffer, “Robust stability of networks of iiss systems: Construction of sum-type lyapunov functions,” *IEEE Transactions on Automatic Control*, vol. 58, no. 5, pp. 1192–1207, May 2013, ISSN: 2334-3303. DOI: [10.1109/TAC.2012.2231552](https://doi.org/10.1109/TAC.2012.2231552).
- [268] Y. Wang, “A converse lyapunov theorem with applications to iss-disturbance attenuation1,” *IFAC Proceedings Volumes*, vol. 29, no. 1, pp. 1960–1965, 1996, 13th World Congress of IFAC, 1996, San Francisco USA, 30 June - 5 July, ISSN: 1474-6670. DOI: [https://doi.org/10.1016/S1474-6670\(17\)57958-6](https://doi.org/10.1016/S1474-6670(17)57958-6).
- [269] S. Veer, Rakesh, and I. Poulakakis, “Poincaré analysis for hybrid periodic orbits of systems with impulse effects under external inputs,” *CoRR*, vol. abs/1712.03291, 2017.
- [270] S. Kolathaya and A. D. Ames, “Parameter to state stability of control Lyapunov functions for hybrid system models of robots,” *Nonlinear Analysis: Hybrid Systems*, vol. 25, pp. 174–191, 2017.
- [271] S. Kolathaya, J. Reher, A. Hereid, and A. D. Ames, “Input to state stabilizing control lyapunov functions for robust bipedal robotic locomotion,” in *2018 Annual American Control Conference (ACC)*, IEEE, 2018, pp. 2224–2230.
- [272] J. Hauser and Chung Choo Chung, “Converse lyapunov functions for exponentially stable periodic orbits,” *Systems & Control Letters*, vol. 23, no. 1, pp. 27–34, 1994, ISSN: 0167-6911. DOI: [https://doi.org/10.1016/0167-6911\(94\)90078-7](https://doi.org/10.1016/0167-6911(94)90078-7).
- [273] P. J. From, I. Schjølberg, J. T. Gravdahl, K. Y. Pettersen, and T. I. Fossen, “On the boundedness and skew-symmetric properties of the inertia and coriolis matrices for vehicle-manipulator systems,” *IFAC Proceedings Volumes*, vol. 43, no. 16, pp. 193–198, 2010, 7th IFAC Symposium on Intelligent Autonomous Vehicles, ISSN: 1474-6670. DOI: <https://doi.org/10.3182/20100906-3-IT-2019.00035>.
- [274] J. Reher and A. D. Ames, “A control lyapunov function-based controller for compliant hybrid zero dynamic walking on cassie,” *Submitted to IEEE Transactions on Robotics (T-RO)*, 2021.
- [275] A. Hereid, M. J. Powell, and A. D. Ames, “Embedding of slip dynamics on underactuated bipedal robots through multi-objective quadratic program based control,” in *53rd IEEE Conference on Decision and Control*, 2014, pp. 2950–2957. DOI: [10.1109/CDC.2014.7039843](https://doi.org/10.1109/CDC.2014.7039843).
- [276] Q. Nguyen and K. Sreenath, “Optimal robust control for bipedal robots through control lyapunov function based quadratic programs,” Jul. 2015. DOI: [10.15607/RSS.2015.XI.048](https://doi.org/10.15607/RSS.2015.XI.048).

- [277] S. Kolathaya, A. Hereid, and A. D. Ames, “Time dependent control lyapunov functions and hybrid zero dynamics for stable robotic locomotion,” in *2016 American Control Conference (ACC)*, 2016, pp. 3916–3921. DOI: 10.1109/ACC.2016.7525524.
- [278] H. Zhao and A. D. Ames, “Quadratic program based control of fully-actuated transfemoral prosthesis for flat-ground and up-slope locomotion,” in *American Control Conference (ACC), 2014*, IEEE, 2014, pp. 4101–4107.
- [279] Y. Ding, S. Law, B. Wu, *et al.*, “Average acceleration discrete algorithm for force identification in state space,” *Engineering Structures*, vol. 56, pp. 1880–1892, 2013, ISSN: 0141-0296. DOI: <https://doi.org/10.1016/j.engstruct.2013.08.004>.
- [280] <https://youtu.be/LhIX0HqRqnE>.
- [281] X. Xiong, A. D. Ames, and D. I. Goldman, “A stability region criterion for flat-footed bipedal walking on deformable granular terrain,” in *2017 IEEE/RSJ International Conference on Intelligent Robots and Systems (IROS)*, IEEE, 2017, pp. 4552–4559.
- [282] F. Sup, H. A. Varol, J. Mitchell, T. Withrow, and M. Goldfarb, “Design and control of an active electrical knee and ankle prosthesis,” in *2008 2nd IEEE RAS EMBS International Conference on Biomedical Robotics and Biomechatronics*, 2008, pp. 523–528. DOI: 10.1109/BIOROB.2008.4762811.
- [283] R. D. Gregg, T. Lenzi, L. J. Hargrove, and J. W. Sensinger, “Virtual constraint control of a powered prosthetic leg: From simulation to experiments with transfemoral amputees,” *IEEE Transactions on Robotics*, vol. 30, no. 6, pp. 1455–1471, Dec. 2014, ISSN: 1552-3098.
- [284] T. Elery, S. Rezazadeh, C. Nesler, and R. D. Gregg, “Design and validation of a powered knee–ankle prosthesis with high-torque, low-impedance actuators,” *IEEE Transactions on Robotics*, vol. 36, no. 6, pp. 1649–1668, 2020.
- [285] A. Razak, A. Zayegh, R. Begg, and Y. Wahab, “Foot plantar pressure measurement system: A review,” *Sensors (Basel, Switzerland)*, vol. 12, pp. 9884–9912, Dec. 2012. DOI: 10.3390/s120709884.
- [286] J. C. Horn and R. D. Gregg, “Nonholonomic virtual constraints for control of powered prostheses across walking speeds,” *IEEE Transactions on Control Systems Technology*, pp. 1–10, 2021. DOI: 10.1109/TCST.2021.3133823.
- [287] <https://youtu.be/iGVM-hS9pHc>.
- [288] R. Gehlhar and A. D. Ames, “Estimate-to-state stability for hybrid human-prosthesis systems,” in *2021 60th IEEE Conference on Decision and Control (CDC)*, IEEE, 2021, pp. 705–712. DOI: 10.1109/CDC45484.2021.9683029,

- [289] C. H. Soo and J. M. Donelan, “Mechanics and energetics of step-to-step transitions isolated from human walking,” *Journal of Experimental Biology*, vol. 213, no. 24, pp. 4265–4271, Dec. 2010, ISSN: 0022-0949.
- [290] V. I. Inman, H. J. Ralston, F. Todd, and J. C. Lieberman, *Human Walking*, 5th. Boca Raton, FL, USA: Williams and Wilkins, 1981, ISBN: 9780683043488.
- [291] A. D. Kuo, “Energetics of Actively Powered Locomotion Using the Simplest Walking Model,” *Journal of Biomechanical Engineering*, vol. 124, no. 1, pp. 113–120, Sep. 2001, ISSN: 0148-0731.
- [292] J. P. Reher, A. Hereid, S. Kolathaya, C. M. Hubicki, and A. D. Ames, “Algorithmic foundations of realizing multi-contact locomotion on the humanoid robot durus,” in *Algorithmic Foundations of Robotics XII: Proceedings of the Twelfth Workshop on the Algorithmic Foundations of Robotics*, K. Goldberg, P. Abbeel, K. Bekris, and L. Miller, Eds. Cham: Springer International Publishing, 2020, pp. 400–415, ISBN: 978-3-030-43089-4. DOI: 10.1007/978-3-030-43089-4_26.
- [293] G. Andréasson and L. Peterson, “Effects of shoe and surface characteristics on lower limb injuries in sports,” *International Journal of Sport Biomechanics*, vol. 2, no. 3, pp. 202–209, 1986. DOI: 10.1123/ijspb.2.3.202.
- [294] J. Perry and J. M. Burnfield, *Gait Analysis: Normal and Pathological Function*, 2nd. New York, NY, USA: Slack Incorporated, 2010, ISBN: 9781556427664.
- [295] <https://youtu.be/gdYcPq3Si18>.
- [296] X. Xiong and A. Ames, “3-D underactuated bipedal walking via H-LIP based gait synthesis and stepping stabilization,” *IEEE Transactions on Robotics*, 2022.
- [297] <https://youtu.be/g0hZlTypNI8>.
- [298] Y. Yu, J. Nassar, C. Xu, *et al.*, “Biofuel-powered soft electronic skin with multiplexed and wireless sensing for human-machine interfaces,” *Science robotics*, vol. 5, no. 41, eaaz7946, 2020. DOI: 10.1126/scirobotics.aaz7946,
- [299] https://youtu.be/lF5_ydnct3Q.
- [300] C. Gao, R. Gehlhar, A. D. Ames, S.-C. Liu, and T. Delbruck, “Recurrent neural network control of a hybrid dynamical transfemoral prosthesis with edgedrnn accelerator,” in *2020 IEEE International Conference on Robotics and Automation (ICRA)*, IEEE, 2020, pp. 5460–5466. DOI: 10.1109/ICRA40945.2020.9196984,
- [301] <https://youtu.be/DtAAMKSjeOg>.